

**REPORT DOCUMENTATION PAGE**

AFRL-SR-AR-TR-06-0110

The public reporting burden for this collection of information is estimated to average 1 hour per response, including the time for end maintaining the data needed, and completing and reviewing the collection of information. Send comments regarding this burden including suggestions for reducing the burden, to Department of Defense, Washington Headquarters Services, Directorate for Information Operations and Reports, 1215 Jefferson Davis Highway, Suite 1204, Arlington, VA 22202-4302. Respondents should be aware that notwithstanding any other provision that may require you to provide information for this collection of information if it does not display a currently valid OMB control number.

**PLEASE DO NOT RETURN YOUR FORM TO THE ABOVE ADDRESS.**

1. REPORT DATE (DD-MM-YYYY)		2. REPORT TYPE Final Report		3. DATES COVERED (From - To) 1 Apr 2003 - 31 Dec 2005	
4. TITLE AND SUBTITLE  Modeling of Unilateral Contact Conditions in Aerospace Systems				5a. CONTRACT NUMBER	
				5b. GRANT NUMBER  F49620-03-1-0176	
				5c. PROGRAM ELEMENT NUMBER	
6. AUTHOR(S)  Olivier A. Bauchau				5d. PROJECT NUMBER	
				5e. TASK NUMBER	
				5f. WORK UNIT NUMBER	
7. PERFORMING ORGANIZATION NAME(S) AND ADDRESS(ES) School of Aerospace Engineering Georgia Institute of Technology Atlanta GA 30332-0150				8. PERFORMING ORGANIZATION REPORT NUMBER	
9. SPONSORING/MONITORING AGENCY NAME(S) AND ADDRESS(ES) USAF/APRL AFOSR 875 N. Randolph Street Arlington VA 22203 <i>Dr Alred</i>				10. SPONSOR/MONITOR'S ACRONYM(S)  AFOSR	
				11. SPONSOR/MONITOR'S REPORT NUMBER(S)	
12. DISTRIBUTION/AVAILABILITY STATEMENT  Distribution Statement A. Approved for public release; distribution is unlimited.					
13. SUPPLEMENTARY NOTES					
14. ABSTRACT Multibody dynamics analysis is a powerful tool for the comprehensive simulation of the dynamic response of various flexible aerospace systems that are important to the Air Force. Systems of arbitrary topology and complexity can be readily modeled; they include both aircrafts and spacecrafts. In present formulations, the joints connecting the various flexible bodies are not modeled per se. Rather, the effect of joints, i.e. the constraints they impose on the behavior of the entire system are modeled through a set of kinematic constraints; the piece of hardware that actually constitutes the joint is not modeled.					
15. SUBJECT TERMS					
16. SECURITY CLASSIFICATION OF:			17. LIMITATION OF ABSTRACT	18. NUMBER OF PAGES	19a. NAME OF RESPONSIBLE PERSON
a. REPORT	b. ABSTRACT	c. THIS PAGE			19b. TELEPHONE NUMBER (Include area code)
U	U	U	UU	173	

# MODELING OF UNILATERAL CONTACT CONDITIONS IN AEROSPACE SYSTEMS

## Final Report

### CONTRACT # F49620-03-1-0176

Olivier A. Bauchau, *School of Aerospace Engineering (404) 894-0042*  
[olivier.bauchau@ae.gatech.edu](mailto:olivier.bauchau@ae.gatech.edu)

Aldo A. Ferri, *School of Mechanical Engineering (404) 894-7403*  
[al.ferri@me.gatech.edu](mailto:al.ferri@me.gatech.edu)

*Georgia Institute of Technology*  
*270 Ferst Street*  
*Atlanta GA, 30332-0150, USA.*

### **Abstract**

Multibody dynamics analysis is a powerful tool for the comprehensive simulation of the dynamic response of various flexible aerospace systems that are important to the Air Force. Systems of arbitrary topology and complexity can be readily modeled; they include both aircrafts and spacecrafts. In present formulations, the joints connecting the various flexible bodies are not modeled *per se*. Rather, the effect of joints, *i.e.* the constraints they impose on the behavior of the entire system are modeled through a set of kinematic constraints; *the piece of hardware that actually constitutes the joint is not modeled.*

As multibody formulations become more widely accepted, the need to model a wider array of phenomena increases. In particular, it is necessary to develop methodologies for the analysis of unilateral contact conditions in joints and of the resulting normal and friction forces. The modeling of such effects is of unique importance to the Air Force. For instance, wear and free-play in control surface joints can lead to aeroelastic instabilities or limit cycle oscillations. The accurate modeling of joint frictional behavior is central to the design of precision space structures. Indeed, friction forces are used as a mechanism for damping out undesirable vibrations, but can also lead to locking during the deployment of space structures, or to the inaccurate positioning of precision optical components.

For realistic simulations, the actual piece of hardware and contact mechanics should be modeled more precisely. This involves a host of phenomena such as: contact kinematics, nonlinear normal contact forces between inelastic bodies, tangential loading, and sliding contact. Furthermore, the high level of nonlinearity associated with a number of these phenomena implies challenging numerical issues. Although friction forces can be readily evaluated from Coulomb friction laws, the resulting accuracy is questionable. Sticking and slipping can co-exist in different parts of the contact area, a phenomenon known as micro-slip. The actual relationship between the friction force, the normal pressure and the slip motion is not well understood. In reality, the friction force is known to depend on a host of other factors including the normal load, the instantaneous slip velocity and displacement, the history of the motion, surface roughness and wear, environmental factors such as temperature. A further complication is that the accurate

evaluation of the normal or pressure forces across the slip plane requires modeling of system dynamics in both normal and slip planes. Hence, joint behavior and system dynamics are intimately coupled. Finally, friction forces depend on the motion in a highly nonlinear way, complicating analytical and numerical solution procedures. Numerous models of friction have been developed and presented in the literature, each addressing some of the above issues. Ultimately, overall structural damping of complex jointed structures should be predicted from the frictional behavior of individual joints. These effects are seldom addressed by standard formulations and commercial packages, although they can significantly impact system dynamics.

### ***Statement of Objectives***

The objective of this research is to develop, implement and validate models that capture the behavior of joints in a realistic manner. These models will be presented within the framework of a finite element based, nonlinear multibody dynamics formulation that ensure unconditional nonlinear stability of the computation for complex systems of arbitrary topology. The resulting piece of software will be validated and realistic cases of relevance to the Air Force will be treated. Applications will focus on the deployment and vibration of precision space structures.

The proposed approach can be divided into three parts. The first part deals with *joint configuration*. This purely kinematic part of the problem deals with the description of the configuration of the joint and the evaluation of the relative distance,  $q$ , between the contacting bodies. The second part handles the *contact conditions*. In most cases, contact at the joint will be of an intermittent nature. When contact occurs, normal contact forces and friction forces will arise. This unilateral contact condition is readily expressed in terms of the relative distance as  $q \geq 0$ . The enforcement of the unilateral contact condition is a critical aspect of the computational procedure. Finally, the *contact forces* that arise at the interface between contacting bodies must be evaluated according to a suitable phenomenological law. A survey of the multibody literature reveals that very simple models have been used thus far. For instance, the normal contact forces have been modeled using a quadratic potential that corresponds to a linear force-approach relationship, or the potential corresponding to the Hertz problem. The classical form of Coulomb's law has been the basis for the modeling of frictional phenomena.

The thrust of this proposal is to increase the versatility and accuracy of unilateral contact models in multibody systems. In order to achieve this goal, the three parts of the model must be considerably expanded. The kinematics of the contacting bodies must be generalized so as to allow a wide variety of joint configurations to be considered. In particular, the kinematics of the various types of joints used in space structures should be adequately modeled. The proper enforcement of the contact condition is central to the numerical stability of the proposed procedure. Robust schemes must be used to treat this challenging numerical problem. Finally, contact and frictional forces must be modeled in an accurate manner. Note that the problem is highly coupled because contact and frictional forces depend on the overall dynamic response of the system; joint behavior cannot be investigated without modeling the entire system.

The advantage of the proposed approach is that the three parts of the problem can be formulated and implemented independently. For instance, once a given friction law has been implemented, it can be used for various types of joints and for systems of

arbitrary configurations. It is also possible to evaluate the performance of various friction laws for a given joint configuration by comparing their predictions with experimental measurements. Because the formulation is developed within the framework of finite element based multibody dynamics, it can deal with systems of arbitrary configurations; it is equally applicable to aircraft problems, such as free-play in control surfaces or landing gears, or spacecraft problems such as satellite deployment or precision optical structures.

The last objective of this effort is to investigate mechanism for energy transfer and dissipation. While it is well understood that joint damping converts mechanical energy to heat, it is less obvious that friction can serve as a catalyst for "energy pumping," a phenomenon defined as the controlled one-way transfer of vibrational energy to a passive nonlinear sink, where the energy localizes and dissipates over time. Simple models will be used to demonstrate this phenomenon, and parameters affecting energy transfer and dissipation will be identified

### ***Achievements***

Over the period of the grant, research has focused on two areas of the problem: the development and implementation of joints with new kinematic configurations and energy transfer phenomena in the presence of frictional interfaces.

#### ***New joint configurations***

One of the thrusts of this research is to increase the versatility and accuracy of unilateral contact models in multibody systems. In order to achieve this goal, the kinematics of the contacting bodies must be generalized so as to allow a wide variety of joint configurations to be considered. In particular, the kinematics of the various types of joints used in space structures should be adequately modeled. A large number of configurations can be treated with the following joints: *backlash effects in relative rotation and displacements elements, planar and spherical joints with clearance, the spatial clearance joint, and planar and spatial contact joints.*

These various types of joints enable the modeling of a variety of kinematic configurations that encountered in aerospace systems. Simple problems like backlash can be readily treated, clearance problem in planar and spherical joints are specifically addressed, and finally, the contact between rigid bodies of arbitrary external shape enables the analysis of general, three-dimensional problems. For all joints, normal and tangential forces will develop at the contact point. Simulations were run with the various contact and frictional models developed during the first two years of this effort.

#### ***Accurate Simulation of Frictional Systems***

Friction is a natural phenomenon that occurs in many engineering systems. Although the concept of friction is easily understood, it is notoriously difficult to model and simulate. Many friction models contain a variety of nonlinear features such as discontinuities, hysteresis, internal dynamics, and other complications. These properties cause the friction models to be numerically stiff and therefore computationally cumbersome for simulation purposes. Simple models of friction, derived from the Coulomb friction paradigm, suggest that the friction force changes "discontinuously" as the direction of interfacial slip changes. Two main techniques have been used to deal

with the discontinuity. The first approach "smoothes" or "regularizes" the friction law in the vicinity of the discontinuity. Thus the discontinuous law is replaced with a "steep" albeit smooth friction law. While this partially alleviates the numerical stiffness problem, it introduces approximations that are not based in the physics of interfacial contact. The second approach used for the simulation of discontinuous frictional systems is to utilize a "switching strategy," also known as an event-driven strategy. In this approach, the system is simulated until the slip velocity across any friction interface changes sign. At the so-called switch times, one checks to determine whether the maximum-available friction force is sufficient to prevent slip from occurring. Depending on the outcome of this check, one either continues to integrate the "slipping equations," or one switches to the use of "sticking equations," which model the system with a stuck interface. There are two problems with this approach. First, the accuracy of the method hinges on accurate determination of the switching time. Second, the number of models that needs to be developed grows with the number of frictional interfaces in the structure.

Recently, advanced friction models have been proposed that represent a frictional interface in both the microslip and macroslip regimes. One such model, termed the LuGre friction model, is based on a bristle interpretation of the contacting surfaces. Microslip is captured by the deformation of the bristles prior to slip. The advantages of this model must be weighed against the computational difficulties during simulation. In particular, because the interfacial stiffness is much larger than the stiffness of the structural members themselves, time integration routines must be evaluated for accuracy and stability.

The efficient simulation of LuGre friction models was investigated in [2,3]. First, dynamics of the LuGre dynamics were studied analytically, to investigate the underlying source of the numerical stiffness and to determine the dependence of the stiffness severity on the governing nondimensional parameters. Next, an extensive simulation study was conducted to determine which integration methods worked best. Both explicit and implicit time-integration algorithms were considered. In addition, time-step adaptation schemes were developed that could choose appropriate step size in various sliding regimes.

#### *Energy Transfer through Frictional Interfaces*

It is well known that dry friction accounts for as much as 90% of the total damping of a built-up structure. The energy loss occurs primarily through the transformation of vibratory energy (kinetic and potential) into heat. Less understood is the role of friction in the transfer of energy from one substructure to another, or from one vibratory mode to another. As part of the AFOSR project, two different mechanisms for energy transfer were investigated.

**Structure-to-ground connection.** In the case of a structure-to-ground connection, the frictional interface can act as a catalyst for pumping energy from low-frequency modes to high-frequency modes. Specifically, it is possible for stick-slip motion at the frictional interface to excite and transfer energy to a high-frequency mode, where it may be dissipated more rapidly. In [3,4] this phenomenon was studied using a three-degree-of-freedom (3DOF) system. It was found that favorable tuning conditions exist where the energy transfer is maximized.

**Structure-to-structure connection.** In the case of a structure-to-structure connection, friction still plays a vital role in the dissipation of energy, but the energy pumping scenario is of less importance. Instead, energy dissipation is best when the natural frequencies of the connected substructures are dissimilar. When natural frequencies coincide, sliding across the frictional interface is discouraged, resulting in relatively poor damping. Using controllability concepts, it is possible to predict the friction damping performance based on the controllability of the structure based on joint forces. Such a metric provides a valuable tool in comparing different structural designs from an energy dissipation standpoint.

### ***Publications***

The work performed under this grant has been summarized in a number of papers that are appended to this report.

1. Bauchau, O.A. and Ju, C.K.: "*Modeling Friction Phenomena in Flexible Multibody Dynamics.*" To appear in the special edition of the *Computer Methods in Applied Mechanics and Engineering Journal* on Computational Multibody Dynamics.
2. Do, N., Ferri, A.A., and Bauchau, O.A., 2005 "Efficient Simulation of a Dynamic System with LuGre Friction," 2005 ASME International Design Engineering Technical Conferences & Computers and Information In Engineering Conference, Long Beach, California, September 24-28, 2005. Submitted to the ASME *Journal of Computational and Nonlinear Dynamics.*
3. Do, N., 2005, "Modeling of Frictional Contact Conditions in Structures," School of Mechanical Engineering, Georgia Tech, Atlanta, GA, 30332-0405, August, 2005.
4. Do, N., and Ferri, A.A., "Energy Transfer and Dissipation in a Three-Degree-of-Freedom System with Stribeck Friction," Proceedings of the 2005 ASME IMECE Conference, Orlando, FL, Nov. 5-11. (In preparation for journal submission.)

# Modeling Friction Phenomena in Flexible Multibody Dynamics

Olivier A. Bauchau and Changkuan Ju

*Daniel Guggenheim School of Aerospace Engineering, Georgia Institute of Technology, 270 Ferst Dr., Atlanta, GA 30332, USA*

---

## Abstract

The dynamic response of flexible systems of arbitrary topology and complexity are now readily modeled using multibody dynamics analysis concepts. In most formulations, the joints connecting the flexible bodies of the system are not modeled *per se*: only the effect of joints is modeled through a set of kinematic constraints. This paper focuses on the development of methodologies for the analysis of unilateral contact conditions in joints and of the resulting normal and friction forces. This involves a host of phenomena such as: contact kinematics, contact conditions, and the modeling of the normal and tangential contact forces. Furthermore, the high level of nonlinearity associated with a number of these phenomena implies challenging numerical issues. Although friction forces can be readily evaluated using Coulomb friction law, the resulting accuracy is questionable: sticking and slipping can co-exist in different parts of the contact area, a phenomenon known as micro-slip. Numerous models of friction have been developed and presented in the literature; application of the LuGre model will be discussed in this paper.

*Key words:* Multibody systems, Friction phenomena, LuGre model

---

## 1 Introduction

Multibody dynamics analysis is a powerful tool for the comprehensive simulation of the dynamic response of flexible systems of arbitrary topology and complexity. In present formulations, the joints connecting the various flexible bodies are rarely modeled *per se*. Rather, the effect of joints, *i.e.* the constraints they impose on the behavior of the entire system are modeled through a set of kinematic constraints; *the piece of hardware that actually constitutes the joint is not modeled.*

As multibody formulations become more widely accepted, the need to model a wider array of phenomena increases. In particular, it is necessary to develop methodologies for the analysis

of unilateral contact conditions in joints and of the resulting normal and friction forces. For realistic simulations, the actual piece of hardware and contact mechanics should be modeled more precisely. This involves a host of phenomena such as: contact kinematics, nonlinear normal contact forces, tangential loading, and sliding contact. Furthermore, the high level of nonlinearity associated with a number of these phenomena implies challenging numerical issues. Although friction forces can be readily evaluated from Coulomb friction laws, the resulting accuracy is questionable. Sticking and slipping can co-exist in different parts of the contact area, a phenomenon known as micro-slip. The actual relationship between the friction force, the normal pressure and the slip motion is not well understood. A further complication is that the accurate evaluation of the normal or pressure forces across the slip plane requires modeling of system dynamics in both normal and slip planes. Hence, joint behavior and system dynamics are intimately coupled. Finally, friction forces depend on the motion in a highly nonlinear way, complicating analytical and numerical solution procedures. Numerous models of friction have been developed and presented in the literature, each addressing some of the above issues.

This paper focuses on the development, implementation and validation of models that capture the behavior of joints in a realistic manner. These models will be presented within the framework of a finite element based, nonlinear multibody dynamics formulations that ensure unconditional nonlinear stability of the computation for complex systems of arbitrary topology. The proposed approach can be divided into three parts. First, the modeling of the joint configuration: this purely kinematic part of the problem deals with the description of the configuration of the joint and the evaluation of the relative distance,  $q$ , and the relative tangential velocity,  $v$ , between the contacting bodies. Second, the enforcement of the contact conditions: in most cases, contact at the joint will be of an intermittent nature. This unilateral contact condition is readily expressed in terms of the relative distance as  $q \geq 0$ . The enforcement of the unilateral contact condition is a critical aspect of the computational procedure. Finally, the evaluation of the contact forces, when contact occurs: this last part of the problems deals with the computation of the normal and tangential forces that arise at the interface between contacting bodies. The contact forces must be computed based on suitable phenomenological laws. A survey of the multibody literature reveals that very simple models have been used thus far. For instance, the normal contact forces have been modeled using a quadratic potential that corresponds to a linear force-approach relationship, or the potential corresponding to Hertz's problem [1]. The classical form of Coulomb's law has been the basis for the modeling of frictional phenomena [2].

Increasing the versatility and accuracy of unilateral contact models in multibody systems is the focus of this paper. To achieve this goal, the three parts of the model must be considerably expanded. The kinematics of the contacting bodies must be generalized so as to allow a variety of joint configurations to be considered. The proper enforcement of the contact condition is central to the numerical stability of the proposed procedure. Robust schemes must be used to treat this challenging numerical problem. Finally, contact and frictional forces must be modeled in an accurate manner. Note that the problem is highly coupled because contact and frictional forces depend on the overall dynamic response of the system; joint behavior cannot be investigated without modeling the entire system.

The advantage of the proposed approach is that the three parts of the problem can be formulated and implemented independently. For instance, once a given friction law has been implemented, it can be used for various types of joints and for systems of arbitrary configurations. It is also possible to evaluate the performance of various friction laws for a given joint configuration by comparing their predictions with experimental measurements. Because the formulation is developed within the framework of finite element based multibody dynamics, it can deal with systems of arbitrary configurations. This paper is laid out as follows: section 2 presents the kinematic description of two joints with clearance and the unilateral contact condition associated with the clearance is discussed in section 3. The modeling of the frictional process is presented in sections 4 and 5, and numerical examples of the proposed procedure appear in section 6.

## 2 Kinematic Description of Joints with Clearance

The kinematic description of joints with clearance will be divided into two- and three-dimensional models. For two-dimensional problems, a revolute joint with clearance, called the *planar clearance joint*, is viewed as a planar joint with a unilateral constraint. The clearance, or distance between the inner and outer races, can be evaluated from the kinematic variables associated with the planar joint. A similar approach can be applied to spherical joints with clearance. In the three-dimensional case, a *spatial clearance joint* is developed; the clearance can still be related to the kinematic variables of the joint, although this relationship is more complex.

### 2.1 The Planar Clearance Joint

A revolute joint with clearance can be modeled as a planar joint with the appropriate addition of a unilateral contact condition. Consider the planar joint depicted in fig. 1; the outer and inner races of the joint are modeled as bodies  $K$  and  $L$ , respectively. In the reference configuration, the position of body  $K$  is defined by its position vector  $\underline{u}_0^k$  and its orientation is determined by a body attached orthonormal basis  $\mathcal{B}_0^k = (\bar{e}_{10}^k, \bar{e}_{20}^k, \bar{e}_{30}^k)$ , with  $\bar{e}_{30}^k$  normal to the plane of joint and the over bar indicates a unit vector. The radius of the outer race is denoted  $\rho^k$ . In the deformed configuration, body  $K$  undergoes a displacement  $\underline{u}^k$  and its orientation is defined by an orthonormal basis  $\mathcal{B}^k = (\bar{e}_1^k, \bar{e}_2^k, \bar{e}_3^k)$ . The kinematic variables associated with body  $L$ , which represents the inner race of the revolute joint, are defined in a similar manner. The planar joint is associated with the following constraint conditions

$$C_1 = \bar{e}_1^{kT} \bar{e}_3^k = 0; \quad C_2 = \bar{e}_2^{kT} \bar{e}_3^k = 0; \quad C_3 = \bar{e}_3^{kT} (\underline{u}_0 + \underline{u}) = 0, \quad (1)$$

where  $\underline{u}_0 = \underline{u}_0^\ell - \underline{u}_0^k$  and  $\underline{u} = \underline{u}^\ell - \underline{u}^k$ . Kinematic condition  $C_3 = 0$  implies that body  $L$  remains in the plane normal to  $\bar{e}_3^k$ . Conditions  $C_1 = C_2 = 0$  imply that  $\bar{e}_3^k$  remains normal to that same plane. The implementation of the holonomic constraints, eqs. (1), is discussed in ref. [3].

Contact may occur between the inner and outer races of the joint. As shown in fig. 1, the candidate contact points [2] are readily found as  $\underline{Z}^k = \underline{u}_0^k + \underline{u}^k + \rho^k \bar{n}$  and  $\underline{Z}^\ell = \underline{u}_0^\ell + \underline{u}^\ell + \rho^\ell \bar{n}$ , where  $\bar{n} = (\underline{u}_0 + \underline{u}) / \|\underline{u}_0 + \underline{u}\|$  is the unit vector joining the centers of the two races. The relative distance between the races then becomes

$$q = \bar{n}^T (\underline{Z}^k - \underline{Z}^\ell) = \rho^k - \rho^\ell - \|\underline{u}_0 + \underline{u}\|. \quad (2)$$

The virtual work done by the normal contact force is  $\delta W = f^n \bar{n}^T \delta (\underline{Z}^k - \underline{Z}^\ell) = f^n \bar{n}^T \delta (\underline{u}^k - \underline{u}^\ell) = f^n \delta q$ , where  $f^n$  is the magnitude of the normal contact force. Expanding this result yields

$$\delta W = \begin{bmatrix} \delta \underline{u}^k \\ \delta \underline{u}^\ell \end{bmatrix}^T \underline{F}^n = \begin{bmatrix} \delta \underline{u}^k \\ \delta \underline{u}^\ell \end{bmatrix}^T f^n \begin{bmatrix} \bar{n} \\ -\bar{n} \end{bmatrix}. \quad (3)$$

The present formulation is developed within the framework of the time discontinuous Galerkin procedure [4] that provides algorithms for the integration of multibody systems featuring unconditional nonlinear stability [3]. In this approach, the discretization of the system is based on its configurations at the beginning and end times of a typical time step, denoted  $t_i$  and  $t_f$ , respectively, and the subscripts  $(\cdot)_i$  and  $(\cdot)_f$  denote the values of a quantity at  $t_i$  and  $t_f$ , respectively. In addition, the subscript  $(\cdot)_j$  indicates quantities at time  $t_j$ , immediately after the initial discontinuity. The normal contact force is taken to be constant over a time step and is discretized as

$$\underline{F}_m^n = f_m^n \begin{bmatrix} \underline{n}_m \\ -\underline{n}_m \end{bmatrix}, \quad (4)$$

where  $\underline{u}_m = (\underline{u}_f + \underline{u}_i)/2$ ,  $\underline{n}_m = 2(\underline{u}_0 + \underline{u}_m) / (\|\underline{u}_0 + \underline{u}_f\| + \|\underline{u}_0 + \underline{u}_i\|)$ , and  $f_m^n$  the constant magnitude of the contact force over the time step. Note that the discretization of the contact force does not involve discretized quantities at time  $t_j$ ; this contrasts with the discretization of the elastic forces in the flexible elements of the model that does involve the discretized quantities at time  $t_j$  [3], resulting in a linear in time approximation for these forces. For contact problems, it was found to be preferable to use constant in time approximations for the normal and tangential components of the contact force. It is readily verified that this discretization implies that the work done by the normal contact force over a time step is  $\Delta W = f_m^n (q_f - q_i)$ .

Next, the friction forces will be evaluated. The time derivatives of the candidate contact point positions are  $\dot{\underline{Z}}^k = \dot{\underline{u}}^k + \rho^k \tilde{\omega}^k \bar{n}$  and  $\dot{\underline{Z}}^\ell = \dot{\underline{u}}^\ell + \rho^\ell \tilde{\omega}^\ell \bar{n}$ , where  $(\cdot)$  denotes a derivative with respect to time, and  $\underline{\omega}^k$  and  $\underline{\omega}^\ell$  are the angular velocity vectors of bodies  $K$  and  $L$ , respectively. The relative velocity is  $\underline{V}^r = \dot{\underline{Z}}^\ell - \dot{\underline{Z}}^k$ , and the relative tangential velocity,  $\underline{V}^t$ , then becomes

$$\underline{V}^t = P \underline{V}^r, \quad (5)$$

where  $P = U - \bar{n} \bar{n}^T$  is the operator that projects the relative velocity vector onto the common tangential plane at the point of contact;  $U$  is the identity matrix. The unit vector along the relative tangential velocity is denoted  $\bar{e} = \underline{V}^t / V^t$ , where  $V^t = \|\underline{V}^t\|$ . The virtual work done

by the friction force is  $\delta W = -f^t \bar{e}^T (\delta \underline{Z}^\ell - \delta \underline{Z}^k)$ , where  $f^t$  is the magnitude of the frictional force. Expanding this expression yields

$$\delta W = \begin{bmatrix} \delta \underline{u}^k \\ \delta \psi^k \\ \delta \underline{u}^\ell \\ \delta \psi^\ell \end{bmatrix}^T \underline{F}^t = \begin{bmatrix} \delta \underline{u}^k \\ \delta \psi^k \\ \delta \underline{u}^\ell \\ \delta \psi^\ell \end{bmatrix}^T f^t \begin{bmatrix} \bar{e} \\ \rho^k \tilde{n} \bar{e} \\ -\bar{e} \\ -\rho^\ell \tilde{n} \bar{e} \end{bmatrix}. \quad (6)$$

The discretized friction force is selected as

$$\underline{F}_m^t = f_m^t \begin{bmatrix} \bar{e}_m \\ \rho^k \tilde{n}_m \bar{e}_m \\ -\bar{e}_m \\ -\rho^\ell \tilde{n}_m \bar{e}_m \end{bmatrix}, \quad (7)$$

where  $f_m^t$  is the constant magnitude of the tangential contact force over the time step. The work done by the friction forces over a single time step then becomes  $\Delta W = -f_m^t \Delta t V_m^t$ , provided the following definitions are made:  $\underline{V}_m^t = (U - \underline{n}_m \underline{n}_m^T) \underline{V}_m^r$ ,  $\bar{e}_m = \underline{V}_m^t / V_m^t$  and  $\Delta t \underline{V}_m^r = (\underline{u}_f - \underline{u}_i) + \rho^\ell \tilde{n}_m^T \underline{r}^\ell - \rho^k \tilde{n}_m^T \underline{r}^k$ , where  $\underline{r}^k$  and  $\underline{r}^\ell$  are the incremental rotations of bodies  $K$  and  $L$ , respectively. If the friction is dissipative,  $f^t \Delta t V^t \geq 0$ , and the above discretization guarantees that  $\Delta W = -f_m^t \Delta t V_m^t \leq 0$ , *i.e.* the discretization of the frictional process is dissipative. Note that the formulation presented here is also valid for a spherical joint with clearance.

## 2.2 The Spatial Clearance Joint

When the motion of the joint cannot be assumed to remain planar, a more complex, three-dimensional configuration must be considered, such as that presented in fig. 2. The outer race of the joint, denoted body  $K$ , is idealized as a cylinder of radius  $\rho^k$ . The inner race, denoted body  $L$ , is idealized as a thin disk of radius  $\rho^\ell$ . In the reference configuration, the position of the outer race is defined by the position vector  $\underline{u}_0^k$  of its center and its orientation is determined by a body attached orthonormal basis  $\mathcal{B}_0^k = (\bar{e}_{10}^k, \bar{e}_{20}^k, \bar{e}_{30}^k)$ , with  $\bar{e}_{30}^k$  along the axis of the cylinder. In the deformed configuration, the outer race center undergoes a displacement  $\underline{u}^k$  and its orientation is defined by an orthonormal basis  $\mathcal{B}^k = (\bar{e}_1^k, \bar{e}_2^k, \bar{e}_3^k)$ . The kinematic variables associated with body  $L$  are defined in a similar manner, with  $\bar{e}_{30}^\ell$  normal to the plane of the disk. An orthonormal basis  $\bar{d}_1^k, \bar{d}_2^k, \bar{d}_3^k$  is now defined in the following manner:  $\bar{d}_3^k = \bar{e}_3^k$  is along the axis of the cylinder,  $\bar{d}_1^k$  makes an arbitrary angle  $\phi$  with  $\bar{e}_1^k$ , and  $\bar{d}_2^k$  completes the basis

$$\bar{d}_1^k = \cos \phi \bar{e}_1^k + \sin \phi \bar{e}_2^k; \quad \bar{d}_2^k = -\sin \phi \bar{e}_1^k + \cos \phi \bar{e}_2^k; \quad \bar{d}_3^k = \bar{e}_3^k. \quad (8)$$

Consider now the plane tangent to the cylinder, defined by vectors  $\bar{d}_2^k$  and  $\bar{d}_3^k$ , as depicted in fig. 3. Point P, of position vector  $\underline{u}_0^k + \underline{u}^k + \rho^k \bar{d}_1^k$ , belongs to this plane.

The relative distance  $\bar{q}$  between disk  $L$  and this tangent plane is now evaluated. The candidate contact points on the plane and disk are denoted  $\underline{Z}^k$  and  $\underline{Z}^\ell$ , respectively, see fig. 3. The tangent to the disk at the candidate contact point must be in the plane of the disk and parallel to the contacting plane, *i.e.* normal to  $\bar{e}_3^\ell$  and  $\bar{d}_1^k$ , respectively. The following basis is now defined

$$\bar{d}_2^\ell = -\frac{\bar{d}_1^k \bar{e}_3^\ell}{h_1}; \quad \bar{d}_3^\ell = \bar{e}_3^\ell; \quad \bar{d}_1^\ell = \bar{d}_2^\ell \bar{e}_3^\ell, \quad (9)$$

where  $h_1 = \|\bar{d}_1^k \bar{e}_3^\ell\|$ . Clearly,  $\bar{d}_2^\ell$  is parallel to the tangent at the candidate contact point,  $\bar{d}_1^\ell$  points toward the candidate contact point, and  $\bar{d}_3^\ell$  is normal to the plane of the disk. The vector from point P to point  $\underline{Z}^\ell$  is

$$\underline{PZ}^\ell = [(\underline{u}_0^\ell + \underline{u}^\ell) + \rho^\ell \bar{d}_1^\ell] - [(\underline{u}_0^k + \underline{u}^k) + \rho^k \bar{d}_1^k] = \underline{u}_0 + \underline{u} + \rho^\ell \bar{d}_1^\ell - \rho^k \bar{d}_1^k, \quad (10)$$

where  $\underline{u}_0 = \underline{u}_0^\ell - \underline{u}_0^k$ , and  $\underline{u} = \underline{u}^\ell - \underline{u}^k$ . The relative distance  $\bar{q}$  is found by projecting  $\underline{PZ}^\ell$  along the unit vector  $-\bar{d}_1^k$ , see fig. 3, to find

$$\bar{q} = -\bar{d}_1^{kT} \underline{PZ}^\ell = -\bar{d}_1^{kT} (\underline{u}_0 + \underline{u}) - \rho^\ell \bar{d}_1^{kT} \bar{d}_1^\ell + \rho^k. \quad (11)$$

As shown in fig. 3, the candidate contact point  $\underline{Z}^k$  is in the tangent plane, but not necessarily on the cylindrical surface defining the outer race of the joint. The relative distance  $\bar{q}$  defined by eq. (11) is clearly a function of the angle  $\phi$  that defines the location of the tangent plane around the cylinder. The relative distance  $q$  between the cylinder and disk is found by minimizing  $\bar{q}$  with respect to the choice of  $\phi$ , *i.e.* by setting  $d\bar{q}/d\phi = 0$  to find

$$\bar{d}_2^{kT} [\rho^\ell \frac{g_1}{h_1} \bar{e}_3^\ell - (\underline{u}_0 + \underline{u})] = 0, \quad (12)$$

where  $g_1 = \bar{e}_3^{\ell T} \bar{d}_1^k$ . Note that for small angles  $g_1 \approx 0$  and  $h_1 \approx 1$ . The same result could be obtained by imposing the condition that  $\underline{PZ}^\ell$  be orthogonal to  $\bar{d}_2^k$ . In summary, the relative distance between the inner and outer races of the joint is

$$q = \rho^k - \rho^\ell h_1 - \bar{d}_1^{kT} (\underline{u}_0 + \underline{u}), \quad (13)$$

where  $h_1 = \|\bar{d}_1^k \bar{e}_3^\ell\| = \bar{d}_1^{kT} \bar{d}_1^\ell$ , and angle  $\phi$  is implicitly defined by eq. (12).

If contact occurs, the virtual work done by the normal contact force is  $\delta W = f^n \bar{d}_1^{kT} \delta(\underline{Z}^k - \underline{Z}^\ell) = f^n \bar{d}_1^{kT} \delta(q \bar{d}_1^k) = f^n \delta q$ , where  $f^n$  is the magnitude of the normal contact force. Expand-

ing this result yields

$$\delta W = \begin{bmatrix} \delta \underline{u}^k \\ \delta \psi^k \\ \delta \underline{u}^\ell \\ \delta \psi^\ell \end{bmatrix}^T \underline{F}^n = \begin{bmatrix} \delta \underline{u}^k \\ \delta \psi^k \\ \delta \underline{u}^\ell \\ \delta \psi^\ell \end{bmatrix}^T f^n \begin{bmatrix} \bar{d}_1^k \\ (\rho^\ell g_1/h_1) \underline{h}_1 - \bar{d}_1^k(\underline{u}_0 + \underline{u}) \\ -\bar{d}_1^k \\ -(\rho^\ell g_1/h_1) \underline{h}_1 \end{bmatrix}, \quad (14)$$

where  $\underline{h}_1 = \bar{d}_1^k \bar{e}_3^\ell$ . The proposed discretization of the normal contact force, taken to be constant over a time step, is

$$\underline{F}_m^n = f_m^n \begin{bmatrix} \underline{d}_{1m}^k \\ (\rho^\ell g_{1m}/h_{1m}) \underline{h}_{1m} - \bar{d}_{1m}^k(\underline{u}_0 + \underline{u}_m) \\ -\underline{d}_{1m}^k \\ -(\rho^\ell g_{1m}/h_{1m}) \underline{h}_{1m} \end{bmatrix}, \quad (15)$$

where  $\underline{d}_{1m}^k = (\bar{d}_{1f}^k + \bar{d}_{1i}^k)/2$ ,  $\underline{e}_{3m}^\ell = (\bar{e}_{3f}^\ell + \bar{e}_{3i}^\ell)/2$ ,  $\underline{h}_{1m} = \bar{d}_{1m}^k \underline{e}_{3m}^\ell$ ,  $h_{1m} = (h_{1f} + h_{1i})/2$ ,  $g_{1m} = (g_{1f} + g_{1i})/2$ , and  $f_m^n$  is the constant magnitude of the contact force over the time step. It is readily verified that this discretization implies that the work done by the normal contact force over a time step is  $\Delta W = f_m^n (q_f - q_i)$ .

Next, the friction forces will be evaluated. The time derivatives of the candidate contact point positions are  $\dot{\underline{z}}^k = \dot{\underline{u}}^k + \bar{\omega}^k \underline{\lambda}$  and  $\dot{\underline{z}}^\ell = \dot{\underline{u}}^\ell + \rho^\ell \bar{\omega}^\ell \bar{d}_1^\ell$ , where  $\underline{\lambda} = (\underline{u}_0 + \underline{u}) + \rho^\ell \bar{d}_1^\ell + q \bar{d}_1^k$ . The relative velocity is  $\underline{V}^r = \dot{\underline{z}}^\ell - \dot{\underline{z}}^k$ , and the relative tangential velocity,  $\underline{V}^t$ , then becomes

$$\underline{V}^t = P \underline{V}^r, \quad (16)$$

where  $P = U - \bar{d}_1^k \bar{d}_1^{kT}$  is the operator that projects the relative velocity vector onto the common tangential plane at the point of contact. The unit vector along the relative tangential velocity is denoted  $\bar{e} = \underline{V}^t / V^t$ , where  $V^t = \|\underline{V}^t\|$ . The virtual work done by the friction force is  $\delta W = -f^t \bar{e}^T (\delta \underline{Z}^\ell - \delta \underline{Z}^k)$ , where  $f^t$  is the magnitude of the frictional force. Expanding this expression yields

$$\delta W = \begin{bmatrix} \delta \underline{u}^k \\ \delta \psi^k \\ \delta \underline{u}^\ell \\ \delta \psi^\ell \end{bmatrix}^T \underline{F}^t = \begin{bmatrix} \delta \underline{u}^k \\ \delta \psi^k \\ \delta \underline{u}^\ell \\ \delta \psi^\ell \end{bmatrix}^T f^t \begin{bmatrix} \bar{e} \\ \bar{\lambda} \bar{e} \\ -\bar{e} \\ -\rho^\ell \bar{d}_1^\ell \bar{e} \end{bmatrix}. \quad (17)$$

The discretized friction force is selected as

$$\underline{F}_m^t = f_m^t \begin{bmatrix} \bar{e}_m \\ \tilde{\lambda}_m \bar{e}_m \\ -\bar{e}_m \\ -\rho^\ell \tilde{d}_{1m}^\ell \bar{e}_m \end{bmatrix}, \quad (18)$$

where  $f_m^t$  the constant magnitude of the contact force over the time step. The work done by the friction forces over a single time step then becomes  $\Delta W = -f_m^t \Delta t V_m^t$ , provided the following definitions are made:  $\underline{V}_m^t = (U - \underline{d}_{1m}^k \underline{d}_{1m}^{kT}) \underline{V}_m^r$ ,  $\bar{e}_m = \underline{V}_m^t / V_m^t$  and  $\Delta t \underline{V}_m^r = (\underline{u}_f - \underline{u}_i) + \rho^\ell \tilde{d}_{1m}^{\ell T} \underline{r}^\ell - \tilde{\lambda}_m^T \underline{r}^k$ , where  $\underline{r}^k$  and  $\underline{r}^\ell$  are the incremental rotations of bodies  $K$  and  $L$ , respectively. If the friction is dissipative,  $f^t \Delta t V^t \geq 0$ , and the above discretization guarantees that  $\Delta W = -f_m^t \Delta t V_m^t \leq 0$ , *i.e.* the discretization of the frictional process is dissipative. A realistic model of a journal bearing with clearance is obtained by using two spatial clearance joints connected by a rigid body, as depicted in fig. 4.

### 3 The Unilateral Contact Condition

The approaches to the modeling of unilateral contact conditions can be categorized in two main classes. The first one considers impact to be an impulsive phenomenon of null duration [5,6,7]. The configuration of the system is "frozen" during the impact, and an appropriate model is used to relate the states of the system immediately before and immediately after the event. There are two alternative formulations of this theory: Newton's and Poisson's methods. The first relates the relative normal velocities of the contacting bodies through the use of an appropriate restitution coefficient. The second divides the impact into two phases. At first, a compression phase brings the relative normal velocity of the bodies to zero through the application of an impulse at the contact location. Then, an expansion phase applies an impulse of opposite sign. The restitution coefficient relates the magnitudes of these two impulses. Although these methods have been used with success for multibody contact/impact simulations, it is clear that their accuracy is inherently limited by the assumption of a vanishing impact duration.

In the second approach, contact/impact events are of finite duration, and the time history of the resulting interaction forces is computed as a by-product of the simulation [8,9,10]. This is achieved by introducing a suitable phenomenological law for the contact forces, usually expressed as a function of the inter-penetration, or "approach," between the contacting bodies. This approach is obtained at each instant of the simulation by solving a set of kinematic equations that also express the minimum distance between the bodies when they are not in contact, such as eqs. (2) or (13). When the bodies are in contact, the relationship between the normal contact force and the approach is given by a constitutive law; various laws can be used, but the classical solution of the static contact problem presented by Hertz [1] has been implemented by many investigators. Energy dissipation can be added in

an appropriate manner, as proposed by Hunt and Crossley [11]. If the normal contact forces can be derived from a potential,  $V(q)$ , the work done by these forces over a time step of the simulation is  $\Delta W = f_m^n(q_f - q_i)$ , as implied by the time discretizations proposed in eqs. (4) and (15). The work done by these forces then becomes  $\Delta W = V(q_f) - V(q_i)$ , as expected, if the normal forces are discretized as  $f_m^n = (V(q_f) - V(q_i))/(q_f - q_i)$

To be successful, the approach described above must be complemented with a time step size selection procedure. When contact between the two bodies is about to take place, the contact model will dictate the time step for the analysis. Let  $q_0$  and  $q_1$  be the relative distances between the bodies for two consecutive time steps of size  $\Delta t_0$  and  $\Delta t_1$ , respectively. To avoid large penetration distances and the ensuing large normal contact forces at the first time step after contact, the time step size will be selected so that the change in relative distance,  $\Delta q = q_1 - q_0$ , be of the order of a user defined "characteristic penetration distance,"  $\varepsilon_p$ . To achieve this goal, the desired change in relative distance is selected as

$$\Delta q = \varepsilon_p \begin{cases} 1 & \text{if } \kappa \leq 1 \\ \kappa^\alpha & \text{if } \kappa > 1 \end{cases}, \quad (19)$$

where the quantity  $\kappa$ , defined as  $\kappa = (q_1/\varepsilon_p)/\bar{q}_{\min}$ , measures the proximity to contact. The desired time step size is then estimated as

$$\Delta t_{\text{new}} = \frac{\Delta q}{v_m}, \quad (20)$$

where  $v_m$  is the average relative velocity during the previous time step,  $v_m = 2(q_1 - q_0)/(\Delta t_0 + \Delta t_1)$ . The following values were found to give good results for a wide range of problems:  $\bar{q}_{\min} = 5$  and  $\alpha = 1.2$ .

It is important to note that the success of the present approach hinges upon two features of the model: the local flexibility of the contacting bodies and time adaptivity. If the contacting bodies are assumed to be rigid, the contact forces present a discontinuity at the instant of contact that causes numerical problems during the simulation. Taking local flexibility into account transforms the discontinuous force into a force with steep time gradients that are then resolved using time adaptivity. This contrasts with "event driven" computational strategies that first involve the determination of the exact time of contact, then a different set of governing equations is used when the bodies are in contact. If several contacts occur simultaneously, the complementarity principle is then a very effective solution strategy [2]. The choice between these two contrasting approaches is one based on computational considerations. For instance, the event driven approach is effective when dealing with systems of rigid bodies featuring multiple contacts; the complementarity principle then gives an elegant solution to an otherwise untractable problem. On the other hand, when dealing with systems modeled with finite element techniques, the approach proposed here seems to be more effective.

## 4 Modeling the Frictional Process

The detailed modeling of frictional forces poses unique computational challenges that will be illustrated using Coulomb's law as an example. When sliding takes place, Coulomb's law states that the friction force,  $\underline{F}^f$ , is proportional to the magnitude of the normal contact force,  $f^n$ ,  $\underline{F}^f = -\mu_k(v) f^n \underline{v}/v$ , where  $\mu_k(v)$  is the coefficient of kinetic friction and  $v$  the magnitude of the relative velocity vector tangent to the friction plane,  $\underline{v}$ . If the relative velocity vanishes, sticking takes place. In this case, the frictional force is  $|\underline{F}^f| \leq \mu_s f^n$ , where  $\mu_s$  is the coefficient of static friction.

Application of Coulomb's law involves discrete transitions from sticking to sliding and vice-versa, as dictated by the vanishing of the relative velocity or the magnitude of the friction force. These discrete transitions can cause numerical difficulties that are well documented, and numerous authors have advocated the use of a continuous friction law [12,13,14,10], typically written as

$$\underline{F}^f = -\mu_k(v) f^n \frac{\underline{v}}{v} (1 - e^{-|v|/v_0}), \quad (21)$$

where  $(1 - e^{-|v|/v_0})$  is a "regularization factor" that smoothes out the friction force discontinuity and  $v_0$  a characteristic velocity usually chosen to be small compared to the maximum relative velocity encountered during the simulation. The continuous friction law describes both sliding and sticking behavior, *i.e.* it completely replaces Coulomb's law. Sticking is replaced by "creeping" between the contacting bodies with a small relative velocity. Various forms of the regularizing factor have appeared in the literature; a comparison between these various models appears in [15].

Replacing Coulomb's friction law by a continuous friction law is a practice widely advocated in the literature; however, this practice presents a number of shortcomings [16]. First, it alters the physical behavior of the system and can lead to the loss of important information such as abrupt variations in frictional forces; second, it negatively impacts the computational process by requiring very small time step sizes when the relative velocity is small; and finally, it does not appear to be able to deal with systems presenting different values for the static and kinetic coefficients of friction.

In reality, frictional forces do not present the discontinuity described by Coulomb's law but rather, a velocity dependent, rapid variation. The regularization factor discussed above smoothes the discontinuity through a purely mathematical artifact that makes no attempt to more accurately represent the physical processes associated with the friction phenomenon. On the other hand, physics based models address the behavior of the frictional interface under small relative velocity. Typically, these micro-slip models allow small relative displacements to take place during "sticking;" the frictional interface then behaves like a very stiff viscous damper. Of course, such models are incapable of capturing the tangential stiffness of the joint during micro-slip. The most common micro-slip model is the Iwan model [17], also named elastic-perfectly plastic model [18]. In this approach, the frictional interface is modeled as a spring in series with a Coulomb friction element featuring a friction force of magnitude  $\mu f^n$ . When the force in the spring reaches this magnitude, the force in the Iwan model saturates

until the direction of slip reverses. An alternative approach to the treatment of micro-slip involves modification of the friction law itself.

Over the years, several friction models have been proposed that more accurately model various physical aspects of the friction process, such as the Valanis model [19]. Dahl [20] proposed a differential model able to emulate the hysteretic force-displacement behavior that characterizes micro-slip. The primary shortcoming of the Dahl model is that it does not include the dependence of the friction coefficient on slip velocity. In particular, it does not capture the rapid decrease in the friction coefficient as the interface begins to slip. Since this drop is a major contributor to stick-slip oscillations, its omission could be a major drawback in its application to joint dynamics. More recently, Canudas de Wit *et al.* have proposed the LuGre model [21] that is based on a phenomenological description of friction. This model is able to capture experimentally observed phenomena such as pre-sliding displacements, the hysteretic relationship between the friction force and the relative velocity, the variation of the break-away force as a function of force rate, and stick-slip motion associated with the Stribeck effect. The LuGre model has further been refined by Swevers *et al.* [22] and Lampaert *et al.* [23].

## 5 The LuGre Friction Model

The state of the art in friction modeling was advanced using the paradigm of intermeshing “bristles” to explain the friction forces between two contacting bodies [24]. The bristle model captures micro-slip and also accounts for the drop in friction force as the sliding speed is increased. However, according to its authors, the model is computationally burdensome. One of the more promising friction models developed from the bristle paradigm is the LuGre model [21], which captures the variation in friction force with slip velocity, making it a good candidate for studies involving stick-slip oscillations. Also, when linearized for very small motions, the LuGre model is shown to be equivalent to a linear spring/damper arrangement.

The LuGre model is an analytical friction model summarized by the following two equations.

$$\mu = \sigma_0 z + \sigma_1 \frac{dz}{dt} + \sigma_2 v; \quad (22)$$

$$\frac{dz}{dt} = v - \frac{\sigma_0 |v|}{\mu_k + (\mu_s - \mu_k) e^{-|v/v_s|^\gamma}} z. \quad (23)$$

The first equation predicts the instantaneous friction coefficient  $\mu$  as a function of the relative velocity,  $v$ , of the two contacting bodies and an internal state of the model,  $z$ , that represents the average deflection of elastic bristles whose interactions result in equal and opposite friction forces on the two bodies. The second equation is an evolution equation for the average bristle deflection. The coefficients  $\sigma_0$ ,  $\sigma_1$ , and  $\sigma_2$  are parameters of the model;  $\mu_s$  and  $\mu_k$  are the static and kinetic friction coefficients, respectively;  $v_s$  the Stribeck velocity; and  $\gamma$  a final model parameter which is often selected as  $\gamma = 2$ . The friction force acting

between the bodies is then

$$f^f = \mu f^n, \quad (24)$$

where  $f^n$  is the normal contact force.

For convenience, the model is now rewritten in nondimensional form as

$$\hat{\mu} = (1 - \hat{\beta}\hat{\sigma}_1)\hat{z} + (\hat{\sigma}_1 + \hat{\sigma}_2)\hat{v}; \quad (25)$$

$$\dot{\hat{z}} = \hat{v} - \hat{\beta}\hat{z}, \quad (26)$$

where  $\hat{\mu} = \mu/\mu_k$ ,  $\hat{v} = v/v_s$ ,  $\hat{z} = \sigma_0 z/\mu_k$ ,  $\hat{\sigma}_1 = \sigma_1 v_s/\mu_k$  and  $\hat{\sigma}_2 = \sigma_2 v_s/\mu_k$ . The nondimensional time is  $\tau = \Omega t$ , where

$$\Omega = \frac{\sigma_0 v_s}{\mu_k} \quad (27)$$

is the inverse of the time constant of the LuGre model. The notation  $(\cdot)'$  indicates a derivative with respect to this nondimensional time. Finally,  $\hat{\beta} = |\hat{v}|/\hat{g}(\hat{v})$ , where

$$\hat{g}(\hat{v}) = 1 + (\mu_s/\mu_k - 1)e^{-|\hat{v}|^\gamma}. \quad (28)$$

The evolution equation of the LuGre model, eq. (26), will be discretized in the following manner, based on a time discontinuous Galerkin procedure [4],

$$\frac{z_f - z_i}{\Delta\tau} + \beta_g \frac{z_f + z_j}{2} = v_g, \quad \frac{z_j - z_i}{\Delta\tau} - \beta_g \frac{z_f - z_j}{6} = 0, \quad (29)$$

where, for simplicity, the hat was dropped from all symbols. The subscript  $(\cdot)_g$  indicates the following average  $(\cdot)_g = 1/2((\cdot)_f + (\cdot)_j)$ . Note the presence of quantities at time  $t_j$  that will bring about the numerical dissipation required for the simulation of the frictional process.

### 5.1 Properties of the Proposed Discretization

For steady state solutions  $z_f = z_j = z_i = z_{ss}$ , eq. (29<sub>b</sub>) is identically satisfied, whereas eq. (29<sub>a</sub>) implies  $\beta_{ss} z_{ss} = v_{ss}$ , which can be written as  $|v|_{ss}(s_{v_{ss}} s_{z_{ss}} - |z|_{ss}/g(v_{ss})) = 0$ , where  $s_{v_{ss}} = \text{sign}(v_{ss})$  and  $s_{z_{ss}} = \text{sign}(z_{ss})$ . The first solution of this equation is  $|v|_{ss} = 0$ , which corresponds to sticking. The second is  $|z|_{ss} = g(v_{ss})$  with  $s_{v_{ss}} s_{z_{ss}} = 1$ , corresponding to steady state sliding. For large sliding velocity,  $g(v_{ss}) \approx 1$ , and hence,  $|z|_{ss} \approx 1$ .

The discretization also implies an important evolution law for the strain energy of the bristles. This evolution law is obtained by summing up eqs. (29<sub>a</sub>) and (29<sub>b</sub>) multiplied by  $(z_f + z_j)/2$  and  $-(z_f - z_j)/2$ , respectively, to yield

$$\frac{V_f - V_i}{\Delta\tau} = -|z|_g |v|_g \left( \frac{|z|_g}{g(v_g)} - s_{v_g} s_{z_g} \right) - \frac{1}{2\Delta\tau} \left( 1 + \frac{6}{\beta_g \Delta\tau} \right) (z_j - z_i)^2, \quad (30)$$

where  $V = 1/2 z^2$  is the nondimensional strain energy stored in the bristles. The second term of the evolution law, eq. (30), is a numerical dissipation term that is always negative. As the

time step decreases,  $z_j \rightarrow z_i$  as implied by the time discontinuous Galerkin approximation, and the numerical dissipation vanishes. The first term is negative whenever  $s_{v_g} s_{z_g} = -1$ , or when  $s_{v_g} s_{z_g} = 1$  and  $|z|_g / g(v_g) > 1$ . In summary,  $(V_f - V_i) / \Delta\tau < 0$  when  $|z|_g > g(v_g)$ . This implies the decreasing of the strain energy of the elastic bristles whenever  $|z|_g > g(v_g)$ . Since the strain energy is a quadratic form of the bristle average deflection, this implies the decreasing of the bristle deflection under the same conditions. Consequently, the bristle deflection must remain smaller than the upper bound of  $g(v_g)$ , which, in view of eq. (28), is equal to  $\mu_s / \mu_k$ . It follows that  $|z|_g < \mu_s / \mu_k$ . This inequality implies the finiteness of the bristle deflection and of its strain energy.

The discretizations of the friction forces for the clearance joints proposed in this work, eqs. (7) and (18), imply that the work done by the friction force over one time step is  $\Delta W = -f_m^t \Delta t V_m^t = -\mu_g f_g^n \Delta t v_g$ ; introducing eq. (25) then yields

$$\frac{\sigma_0 \Delta W}{\mu_k^2 \Delta\tau f_g^n} = -[(1 - \beta_g \sigma_1) z_g + (\sigma_1 + \sigma_2) v_g] v_g. \quad (31)$$

With the help of eq. (30), this work can be expressed as

$$\begin{aligned} \frac{\sigma_0 \Delta W}{\mu_k^2 \Delta\tau f_g^n} = & -\sigma_2 v_g^2 - \frac{z_g^2}{g(v_g)} |v|_g - \frac{V_f - V_i}{\Delta\tau} - \sigma_1 \left( 1 - \frac{|z|_g}{g(v_g)} s_{v_g} s_{z_g} \right) v_g^2 \\ & - \frac{1}{2\Delta\tau} \left( 1 + \frac{6}{\beta_g \Delta\tau} \right) (z_j - z_i)^2. \end{aligned} \quad (32)$$

The first two terms are always dissipative, with the second term corresponding to the main energy dissipation during sliding. The third term corresponds to the change in the potential of the elastic deformation of the bristles. Although this term can be positive or negative, it is finite since the potential is, itself, finite. As discussed earlier, when  $|z|_g > g(v_g)$ ,  $(V_f - V_i) / \Delta\tau < 0$  and the potential energy of the bristle deflection is released to the system. Under a similar condition,  $s_{v_g} s_{z_g} = 1$  and  $|z|_g > g(v_g)$ , the fourth term also becomes positive. Clearly, the third and fourth terms are non-dissipative only when the potential of the elastic bristles is released. As discussed earlier, this potential is finite and increases in its value stem from work done against friction forces; it is this very work that could be released at a later time. Finally, the last term is a numerical dissipation term. Note that as the time step size is decreased,  $(z_j - z_i)^2$  rapidly decreases, and the numerical dissipation vanishes. In summary, the proposed discretization of LuGre model guarantees the dissipative nature of the friction forces, when combined with the proposed discretizations for the friction forces, eqs. (7) and (18).

To be successful, the approach described above must be complemented with a time step size selection procedure. When friction occurs, the friction model will dictate the time step for the analysis. In view of the rapid variation of the function  $g(v)$  for small relative velocities, the time step size must be reduced when the relative velocity is of the order of the Stribeck

velocity  $v_s$ . To achieve this goal, the time step size for the next time step is selected as

$$\Omega \Delta t_{\text{new}} = \Delta \tau_{\text{min}} \begin{cases} 1 & \text{if } \nu \leq 1 \\ \nu^\alpha & \text{if } \nu > 1 \end{cases}, \quad (33)$$

where  $\Omega$ , given by eq. (27), is the inverse of the time constant of the LuGre model and the quantity  $\nu$ , defined as  $\nu = (V_r/v_s)/(\hat{v}_{\text{min}})$ , measures the smallness of the relative velocity. The existence of a time constant,  $1/\Omega$ , associated with the friction process as described by the LuGre model, enable a rational time adaptivity strategy. The following values of the parameters give good results for a wide range of problems:  $\Delta \tau_{\text{min}} = 0.02$ ,  $\hat{v}_{\text{min}} = 5$ , and  $\alpha = 1.2$ .

Here again, the success of the present approach hinges upon two features of the model: the physics based model of the friction force between the contacting bodies and time adaptivity. The discontinuous friction force implied by Coulomb's law is replaced by a force with steep time gradients that are then resolved using time adaptivity. This contrasts with "event driven" computational strategies that first involve the determination of transition times (from stick to slip or slip to stick), then different sets of governing equations are used depending on the specific friction regime. The complementarity principle can also be used to formulate friction problems [2]. When dealing with systems modeled with finite element techniques, the approach proposed here seems to be more effective because it involves a single set of governing equations for all friction regimes and furthermore, the unconditional stability of the integration process can be guaranteed based on energy arguments.

## 6 Numerical Examples

Two examples will be studied in this section. The same contact and friction models were used for both examples. A linear spring of stiffness constant  $k = 15$  MN/m was used for the contact model. The parameters for the time adaptivity algorithm, eq. (20), are:  $\epsilon_p = 3.0 \cdot 10^{-6}$  m,  $\hat{q}_{\text{min}} = 5$ , and  $\alpha = 1.2$ . The LuGre model was used to model the friction phenomena with the following parameters:  $\sigma_0 = 10^5$  m<sup>-1</sup>,  $\sigma_1 = \sigma_2 = 0$  s/m,  $v_s = 10^{-3}$  m/s,  $\mu_k = \mu_s = 0.30$ , and  $\gamma = 2$ .

### 6.1 The Spatial Mechanism

The spatial mechanism depicted in fig. 5 consists of crank of length  $L_a = 0.2$  m connected to the ground at point S by means of a revolute joint that allows rotation about an axis parallel to  $\bar{i}_1$ . The motion of the crank is prescribed as  $\theta = \Omega t$ , where  $\Omega = 20$  rad/s. At point P, the crank connects to a flexible link of length  $L_b = 1$  m through a universal joint that allows rotations about axes  $\bar{i}_2$  and  $\bar{i}_3$ . The other end of the link attaches to a spherical joint at point Q. In turns, this joint connects a to prismatic joint of mass  $m_Q = 5$  kg

that allows relative displacements along axis  $\bar{z}_1$ . Finally, this prismatic joint is attached to a flexible beam, cantilevered at point  $\mathbf{O}$ . The physical properties of the flexible beam are: bending stiffnesses,  $I_{22} = I_{33} = 23 \text{ kN}\cdot\text{m}^2$ , torsional stiffness,  $GJ = 18 \text{ kN}\cdot\text{m}^2$ , and mass per unit span,  $m = 1.6 \text{ kg/m}$ ; those of the link are: bending stiffnesses,  $I_{22} = I_{33} = 12 \text{ kN}\cdot\text{m}^2$ , torsional stiffness,  $GJ = 9 \text{ kN}\cdot\text{m}^2$ , and mass per unit span,  $m = 0.85 \text{ kg/m}$ ; finally, the sectional properties of the crank are: bending stiffnesses,  $I_{22} = 23.2$ ,  $I_{33} = 29.8 \text{ kN}\cdot\text{m}^2$ , torsional stiffness,  $GJ = 28 \text{ kN}\cdot\text{m}^2$ , and mass per unit span,  $m = 1.6 \text{ kg/m}$ .

Two cases will be contrasted in this example; for *case 1*, the spherical joint at point  $\mathbf{Q}$  is treated as a kinematic constraint, whereas in *case 2*, the same spherical joint features the clearance model described in section 2.1 with  $\rho^k = 50$  and  $\rho^\ell = 49.5 \text{ mm}$ . For *case 1*, the simulation was run at a constant time step of  $\Delta t = 10^{-3} \text{ s}$ ; for *case 2*, the time adaptivity algorithms were used. Simulations were run for a total of six revolutions of the crank to obtain a periodic solution, and results will be presented for the fifth revolution of the crank.

The relative tangential velocity at the clearance joint is shown in fig. 6 for *case 2*. Note the several occurrences of nearly vanishing relative velocities at crank angular positions from 150 to 250 degrees. The resulting frictional force is shown in fig. 7. Note that at crank angle of about 275 degrees, contact in the joint is lost and the frictional force vanishes. This intermittent contact behavior, coupled with the elastic response of the system, creates rapid variations in the normal contact force that are reflected in the friction force. Fig. 8 shows the time history of the root forces in the beam at point  $\mathbf{O}$ . Whereas the overall responses for *cases 1* and *2* are qualitatively similar, it is clear that the strong variations in both normal and tangential contact forces excite the elastic modes of the system, resulting in full coupling between the dynamic response of the system and the behavior of the contact forces. The same comments can be made concerning the link mid-span forces shown in fig. 9; the oscillatory component of the stresses would strongly impact the fatigue life of these structural components. Finally, the implication of the varying relative velocity on the time step size used in the simulation is evident in fig. 10; clearly, for this problem, the time step size for the simulation is driven by the friction model. The parameters associated with the time step size control algorithm for friction, eq. (33), are:  $\Delta\tau_{\min} = 5.0 \cdot 10^{-4}$ ,  $\hat{v}_{\min} = 5$ , and  $\alpha = 1.5$ .

## 6.2 The Supercritical Rotor

The simple rotor system depicted in fig. 11 features a flexible shaft of length  $L_s = 6 \text{ m}$  with a mid-span rigid disk of mass  $m_d = 5 \text{ kg}$  and radius  $R_d = 15 \text{ mm}$ . The shaft is a thin-walled, circular tube of mean radius  $R_m = 50 \text{ mm}$  and thickness  $t = 5 \text{ mm}$ ; its sectional properties are: bending stiffnesses,  $I_{22} = 28.2$  and  $I_{33} = 28.7 \text{ kN}\cdot\text{m}^2$ , torsional stiffness,  $GJ = 22.1 \text{ kN}\cdot\text{m}^2$ , and mass per unit span,  $m = 0.848 \text{ kg/m}$ . The center of mass of the shaft is located at a 1 mm offset from its geometric center. At point  $\mathbf{R}$ , the shaft is connected to the ground by means of a revolute joint; at point  $\mathbf{T}$ , it is supported by a spatial clearance joint. The radius of the cylinder is  $\rho^k = 80.8 \text{ mm}$  and that of the disk is  $\rho^\ell = 80 \text{ mm}$ . At first, the natural frequencies of the shaft were computed and the first critical speed zone was found

to correspond to shaft angular speeds  $\Omega \in [44.069, 44.453]$  rad/s.

The system is initially at rest and a torque is applied at point **R** with the following schedule

$$Q(t) = Q_0 \begin{cases} (1 - \cos 2\pi t) & t \leq t_s \\ (1 - \cos 2\pi t_s) & t > t_s \end{cases},$$

where  $Q_0 = 0.825$  N·m and  $t_s = 0.93$  s. The time history of the resulting angular velocity of the shaft is depicted in fig. 12 which also indicates the unstable region. After 2 s, the rotor has crossed the unstable region of operation and stabilizes at a supercritical speed of about 50 rad/sec. The trajectory of the mid-span point **M** is shown in fig. 13. Since the shaft must first cross the unstable operation zone, the trajectory first spirals away from the axis of rotation of the shaft, as expected. Once the unstable zone is crossed, the shaft regains equilibrium and due to the friction in the spatial clearance joint, the amplitude of the motion decreases. Since in supercritical operation the shaft is self centering, a displacement of about 1 mm (corresponding to the center of mass offset) is expected for point **M**. The time history of the normal contact force is depicted in fig. 14; large contact forces are generated as the shaft crosses the unstable zone, however, while regaining stability, intermittent contact episodes are observed, 2.1 and 2.6 s into the simulation. When contact is restored, large impact forces are experienced, up to about 100 N, *i.e.* an order of magnitude larger than those observed during the continuous contact regime. In supercritical operation, the contact force decreases to smaller levels. Similar behavior is observed in fig. 15 that depicts the bending moments at the root of the shaft. The parameters associated with the time step size control for friction, eq. (33), were selected as:  $\Delta\tau_{\min} = 0.1$ ,  $\hat{v}_{\min} = 500$ , and  $\alpha = 1.2$ .

In this example, the relative velocity at the spatial clearance joint always remains much larger than the Stribeck velocity, and hence, application of Coulomb's law would probably give satisfactory results. On the other hand, the first example presents numerous stick-slip transitions: the relative velocity at the joint vanishes numerous times at each revolution of the crank. These two examples show that the proposed approach to the modeling of friction forces by means of the LuGre model is capable of dealing the *various regimes of friction*. In the case of high relative velocity, the computational cost associated with the LuGre model is minimum, because its use has no impact on the required time step size, on the other hand, when low relative velocities imply stick slip events, the proposed approach still perform well, although small time step sizes are required.

## 7 Conclusions

The present paper has proposed an approach to increase the versatility and accuracy of unilateral contact models in multibody systems. Two joint configurations were developed, the planar and spatial clearance joints that can deal with typical configurations where contact and clearance are likely to occur. More general configurations could be developed based on the same principles. The kinematic analysis of the joint yields two important quantities:

the relative distance between the bodies that drives the intermittent contact model and the relative tangential velocity that drives the friction model. An arbitrary contact force-approach relationship can be used for the contact model. For the friction model, the use of the LuGre model was proposed in this work. This physics based model is capable of capturing a number of experimentally observed phenomena associated with friction. From a numerical stand point, it eliminates the discontinuity associated with Coulomb's friction law. Discretizations were proposed for both normal contact and friction forces that imply an energy balance for the former and energy dissipation for the latter. When combined with the energy decaying schemes used in this effort, these properties of the discretizations guarantee the nonlinear stability of the overall numerical process. The numerical simulations rely on time step adaptivity; simple, yet effective strategies were given to evaluate the required time step size when contact and friction are occurring. The efficiency of the proposed approach was demonstrated by realistic numerical examples that demonstrate the coupling between contact and friction forces and the overall dynamic response of the system.

## 8 Acknowledgments

This work was supported by the Air Force Office of Scientific Research under Contract # F49620-03-1-0176; Capt. Clark Allred is the contract monitor.

## References

- [1] S.P. Timoshenko and J.M. Gere. *Theory of Elastic Stability*. McGraw-Hill, Inc., New York, 1961.
- [2] F. Pfeiffer and C. Glocker. *Multi-Body Dynamics with Unilateral Contacts*. John Wiley & Sons, Inc, New York, 1996.
- [3] O.A. Bauchau. Computational schemes for flexible, nonlinear multi-body systems. *Multibody System Dynamics*, 2(2):169–225, 1998.
- [4] C. Johnson. *Numerical Solutions of Partial Differential Equations by the Finite Element Method*. Cambridge University Press, Cambridge, 1987.
- [5] T.R. Kane. Impulsive motions. *Journal of Applied Mechanics*, 15:718–732, 1962.
- [6] E.J. Haug, R.A. Wehage, and N.C. Barman. Design sensitivity analysis of planar mechanisms and machine dynamics. *ASME Journal of Mechanical Design*, 103:560–570, 1981.
- [7] Y.A. Khulief and A.A. Shabana. Dynamic analysis of constrained systems of rigid and flexible bodies with intermittent motion. *ASME Journal of Mechanisms, Transmissions, and Automation in Design*, 108:38–44, 1986.
- [8] Y.A. Khulief and A.A. Shabana. A continuous force model for the impact analysis of flexible multi-body systems. *Mechanism and Machine Theory*, 22:213–224, 1987.

- [9] H.M. Lankarani and P.E. Nikravesh. A contact force model with hysteresis damping for impact analysis of multi-body systems. *Journal of Mechanical Design*, 112:369–376, 1990.
- [10] A. Cardona and M. Géradin. Kinematic and dynamic analysis of mechanisms with cams. *Computer Methods in Applied Mechanics and Engineering*, 103:115–134, 1993.
- [11] K.H. Hunt and F.R.E. Crossley. Coefficient of restitution interpreted as damping in vibroimpact. *Journal of Applied Mechanics*, 112:440–445, 1975.
- [12] J.C. Oden and J.A.C. Martins. Models and computational methods for dynamic friction phenomena. *Computer Methods in Applied Mechanics and Engineering*, 52:527–634, 1985.
- [13] T. Baumeister, E.A. Avallone, and T. Baumeister III (eds.). *Marks' Mechanical Engineers Handbook*. McGraw-Hill, Inc., New York, 1978.
- [14] J.E. Shigley and C.R. Mischke. *Mechanical Engineering Design*. McGraw-Hill, Inc., New York, 1989.
- [15] A.K. Banerjee and T.R. Kane. Modeling and simulation of rotor bearing friction. *Journal of Guidance, Control and Dynamics*, 17:1137–1151, 1994.
- [16] O.A. Bauchau and J. Rodriguez. Modeling of joints with clearance in flexible multibody systems. *International Journal of Solids and Structures*, 39:41–63, 2002.
- [17] W.D. Iwan. On a class of models for the yielding behavior of continuous and composite systems. *ASME Journal of Applied Mechanics*, 89:612–617, 1967.
- [18] A.A. Ferri. Friction damping and isolation systems. *ASME Journal of Vibration and Acoustics*, 117B:196–206, 1995.
- [19] K.C. Valanis. A theory of viscoplasticity without a yield surface. *Archives of Mechanics*, 23(4):171–191, 1971.
- [20] P.R. Dahl. Solid friction damping of mechanical vibrations. *AIAA Journal*, 14:1675–1682, 1976.
- [21] C. Canudas de Wit, H. Olsson, K.J. Astrom, and P. Lischinsky. A new model for control of systems with friction. *IEEE Transactions on Automatic Control*, 40:419–425, 1995.
- [22] J. Swevers, F. Al-Bender, C.G. Ganesman, and T. Prajogo. An integrated friction model structure with improved presliding behavior for accurate friction compensation. *IEEE Transactions on Automatic Control*, 45(4):675–686, 2000.
- [23] V. Lampaert, J. Swevers, and F. Al-Bender. Modification of the Leuven integrated friction model structure. *IEEE Transactions on Automatic Control*, 47(4):683–687, 2002.
- [24] D.A. Haessig and B. Friedland. On the modeling and simulation of friction. *ASME Journal of Dynamic Systems, Measurement, and Control*, 113:354–362, 1991.

## List of Figures

1	Configuration of the planar clearance joint.	20
2	Configuration of the spatial clearance joint.	21
3	Relative distance between the candidate contact points.	22
4	Model of a journal bearing using two spatial clearance joints.	23
5	Configuration of the spatial mechanism.	24
6	Relative tangential velocity at the spherical joint for <i>case 2</i> .	25
7	Friction force at the spherical joint for <i>case 2</i> .	26
8	Beam root forces at point <b>O</b> . <i>Case 1</i> : dashed line; <i>case 2</i> : solid line. Force component $F_2$ : $\diamond$ , $F_3$ : $\circ$	27
9	Link mid-span forces. <i>Case 1</i> : dashed line; <i>case 2</i> : solid line.	28
10	Time step size used in the simulation for <i>case 2</i> .	29
11	Configuration of the supercritical rotor system.	30
12	Time history of the angular velocity of the shaft. The dashed lines indicate the unstable zone of operation: $\Omega \in [44.069, 44.453]$ rad/s.	31
13	Trajectory of the shaft mid-span point <b>M</b> . For $0 < t < 0.875$ s: solid line; for $0.875 < t < 1.065$ s: dashed line; for $1.065 < t < 1.340$ s: dashed-dotted line; for $1.340 < t < 1.650$ s: dotted line.	32
14	Time history of the normal contact force for the spatial clearance joint at point <b>T</b> .	33
15	Time history of root bending moments in the shaft at point <b>R</b> .	34

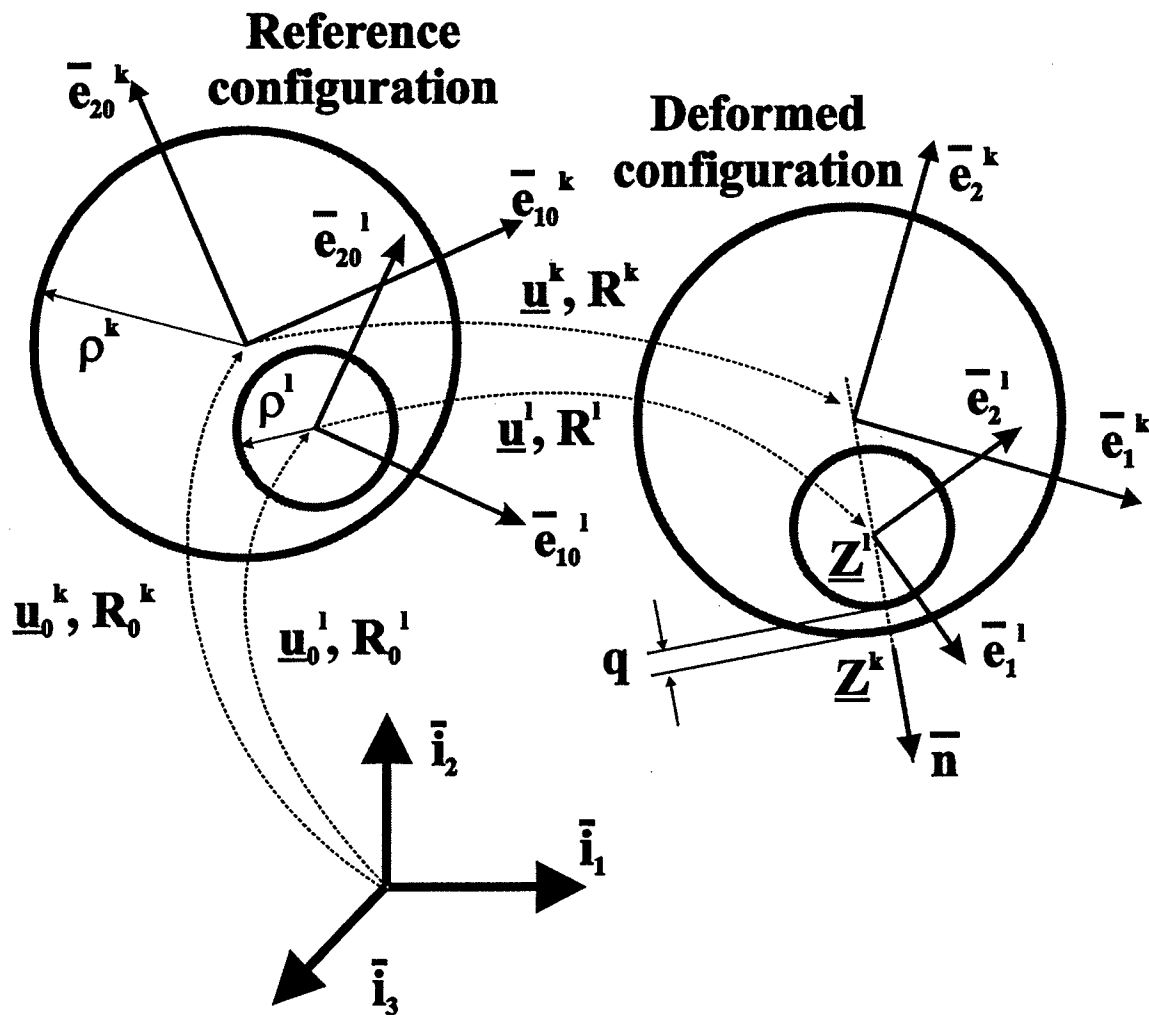


Figure 1. Configuration of the planar clearance joint.

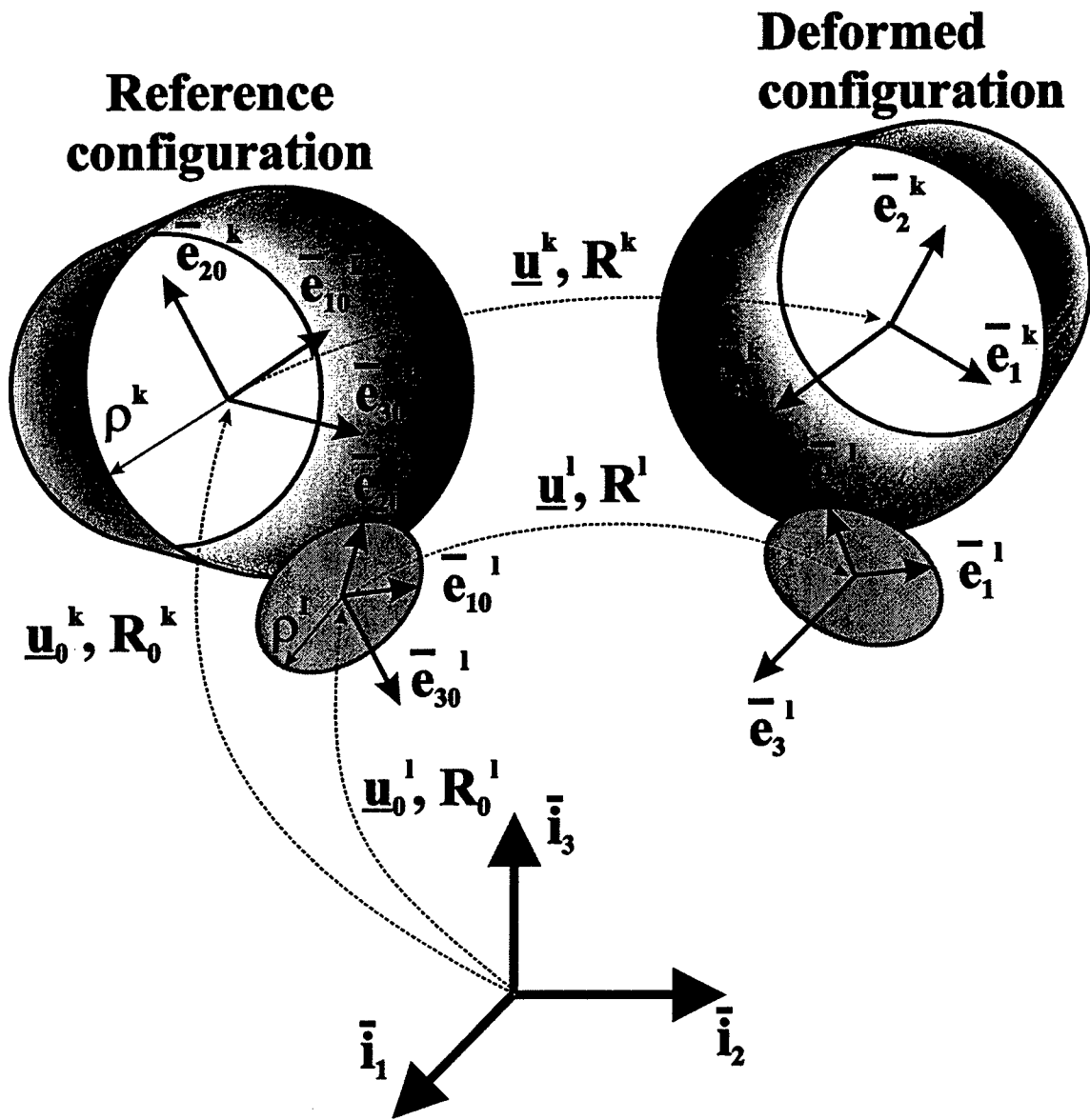


Figure 2. Configuration of the spatial clearance joint.

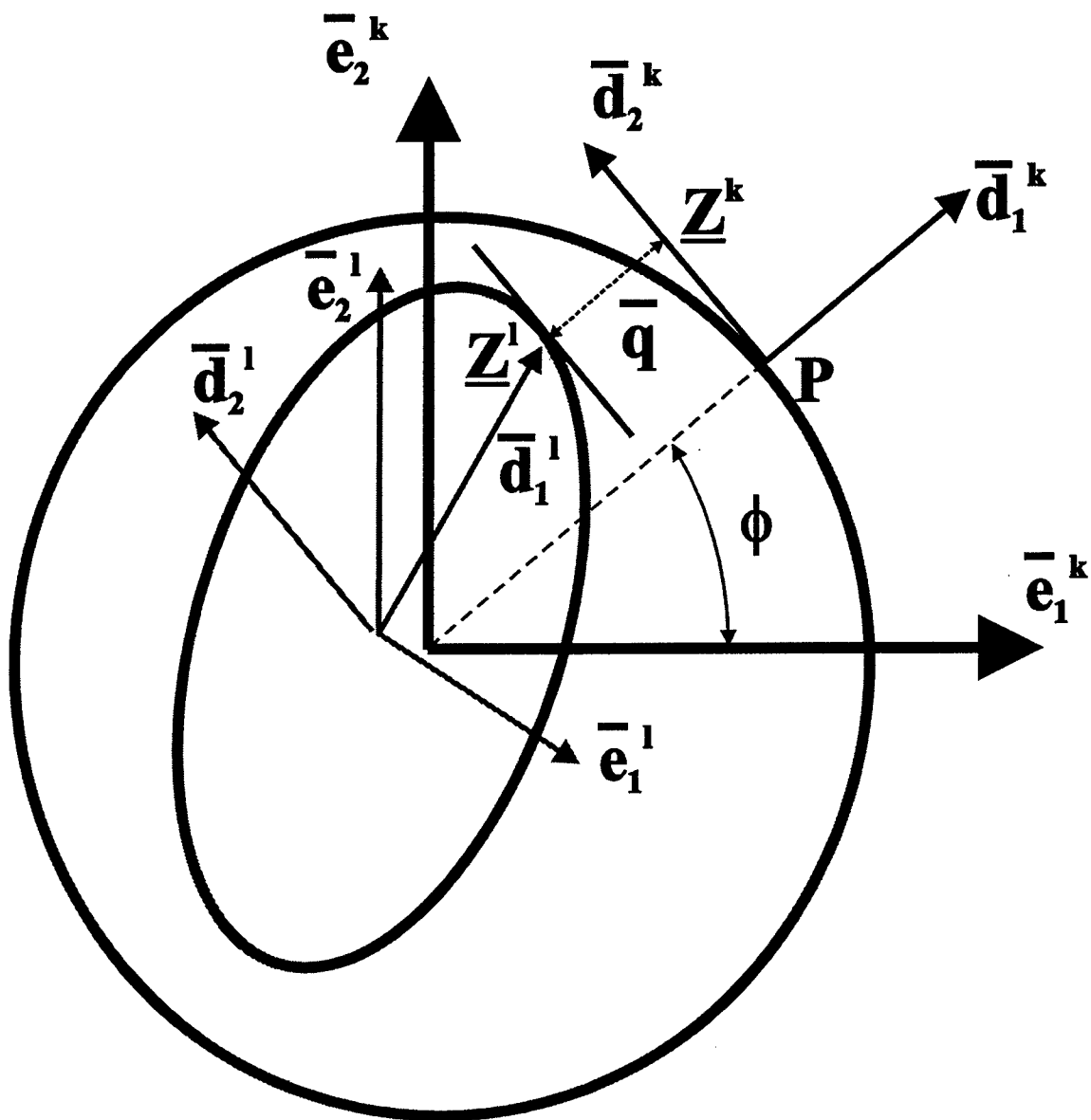


Figure 3. Relative distance between the candidate contact points.

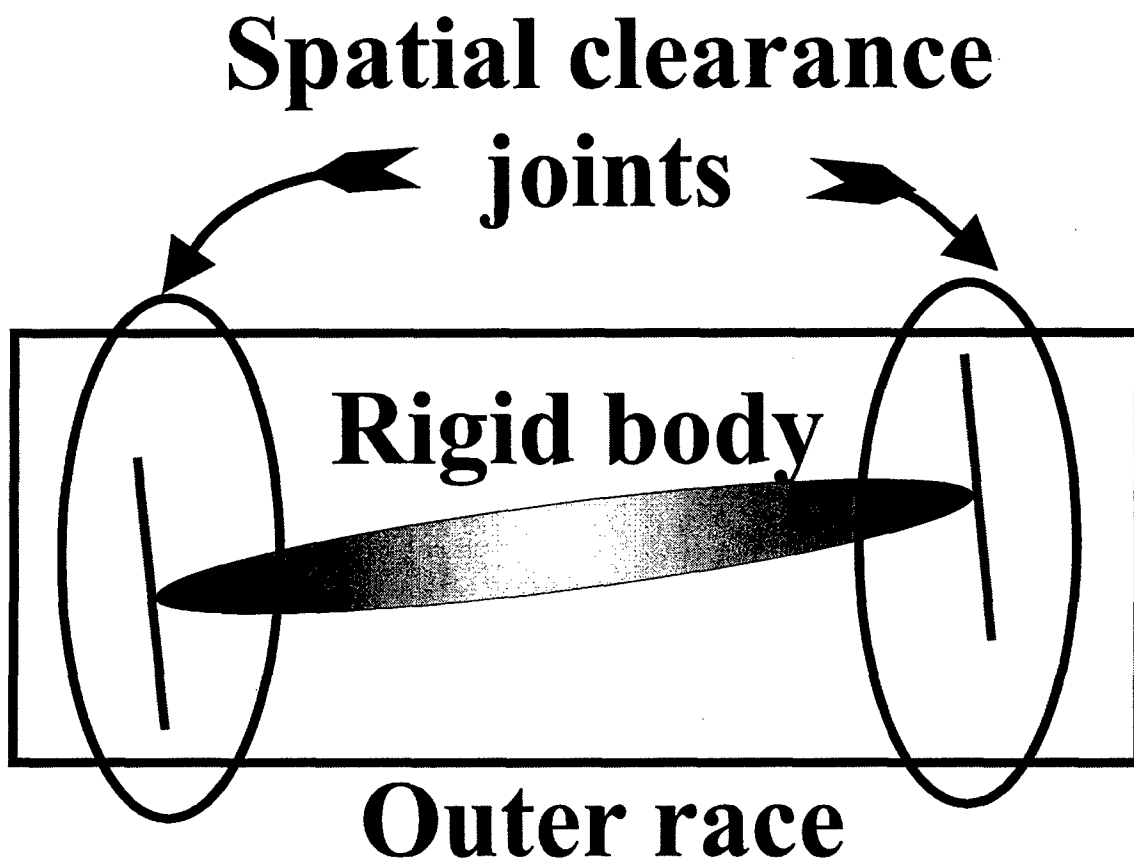


Figure 4. Model of a journal bearing using two spatial clearance joints.

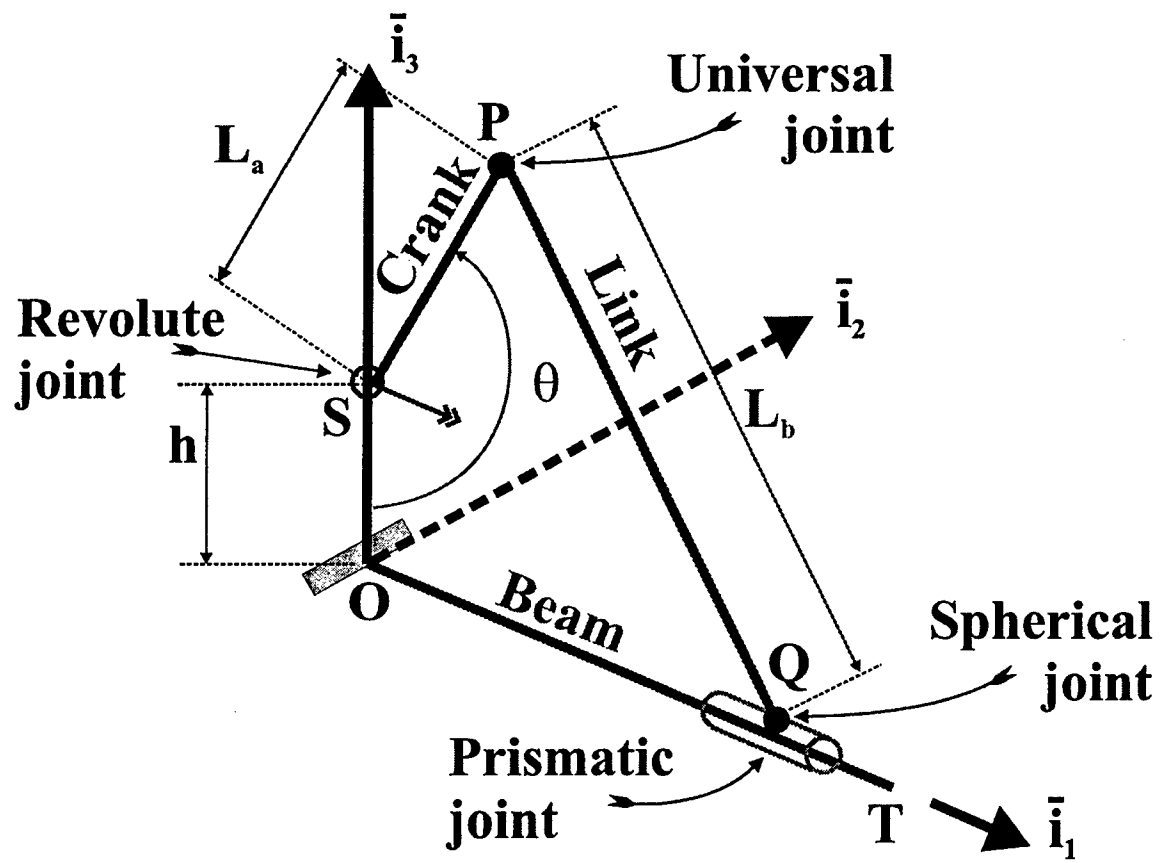


Figure 5. Configuration of the spatial mechanism.

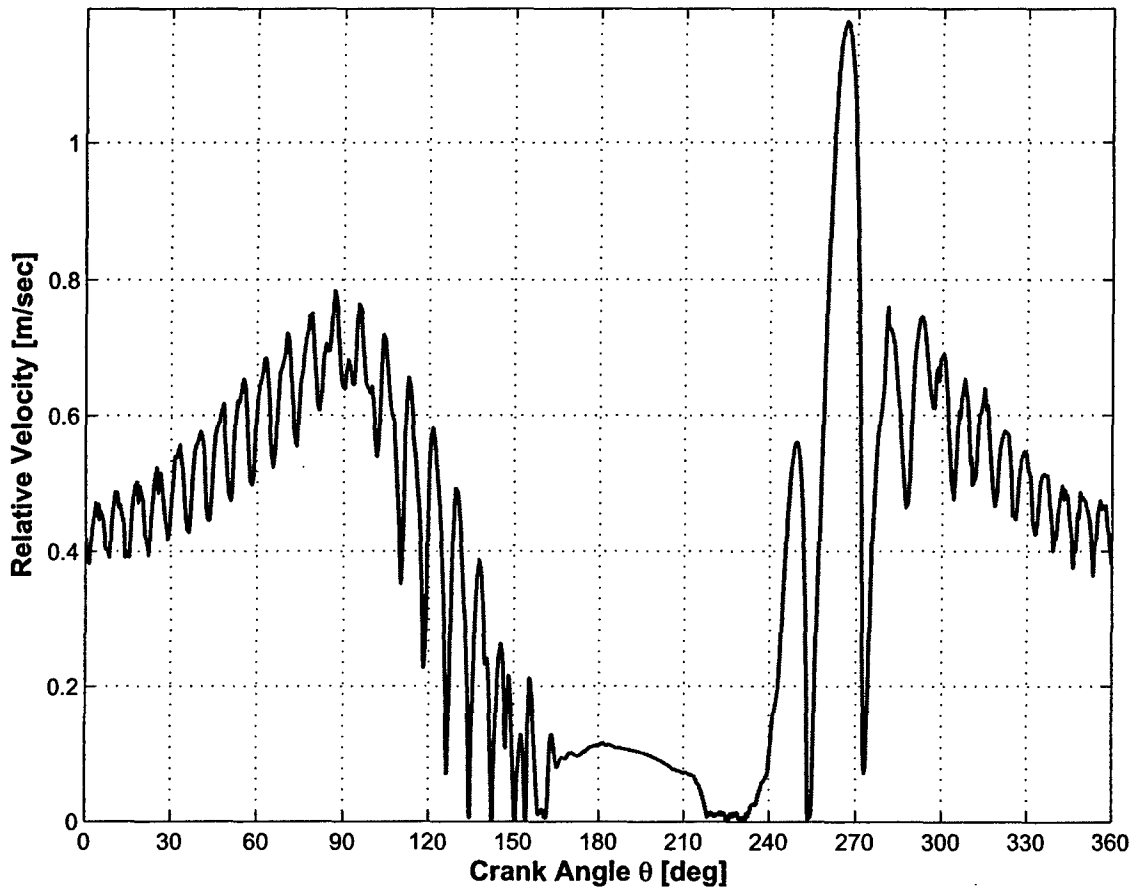


Figure 6. Relative tangential velocity at the spherical joint for case 2.

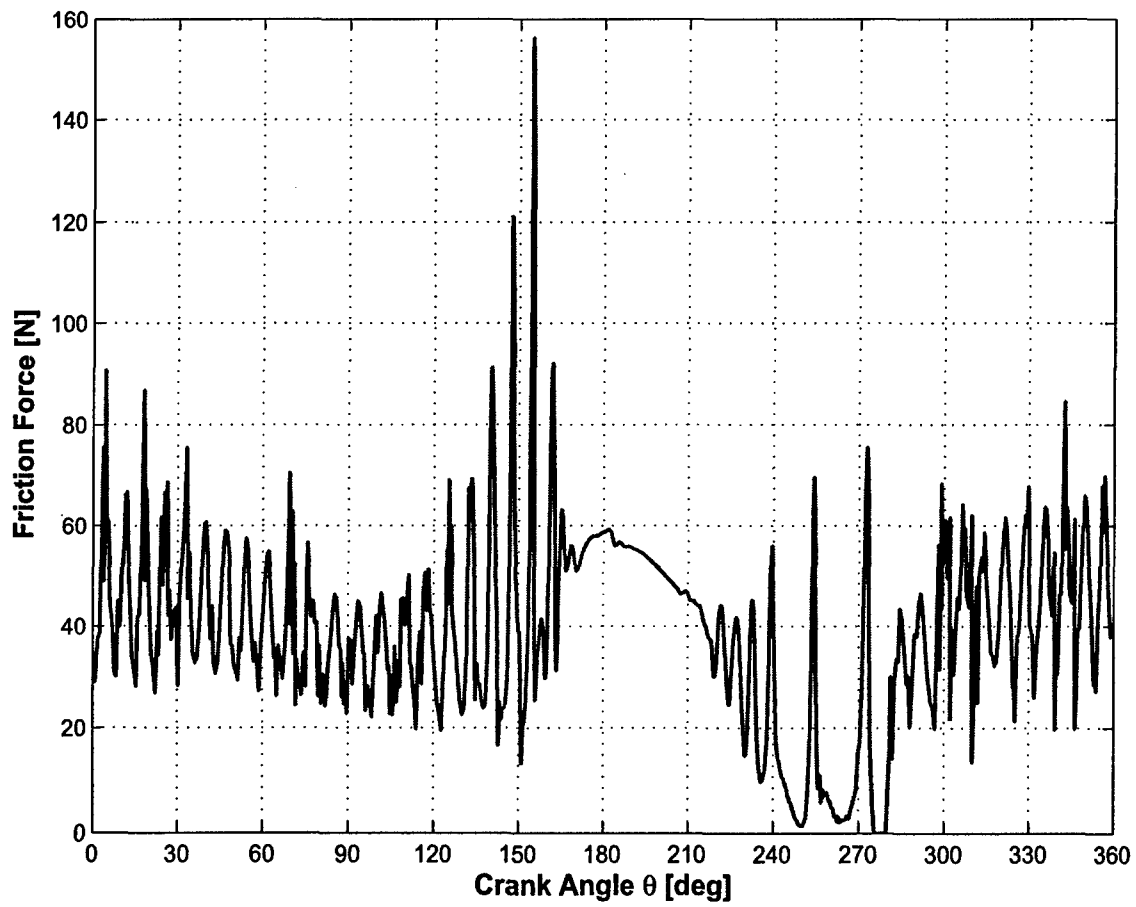


Figure 7. Friction force at the spherical joint for *case 2*.

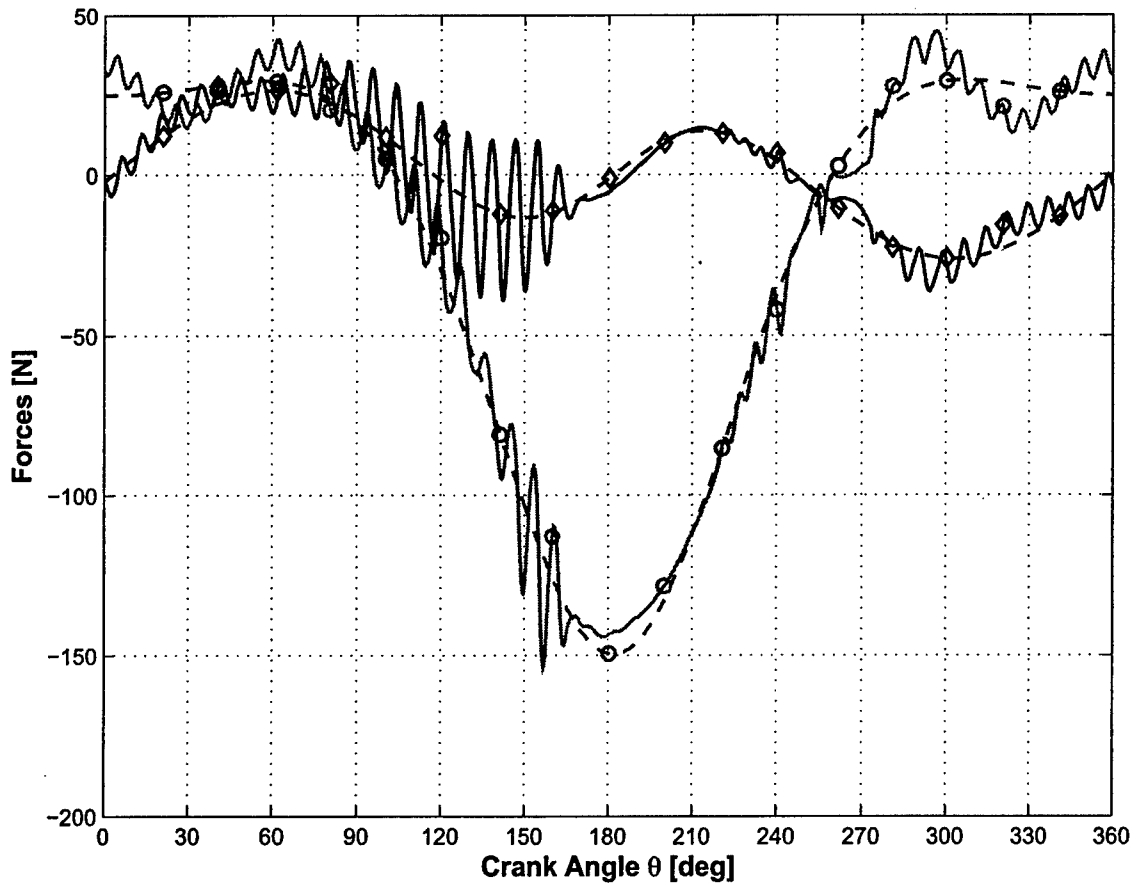


Figure 8. Beam root forces at point O. Case 1: dashed line; case 2: solid line. Force component  $F_2$ :  $\diamond$ ,  $F_3$ :  $\circ$

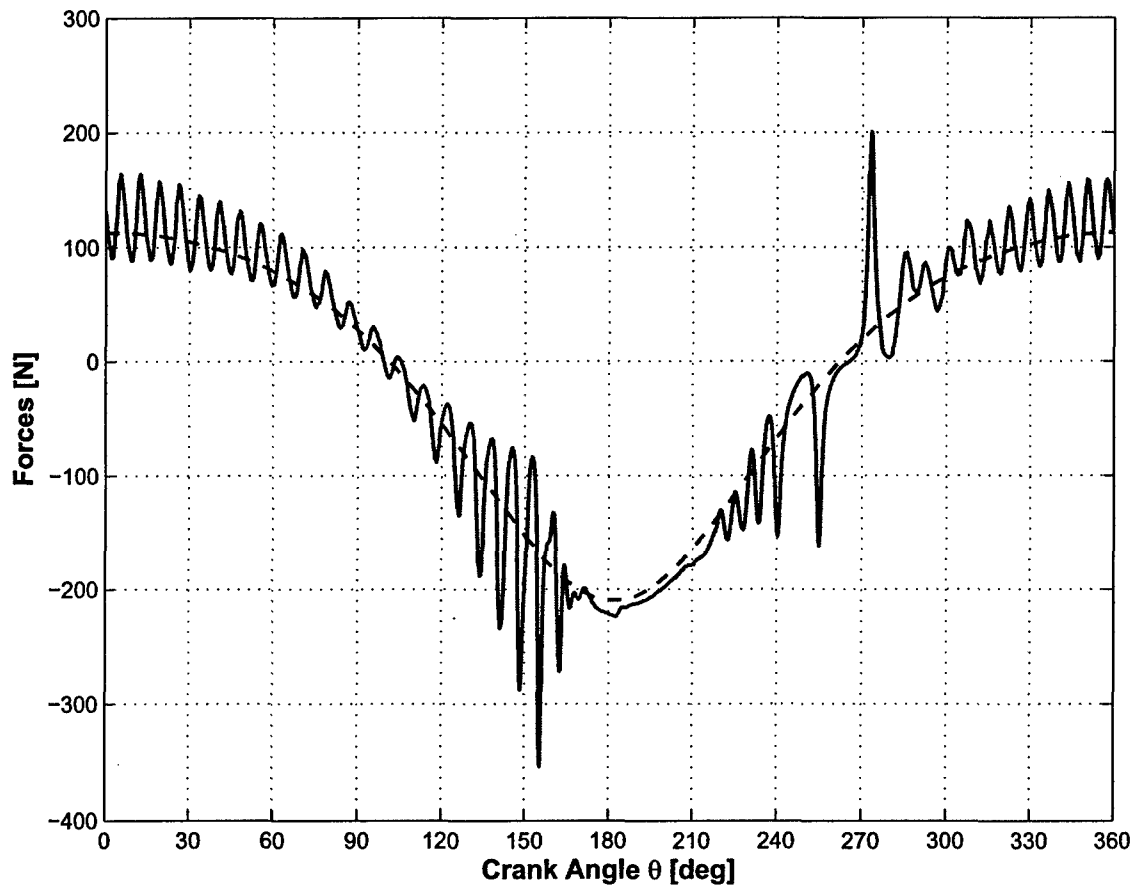


Figure 9. Link mid-span forces. *Case 1*: dashed line; *case 2*: solid line.

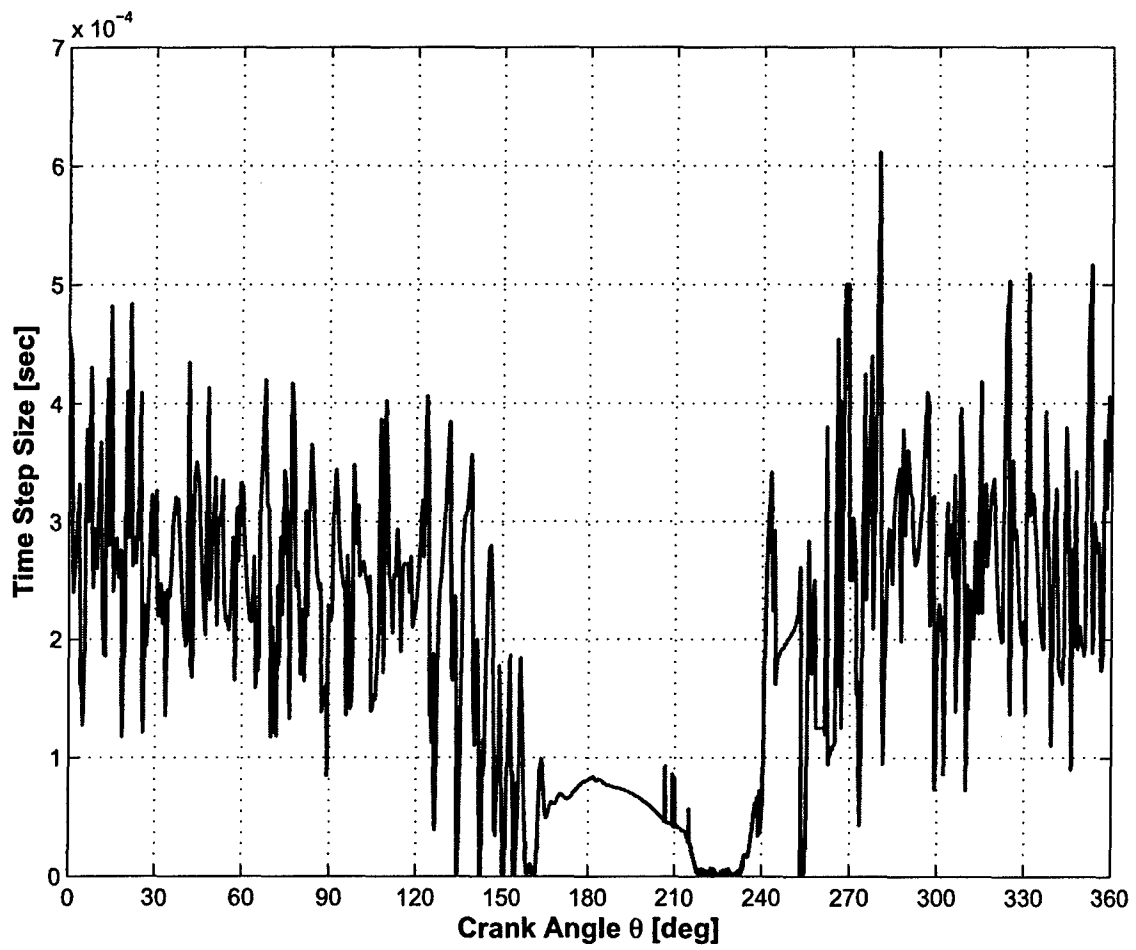


Figure 10. Time step size used in the simulation for *case 2*.

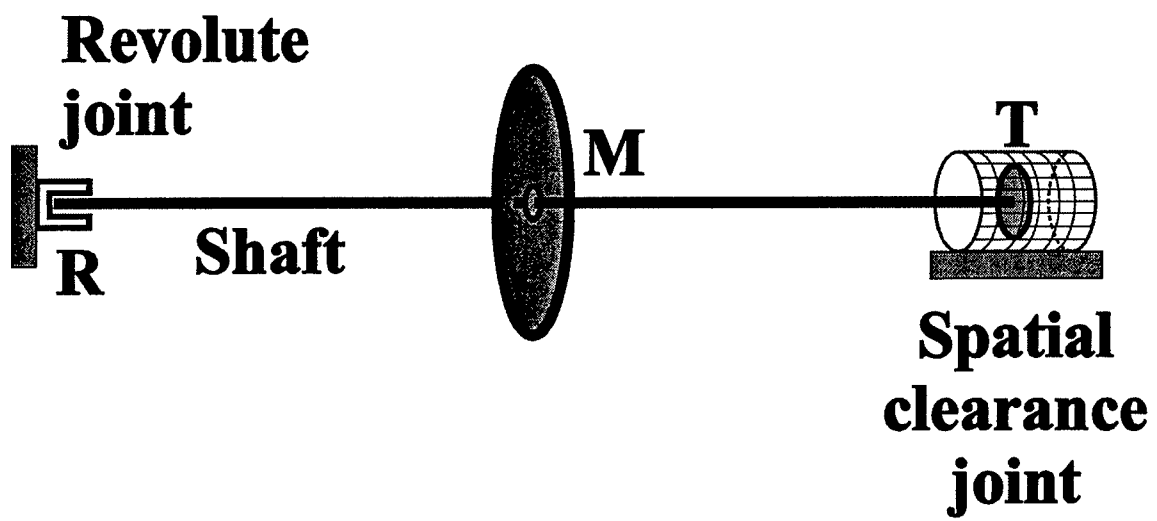


Figure 11. Configuration of the supercritical rotor system.

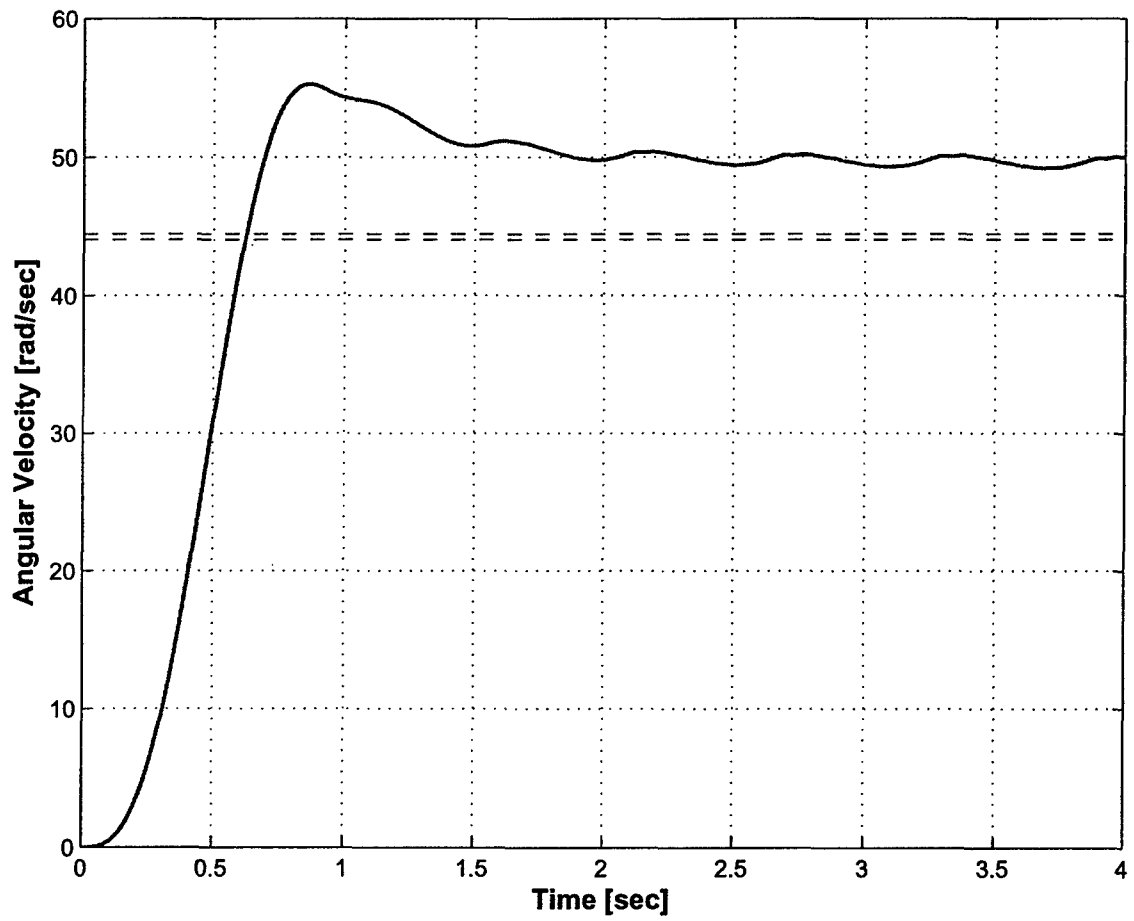


Figure 12. Time history of the angular velocity of the shaft. The dashed lines indicate the unstable zone of operation:  $\Omega \in [44.069, 44.453]$  rad/s.

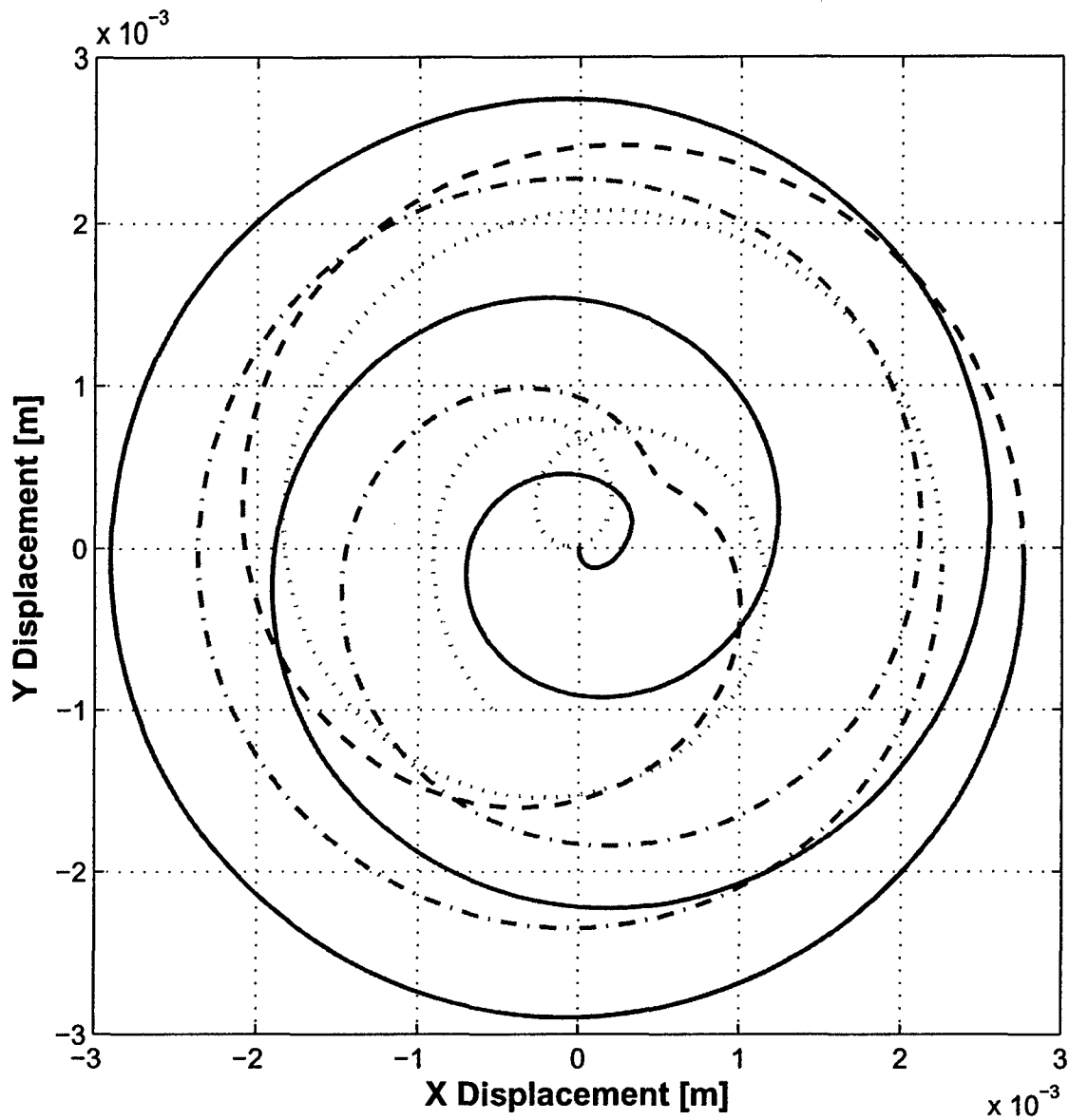


Figure 13. Trajectory of the shaft mid-span point M. For  $0 < t < 0.875$  s: solid line; for  $0.875 < t < 1.065$  s: dashed line; for  $1.065 < t < 1.340$  s: dashed-dotted line; for  $1.340 < t < 1.650$  s: dotted line.

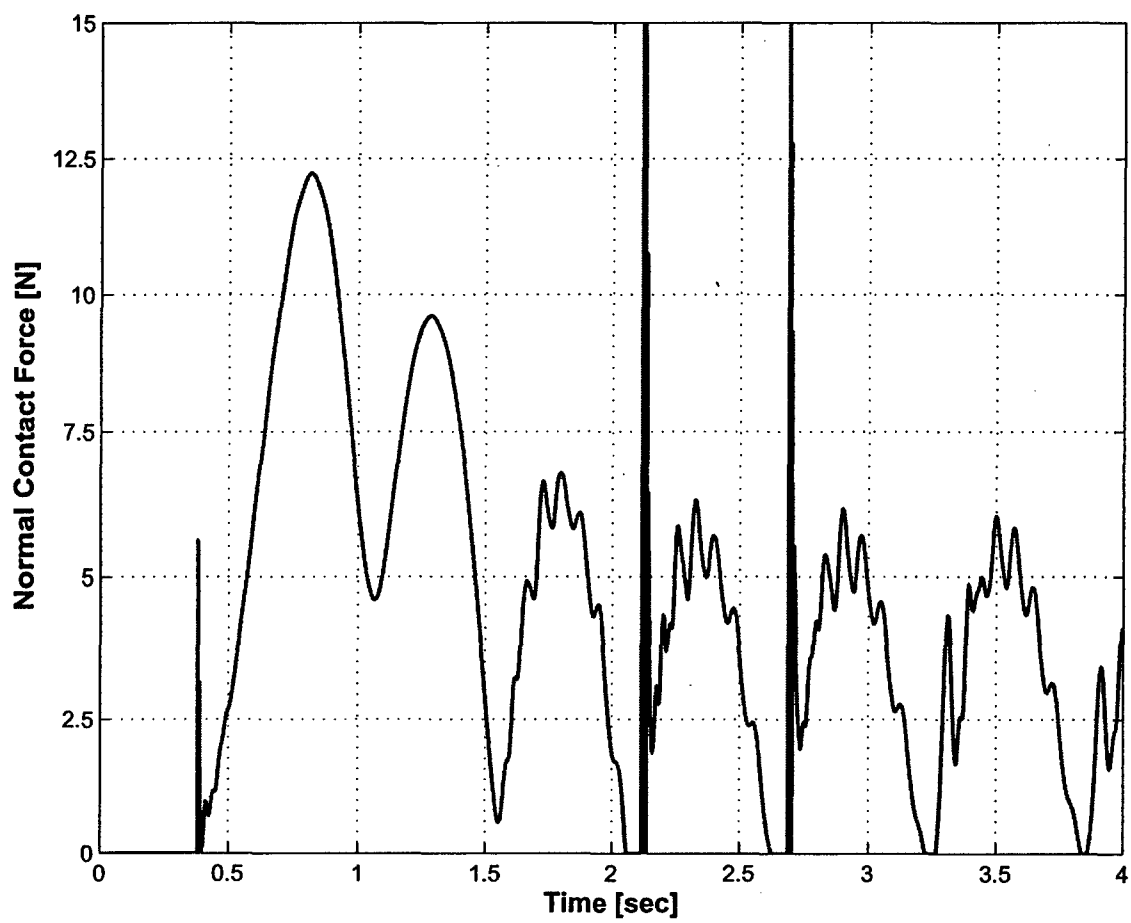


Figure 14. Time history of the normal contact force for the spatial clearance joint at point T.

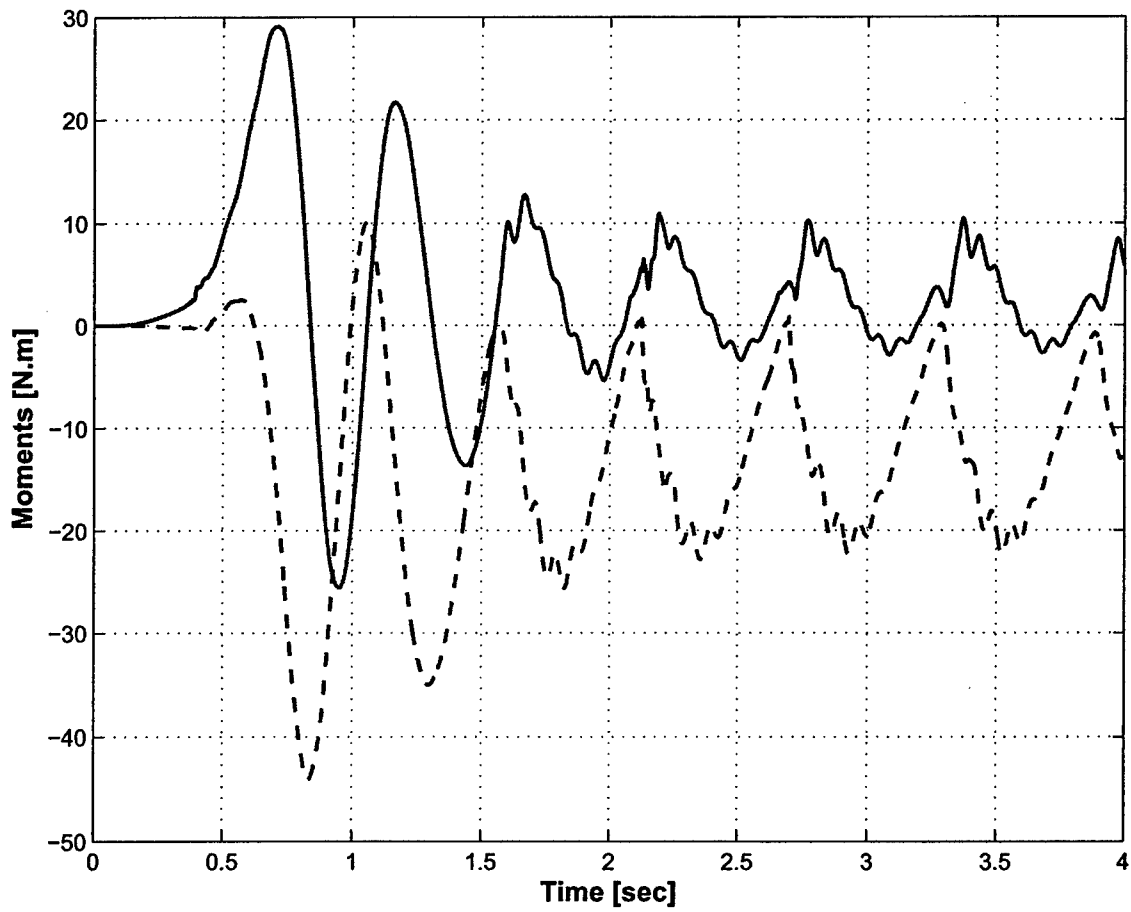


Figure 15. Time history of root bending moments in the shaft at point R.

IMECE2005-81369

## ENERGY TRANSFER AND DISSIPATION IN A THREE-DEGREE-OF-FREEDOM SYSTEM WITH STRIBECK FRICTION

Nguyen Do

School of Mechanical Engineering  
Georgia Institute of Technology  
Atlanta, GA, 30332-0405, U.S.A.

Aldo A. Ferri

School of Mechanical Engineering  
Georgia Institute of Technology  
Atlanta, GA, 30332-0405, U.S.A.

### ABSTRACT

Friction at connecting joints is a key mechanism by which passive damping occurs in built-up structures. This paper explores the ability of friction to transfer energy between subsystems of an interconnected system. Two single-degree-of-freedom (SDOF) systems are used to represent separate subsystems and a third mass is used to represent the connecting joint. A Stribeck friction model is used to represent the resistive force acting on this coupling mass. Through numerical simulation studies, the influence of the subsystem dynamics on the overall energy dissipation levels is investigated. In particular, it is seen that favorable tuning conditions exist that result in a "pumping" of energy from the low-frequency motion of one subsystem to the higher-frequency motion of the other subsystem. It is also seen that one-way energy transfer can occur in such a system due to the eventual joint lock-up that can occur when the connecting mass sticks.

### 1. INTRODUCTION

Friction in connecting joints plays an important role in the damping capacity of built-up structures. It is estimated that as much as 90% of mechanical energy loss in space structures is due to dry friction at the connecting joints [1, 2]. This fact is especially important for space structures because free vibration during deployment or positioning is undesirable and because alternate means of increasing damping are limited. An accurate prediction of how much damping one can expect from a particular structural design is a topic of much research. In a series of experimental studies, Folkman *et al.* found that the loss factor of a truss structure depended on the structure's orientation and the amplitude of vibration [3, 4]. The damping supplied by dry friction depends on the joint preload, which varies depending on the structure's orientation. Other studies have shown that the compliance of the joints themselves can influence the nature and level of passive damping. For example,

some studies have shown that variable normal forces in a frictional joint can give rise to largely "linear" structural damping [5, 6]. In such cases, the free response is characterized by exponential-like (rather than linear) envelopes of decay. A number of review articles have surveyed the research done on the effects of joint friction on structural damping [7 - 9].

Rather than focusing on characterizing the damping of a complex built-up structure, this paper explores the energy dissipation caused by dry friction at a connecting joint. It is understood that joint friction affects damping by converting mechanical energy into heat by rubbing. Less obvious, however, is that friction can serve as a catalyst for energy pumping. The phenomenon of energy pumping is defined as the controlled one-way transfer of vibrational energy to a passive nonlinear sink, where the energy localizes and dissipates over time [10]. It is hypothesized that joint friction can be a means to pump low-frequency vibrational energy to high-frequency vibrational energy, through the action of stick-slip oscillations. In a finite element simulation of a truss structure, Onoda *et al.* found that backlash nonlinearity at the joint transferred vibrational energy from lower modes to higher modes [11]. Since energy can be dissipated faster at higher frequencies, this pumping of energy to excite higher resonances may serve as a tool for increased energy dissipation. In this manner, an inherent property of friction can be exploited to improve the overall damping capacity of the system.

A simplified model of a connecting joint with friction is presented first. The model consists of a 3 degrees-of-freedom (3DOF) spring-mass-damper system with a frictional interface. The algorithm used to calculate the friction forces and the simulation parameters are presented as well. Simulations were performed using Matlab and the equations of motion were solved using the 4<sup>th</sup> order Runge-Kutta method. The steady-state and free vibration responses of the system are explored, followed by a wavelet analysis of the free response. Next, a

parametric study of the energy dissipation in the system is conducted. Finally, conclusions are made concerning the advantage of using friction as a tool for increased energy dissipation.

## 2. SYSTEM MODEL

To model the friction contact at a connection joint, a 3 degree-of-freedom spring-mass-damper system was used. This system, shown in Figure 1, represents two structures modeled as single-degree-of-freedom systems that are coupled by a mass sliding against a friction surface. The sliding mass ( $m_2$ ) is an order of magnitude smaller than masses  $m_1$  and  $m_3$ . The absolute position and velocity of each mass are denoted by  $x_i$  and  $v_i$ , respectively, while the parameters  $k_i$  and  $c_i$  denote spring and viscous damping constants, respectively. The function,  $P(t)$ , represents an external force applied to mass 1.

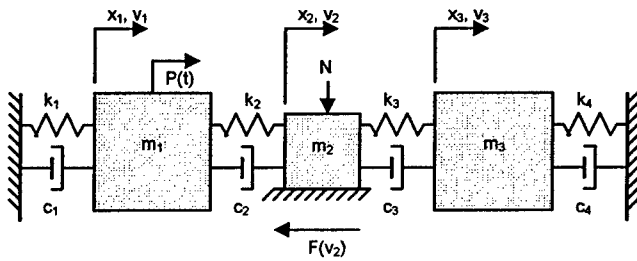


Figure 1. System model of frictional contact at a connection joint.

The friction force,  $F(v)$ , is defined as

$$F(v) = \mu N \operatorname{sgn}(v) \quad (1)$$

where  $v$  is the slip velocity,  $\mu$  is the friction coefficient,  $N$  is the normal force, and  $\operatorname{sgn}(v)$  is the signum function where  $\operatorname{sgn}(v) = v/|v|$ ,  $v \neq 0$ . Using the Stribeck friction model, the friction coefficient,  $\mu$ , is given by

$$\mu = \mu^* + \gamma(e^{-\beta|v|} - 1) + \alpha|v| \quad (2)$$

where  $\mu^*$  is the static friction coefficient and parameters  $\gamma$ ,  $\beta$ , and  $\alpha$  are constants [12]. Figure 2 shows the relationship between the Stribeck friction force and the slip velocity. The key feature is the decrease in friction force as  $|v|$  increases around zero. This feature is believed to be responsible for stick-slip behavior, which is central to the energy pumping and energy dissipation phenomenon under study [13]. In equation (2), the parameter  $\gamma$  specifies the difference between the static and sliding friction coefficients while  $\beta$  determines the steepness of the transition. The coefficient  $\alpha$  was set to zero because it is typically associated with a viscous-damping characteristic of lubricated contact. Setting  $\alpha$  equal to zero

allows one to distinguish between the energy dissipation by viscous damping from the energy dissipated due to dry friction.

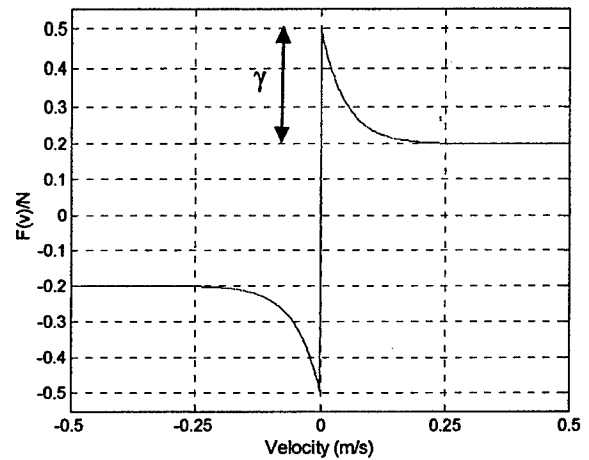


Figure 2. Stribeck friction coefficient as a function of velocity.

As seen in Figure 2, there is a discontinuity in the friction force when the slip velocity is zero. This condition presents many numerical difficulties and is difficult to simulate [14]. In this study, a sliding mode control (variable structure system theory) algorithm was used to handle the discontinuity [15]. A derivation of the equations of motion and a discussion of the numerical solution technique is presented below.

The equations of motion for the 3-DOF system can be written in the form

$$[M]\{\ddot{x}\} + [C]\{\dot{x}\} + [K]\{x\} = \{e_1\}P - \{e_2\}F \quad (3)$$

where  $\{x\} = [x_1 \ x_2 \ x_3]^T$ ,  $\{e_1\} = [1 \ 0 \ 0]^T$ ,  $\{e_2\} = [0 \ 1 \ 0]^T$ , and the overdot represents a derivative with respect to time. The matrices  $[M]$ ,  $[C]$ , and  $[K]$  are the mass, damping, and stiffness matrices, respectively, and are defined as

$$M = \begin{bmatrix} m_1 & 0 & 0 \\ 0 & m_2 & 0 \\ 0 & 0 & m_3 \end{bmatrix},$$

$$K = \begin{bmatrix} k_1 + k_2 & -k_2 & 0 \\ -k_2 & k_2 + k_3 & -k_3 \\ 0 & -k_3 & k_3 + k_4 \end{bmatrix},$$

$$C = \begin{bmatrix} c_1 + c_2 & -c_2 & 0 \\ -c_2 & c_2 + c_3 & -c_3 \\ 0 & -c_3 & c_3 + c_4 \end{bmatrix}.$$

In order to simulate the response of the 3-DOF system, the equations given by (3) are rewritten in the first-order, state-space form

$$\{\dot{y}\} = [A]\{y\} + \{B\}F + \{\Gamma\}P \quad (4)$$

where  $\{y\} = [x1 \ x2 \ x3 \ v1 \ v2 \ v3]^T$ ,  $\{B\} = -[0 \ 0 \ 0 \ ([M]^{-1}\{e_2\})^T]^T$ , and  $\{\Gamma\} = [0 \ 0 \ 0 \ ([M]^{-1}\{e_1\})^T]^T$ . The 6x6 state matrix  $[A]$  is defined as

$$[A] = \begin{bmatrix} [0] & [I] \\ -[M]^{-1}[K] & -[M]^{-1}[C] \end{bmatrix}$$

where  $[0]$  is a 3x3 zero matrix and  $[I]$  is a 3x3 identity matrix. The friction force,  $F$ , was calculated using a sliding mode control algorithm, which is discussed next.

The techniques developed and used in the area of sliding mode control can be used to define the "equivalent dynamics" that exist when sticking takes place. Numerically, sticking is assumed to be possible when  $|v_2| \leq 0.001$  m/s. Note that  $v_2$  can be expressed as

$$v_2 = [T]\{y\} \quad (5)$$

where  $[T] = [0 \ 0 \ 0 \ 0 \ 1 \ 0]$ . During sticking, the slip velocity is identically zero; hence its time derivative must also be zero. Taking the time derivative of (5) yields

$$\dot{v}_2 = [T]\{\dot{y}\} = [T]\{[A]\{y\} + \{B\}F + \{\Gamma\}P\} = 0. \quad (6)$$

Since equation (6) represents the condition when the slip velocity is zero, the friction force,  $F$ , must be the force necessary to impose the sticking condition. This force is known as the equivalent friction force,  $F_{eq}$ . Solving (6) for  $F$  yields

$$F_{eq} = -([T]\{B\})^{-1}[T]\{[A]\{y\} + \{\Gamma\}P\}. \quad (7)$$

Figure 3 shows a flow chart of the logic steps to calculate the friction force. If the slip velocity is equal to or smaller than the Stribeck velocity ( $v_s = 0.001$  m/s), then the equivalent friction force is calculated. However, if this equivalent force is greater than the maximum static friction force ( $\mu^*N$ ), then the mass is assumed to break free, and the friction force is set equal to the dynamic friction force given by (1) and (2).

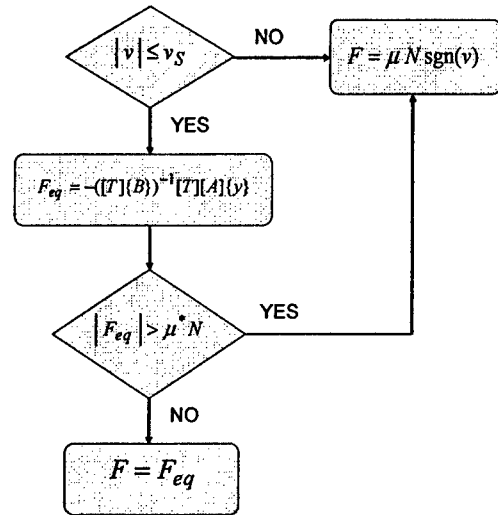


Figure 3. Flow chart to calculate friction force ( $P = 0$  case).

To observe the stick-slip behavior of the 2<sup>nd</sup> mass, the steady-state and free vibration responses of the system were simulated. The goal was to excite the 1<sup>st</sup> mass to induce stick-slip motion in the 2<sup>nd</sup> mass. This stick-slip motion would pump energy from the vibration of the 1<sup>st</sup> subsystem to the 3<sup>rd</sup> subsystem.

### 3. SYSTEM SIMULATION

Once the equations of motion and the sliding mode control algorithm were established, simulation of the 3-DOF system was straight-forward. The method used to simulate the system was the 4<sup>th</sup> order Runge-Kutta scheme with a fixed time step of 1 ms. Table 1 summarizes the values used for the simulation.

Table 1. Simulation Parameters

System Parameters	Value	Friction Parameters	Value
$m_1, m_3$	100, 50 kg	$\mu^*$	0.50
$m_2$	0.25 kg	$\gamma$	0.30
$k_1, k_4$	1000 N/m	$\beta$	20.0
$k_2, k_3$	100 N/m	$v_s$	0.001 m/s
$\zeta_{1,2,4}, \zeta_3$	0.01, 0.05	$N$	100 N

The 3DOF system can be divided into three subsystems; each subsystem assumes only one of the masses is moving. The natural frequencies for each subsystem are therefore given by

$$\omega_1 = \sqrt{\frac{k_1 + k_2}{m_1}}, \quad \omega_2 = \sqrt{\frac{k_2 + k_3}{m_2}}, \quad \omega_3 = \sqrt{\frac{k_3 + k_4}{m_3}}. \quad (8)$$

A small amount of viscous damping was added to the system in order to study the interaction of stick-slip energy dissipation and structural damping. The damping coefficients were chosen based on the following relations:

$$\begin{aligned} c_1 &= 2\zeta_1\omega_1m_1, & c_2 &= 2\zeta_2\omega_2m_2 \\ c_3 &= 2\zeta_3\omega_3m_3, & c_4 &= 2\zeta_4\omega_4m_4 \end{aligned} \quad (9)$$

where  $\zeta_i$  are closely related to the damping ratios of the individual subsystems. The damping ratios are all 1%, except for the 3<sup>rd</sup> damper, which is 5%. This higher damping ratio for  $\zeta_3$  was chosen to ensure adequate excitation of the third subsystem. The partition into three subsystems was useful in analyzing the behavior of the 3-DOF system. During periods of sticking by the 2<sup>nd</sup> mass, the 1<sup>st</sup> and 3<sup>rd</sup> masses oscillate like linear single-degree-of-freedom (SDOF) systems with natural frequencies given by  $\omega_1$  and  $\omega_3$ , respectively.

### 3.1 Steady-State Vibration Response

In order to understand the behavior of the system, the 3DOF system was subjected to harmonic excitation of the form:

$$P(t) = W \sin(\omega_d t) \quad (10)$$

where  $W$  is the force amplitude (1500N),  $\omega_d$  is the driving frequency, and  $t$  is the time. Since the stick-slip motion of the 2<sup>nd</sup> mass exhibits odd numbered harmonics, tuning the 3<sup>rd</sup> subsystem to one of the harmonics would theoretically produce an internal resonance in the response [16]. The 3<sup>rd</sup> subsystem was tuned by keeping  $k_3$  and  $m_3$  constant and varying  $k_4$  so that

$$k_4 = \left(\frac{m_3}{m_1}\right)r^2(k_1 + k_2) - k_3 \quad (11)$$

where  $r$  is the *tuning ratio* defined as  $\omega_3/\omega_1$ .

Before the steady-state response is presented, it is instructive to examine the linear modes of the 3DOF system in the absence of friction. Mode 1 is mostly dominated by mass 1, mode 2 is dominated by mass 3, and mode 3 is dominated by mass 2. The modes are fairly localized, except when the tuning ratio is 1. When  $r = 1$ , modes 1 and 2 have nearly the same natural frequencies. As the frequency ratio is increased from 1, only the natural frequency of mode 2 is increased, whereas the natural frequencies of modes 1 and 3 remain relatively constant.

The steady-state response of the 3-DOF system was obtained by simulating the system until the transient dynamics disappeared. Rather than using the peak displacement per cycle, the amplitude of the steady state response of each mass was described by its root-mean-squared (RMS) displacement:

$$X_{RMS} = \sqrt{\frac{1}{T} \int_{t_1}^{t_2} x^2 dt} \quad (12)$$

where  $T$  is some time duration in the steady-state and is given as  $T = t_2 - t_1$ . The time duration  $T$  was defined to be the last 5 periods of the forcing frequency at the end of each simulation. The RMS response was captured over a span of excitation frequency ratios,  $d$ , defined as  $d = \omega_d/\omega_1$ . To expedite the simulations, the end states of the each steady-state response were used as the initial conditions for the next frequency ratio. (Simulations were always terminated after an integer number of excitation periods had passed.)

Figure 4 shows the RMS displacements of the 3<sup>rd</sup> mass as a function of driving ratio for four tuning ratios,  $r$ . This plot shows the presence of internal resonances when the driving frequency is roughly one-third of the tuned natural frequency of the 3<sup>rd</sup> subsystem. For example, there is an internal resonance at a driving ratio of 1.33 when the frequency ratio is 4.0. This phenomenon occurred at all the tuning ratios except when  $r = 3.0$ . At this frequency ratio, the internal resonance would occur at  $d = 1.0$ , which is overshadowed by the resonance of the 1<sup>st</sup> subsystem. Also noticeable in Figure 4 are the internal resonances corresponding to one-fifth of the frequency ratio; e.g., the small peak at  $d = 0.6$  for the case  $r = 3$ . Lastly, the double peak near  $d = 1$  for the case  $r = 1$  is due to resonances of the 1<sup>st</sup> and 2<sup>nd</sup> modes being closely spaced together.

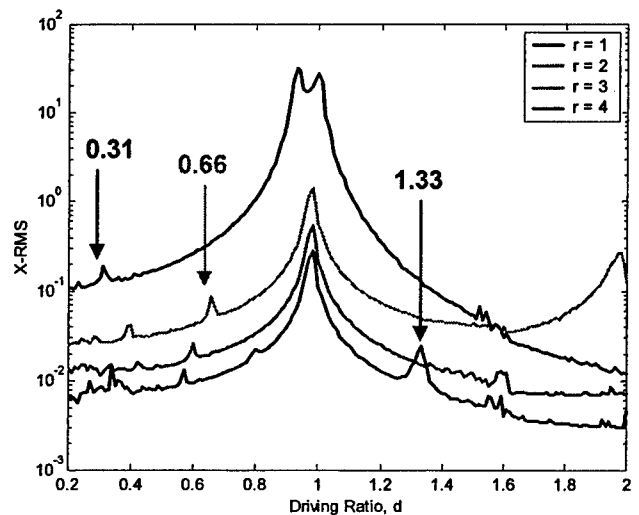


Figure 4. RMS displacement of the 3<sup>rd</sup> mass as a function of driving frequency.

An examination of the time histories of the steady-state responses revealed a significant amount of stick-slip of the 2<sup>nd</sup> mass. Thus, excitation at a single frequency is converted into multi-harmonic response by means of the friction nonlinearity.

Under favorable tuning conditions, these higher harmonics excite internal resonances as expected. In the following section, we examine the extent to which subsystem tuning can lead to enhanced energy dissipation during free response.

### 3.2 Free Vibration Response

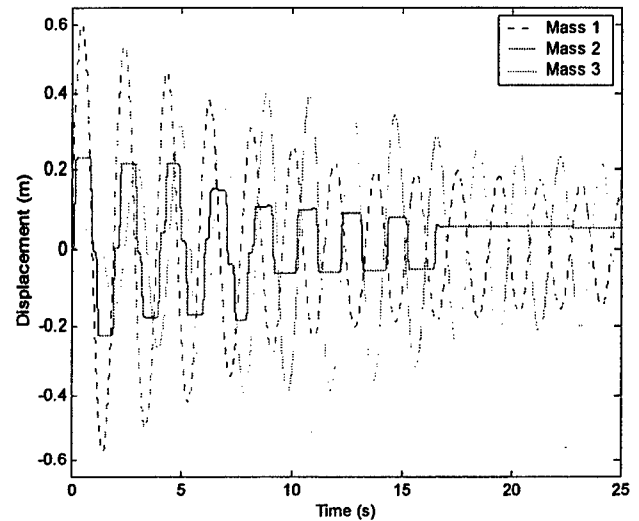
The free vibration response of the 3-DOF system was simulated to quantify the energy transfer from one subsystem to the other and from low frequencies to higher frequencies. Furthermore, it was necessary to understand under what states of excitation, friction level, and tuning of the 3<sup>rd</sup> subsystem did favorable conditions exist for maximum energy dissipation. To simulate the free response, the external force  $P(t)$  was set to zero and an initial velocity of 2.0 m/s was applied to mass 1.

Figure 5 shows a typical free response of the 3-DOF system for a normal force of 40 N and a tuning ratio of  $r = 1$ . While the displacement and velocity of the 1<sup>st</sup> mass decrease with approximately linear envelopes of decay, the 2<sup>nd</sup> mass shows periodic stick-slip behavior until it is completely stuck at a time of about 20 s. This stick-slip behavior is more evident in the velocity of the 2<sup>nd</sup> mass shown in Figure 5b. The result demonstrates that there is a one-way transfer of vibratory energy from the 1<sup>st</sup> mass to the 3<sup>rd</sup> mass because once mass 2 is stuck, masses 1 and 3 oscillate like damped, isolated SDOF systems. Lastly, note that the free response of the 1<sup>st</sup> mass is similar to having a persistent, nearly harmonic excitation of masses 2 and 3 through the force in spring  $k_2$  and viscous damper  $c_2$ .

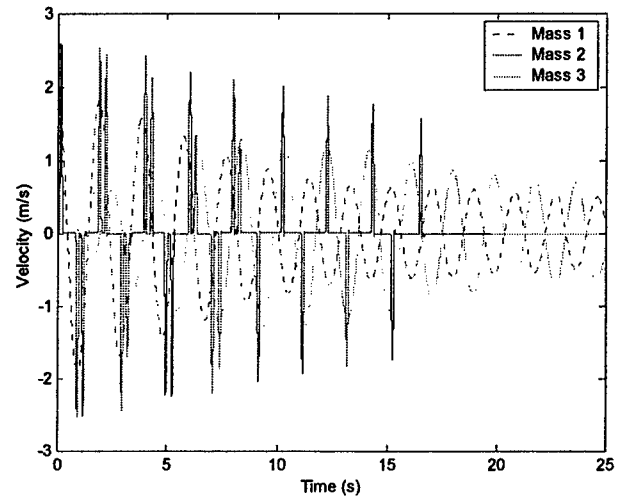
As shown in Figure 5, it is clear that there is a transfer of energy from the 1<sup>st</sup> mass to the 3<sup>rd</sup> mass. However, we wish to examine whether friction indeed pumps energy to higher frequencies, particularly at tuning ratios,  $r$ , higher than one. To accomplish this task, the free response of the 3-DOF system was analyzed in both time and frequency domains using the continuous wavelet transform (CWT).

### 3.3 Wavelet Analysis of the Free Response

The wavelet transform has been popular because of its ability to analyze non-stationary signals. Furthermore, unlike the Fourier transforms, the wavelet transform is capable of good resolution in both frequency and time domains. Figure 6 shows the velocity time history of the free response of the 3-DOF system for  $N = 40\text{N}$  and  $r = 2$ . Similar to Figure 5b, the velocity of the mass 1 oscillates at one frequency and decreases almost linearly while mass 2 exhibits significant stick-slip oscillations. Although difficult to determine from this Figure, mass 3 appears to contain higher frequency content.



(a)



(b)

Figure 5. (a) Displacement and (b) velocity time histories of the 3-DOF system ( $N = 40\text{N}$ ,  $r = 1$ ).

Figure 7 shows the CWT (using a Morlet wavelet) of the velocity of mass 3. The transform was implemented using the WaveLab 802 package for Matlab [17]. The colors indicate the magnitude of the wavelet transform, with blues indicating peaks. From Figure 7, there are two distinct frequency bands. Initially, the lower frequency band has a relatively large magnitude and decreases as time increases. Just as the lower frequency band diminishes, the higher frequency band appears. Since kinetic energy is the square of the velocity, Figure 7 shows that through the frictional interface, kinetic energy at one frequency is pumped to a higher frequency. Similar analysis of the displacement yields the same conclusion regarding the potential

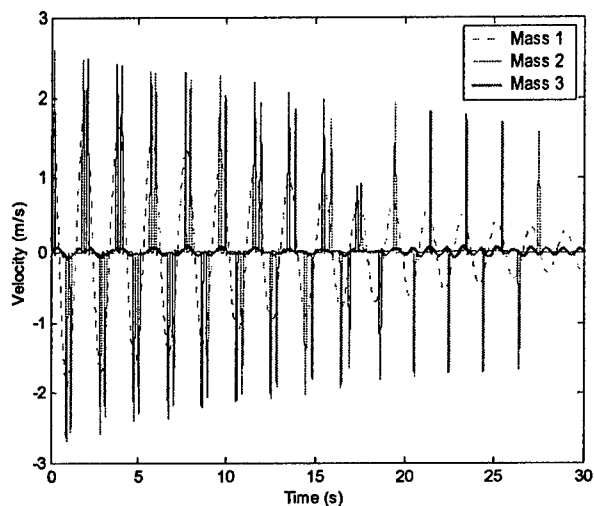


Figure 6. Velocity time history for  $N = 40N$  and  $r = 2$ .

energy in the system. Lastly, notice that the frequency in on a logarithmic scale of base 2. On a linear scale, the nominal value of the higher frequency band is twice that of the nominal value of the lower band. This result is consistent with the tuning ratio of 2.

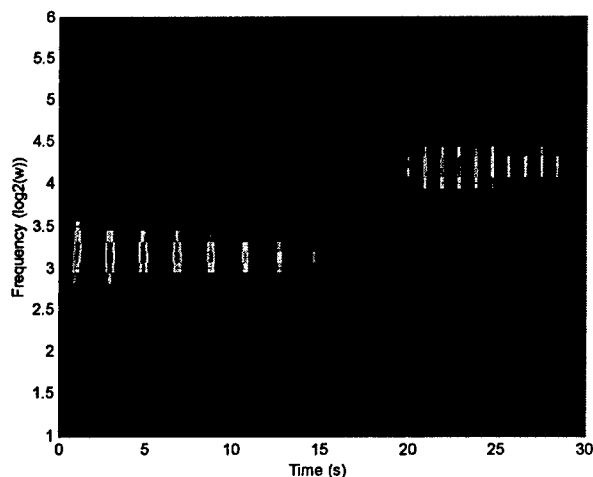


Figure 7. CWT of the velocity of mass 3 for  $N = 40N$  and  $r = 2$ .

To be sure that friction is indeed the mechanism for pumping energy to higher frequency, a CWT is calculated for the velocity response of mass 3 when friction is not present ( $N = 0N$ ), as shown in Figure 8. Compared to Figure 7, there is no significant frequency band at the higher frequency in Figure 8. In fact, there is some energy in the higher band at the early times, however, this energy dissipates quickly and the majority of the energy in the system is in the lower frequency band. The energy at the higher band can be attributed to the fact that an

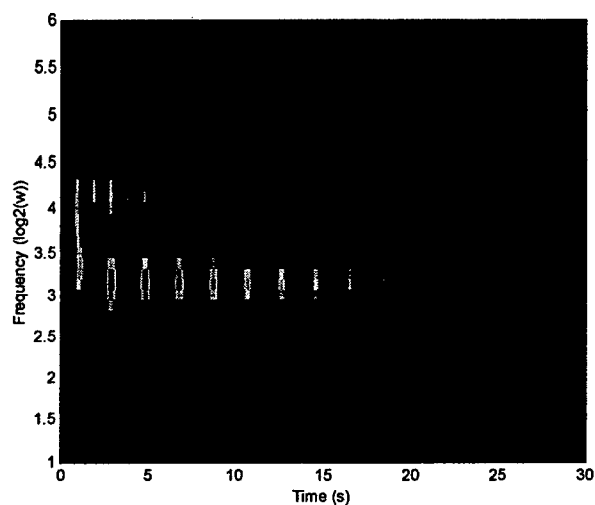


Figure 8. CWT of the velocity of mass 3 for  $N = 0N$  and  $r = 2$ .

impulsive force (initial velocity) is applied to mass 1 as the excitation. This impulsive force provides a broad range of frequencies to the system.

#### 4. ENERGY DISSIPATION

To quantify how much energy was transferred, it was necessary to look at the energies in the combined system as well as in the individual subsystems. Of further interest was the energy transfer at frequencies higher than that of the fundamental frequency of the 1<sup>st</sup> mass. To accomplish this task, the 3<sup>rd</sup> subsystem was tuned for a range of tuning ratios,  $r$ . When the stick-slip motion excited a resonance of the 3<sup>rd</sup> subsystem, there would be a corresponding increase in displacement and velocity. This increased velocity would correlate to higher energy dissipation by the dampers connected to the 3<sup>rd</sup> mass. Therefore, by examining the energy dissipation in the 3-DOF system, one could quantify the amount of total energy transfer and the energy transfer at higher frequencies.

The total energy,  $E_{Total}$ , in the 3-DOF system is defined as

$$E_{Total} = \frac{1}{2} \{y\}^T \begin{bmatrix} [K] & [0] \\ [0] & [M] \end{bmatrix} \{y\} \quad (13)$$

where  $[0]$  is a  $3 \times 3$  zero matrix. Therefore, the total energy dissipated,  $E_{dis}$ , is given by

$$E_{dis} = (E_{Total})_{t=0} - (E_{Total})_{t=t_f} \quad (14)$$

where  $t_f$  is the end time of the simulation. The total energy dissipated can be separated into the sum of the energy dissipated by viscous dampers and the energy dissipated by Coulomb friction. If the power dissipated by each viscous

damper is denoted as  $P_i$ , the total dissipated energy can be expressed as

$$E_{dis} = \sum_{i=1}^4 \int_0^{t_f} P_i dt + (E_{dis})_{friction} \quad (15)$$

where

$$\begin{aligned} P_1 &= c_1 \cdot v_1^2 & P_2 &= c_2 (v_2 - v_1)^2 \\ P_3 &= c_3 (v_3 - v_2)^2 & P_4 &= c_4 \cdot v_3^2 \end{aligned} \quad (16)$$

By (15), it is then possible to indirectly calculate the energy dissipated by friction.

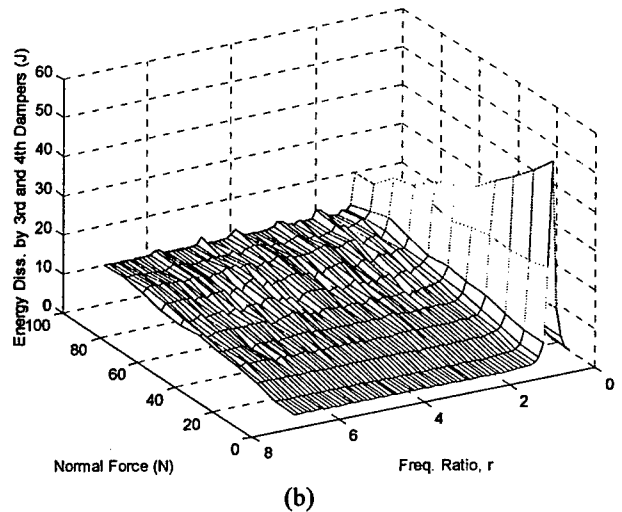
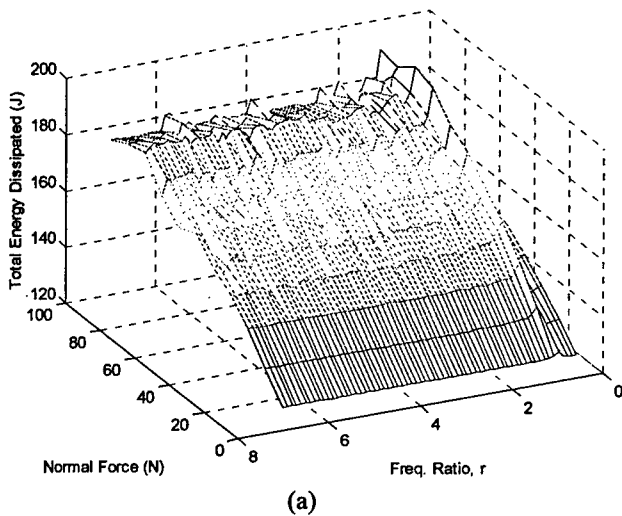


Figure 9. Energy dissipated by the (a) entire system and (b) the 3<sup>rd</sup> and 4<sup>th</sup> dampers.

To find the optimal condition for friction to pump energy to higher frequencies, several factors were considered. The total energy of the system was evaluated as a function of the mass

ratio ( $m_3/m_1$ ), the tuning ratio ( $r = \omega_3/\omega_1$ ), the normal force, and the simulation time. A mesh was used to visualize how the total dissipated energy varied as a function of two variables. For the mesh shown in Figure 9, the constant values are the mass ratio (0.5) and the simulation time (15.1 s). This simulation time corresponds to one-half of the time constant of the 1<sup>st</sup> subsystem, where the time constant =  $1/(\omega_1 \zeta_1)$ . The normal force is varied from 0 to 100 N, in increments of 10 N; and, the tuning ratio is varied from 0.6 to 8.0, in increments of 0.1. Figure 9a shows the total energy dissipated after 15.1 s of free response. There is a large peak near a tuning ratio of  $r = 1$ , but there are some smaller peaks as  $r$  is increased and  $N$  is greater than 80 N. To study this feature more closely, the energy dissipated by the 3<sup>rd</sup> and 4<sup>th</sup> dampers over the same time interval are examined, as shown in Figure 9b.

From Figure 9b, there is a large peak in dissipated energy near a tuning ratio of 1. This peak appears to be the result of a “vibration-absorber” effect. As the normal force increases, the absorber effect is less prominent and ripples in the energy dissipation at higher tuning ratios can be seen. Finally, at  $N = 100$  N, there are definite peaks that are evident at certain tuning ratios. The peaks suggest that the force input to mass 3 excites a resonance, thereby causing greater energy dissipation.

A slice of the mesh in Figure 9b at  $N = 100$  N is shown in Figure 10. This plot clearly shows five distinct peaks between the tuning ratios of 2 and 7. These peaks correspond to tuning ratios of  $r = 2.0, 2.9, 3.9, 4.7,$  and  $5.7$ . In other words, when tuned to these higher frequencies, the resonance of the 3<sup>rd</sup> subsystem was excited by the stick-slip motion of the 2<sup>nd</sup> mass. Therefore, favorable energy dissipation occurred when the 3<sup>rd</sup> subsystem was tuned to the stick-slip frequencies. As mentioned previously, the natural frequencies of the 3<sup>rd</sup> subsystem and that of mode 2 in the linear (frictionless) system are closely related. In fact, the natural frequencies of the 3<sup>rd</sup> subsystem and that of mode 2 are nearly identical for tuning

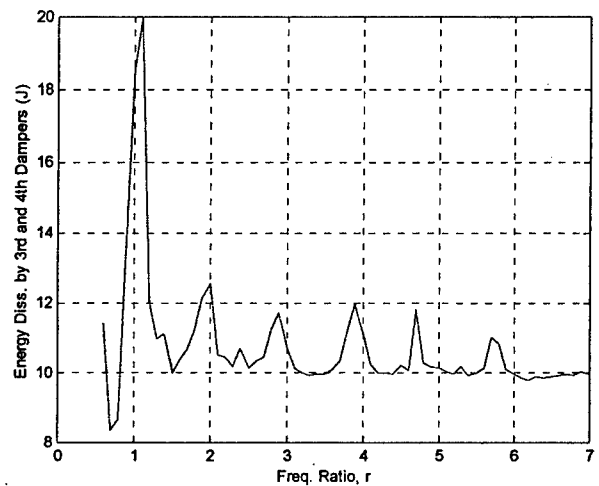


Figure 10. Energy dissipated by the 3<sup>rd</sup> and 4<sup>th</sup> dampers at  $N = 100$  N.

ratios above 1. Therefore, exciting a resonance of the 3<sup>rd</sup> subsystem is analogous to exciting the 2<sup>nd</sup> mode in the linear system.

The result shown in Figure 10 is interesting because it does not agree with the result from the steady-state response. Although the peaks in Fig. 7 appear in somewhat regular intervals, they do not occur at only odd harmonics of the frequency of free vibration of the 1<sup>st</sup> subsystem. This behavior could be attributed to the stick-slip motion during free response (see Fig. 5b). Since the stick-slip lasts for a finite amount of time, the input into the 3<sup>rd</sup> subsystem looks like a series of impulses. The impulses have broad frequency content and can excite many frequencies.

To find the best condition for energy dissipation, the energy dissipated by the 3<sup>rd</sup> and 4<sup>th</sup> dampers was examined for different levels of normal force and mass ratios ( $m_2/m_1$ ). Figures 11 and 12 examine how the energy dissipated by the 3<sup>rd</sup> and 4<sup>th</sup> dampers varies with mass ratio and normal force, respectively. Simulation duration times of longer than 15 s did not have a significant effect on the energy dissipation trends because permanent sticking occurred shortly after 15 s.

Figures 11 and 12 show that the energy dissipation is sensitive to system parameters. In Figure 11, the peaks increase as the 3<sup>rd</sup> mass decreases. This trend is consistent with a vibration absorber, in which a smaller absorber mass leads to increased absorption over a smaller frequency range. At a mass ratio of 0.25, there is a sharp rise in the 1<sup>st</sup> peak. However, the 5<sup>th</sup> and 6<sup>th</sup> peaks are not as pronounced when compared to a mass ratio of 0.5. Similarly, a mass ratio of 1.0 does not produce noticeable peaks, except when  $r$  is near 1.

In Figure 12, the peaks at  $r = 1$  decreases as the normal force increases, as mentioned earlier. Similar to the mass ratio, the peaks at tuning ratios larger than 1 are best accentuated at a particular value. In this case, the value is a normal force of 100

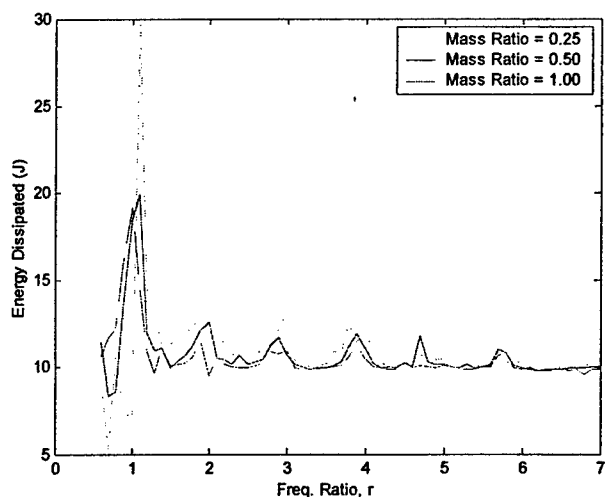


Figure 11. Energy dissipated by the 3<sup>rd</sup> and 4<sup>th</sup> dampers with varying mass ratios ( $N = 100$  N,  $t_f = 15.1$  s).

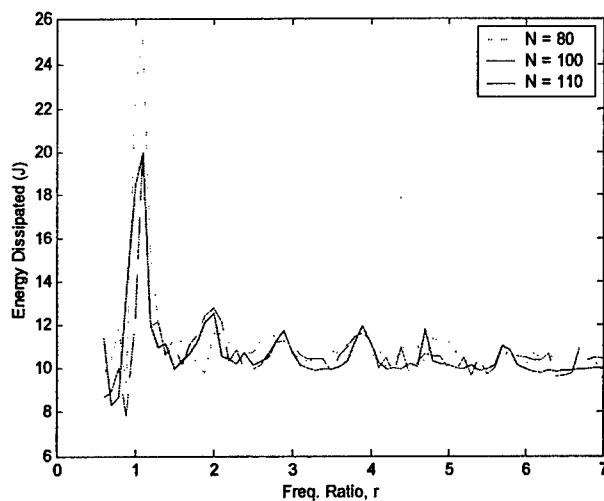


Figure 12. Energy dissipated by the 3<sup>rd</sup> and 4<sup>th</sup> dampers with varying  $N$  (mass ratio = 0.5,  $t_f = 15.1$  s).

$N$ . At normal forces above 110 N, mass 2 is completely stuck at all times for the initial condition considered here.

The previous results show that friction pumps energy to higher resonances, which serves to increase energy dissipation at the higher resonances. However, it is important to note that the majority of energy dissipation in the 3-DOF system is due to friction on mass 2 and the dampers connected to the 1<sup>st</sup> mass, where the motion originated. For example, at a tuning ratio of 1.1, the energy dissipated by the 3<sup>rd</sup> and 4<sup>th</sup> dampers accounts for 11% of the total energy dissipated. At a tuning ratio of 2.0, the energy dissipated by the 3<sup>rd</sup> and 4<sup>th</sup> dampers accounts for 7% of the total energy dissipated.

Despite the modest amounts of energy dissipation attributed to the 3<sup>rd</sup> and 4<sup>th</sup> dampers, it is necessary to evaluate the advantage of the energy pumping phenomenon versus the case where friction is not present (normal force = 0). To make this comparison, the ratio of the energy dissipated by the 3<sup>rd</sup> and 4<sup>th</sup> dampers to the total energy dissipated was evaluated for the friction and non-friction cases. Table 2 summarizes the comparison when the normal force is 100 N versus 0 N at tuning ratios corresponding to the peaks in Figure 10. For the frictionless case, the energies dissipated are constant after an initial peak at a tuning ratio of 1.

Table 2. Percentage of Energy Dissipated by the 3<sup>rd</sup> and 4<sup>th</sup> Dampers to the Total Energy Dissipated

Freq. Ratio	1.1	2.0	2.9	3.9	4.7	5.7
$N = 100$ N	11	7.0	6.7	6.6	6.7	6.1
$N = 0$ N	42	2.7	2.7	2.7	2.7	2.7

Table 2 shows that there is greater dissipation for the friction case except when the tuning ratio is at 1.1. Although the advantage is small (about 4% of the total energy dissipated), this result demonstrates that the pumping of energy to higher resonances can serve as a tool for increased dissipation. As for the case where the tuning ratio is 1.1, there is greater dissipation by the 3<sup>rd</sup> and 4<sup>th</sup> dampers of the frictionless system; however, the total energy dissipation is greater in the system with friction. At this tuning ratio, the total energy dissipated by the frictionless system is 130.4 J, versus 189.7 J for the system with friction.

## 5. CONCLUSION

The purpose of this study is to explore the effects on energy dissipation by dry friction at a connection between subsystems. In particular, the ability of friction to pump energy from a low vibrational frequency to higher frequencies was investigated. This pumping could serve to increase the overall energy dissipation in the system. From numerical simulations of the steady-state forced and free responses, several aspects of the system were observed. In the case of harmonic excitation, the frictional interface produced a stick-slip response that excited internal resonances at odd harmonics of the driving frequency. Second, there was a one-way transfer of energy from one subsystem to the other in the free response. Third, a wavelet analysis of the free response concluded that the frictional interface pumped energy to a higher frequency. Finally, by studying the energies in the 3-DOF system, it was shown that tuning produced favorable conditions for energy dissipation. When the 3<sup>rd</sup> subsystem was tuned to the higher frequencies generated by the frictional interface, there was an increase in energy dissipation versus the case where friction was not present. This increase in energy dissipation could lead to an improved damping capacity of the overall system.

This investigation is admittedly simple in order to permit a more thorough understanding of the phenomenon. The subsystems are SDOF spring-mass-damper systems and the friction model is of the Stribeck type. Future studies could employ more complicated joint models and different friction models. Application of these studies to more complicated structural subsystems could validate the general observations about the importance of tuning of natural frequencies to the stick-slip frequencies. Ultimately, it would be desirable to develop design rules that lead to enhanced damping levels of the global structural system.

## ACKNOWLEDGMENTS

The authors would like to thank the Air Force Office of Scientific Research (AFOSR), under contract number F49620-03-1-0176, for providing funding for this research.

## REFERENCES

1. Ungar, E.E., "The Status of Engineering Knowledge Concerning the Damping of Built-up Structures," *Journal of Sound and Vibration*, vol. 26, pgs. 141-154, 1973.
2. Beards, C.F., "Damping in Structural Joints," *The Shock and Vibration Digest*, vol. 24, pgs. 3-7, 1992.
3. Folkman, S.L., and F.J. Redd, "Gravity Effects on Damping of a Space Structure with Pinned Joints," *AIAA Journal of Guidance, Control, and Dynamics*, vol. 13, pgs. 228-233, 1990.
4. Folkman, S.L., E.A. Rowsell, and G.D. Ferney, "Influence of Pinned Joints on the Damping and Dynamic behavior of a Truss," *AIAA Journal of Guidance, Control, and Dynamics*, vol. 18, pgs. 1398-1403, 1995.
5. Hertz, T.J. and E.F. Crawley, "Displacement Dependent Friction in Space Structural Joints," *AIAA Journal*, vol. 23, pgs. 1998-2000, 1985.
6. Ferri, Aldo A., "Modeling and Analysis of Nonlinear Sleeve Joints at Large Space Structures," *AIAA Journal of Spacecraft and Rockets*, vol. 25, pgs. 354-360, 1988.
7. Ferri, A.A., "Friction Damping and Isolation Systems," *ASME Journal of Vibration and Acoustics*, Vol. 117(B), June 1995, pp. 196-206
8. Ferri, A.A., "Damping Through Use of Passive and Semi-Active Dry Friction Forces," in Dynamics with Friction: Modeling, Analysis, and Experiment, Part II, Vol. 7, Series on Stability, Vibration, and Control of Structures, World Scientific Publishing, 2001, pp. 253-308.
9. Gaul, L. and R. Nitsche, "The Role of Friction in Mechanical Joints," *Applied Mechanics Reviews*, vol. 54, pgs. 93-105, 2001.
10. Gendelman, O., L.I. Manevitch, A.F. Vakakis, and R. M'Closkey, "Energy Pumping in Nonlinear Mechanical Oscillators: Part I – Dynamics of the Underlying Hamiltonian Systems," *ASME Journal of Applied Mechanics*, vol. 68, pgs. 34-41, 2001.
11. Onoda, Junjiro, Tetsuji Sano, and Kenji Minesugi, "Passive Vibration Suppression of Truss by Using Backlash," *The 34<sup>th</sup> AIAA/ASME/ASCE/AHS/ASC Structures, Structural Dynamics, and Materials Conference*, La Jolla, CA, April 19-22, 1993.

12. Bindemann, A.C., and A.A. Ferri, "The Influence of Friction Models on the Passive Damping and Dynamic Response of a Flexible Beam Structure," *Proceedings of the 36th Structures, Structural Dynamics, and Materials Conf.*, New Orleans, LA, April 10-12, 1995, pp. 180-189.
13. Ibrahim, R.A., "Friction Induced Vibration, Chatter, Squeal, and Chaos: Part I – Mechanics of Friction," *Applied Mechanics Reviews*, vol. 47, no. 7, pgs. 209-253, 1994.
14. Mitiguy, P.C., and A.K. Banerjee, "Efficient Simulations of Motion Involving Coulomb Friction," *AIAA Journal of Guidance, Control, and Dynamics*, vol. 22, pgs. 78-86, 1999.
15. Ferri, A.A., and B.S. Heck, "Analysis of Stick-Slip Motion in Coulomb Damped Systems Using Variable Structure System Theory," *Proceedings of the 1997 ASME Design and Technical Conferences*, Sacramento, CA, Sept. 14-17, 1997.
16. Nayfeh, Ali Hasan, and Dean T. Mook, 1979, *Nonlinear Oscillations*, John Wiley and Sons, New York.
17. Donoho, David, Mark Reynold Duncan, Xiaoming Huo, and Ofer Levi, *WaveLab 802 for Matlab5.x*. <http://www-stat.stanford.edu/~wavelab/>, Oct. 3, 1999.

**DETC2005-85339**

## EFFICIENT SIMULATION OF A DYNAMIC SYSTEM WITH LUGRE FRICTION

**Nguyen B. Do**  
 School of Mechanical  
 Engineering, Georgia Institute of  
 Technology, Atlanta, GA  
 30332-0405, U.S.A.

**Aldo A. Ferri**  
 School of Mechanical  
 Engineering, Georgia Institute of  
 Technology, Atlanta, GA  
 30332-0405, U.S.A.

**Olivier Bauchau**  
 School of Aerospace  
 Engineering, Georgia Institute of  
 Technology, Atlanta, GA  
 30332-0405, U.S.A.

### ABSTRACT

Friction is a difficult phenomenon to model and simulate. One promising friction model is the LuGre model, which captures key frictional behavior from experiments and from other friction laws. While displaying many modeling advantages, the LuGre model of friction can result in numerically stiff system dynamics. In particular, the LuGre friction model exhibits very slow dynamics during periods of sticking and very fast dynamics during periods of slip. This paper investigates the best simulation strategies for application to dynamic systems with LuGre friction. Several simulation strategies are applied including the explicit Runge-Kutta, implicit Trapezoidal, and implicit Radau-IIA schemes. It was found that both the Runge-Kutta and Radau-IIA methods performed well in simulating the system. The Runge-Kutta method had better accuracy, but the Radau-IIA method required less integration steps.

### INTRODUCTION

Friction is a natural phenomenon that occurs in many engineering systems. In cases where the effects of friction cannot be ignored, a good friction model is necessary for the design, control, and analysis of the system. Although the concept of friction is easily understood, it is notoriously difficult to model and simulate. Many friction models contain a variety of nonlinear features such as discontinuities, hysteresis, internal dynamics, and other complications. These properties cause the friction models to be numerically stiff and therefore computationally cumbersome. For that reason, it would be advantageous to efficiently simulate a model that captures key characteristics of friction. In this paper, we will first present a brief summary of some classical friction models together with the LuGre friction model. Secondly, a simple dynamic model is presented to analyze the characteristics of the LuGre friction model. Next, the governing equations of the

LuGre model are analyzed and the dynamic system is simulated using several numerical integration techniques. Finally, conclusions are made concerning the most efficient technique to simulate the LuGre friction model.

### FRICTION MODELING AND SIMULATION

Numerical difficulties associated with simulation of frictional systems are well documented. See, for example, [Armstrong-Helouvry, *et al*, 1994; Mitiguy and Banerjee, 1999], etc. The basic problem is one of numerical stiffness. Simple models of friction, derived from the Coulomb friction paradigm, suggest that the friction force changes “discontinuously” as the direction of interfacial slip changes. Figure 1 shows some typical sketches of friction force versus slip velocity. It should be noted that “sticking” of the frictional interface is characterized by zero slip velocity; therefore, it is not uncommon for the frictional interface to spend intermittent and finite periods of time at zero slip velocity, where the friction law is discontinuous.

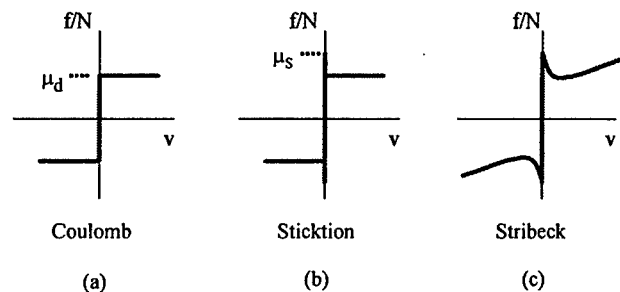


Figure 1. Normalized friction force vs slip velocity. (a) Coulomb, (b) Sticktion, and (c) Stribeck friction laws.

If one starts from the assumption that the friction laws depicted in Figure 1 properly reflect the behavior of sliding

friction, the discontinuity presents a host of analytical and computational challenges. Simulation of the time response requires very fine time steps to maintain accuracy in regions where the slip velocity changes sign or where sticking occurs. Depending on the time-integration method used, it is even possible for numerical instabilities to develop. Two main strategies have been employed to deal with this problem. First, numerous studies have sought to “smooth” or “regularize” the friction law in the vicinity of the discontinuity. For example, the signum type nonlinearity depicted in Figure 1(a), can be replaced with a saturation-type nonlinearity, as in Figure 2, or a smoothly transitioning approximation as shown in Figure 3. In both cases, the infinite slope at  $v = 0$  is replaced with a slope of order  $1/\epsilon$ , where  $\epsilon$  is small relative to some characteristic slip velocity for the problem in question. Obviously, as  $\epsilon \rightarrow 0$ , the numerical stiffness of the problem becomes worse and worse. Consequently, time-simulation of friction-damped systems that experience finite periods of sticking are burdened with very small time steps, necessitating high computation times in order to maintain stability and/or accuracy.

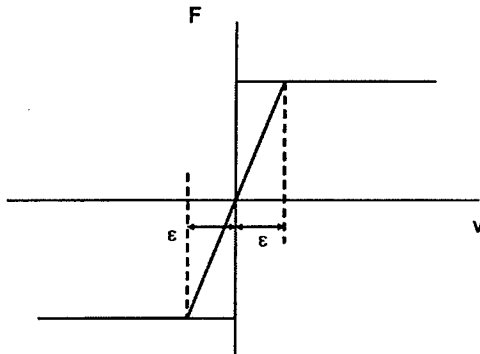


Figure 2. Saturation approximation of signum nonlinearity.

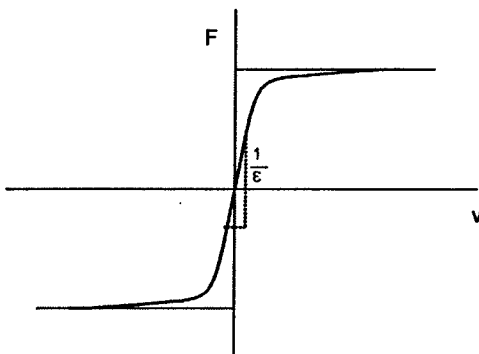


Figure 3. Smooth approximation of signum nonlinearity.

A second approach to address simulation of systems with discontinuous friction is to utilize a “switching strategy,” or also known as an event-driven strategy [Pfeiffer and Glocker, 1996]. In this approach, the system is simulated either using the discontinuous friction law, or using a smoothed version thereof. However, when the slip velocity changes sign, one checks to determine whether the maximum-available friction

force is sufficient to prevent slip from occurring. See, for example, [Ferri and Heck, 1997; Whiteman and Ferri, 1997]. Depending on the outcome of this check, one either continues to integrate the “slipping equations,” or one switches to the use of “sticking equations,” which model the system with a stuck interface. Variations of this idea have also appeared in the literature [Ferri and Heck, 1997, Karnopp, 1985]. While this strategy alleviates the numerical stiffness problems associated with smoothing the discontinuity, they replace it with another problem. As seen in Figure 4, the accuracy of the method hinges on accurate determination of the switching time. The figure shows a transition from slipping to sticking, followed by renewed slip in the opposite direction. Due to errors in the computational solution, this switching time could be “delayed” (or “advanced”) by some small amount of time. Equivalently, delays could occur due to the discrete nature of the numerical solution.

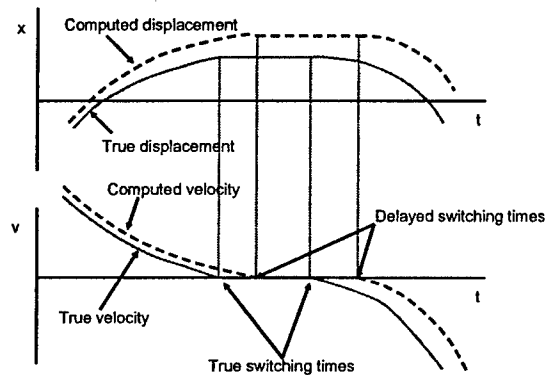


Figure 4. Delayed switching time.

Of course, in reality, the physical friction process is not discontinuous. Various models of friction have been proposed that address this shortcoming, by refining the behavior of the interface when the slipping velocity is small or when it changes sign. For example, “microslip” models allow small amounts of displacement to occur during sticking. The most common such microslip model is the Iwan-model, also termed the elastic-perfectly plastic model [Ferri, 1995]. Conceptually, the model can be thought of as a spring in series with a Coulomb friction element having friction force  $\mu N$ . When the force in the spring reaches a magnitude of  $\mu N$ , the force in the Iwan-model saturates until the direction of slip reverses. Smooth versions of this behavior have also been proposed, for example, the Dahl model [Dahl, 1976], the Valanis model [Gaul and Nitsche, 2001; Valanis, 1971], and Leuven Model [Swevers, et al, 2000; Lampaert, et al, 2002]. Recently, bristle models have been proposed that capture both the microslip and macroslip regimes of interfacial friction. Haessig and Friedland (1991) proposed a bristle model where individual bristles are treated separately, separating as bonds are broken, and then re-adhering. The LuGre friction model, so named because it was developed jointly by researchers at the Lund Institute of Technology in Sweden and the University of Grenoble, in France [Canudas de

Wit, *et al*, 1995], is also based on a bristle interpretation of the frictional interface, but it treats the collection of bristles in an aggregate fashion. The details of this model are presented below.

## LUGRE MODEL

As discussed above, the LuGre model has become popular because it incorporates many of the observed features of frictional behavior. For example, imbedded within the LuGre model is the Stribeck effect, displayed in Figure 1(c). The Stribeck model exhibits a negative derivative with respect to slip velocity, for small levels of slip velocity. This is one of the key features of friction that contributes to limit-cycle behavior and stick-slip oscillations in frictional systems. Furthermore, the LuGre model behaves like a linear spring/damper pair when it is linearized for small motions.

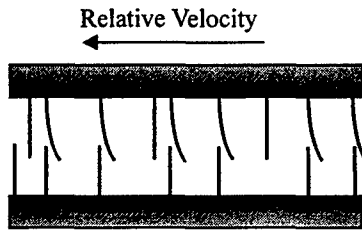


Figure 5. Description of the frictional interface in the LuGre model.

A qualitative description of the LuGre model is shown in Figure 5. At the microscopic level, two surfaces make contact at various asperities. These asperities are represented with bristles, and the bristles deflect like a spring when there is a relative velocity between the two surfaces. The deflection of the springs gives rise to the friction force. If the deflection is sufficiently large, then the bristles will slip in a highly random manner because of the irregular surfaces. Although the deflection of the bristles is random, the LuGre model only considers the average deflection. The average deflection of the bristles,  $Z$ , is modeled by the first-order differential equation

$$\dot{Z} = V - \frac{|V|}{G(V)} Z \quad (1)$$

where  $V$  is the relative velocity between the two surfaces and  $G(V)$  is a function that describes the Stribeck effect. The function  $G(V)$  allows the LuGre model to accommodate a higher static coefficient of friction than dynamic coefficient of friction:

$$G(V) = \frac{1}{\sigma_0} \left\{ F_C + (F_S - F_C) e^{-(V/V_S)^2} \right\} \quad (2)$$

where  $F_C$  is the kinetic friction force,  $F_S$  is the static friction force,  $\sigma_0$  is the aggregate bristle stiffness, and  $V_S$  is the Stribeck velocity. Finally, the LuGre friction force is given by

$$F_L(V, Z) = \sigma_0 Z + \sigma_1 \dot{Z} + \sigma_2 V \quad (3)$$

where  $\sigma_1$  is a damping coefficient and  $\sigma_2$  accounts for viscous friction. For this study, the values used for the LuGre parameters are listed in Table 1. Note that  $V_S$  is a very small slip velocity, below which the frictional interface can be thought of as being "stuck" or undergoing microslip.

Table 1. LuGre Friction Model Parameters [Canudas de Wit, *et al.*, 1995]

Parameter	Value	Unit
$\sigma_0$	$10^5$	N/m
$\sigma_1$	$\sqrt{10^5}$	Ns/m
$\sigma_2$	0.4	Ns/m
$F_C$	1	N
$F_S$	1.5	N
$V_S$	.001	m/s

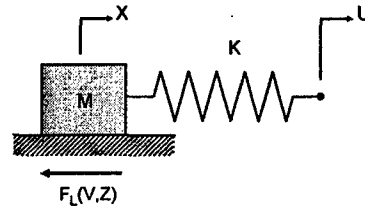


Figure 6. Stick-slip system. The parameters are  $M = 1$  kg,  $K = 2$  N/m, and  $U = 0.1$  m.

## SYSTEM MODELING

To analyze the characteristics of the LuGre model, a system proposed by Canudas de Wit, *et al* (1995) is used to focus the present discussion. The system, shown in Figure 6, represents a mass,  $M$ , connected to a spring  $K$  that is being pulled by a constant velocity,  $\dot{U} = R$ . As the mass slides along, the LuGre friction force,  $F_L(V, Z)$ , opposes the motion of the mass. The position of the mass is denoted by  $X$  and its velocity is  $V$ . Two first-order equations govern the motion of the mass:

$$\dot{X} = V \quad (4)$$

$$\dot{V} = (KU - KV - F_L(V, Z))/M \quad (5)$$

It is useful to nondimensionalize the equations governing the mass as well as that of the LuGre force by introducing the following terms:

$$y_1 = \frac{KV}{F_C}, \quad y_2 = \frac{V}{V_S}, \quad y_3 = \frac{\sigma_0 Z}{F_C}, \quad (6a)$$

$$u = \frac{KU}{F_C}, \quad \omega_n = \sqrt{K/M}, \quad \tau = \omega_n t$$

$$\alpha = \frac{KV_S}{\omega_n F_C}, \gamma = \frac{F_S - F_C}{F_C}, \varepsilon = K/\sigma_0$$

$$s_1 = \frac{\sigma_1 V_S}{F_C}, s_2 = \frac{\sigma_2 V_S}{F_C} \quad (6b)$$

When (6) is introduced into equations (4), (5), and (1), the following three equations are obtained:

$$y_1' = \alpha y_2 \quad (7)$$

$$y_2' = (u - y_1 - f_L(y_2, y_3))/\alpha \quad (8)$$

$$\varepsilon y_3' = \alpha y_2 - \alpha \frac{|y_2|}{g(y_2)} y_3 \quad (9)$$

where ' denotes a derivative with respect to nondimensional time,  $\tau$ , and

$$f_L(y_2, y_3) = y_3 + s_1 \left( y_2 - \frac{|y_2|}{g(y_2)} y_3 \right) + s_2 y_2 \quad (10)$$

$$g(y_2) = 1 + \gamma \exp(-y_2^2) \quad (11)$$

Equations (7), (8), and (9) can be conveniently represented in state-space form:

$$y' = f(y, u) \quad (12)$$

where  $y$  is the state vector  $[y_1 \ y_2 \ y_3]^T$ .

The function  $g$  dies out rapidly with  $y_2$ , as shown in Figure 7;  $g$  is approximately equal to 1 for  $|y_2| > 3$ . Also note that the slope of  $g$  is zero at  $y_2 = 0$ , and is approximately zero outside the range  $|y_2| > 3$ . The magnitude of the slope is maximum at  $y_2 = \pm 1/\sqrt{2}$ , implying that the dynamics can change rapidly when the velocity is in the "sticking range," defined to be  $|y_2| < 1$ .

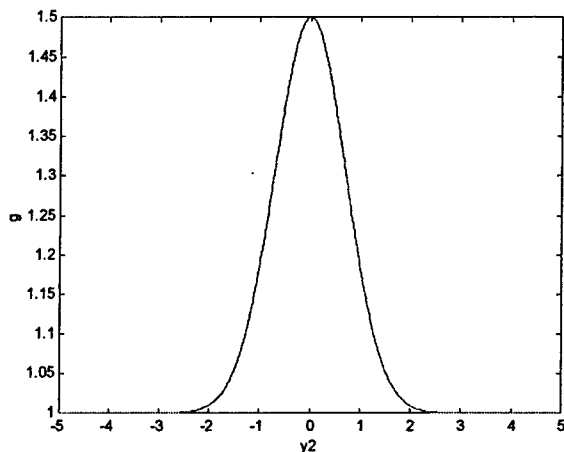


Figure 7. LuGre function  $g$  versus  $y_2$  using values in Table 1.

It may be noted that equations (7), (8) and (9) are in standard, singular perturbation form [Kokotovic, et al, 1986]. The stiffness ratio  $\varepsilon = K/\sigma_0$  (not to be confused with  $\varepsilon$  in Figures 2 and 3) is typically small, due to the relatively high

bristle stiffness. Using the numerical values of Table 1,  $\varepsilon$  is equal to  $2 \times 10^{-5}$ . The smallness of the parameter  $\varepsilon$  is partially to blame for the "numerical stiffness" of the system of equations. Numerical stiffness makes it difficult to simulate the response of the system, because it necessitates very small time steps to ensure algorithm stability and accuracy. The problem is compounded when the system in question is more realistic, such as a multi-degree-of-freedom structure with multiple frictional interfaces. As the present system is only single-degree-of-freedom, it is possible to study the numerical stiffness problem analytically.

In order to examine the numerical stiffness of the LuGre dynamics, one can examine the Jacobian of the state dynamics:

$$J = \begin{bmatrix} \frac{\partial f_1}{\partial y_1} & \frac{\partial f_1}{\partial y_2} & \frac{\partial f_1}{\partial y_3} \\ \frac{\partial f_2}{\partial y_1} & \frac{\partial f_2}{\partial y_2} & \frac{\partial f_2}{\partial y_3} \\ \frac{\partial f_3}{\partial y_1} & \frac{\partial f_3}{\partial y_2} & \frac{\partial f_3}{\partial y_3} \end{bmatrix} = A + B(y_2, y_3) + C(y_2) \quad (13)$$

where

$$A = \begin{bmatrix} 0 & \alpha & 0 \\ -1/\alpha & -(s_1 + s_2)/\alpha & -1/\alpha \\ 0 & \alpha/\varepsilon & 0 \end{bmatrix} \quad (14)$$

$$B(y_2, y_3) = \begin{bmatrix} 0 & 0 & 0 \\ 0 & s_1 y_3 / \alpha & 0 \\ 0 & -\alpha y_3 / \varepsilon & 0 \end{bmatrix} \left\{ \frac{g + 2\gamma y_2^2 \exp(-y_2^2)}{g^2} \right\} \text{Sgn}(y_2) \quad (15)$$

and

$$C(y_2) = \begin{bmatrix} 0 & 0 & 0 \\ 0 & 0 & s_1 / \alpha \\ 0 & 0 & -\alpha / \varepsilon \end{bmatrix} \left\{ \frac{|y_2|}{g} \right\} \quad (16)$$

As it describes the "local dynamics" of the system, the Jacobian is useful in analyzing the source of the numerical stiffness when (12) is time integrated. In the case of explicit numerical integration routines, the stability of the algorithm depends on the size of the nondimensional time step,  $h$ . The maximum allowable time step is inversely proportional to the largest magnitude eigenvalue of  $J$ . As seen above,  $A$  has no dependence on the state vector  $y$ . For sufficiently large  $|y_2|$ ,  $B$  becomes independent of  $y_2$ , except for a dependence on the sign of  $y_2$ . The matrix  $C$ , however, grows linearly with  $|y_2|$ , dominating matrices  $A$  and  $B$  for high slip velocities ( $|y_2| \gg 10$ ). Thus, an expression for the largest magnitude eigenvalue of  $J$  that holds asymptotically as  $|y_2|$  gets larger and larger can be derived based on the nonzero eigenvalue of  $C$ :

$$\lambda_{\max}(J) = \frac{\alpha |y_2|}{\varepsilon g} \quad (17)$$

It is seen that  $\lambda_{\max}$  grows linearly with  $|y_2|$ . Therefore, as the velocity of the mass becomes large compared to the Stribeck velocity,  $V_S$ , the maximum allowable time step becomes smaller. It is also seen that  $\lambda_{\max}$  is inversely proportional to  $\varepsilon = K/\sigma_0$ . Thus as the aggregate bristle stiffness  $\sigma_0$  grows larger, the numerical stiffness problem worsens, especially during episodes of high slip velocity. In dimensional terms,  $\lambda_{\max}(J) = V\sigma_0/F_c \text{ sec}^{-1}$ .

An alternate interpretation of (17) is obtained by inspection of the LuGre dynamics (9). If, over a small interval, the nondimensionalized velocity ( $y_2$ ) is assumed to be constant, then the coefficients of (9) are constant over this interval. Subsequently, (9) becomes a linear first-order differential equation with a time constant,  $T_c$ :

$$y_3' = \frac{\alpha}{\varepsilon} y_2 - \frac{\alpha}{\varepsilon} \frac{|y_2|}{g(y_2)} y_3 = \frac{\alpha}{\varepsilon} y_2 - \frac{y_3}{T_c} \quad (18)$$

where

$$T_c = \frac{\varepsilon g}{\alpha |y_2|} \quad (19)$$

From (19), it is evident that the time constant is equal to the inverse of the maximum eigenvalue given by (17). For very low values of  $y_2$ , the time constant is very large, indicating very slow friction dynamics. As the velocity emerges from the sticking range,  $|y_2| \approx 1$ ,  $g$  falls off rapidly, decreasing the time constant. For  $|y_2| > 3$ ,  $g(y_2)$  is approximately 1 and  $T_c$  decreases inversely to  $y_2$ . As the time constant tends to zero, the dynamics of the friction model are much faster than that of the mechanical system. Qualitatively, this behavior can be attributed to the movement of the bristles. During microslip, the bristles move in a slow, linear manner. When the critical limit is reached, the bristles "snap" back to place and cause an increase in the speed of the friction dynamics. As the velocity increases, the frequency of contact between the bristles increases, therefore causing the bristles to move faster. The difference between the speed of the friction dynamics and that of the mass-spring-system is what leads to numerical stiffness. This difference results in the requirement of small time steps and the associated long computation times.

During sticking, which corresponds to zero values of both  $y_2$  and  $y_3$ , the eigenvalues of  $J$  are given by  $A$  alone. By inspection, one eigenvalue of  $A$  is identically zero. Using the friction parameters of Table 1,  $K = 2 \text{ N/m}$ , and  $M = 1 \text{ kg}$ , the remaining two eigenvalues are  $-111.94 \pm 193.57i$ , which correspond to a magnitude of  $\lambda_{\max}(J) = 223.61$  and a damping ratio of 0.50. For small-to-moderate values of  $y_2$ , one must compute  $\lambda_{\max}(J)$  numerically. Due to the presence of  $B$ ,  $\lambda_{\max}$  is a function of both  $y_2$  and  $y_3$ . Also note that the matrix  $B$  describes sensitivity of the Jacobian to the high slope of the function  $g$  within the range  $|y_2| < 1$ . Figure 8 shows  $\lambda_{\max}(J)$  versus  $y_2$  for  $y_3 = \pm 1$ . Also shown is the asymptotic expression for  $\lambda_{\max}(J)$  given by (17). For small velocities, the bristle displacement  $y_3$  produces a difference in the maximum eigenvalue from the asymptotic result. However, as  $|y_2|$

increases, this difference becomes less and less significant when viewed as a percent of  $\lambda_{\max}(J)$ .

A number of conclusions can be drawn from Figure 8. It is seen that the system is relatively well conditioned for low velocities ( $|y_2| < 3$ ), including the microslip region. The system becomes more and more ill-conditioned as the slip velocity grows. This is in stark contrast to the regularization schemes portrayed in Figures 2 and 3. When the discontinuity is smoothed in the vicinity of the zero-slip point, the system of equations are ill-conditioned for small velocities (microslip) and become better conditioned as the slip velocity increases in magnitude.

This contrast may appear at first to be counterintuitive, because it is at odds with the behavior of standard approaches of friction modeling and simulation discussed in the Introduction. Whether one smoothes the discontinuity or uses switching between sticking and slipping dynamical systems, the numerical problems are all located in the vicinity of *small slip velocities*. In the LuGre model of friction, sticking and near-sticking conditions are where the system is *relatively well conditioned*; ill-conditioning develops as the slipping velocity gets larger.

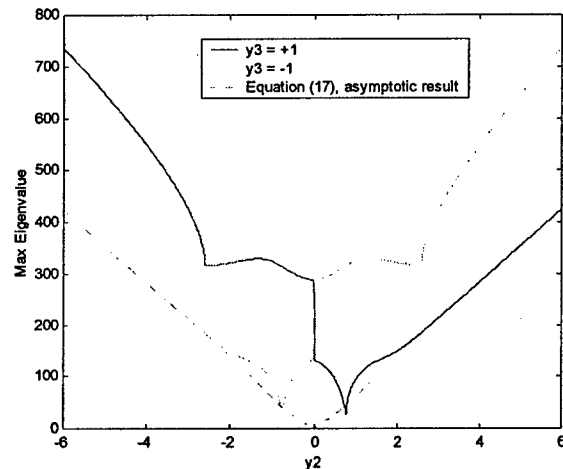


Figure 8. Maximum magnitude eigenvalue vs  $y_2$ .

## NUMERICAL SIMULATION RESULTS

To initially simulate the stick-slip system, the Matlab function *ode45* was used. The *ode45* function is based on an explicit Runge-Kutta formula, the Dormand-Prince pair [Forsythe, *et al.*, 1977; Kahaner, *et al.*, 1989]. The routine uses a variable time step, based on specified tolerances: a relative tolerance,  $RelTol$ , whose default value is  $1 \times 10^{-3}$ , and an absolute tolerance,  $AbsTol$ , whose default value is  $1 \times 10^{-6}$ . Figures 9 through 11 show the nondimensional state quantities while Figure 12 shows the nondimensional LuGre friction force,  $f_i(y_2, y_3)$ . In the case shown,  $RelTol = 1 \times 10^{-4}$ , and  $AbsTol = 1 \times 10^{-6}$ . Note that the friction force behaves irregularly during the stick-slip regions. This irregular behavior can be attributed to the sudden change from the static friction force to

the kinetic friction force. Further examination shows that at the instant the system begins to slip, the friction force initially decreases before increasing with increasing velocity. This phenomenon is consistent with the Stribeck effect. Lastly, like the elastic friction model, the friction force during the sticking phase acts like a linear spring.

From Figures 9 and 10, the displacement and velocity are fairly smooth and accurate, with results closely matching scaled results from [Canudas de Wit, et. al., 1995]. The LuGre force, on the other hand, exhibits a noticeable “ringing” in time intervals of high slip velocity. The ringing largely disappears when RelTol and AbsTol are lowered to  $1 \times 10^{-8}$ .

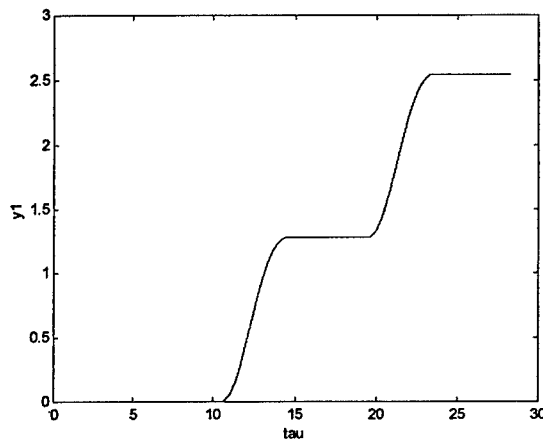


Figure 9:  $y_1$  vs.  $\tau$  using *ode45* with RelTol =  $1 \times 10^{-4}$  and AbsTol =  $1 \times 10^{-6}$ .

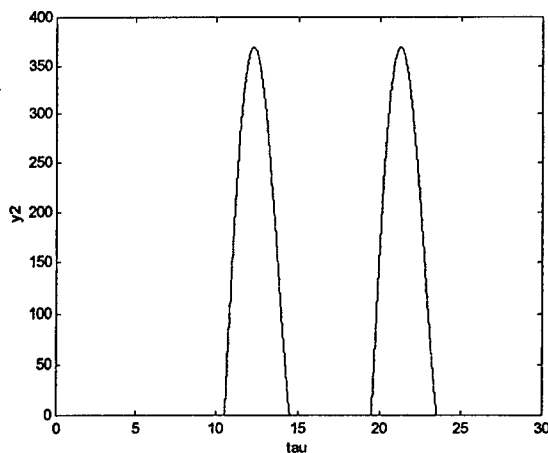


Figure 10:  $y_2$  vs.  $\tau$  using *ode45* with RelTol =  $1 \times 10^{-4}$  and AbsTol =  $1 \times 10^{-6}$ .

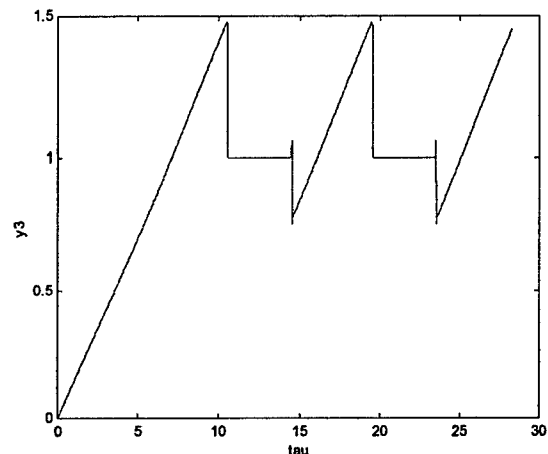


Figure 11:  $f_2$  vs.  $\tau$  using *ode45* with RelTol =  $1 \times 10^{-4}$  and AbsTol =  $1 \times 10^{-6}$ .

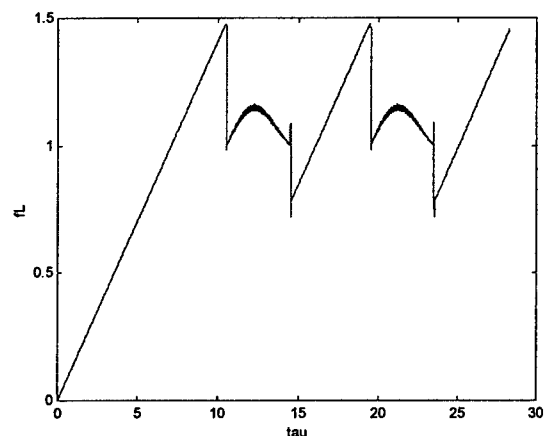


Figure 12:  $f_L$  vs.  $\tau$  using *ode45* with RelTol =  $1 \times 10^{-4}$  and AbsTol =  $1 \times 10^{-6}$ .

The reason for the ringing in the friction force is uncovered by examining the Jacobian at each point along the state trajectory. Figure 13 shows  $\lambda_{\max}(J)$  vs  $\tau$  from a more accurate simulation using *ode45* with RelTol =  $1 \times 10^{-7}$  and AbsTol =  $1 \times 10^{-7}$ . It is seen that the time intervals in which the largest eigenvalue magnitudes occur is closely related to occurrences of high slip velocities. Figures 14a shows a close up of  $\lambda_{\max}(J)$  just as the mass transitions from microslip to macroslip, and Figure 14b shows  $\lambda_{\max}(J)$  just after the first interval of macroslip comes to an end. For comparison, the figures also show the asymptotic result calculated by Equation (17). As the slip velocity increases, the asymptotic result (or equivalently, the inverse of the time constant) agrees very closely with  $\lambda_{\max}(J)$ . However, it should be noted that in the transition region, the inverse of the time constant significantly under-predicts the true  $\lambda_{\max}(J)$ .

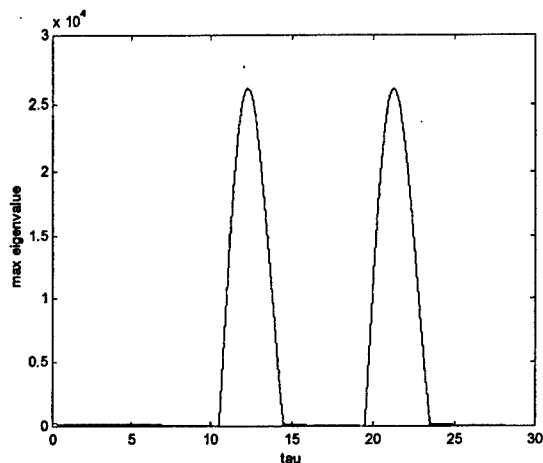


Figure 13:  $\lambda_{\max}(J)$  vs  $\tau$ ; from *ode45* with  $\text{RelTol} = 1 \times 10^{-7}$  and  $\text{AbsTol} = 1 \times 10^{-7}$

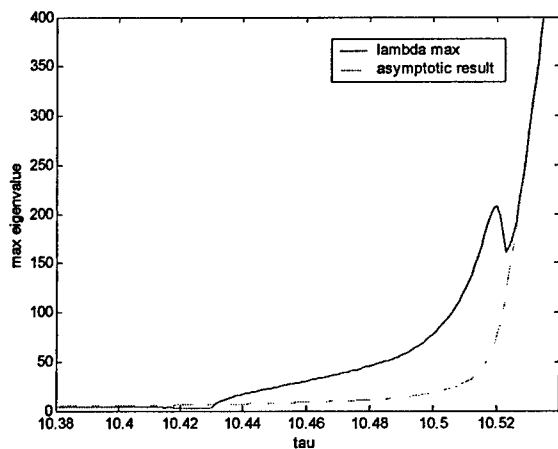


Figure 14(a): Maximum eigenvalue during the transition from microslip to macroslip.

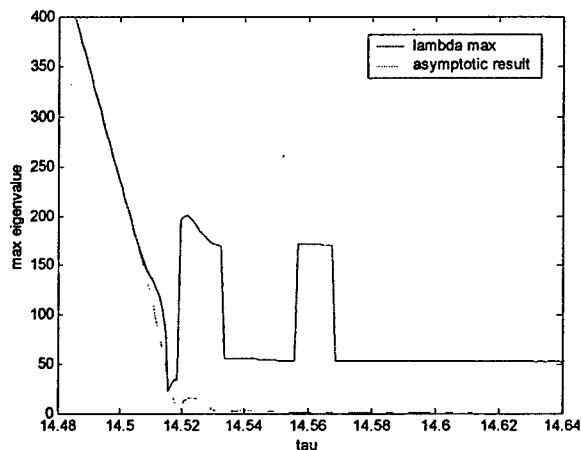


Figure 14(b): Maximum eigenvalue during the transition from macroslip to microslip.

The large size of  $\lambda_{\max}(J)$  during periods of high slip velocity is the major source of the ringing that is evident in the LuGre friction force. However, the ringing that is present in the state vector itself is far less pronounced. In fact, only the bristle displacement  $y_3$  displays any appreciable ringing during high slip rates. Figure 15 shows a close up of  $y_3$  during the period of maximum slip. It is seen that the ringing in  $y_3$  amounts to approximately 0.01% of the nominal value. The ringing is amplified in the LuGre force because of the way that  $f_L$  is calculated; in particular, the expression in parentheses in (10) involves the subtraction of two terms that are large, and almost exactly equal. Operations of this type are prone to round-off errors during computation.

The nondimensionalization of the terms associated with the LuGre friction model is very important. Due to the size of the bristle stiffness, the displacement  $Z$  is orders of magnitude smaller than  $X$  and  $V$ . Consequently, direct integration of the dimensional system of equations is less accurate due to round-off errors.

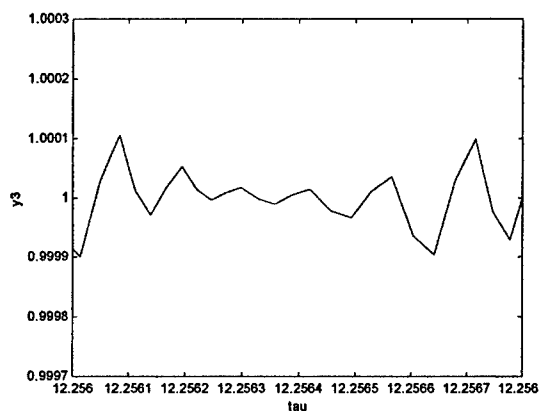


Figure 15: Close-up of  $y_3$  vs  $\tau$ , *ode45* with  $\text{RelTol} = 1 \times 10^{-4}$  and  $\text{AbsTol} = 1 \times 10^{-6}$ .

## COMPARISON OF INTEGRATION METHODS

To find the best strategies to simulate the stick-slip system, several techniques were considered. Aside from using built-in Matlab functions, the techniques included user-defined explicit and implicit time integration methods. The main difference between explicit and implicit integration schemes is in the formulation. Explicit schemes use past states to define the current states, whereas implicit schemes define the current states using past and current results. Furthermore, one can guarantee the stability of the result using implicit methods. As a note, all computer simulations were done using Matlab 6.1 on a Pentium 4, 2.4 GHz computer. Also, the simulation time was from 0 to 20 seconds.

### Explicit Integration Methods

Although the use of a Matlab function was useful as a first attempt to solve the system, it was necessary to write a user-defined integration scheme to fully understand and control the simulation process. Because of its popularity and efficiency,

the 4<sup>th</sup> order Runge-Kutta method was chosen as the explicit solver. Like the *ode45* function, this Runge-Kutta method is an explicit, time-marching scheme with a time step,  $h$ , a local error on the order of  $h^5$ , and a global error on the order of  $h^4$  [Faires and Burden, 1998]. Since the maximum allowable time step is proportional to the inverse of the largest magnitude eigenvalue of the Jacobian, a time step based on this value was used for the baseline simulation. From (17),  $\lambda_{\max} = 2.62 \times 10^4$  for the maximum value of  $|y_2|$  in the simulation, which corresponds to a minimum time constant of  $3.82 \times 10^{-5}$ . To best capture the dynamics of the system, a time step of  $10^{-5}$  was used, which was more than three times less than the minimum time constant. Note that the time step used,  $h$ , is in nondimensional form defined by  $h = \omega_n H$ , where  $H$  is the dimensional time step.

Although the baseline simulation ( $h = 10^{-5}$ ) gave the best results, it was not necessary to use such a small time step at all times. From previous analyses, the dynamics of the system is fast during periods of slip, but slow during microslip. Hence, it would be advantageous to base the time step based on the local dynamics of the system. One way to vary the time step was to define  $h$  based on the inverse of the maximum eigenvalue, as shown in Figure 13. However, this would be cumbersome because finding the eigenvalues of the Jacobian at each time step requires too many calculations. The added overhead for such a technique would be prohibitive, especially for realistic systems having a higher number of degrees of freedom.

Another way to estimate the time step necessary to simulate the system was to use the time constant, as defined by (19). From Figures 14a and 14b, the inverse of the time constant agrees well with the maximum eigenvalue during moderate to high levels of slip. The periods where these values do not agree are the transitional periods and during sticking. However, this disagreement was addressed by setting a maximum time step such that the integration scheme remained stable. For the system under consideration here, this maximum time step was set at  $10^{-3}$ . During periods of slip, estimated as  $T_c < 0.02$ , the time step was set to one-third of the time constant. Otherwise, the time step was set to  $10^{-3}$ .

To make the simulation more efficient, another method based on the velocity was used to estimate the time step. Because the dynamics of the system change rapidly at the stick/stick transition periods, a small time step ( $10^{-4}$ ) was used in this region. Otherwise, the time step was set to  $10^{-3}$ . This stick/slip transition region was defined as the range  $0.1 \leq |y_2| < 5$ .

Table 2 compares the different explicit methods in order of decreasing simulation time. In addition to the baseline case (4th order Runge-Kutta with  $h = \text{constant} = 10^{-5}$ ), four other cases are shown: 4th order Runge-Kutta with  $h$  switched based on the time constant, *ode45* with  $\text{RelTol} = \text{AbsTol} = 10^{-8}$ , 4th order Runge-Kutta with  $h$  switched based on  $|y_2|$ , and 4th order Runge-Kutta with  $h = \text{constant} = 10^{-3}$ . Two different error metrics were employed. First, the error,  $E$ , was computed by taking the absolute value of the difference in the

dimensionalized friction forces at each instant in time. The first error metric listed in Table 2 is simply the maximum of  $E$  over the duration of the simulation. The second error metric is the root-mean-squared error,  $E_{RMS}$ , is calculated by

$$E_{RMS} = \frac{1}{T} \sqrt{\int_0^T E^2 dt} \quad (20)$$

where  $T$  is the final time. Since the number of time steps was different for each method, the data was interpolated from the baseline data set for comparison. Lastly, the simulation time is reported as a percentage to the baseline simulation time, which is 1651s, or 27.5 minutes.

Table 2. Comparison of Explicit Methods

Simulation Method	Time Step	Error (N)		Simulation Time (%)	Steps
		Max	RMS		
Runge-Kutta (Baseline)	$10^{-5}$	n/a	n/a	100	2.828e6
Runge-Kutta (Time constant)	$(1/3)T_c$ or $10^{-3}$	0.207	7.46e-4	14.8	4.020e5
Ode45*	n/a	1.68e-4	4.22e-8	3.62	1.476e5
Runge-Kutta (Velocity)	$10^{-4}$ or $10^{-3}$	0.320	1.30e-3	1.17	3.170e4
Runge-Kutta (Constant)	$10^{-3}$	3.98e-4	1.16e-6	1.14	2.829e4

\* absolute tolerance = relative tolerance =  $10^{-8}$

Table 2 shows that there is a significant improvement in the simulation time by switching the time step based on the time constant of the system. However, the maximum error using this method is unacceptable (~14% error) and the number of steps required is still relatively large. The Runge-Kutta method with  $h$ -switching based on the velocity performed much better in terms of simulation time and number of steps, but its accuracy was the worst. The result using *ode45* had the best accuracy and a very short simulation time compared to the baseline. Finally, using the Runge-Kutta method with a constant time step of  $10^{-3}$  produced errors comparable to the *ode45* method, but with the smallest simulation time and least amount of steps. This last result is surprising since  $10^{-3}$  is roughly 26 times larger than the frictional time constant at the point of maximum slip velocity.

#### Implicit Integration Methods

Despite moderate successes with the explicit methods, implicit integration schemes were used to simulate the stick-slip system. The key advantage of the implicit integration methods is better stability characteristics versus the explicit methods. Therefore, it would be possible to use larger time steps (than the explicit methods) to simulate the LuGre model, even during slip. However, the disadvantage of implicit

methods is the need to iterate at each time step. This iteration is necessary to solve for simultaneous equations at each time instant. Lastly, despite the improved stability characteristics, the accuracy of the implicit methods still depends upon the size of the time step.

The first implicit method to be applied to the stick-slip system was the Trapezoidal method. This technique is effective for solving stiff differential equations [Faires and Burden, 1998]. An extension of the Trapezoidal method is the Radau-IIA method [Hairer and Wanner, 1991]. Both the Trapezoidal integration scheme and the Radau-IIA scheme can be expressed in a common framework. At each time  $t_i$ , two sets of nonlinear equations must be solved for the unknown vectors,  $k_1$  and  $k_2$ :

$$k_1 = f(y(t_i) + c_1 k_1 + c_2 k_2, u(t_i + b_1)) \quad (21)$$

$$k_2 = f(y(t_i) + c_3 k_1 + c_4 k_2, u(t_i + h)) \quad (22)$$

where  $k_1$  and  $k_2$  are  $3 \times 1$  vectors that approximate in some sense the average dynamics over a time step. The value of the state vector at the next time step is expressed in terms of  $k_1$  and  $k_2$  as follows:

$$y(t_i + h) = y(t_i) + c_3 k_1 + c_4 k_2 \quad (23)$$

For trapezoidal integration:

$$c_1 = c_2 = 0, \quad c_3 = c_4 = h/2, \quad b_1 = 0 \quad (24)$$

For Radau-IIA:

$$c_1 = 5h/12, \quad c_2 = -h/12, \quad c_3 = 3h/4, \quad c_4 = h/4, \quad b_1 = h/3 \quad (25)$$

As for the explicit methods, various schemes were investigated for their accuracy and efficiency. The results of the implicit integration methods are summarized in Table 3. The trapezoidal method was implemented with a constant time step of  $h = 0.005$ . The Radau-IIA method was compared using three different schemes for selection of  $h$ :  $h = \text{constant} = 10^{-2}$ ,  $h$  switched based on velocity, and  $h$  switched based on the time constant.

When compared to the explicit methods in Table 2, the implicit methods on average require less time and much fewer integration steps. The primary reason for these improvements is that larger time steps (than the explicit methods) could be used to obtain an accurate solution. Although the equations of the LuGre model are numerically stiff, the implicit integration schemes are well suited to solve them.

Similar to the findings for the Runge-Kutta method, it is observed that the maximum error values for the variable time step methods were unacceptably large. A reason for the relatively large errors was that at the stick/slip transition regions, there was a shift in the solution compared to the baseline.

Table 3. Comparison of Implicit Methods

Simulation Method	Time Step	Error (N)		Simulation Time (%)	Number of Steps
		Max	RMS		
Runge-Kutta (Baseline)	$10^{-5}$	n/a	n/a	100	2.828e6
Trapezoidal	5e-3	0.150	7.54e-3	2.25	5.658e3
Radau-IIA (Constant)	$10^{-2}$	9.33e-2	4.72e-4	1.08	2.830e3
Radau-IIA (Velocity)	$10^{-2}$ or 0.02	0.497	5.90e-3	0.56	1.436e3
Radau-IIA (Time Constant)	$10^{-2}$ or 0.05	0.490	7.20e-3	0.47	1.216e3

This shift occurred for both the explicit and implicit methods that used a variable time step. Since the transitions in the friction force occur very rapidly in time, even a small time shift in one simulation relative to the baseline result can give rise to very large maximum errors.

From Tables 2 and 3, it appears that the best choice to simulate the stick-slip system is to use the Radau-IIA method with a constant time step of  $10^{-2}$ . Surprisingly, the use of 4th order Runge-Kutta with a constant time step of  $10^{-3}$  also displayed a good balance between accuracy and efficiency. In terms of simulation time, both the 4th order Runge-Kutta and Radau-IIA methods are similar. The Runge-Kutta method has errors two orders of magnitude better than the Radau-IIA scheme, however, the Radau-IIA requires an order of magnitude fewer steps. Thus the best choice of integration scheme may depend on the users' preference for accuracy versus speed, as well as on the availability of computer memory.

## CONCLUSIONS

The purpose of this study was to efficiently simulate a dynamic system having LuGre friction. The LuGre friction model was chosen because it incorporated many characteristics of other friction models. To analyze the behavior of the LuGre model, a SDOF spring-mass system sliding against a fixed surface was considered. The equations of motion for this system were converted to a nondimensional form for convenience as well as to prevent round-off errors in the calculations. The spring-mass system was analyzed by observing the linearized dynamics of the entire system as well as the time constant of the LuGre model alone. The analysis shows that the friction dynamics can be very fast and therefore numerically stiff during periods of high slip rate. Furthermore, the dynamics change rapidly at stick-slip transitions. It is found that the system dynamics are relatively well-conditioned during periods of sticking, which stands in contrast to the standard behavior of other friction models.

The SDOF system was simulated using explicit and implicit time integration methods. In general, the explicit methods required smaller time steps than the implicit methods. Consequently, this requirement led to longer simulation times as well as a larger number of integration steps. However, the explicit methods performed better in terms of accuracy. Attempts to reduce the simulation time by varying the time steps performed poorly for both explicit and implicit methods. This poor performance was attributed to a slight time shift in the solution, which caused relatively large errors. The best simulation methods were found to be the explicit Runge-Kutta and implicit Radau-IIA methods with constant time steps of  $10^{-3}$  and  $10^{-2}$ , respectively. Determining which is the best method depends on one's need for better accuracy (Runge-Kutta) or reduced memory usage (Radau-IIA). However, when simulating a large dynamical system, using a larger time step would greatly reduce the computation time. This advantage outweighs improved accuracy afforded by the Runge-Kutta method. Therefore, for large systems with LuGre friction, the Radau-IIA method appears to be the best method for numerical integration.

Natural extensions of this study would be to apply the LuGre model to higher order systems with various types of boundary conditions and excitations. Ultimately, it is the goal of the authors to incorporate this friction model into multi-body and finite element codes to solve large scale problems.

#### ACKNOWLEDGMENTS

The authors would like to thank the Air Force Office of Scientific Research (AFOSR) for providing funding for this research, under contract number F49620-03-1-0176.

#### REFERENCES

- Armstrong-Hélouvy, B., Dupont, P., and Canudas de Wit, C., 1994, "A Survey of Models, Analysis Tools and Compensation Methods for the Control of Machines with Friction," *Automatica*, Vol. 30, No. 7, pp. 1083-1138.
- Canudas de Wit, C., Olsson, H., Astrom, K.J., and Lischinsky, P., 1995, "A New Model for Control of Systems with Friction," *IEEE Trans. on Auto. Control*, Vol. 40, No. 3, pp. 419-425.
- Dahl, P.R., "Solid friction damping of mechanical vibrations," *AIAA Journal*, 14: 1675-1682, 1976.
- Faires, J.D., and Burden, R., 1998, *Numerical Methods, 2nd Edition*, Brooks/Cole Publishing Co., Pacific Grove, CA.
- Ferri, A.A., 1995, "Friction Damping and Isolation Systems," *ASME J. of Vib. and Acoustics*, Vol. 117B, June, pp. 196-206.
- Ferri, A.A., and Heck, B.S., "Analysis of Stick-Slip Motion in Coulomb Damped Systems Using Variable Structure System Theory," *Proceedings of the 1997 ASME Design and Technical Conferences*, Sacramento, CA, September 14-17, 1997.
- Forsythe, G., Malcolm, M., and Moler, C., 1977, *Computer Methods for Mathematical Computations*, Prentice-Hall, New Jersey.
- Gaul, L., and Lenz, J., 1998, "Active Damping of Space Structures by Contact Pressure Control in Joints," *Mechanical Structures and Machines*, Vol. 26, No. 1, pp. 81-100.
- Gaul, L., and Nitsche, R., 2001, "The Role of Friction in Mechanical Joints," *Applied Mechanics Reviews*, Vol 54, No. 2, March, pp. 93-106.
- Haessig, D.A., Jr., and Friedland, B., "On the modeling and simulation of friction," *ASME Journal of Dynamic Systems, Measurement, and Control*, 1991, Vol. 113, p. 354-362.
- Hairer, E., and Wanner, G., 1991, *Solving Ordinary Differential Equations II: Stiff and Differential-Algebraic Problems*, Springer-Verlag, Berlin.
- Kahaner, D., Moler C., and Nash, S., 1989, *Numerical Methods and Software*, Prentice-Hall, New Jersey.
- Karnopp, D., 1985, "Computer Simulation of Stick-Slip Friction in Mechanical Dynamic Systems," *ASME J. of Dynamic Systems, Measurement, and Control*, Vol. 107, No. 1, pp. 100-103.
- Kokotovic, P., Khalil, H., and O'Reilly, J., 1986, *Singular Perturbation Methods in Control: Analysis and Design*, Academic Press, London.
- Lampaert, V., Swevers, J., and Al-Bender, F., 2002, "Modification of the Leuven Integrated Friction Model Structure," *IEEE Trans. on Auto. Control*, Vol. 47, No. 4, April, pp. 683-687.
- Mitiguy, P.C., and Banerjee, A.K., 1999, "Efficient Simulations of Motion Involving Coulomb Friction," *AIAA Journal of Guidance, Control, and Dynamics*, Vol. 22, No. 1, January-February, pp. 78-86.
- Pfeiffer, F., and Glocker, C., 1996, *Multibody Dynamics with Unilateral Contact*, John Wiley and Sons.
- Swevers, J., Al-Bender, F., Ganesman, C.G., and Prajogo, T., 2000, "An Integrated Friction Model Structure with Improved Presliding Behavior for Accurate Friction Compensation," *IEEE Trans. on Auto. Control*, Vol. 45, No. 4, April, pp. 675-686.
- Valanis, K.C., 1971, "A Theory of Viscoplasticity Without a Yield Surface," *Archives of Mechanics*, Vol. 23, No. 4, pp. 171-191.
- Whiteman, W.E., and Ferri, A.A., "Multi-Mode Analysis of Beam-Like Structures Subjected to Displacement-Dependent Dry Friction Damping," *Journal of Sound and Vibration*, Vol. 201, No. 3, 1997, pp. 403-418.

**MODELING OF FRICTIONAL CONTACT CONDITIONS IN STRUCTURES**

**A Thesis  
Presented to  
The Academic Faculty**

**By**

**Nguyen B. Do**

**In Partial Fulfillment  
Of the Requirements for the Degree  
Master of Science in Mechanical Engineering**

**Georgia Institute of Technology**

**August, 2005**

# MODELING OF FRICTIONAL CONTACT CONDITIONS IN STRUCTURES

Approved by:

Dr. Aldo A. Ferri, Advisor  
School of Mechanical Engineering  
*Georgia Institute of Technology*

Dr. Olivier Bauchau  
School of Aerospace Engineering  
*Georgia Institute of Technology*

Dr. Jerry H. Ginsberg  
School of Mechanical Engineering  
*Georgia Institute of Technology*

Date Approved: May 17, 2005

## ACKNOWLEDGEMENTS

*I hear and I forget. I see and I remember: I do and I understand.*  
- Chinese Proverb

First and foremost, I would like to thank my advisor, Dr. Al Ferri, for providing mentorship, guidance, and support for this work. His knowledge, expertise, and insights were invaluable throughout this project and have made me a better student and engineer. I would also like to thank my thesis committee members, Dr. Olivier Bauchau and Dr. Jerry Ginsberg. Lastly, my thanks to the Air Force Office of Scientific Research (AFOSR), who provided funding for this research.

My time here at Georgia Tech would not be as enriching without the support of my family and friends. Whether it was a phone call of encouragement or long study sessions, I truly thank everyone for their help and support.

## TABLE OF CONTENTS

Acknowledgements	iii
List of Tables	vi
List of Figures	vii
Summary	x
Chapter 1 Introduction	1
1.1 Frictional Damping in Built-Up Structures	3
1.2 Friction Modeling and Simulation	5
1.3 Energy Transfer and Dissipation	10
1.4 Outline of Thesis	12
Chapter 2 Friction Modeling and Simulation	14
2.1 Valanis Model	15
2.2 LuGre Model	17
2.3 System Modeling and Analysis	20
2.4 Numerical Simulation Results	28
2.5 Comparison of Integration Methods	34
2.5.1 Explicit Integration Methods	35
2.5.2 Implicit Integration Methods	38
Chapter 3 Energy Transfer and Dissipation: Discrete System	42
3.1 System Model	43
3.2 System Simulation	48
3.3 Steady-State Vibration Response	49
3.4 Free Vibration Response	55

3.5 Energy Dissipation	57
Chapter 4 Energy Transfer and Dissipation: Continuous System	66
4.1 System Model	67
4.1.1 Governing Equations	68
4.1.2 System Properties	70
4.1.3 State-Space Formulation	72
4.2 System Simulation	74
4.2.1 Mode Number Convergence	75
4.2.2 Steady-State Frequency Response	77
4.3 Energy Dissipation	81
4.3.1 System Energies	82
4.3.2 Controllability of the Beam-Mass System	85
4.4 Sensitivity of the Beam-Mass System	88
4.4.1 Sensitivity to Tuning Parameter	89
4.4.2 Sensitivity to Friction Laws	91
Chapter 5 Summary and Conclusions	95
5.1 Summary	95
5.2 Conclusions and Future Work	99
References	101

## LIST OF TABLES

Table 2.1	LuGre Friction Model Parameters	19
Table 2.2	Comparison of Explicit Methods	37
Table 2.3	Comparison of Implicit Methods	40
Table 3.1	Simulation Parameters	48
Table 3.2	Natural Frequencies (rad/s)	53
Table 3.3	Percentage of Energy Dissipated by the 3 <sup>rd</sup> and 4 <sup>th</sup> Dampers to the Total Energy Dissipated	64
Table 4.1	Properties for the Beam-Mass System	71

## LIST OF FIGURES

Figure 1.1	Normalized friction force vs slip velocity. (a) Coulomb, (b) Sticktion, and (c) Stribeck friction laws.	6
Figure 1.2	Saturation approximation of signum nonlinearity.	7
Figure 1.3	Smooth approximation of signum nonlinearity.	7
Figure 1.4	Delayed time of the switching strategy.	9
Figure 2.1	Closed hysteresis of the Valanis friction model.	16
Figure 2.2	Description of the frictional interface in the LuGre model.	17
Figure 2.3	Hysteresis loops for the modified LuGre and the Valanis models.	20
Figure 2.4	Stick-slip system ( $M = 1$ kg, $K = 2$ N/m, and $U = 0.1$ t m).	21
Figure 2.5	LuGre function $g$ versus $y_2$ using values in Table 1.	23
Figure 2.6	Maximum magnitude eigenvalue vs $y_2$ .	28
Figure 2.7	Nondimensional position vs. $\tau$ using <i>ode45</i> with RelTol = $10^{-4}$ and AbsTol = $10^{-6}$ .	29
Figure 2.8	Nondimensional velocity vs. $\tau$ using <i>ode45</i> with RelTol = $10^{-4}$ and AbsTol = $10^{-6}$ .	30
Figure 2.9	Nondimensional bristle displacement vs. $\tau$ using <i>ode45</i> with RelTol = $10^{-4}$ and AbsTol = $10^{-6}$ .	30
Figure 2.10	Nondimensional friction force vs. $\tau$ using <i>ode45</i> with RelTol = $10^{-4}$ and AbsTol = $10^{-6}$ .	31
Figure 2.11	$\lambda_{\max}(J)$ vs $\tau$ from <i>ode45</i> with RelTol = $10^{-7}$ and AbsTol = $10^{-7}$ .	32

Figure 2.12	Maximum eigenvalue during the transition from (a) microslip to macroslip and (b) macroslip to microslip.	33
Figure 2.13	Close-up of $y_3$ vs $\tau$ using <i>ode45</i> with RelTol = $10^{-4}$ and AbsTol = $10^{-6}$ .	34
Figure 3.1	System model of frictional contact at a connection joint.	43
Figure 3.2	Stribeck friction coefficient as a function of velocity.	45
Figure 3.3	Flow chart to calculate friction force ( $P = 0$ case).	47
Figure 3.4	Modal amplitude versus generalized coordinate number for (a) Mode 1, (b) Mode 2, and (c) Mode 3.	52
Figure 3.5	RMS displacement of the 3 <sup>rd</sup> mass as a function of excitation frequency ratio.	54
Figure 3.6	(a) Displacement and (b) velocity time histories of the 3-DOF system ( $N = 40\text{N}$ , $r = 1$ ).	57
Figure 3.7	Energy dissipated by the (a) entire system and (b) the 3 <sup>rd</sup> and 4 <sup>th</sup> dampers.	60
Figure 3.8	Energy dissipated by the 3 <sup>rd</sup> and 4 <sup>th</sup> dampers at $N = 100\text{ N}$ .	61
Figure 3.9	Energy dissipated by the 3 <sup>rd</sup> and 4 <sup>th</sup> dampers with varying mass ratios ( $N = 100\text{ N}$ , $t_f = 15.1\text{ s}$ ).	62
Figure 3.10	Energy dissipated by the 3 <sup>rd</sup> and 4 <sup>th</sup> dampers with varying $N$ (mass ratio = 0.5, $t_f = 15.1\text{ s}$ ).	63
Figure 4.1	Beam-mass system model of a jointed structure.	67
Figure 4.2	Mode function and natural frequencies for the cantilever beam.	72
Figure 4.3	(a) Displacement and (b) velocity response at $x = L$ on the beam.	76
Figure 4.4	Magnitude of the frequency response of the beam at $x = L$ .	78

Figure 4.5	Phase angle of the response of the beam at $x = L$ .	78
Figure 4.6	RMS Displacement frequency response of the beam system at $x = L$ .	79
Figure 4.7	Modal displacement response of the beam system.	81
Figure 4.8	Total system energy after 4.6s of free response.	84
Figure 4.9	Condition number of the controllability matrix versus tuning frequency.	87
Figure 4.10	Total system energy as a function of tuning frequency for $N = 10$ N.	89
Figure 4.11	Relative displacement versus time for two tuning frequencies.	91
Figure 4.12	Total energy remaining after 4.6s versus tuning frequency for different friction laws.	93

## SUMMARY

The purpose of this thesis is to explore two aspects of modeling the behavior of joint friction in structures. The first aspect deals with the accurate and efficient simulation of a simple system that incorporates the LuGre friction law. Energy transfer and dissipation in a structural joint model is the second topic of this thesis. It is hypothesized that friction could serve to pump energy from one frequency to higher frequencies where it might be dissipated more quickly. Motivation for this study stems from the need to have accurate models of high-precision space structures. Because friction at connecting joints plays a major role in the damping capacity of the structure, a good understanding of this mechanism is necessary to predict the vibratory response and enhance the energy dissipation of the structure.

Simulation results of a dynamic system with LuGre friction show that the system is relatively well-conditioned when the slip velocity is small, and ill-conditioned for large slip velocities. Furthermore, the most efficient numerical method to simulate this system is determined to be an implicit integration scheme. To study the energy transfer and dissipation, two models of a jointed structure with friction are considered. Results from the steady-state forced responses of the two structural systems indicate that friction converted low frequency, single harmonic excitation to multi-harmonic response through internal resonances. However, differences in energy dissipation results between the models show that the response of a frictional system is highly sensitive to system parameters and friction laws. Conclusions and suggestions for future research are also discussed.

# CHAPTER 1

## INTRODUCTION

As the 21<sup>st</sup> century begins, new missions in space are being developed that push the limits of science and technology. Whether the mission is to explore galaxies far away or predicting tomorrow's weather, there is a need for high-tech, precision structures. These structures must meet the harsh conditions of launch and the space environment as well as operate at a high level of precision and accuracy. Therefore, disturbances and uncertainties in the dynamics of the structure can be detrimental to the performance of the spacecraft. The success of a mission depends on an accurate modeling or prediction of the uncertainties as well as a good design to minimize the effects of the disturbances.

One form of disturbance to a spacecraft is mechanical vibration in the structure. Because high levels of precision are required, vibrations along the structure are undesirable. These vibrations come from a number of sources. During deployment or positioning, vibrations can develop in large, built-up structures such as solar and sensor arrays. Other sources of vibration include machinery on the spacecraft and thermal differences along the structure. The vibrations propagate throughout the space structure and can cause a myriad of problems such as misalignment of instruments, control difficulties, structural instabilities, and component failures. Furthermore, significant amounts of time, and consequently cost, are wasted waiting for vibrations to damp down to acceptable levels. It is estimated that a robot manipulator system on a shuttle requires a time equivalent to 15 shuttle flights to damp out to an amplitude of  $\pm 1$  inch [1].

Aside from reducing vibration, high precision space structures must meet stringent levels of dimensional stability. For example, NASA's next generation gamma ray telescope has strict requirements for the support structure. After deployment, the structure must get into position and remain fixed and steady within an accuracy of four millionths of an inch. Typically, other deployable structures require relatively lower levels of precision, from three to four thousandths of an inch [2]. These requirements are necessary because the support structure must function as metering structures for optical instruments. Optical instruments are highly sensitive and can even require dimensional stability to within a fraction of the wavelength of light.

To achieve high levels of precision during (and after) deployment and to reduce mechanical vibration in space structures, it is important to examine the role of friction in the structures. Specifically, friction at the connection joints in the structures is considered. During deployment, friction can be a mechanism that leads to a locking of the joint. After deployment, a microdynamic effect known as "microlurch" can occur in a structure [3]. Microlurch is a residual change in the shape of a deployed structure, which occurs after a transient dynamic event. This phenomenon can lead to the misalignment of sensitive instruments. Analytical simulations and experimental data suggest that microlurch is caused by the release of built-up strain energy within the joints and latches of a deployed structure [4]. This release of energy is an artifact of stick-slip instability due to load transfer through friction. Furthermore, it is thought that friction is the cause of small, but noticeable spontaneous vibrations in space structures [5, 6]. Although friction is the cause of microdynamic instabilities in the structure, it can also

play a positive role in the larger, global dynamics of the structure. The next section describes the role of friction in the damping capacity of large, built-up structures.

### **1.1 Frictional Damping in Built-up Structures**

To reduce vibration in space structures, there are several solutions. One solution is to make the structure more rigid to prevent excessive vibration. However, rigid structures are expensive and heavy, which significantly increase the costs and resources necessary to launch the structure. Another way to reduce vibration is to improve the damping capacity of the space structures. This improvement could be achieved by studying the role of friction at the connecting joints in the structure.

Friction in connecting joints plays an important role in the damping capacity of built-up structures. It is estimated that as much as 90% of mechanical energy loss in space structures is due to dry friction at the connecting joints [7, 8]. Many techniques have been developed to use friction to increase damping at the joints. Ferri and Heck analytically explored damping enhancements using passive and active joints [9]. Through simulation results, Gaul and Nitsche showed an increase in damping performance using a semi-active friction damper at the joint [10]. A review of the research done on the effects of joint friction on structural damping may be found in [11].

Although there have been many studies on the effects of joint friction on damping, an accurate prediction of how much damping one can expect from a given system or design is a topic of much research. To add to the complexity of the problem, experimental evaluation of a structure's damping is difficult because the structure will operate in a zero gravity environment. In a series of experimental studies, Folkman *et al.*

found that the loss factor of a truss structure depended on the structure's orientation and the amplitude of vibration [12, 13]. Furthermore, some results showed a linear envelope of decay while others exhibited an exponential-like decay.

Because an experimental estimate of damping for a space structure is difficult, there is an emphasis on the development and simulation of analytical joint models. Although difficult, an important challenge to researchers is to develop analytical models that capture the full range of observed behaviors of joint friction. A number of researchers have developed simplified models to try to explain the complicated damping characteristics of a realistic truss structure. For example, models of a crude sleeve-joint as well as a nonlinear sleeve-joint have shown that variable normal forces in a frictional joint can give rise to mostly "linear" structural damping [14, 15]. In such cases, the free response is characterized by exponential-like (rather than linear) envelopes of decay.

Rather than focusing on characterizing the damping of a complex built-up structure, this thesis will focus on two aspects of modeling the behavior of joint friction. The first aspect deals with the analysis and simulation of an advanced friction model. Since the nature of the friction law has a significant impact on the behavior of joint friction, a good friction model is necessary to predict the dynamic and microdynamic responses of the structure. Furthermore, frictional systems are difficult to simulate due to numerical difficulties. A discussion of some friction models and simulation difficulties is presented in Section 1.2.

The second topic treated in this thesis is the phenomenon of "energy pumping" from one part of a structure to another. Moreover, the concept of energy pumping also

concerns the transfer of energy from low-frequency vibratory modes to higher frequency modes. Section 1.3 discusses these phenomena in greater detail.

## **1.2 Friction Modeling and Simulation**

Although the concept of friction is easily understood, it is notoriously difficult to model and simulate. Many friction models contain a variety of nonlinear features such as discontinuities, hysteresis, internal dynamics, and other complications. These properties cause the friction models to be numerically stiff and therefore computationally cumbersome. For that reason, it would be advantageous to efficiently simulate a model that captures key frictional behavior from experiments and from other friction models.

Numerical difficulties associated with simulation of frictional systems are well documented [16, 17]. The basic problem is the numerical stiffness of such systems. Models of friction derived from the Coulomb friction paradigm suggest that the friction force changes “discontinuously” as the direction of interfacial slip changes. Figure 1.1 shows some typical sketches of friction force versus slip velocity. It should be noted that “sticking” of the frictional interface is characterized by zero slip velocity; therefore, it is not uncommon for the frictional interface to spend intermittent and finite periods of time at zero slip velocity, where the friction law is discontinuous.

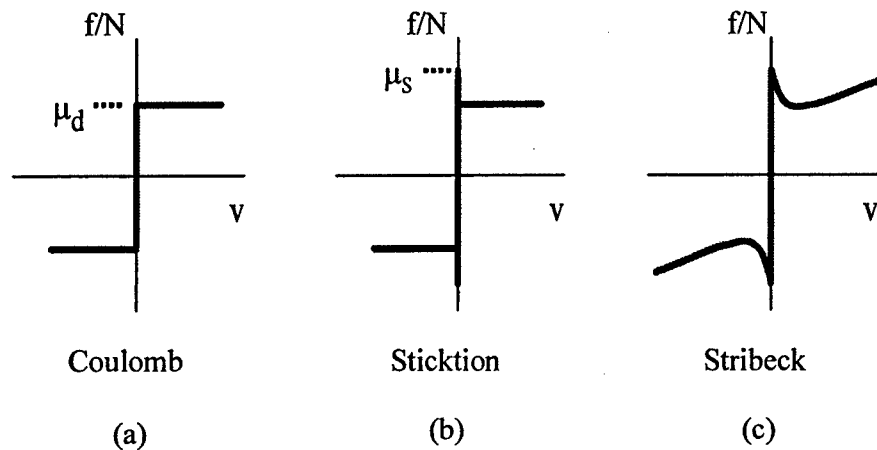


Figure 1.1. Normalized friction force vs slip velocity. (a) Coulomb, (b) Stiction, and (c) Stribeck friction laws.

If it is assumed that the friction laws depicted in Figure 1.1 properly reflect the behavior of sliding friction, the discontinuity presents a host of analytical and computational challenges. Simulation of the time response requires very small time steps to maintain accuracy in regions where the slip velocity changes sign or where sticking occurs. Depending on the time-integration method used, it is even possible for numerical instabilities to develop. Two main strategies have been employed to deal with this problem. First, numerous studies have sought to “smooth” or “regularize” the friction law in the vicinity of the discontinuity. For example, the signum type nonlinearity depicted in Figure 1.1(a), can be replaced with a saturation-type nonlinearity, as in Figure 1.2, or a smoothly transitioning approximation as shown in Figure 1.3. In both cases, the infinite slope at zero velocity is replaced with a slope of order  $1/\epsilon$ , where  $\epsilon$  is small relative to some characteristic slip velocity for the problem in question. As  $\epsilon$  approaches zero, the numerical stiffness of the problem becomes poorer. Consequently, time-simulation of friction-damped systems that experience finite periods of sticking are

burdened with very small time steps, necessitating high computation times in order to maintain stability and/or accuracy.

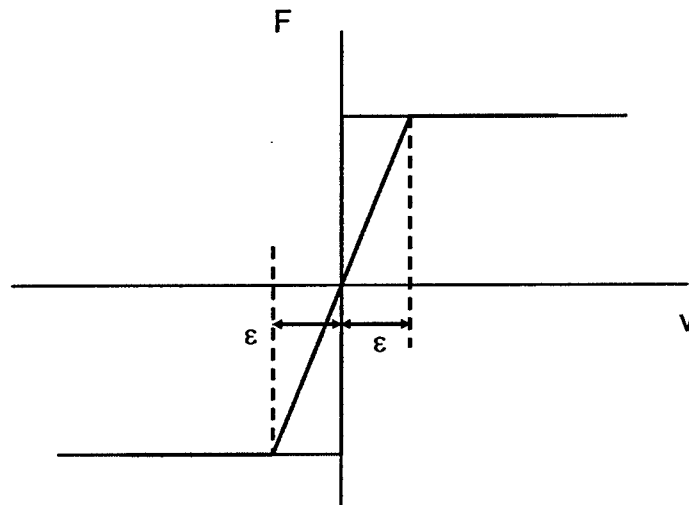


Figure 1.2. Saturation approximation of signum nonlinearity.

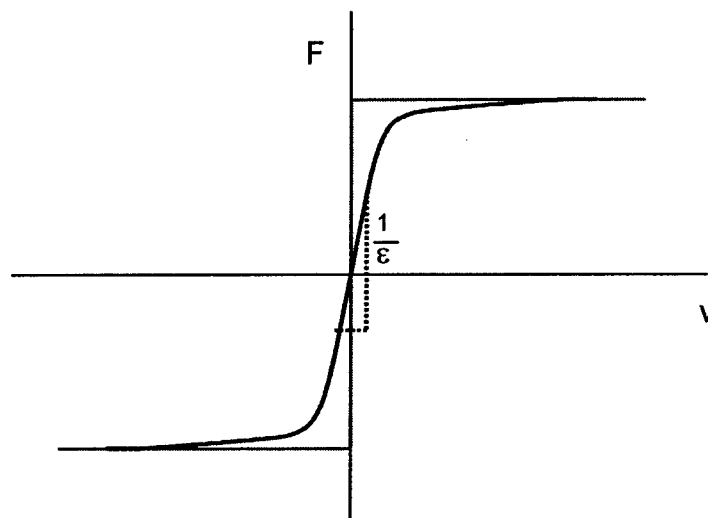


Figure 1.3. Smooth approximation of signum nonlinearity.

A second approach to address simulation of systems with discontinuous friction is to utilize a “switching strategy,” or also known as an event-driven strategy [18]. In this approach, the system can be simulated using a discontinuous friction law, a saturation approximation, or a smooth approximation. However, when the slip velocity changes sign, a check is performed to determine whether the maximum-available friction force is sufficient to prevent slip from occurring [19, 20]. If the friction force is large enough to prevent slip, then a set of “sticking equations” (which model the system with a stuck interface) are integrated. Otherwise, integration of the “slipping equations” is continued. Details of this procedure are discussed in Chapter 3.

While the switching strategy alleviates the numerical stiffness problems associated with smoothing the discontinuity, another problem arises. As seen in Figure 1.4, the accuracy of the method hinges on accurate determination of the switching time. Figure 1.4 shows a transition from slipping to sticking, followed by renewed slip in the opposite direction. Due to errors in the computational solution, this switching time could be “delayed” (or “advanced”) by some small amount of time. Equivalently, delays could occur due to the discrete nature of the numerical solution.

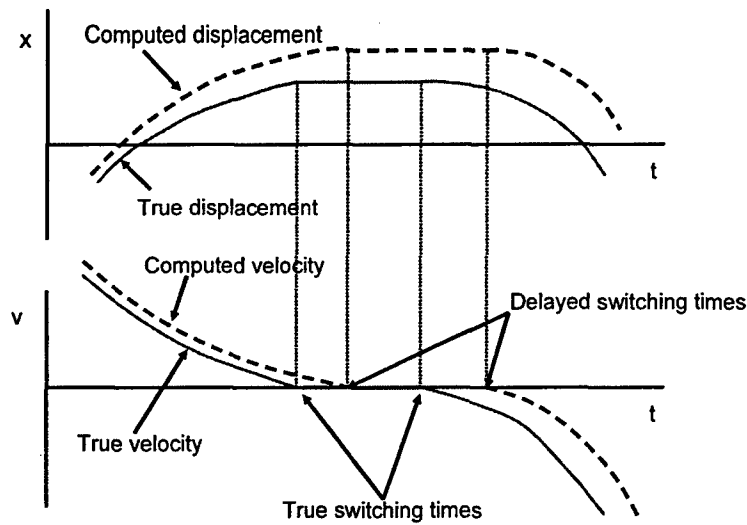


Figure 1.4. Delayed time of the switching strategy.

In reality, the physical friction process is not discontinuous. Various models of friction have been proposed that address this shortcoming by refining the behavior of the interface when the slipping velocity is small or when it changes sign. For example, “microslip” models allow small amounts of displacement to occur during sticking. A common microslip model is the Iwan-model, also termed the elastic-perfectly plastic model [21]. Conceptually, the model can be thought of as a spring in series with a Coulomb friction element having friction force  $\mu N$ , where  $\mu$  is the coefficient of friction and  $N$  is the normal force. When the force in the spring reaches a magnitude of  $\mu N$ , the force in the Iwan-model saturates until the direction of slip reverses. Smooth versions of this behavior have also been proposed. Examples of friction models with smooth microslip behavior include the Dahl model [22], the Valanis model [23, 24], and the Leuven model [25, 26]. Recently, bristle models have been proposed that capture both the microslip and macroslip (sliding) regimes of interfacial friction. Haessig and Friedland proposed a bristle model where individual bristles are treated separately,

separating as bonds are broken, and then re-adhering [27]. The LuGre friction model, so named because it was developed jointly by researchers at the Lund Institute of Technology in Sweden and the University of Grenoble in France [28], is also based on a bristle interpretation of the frictional interface. However, this model treats the collection of bristles in an aggregate fashion.

The previous discussion only surveyed a small sample of the number of friction models in the literature. Applications of the friction models vary widely depending on the type and complexity of the system being simulated. Of the different friction models discussed, several have been used to study friction at structural joints. Two of the models, the Valanis model and the LuGre model, are discussed in further detail in Chapter 2. The LuGre friction model is a promising model because it captures both sticking and sliding regimes of interfacial friction. Similarly, the Valanis model shows potential because it agrees well with experimental results of friction in a joint. A comparison of the Valanis model to the LuGre model is made in Chapter 2.

Once the complexities and simulation challenges of a frictional system are understood, the effects of friction on joint behavior are investigated. The next section explores the energy transfer and dissipation due to friction at a connecting joint.

### **1.3 Energy Transfer and Dissipation**

The second aspect of this thesis is the passive damping capabilities of joint friction. It is understood that joint friction affects damping by converting mechanical energy into heat by rubbing. Less obvious, however, is that friction can serve as a catalyst for energy pumping. The phenomenon of energy pumping is defined as the

controlled one-way transfer of vibrational energy to a passive nonlinear sink, where the energy localizes and dissipates over time [29]. Through stick-slip oscillations, it is hypothesized that joint friction can be a means to pump low-frequency vibrational energy to high-frequency vibrational energy, which can excite higher modes in the system. In a finite element simulation of a truss structure, Onoda *et al.* found that backlash nonlinearity at the joint transferred vibrational energy from lower modes to higher modes [30]. Since energy can be dissipated faster at higher frequencies, this transfer of energy to excite higher resonances may serve as a tool for increased energy dissipation. Chapter 3 explores this concept and applies it to a joint structure modeled as a simple 3 degrees-of-freedom (3DOF) system. Simulations of the steady-state and free responses of the system are performed to demonstrate the feasibility of the hypothesis.

The concepts of energy transfer and dissipation can be extended to a more complicated model. In Chapter 4, the structure is modeled as a continuous beam connected to a single degree-of-freedom (SDOF) system, with the connecting element modeled as a friction interface. An investigation of a system with a similar configuration shows the presence of internal resonances in the response of the beam [20, 31]. These internal resonances are caused by stick-slip oscillations, which excite modes at higher frequencies than the excitation frequency. In Chapter 4, the excitation of internal resonances in free and forced response is discussed. As in the 3DOF system, it is hypothesized that the vibrational energy transferred to the higher modes should dissipate faster. Simulation of the responses of the beam system is performed to validate these claims.

## 1.4 Outline of Thesis

This thesis deals with two topics concerning the modeling of joint friction behavior. Discussed in Chapter 2, the first topic deals with the modeling of friction and simulation strategies for frictional systems. Furthermore, Chapter 2 explores the best and most efficient simulation strategies to simulate a simple dynamical system with LuGre friction. Numerical difficulties associated with the LuGre model are examined by looking at the eigenvalues and time constants of the linearized system. With a better understanding of the dynamics of the system, the performances of several numerical integration schemes are evaluated. These schemes include both explicit and implicit numerical methods.

The second topic concerns the energy transfer and dissipation in systems with a frictional interface. Chapters 3 and 4 explore these concepts by simulating the responses of jointed structures modeled as dynamical systems. In Chapter 3, the energy transfer among subsystems of a discrete, 3DOF system is studied. Additionally, a parametric analysis of the energy dissipation in the system is performed by tuning one of the subsystems to the stick-slip frequencies. Chapter 4 extends the results of Chapter 3 to a jointed structure represented by a continuous model. Likewise, the responses of this system are simulated to study the energy transfer and dissipation. Furthermore, Chapter 4 examines the sensitivity of the frictional system to changes in system parameters. Lastly, concluding remarks as well as recommendations for future studies and research are made in Chapter 5.

The research presented in this Thesis provides a framework to study the behavior of joint friction. The selection and accurate simulation of a friction law could lead to a

more precise evaluation of the performance of a space structure. Application of the studies in Chapters 3 and 4 could serve as a preliminary guide to model and simulate specific joint structures. Ultimately, it would be desirable to develop design rules that lead to enhanced damping levels of the global structural system.

## CHAPTER 2

### FRICITION MODELING AND SIMULATION

Friction plays an important role in the dynamics of large, built-up structures such as space structures. Specifically, dry friction at connecting joints contributes to the majority of the damping capacity of the system. Furthermore, joint friction can lead to the locking of joints during deployment of booms and contribute to microdynamic instabilities after deployment. Since the nature of the friction law has a significant impact on the behavior of joint friction, a good friction model is necessary for the design, control, and analysis of the system.

Simulation difficulties in frictional systems are caused by the numerical stiffness of the systems. The stiffness is especially pronounced when the friction force changes discontinuously as the velocity of the slip interface changes direction. As discussed in Chapter 1, the problem can be somewhat alleviated through the use of “smoothed” versions of the friction law and/or adapting a switching strategy. However, this chapter explores an alternate approach.

In reality, the discontinuity in the friction law is an artifact that originates from modeling simplifications. Chapter 1 mentioned several more complicated friction models that have been proposed to capture the true interfacial forces in both regimes of microslip and macroslip. These models allow the transition between microslip and macroslip to be smooth and not discontinuous. They include the Dahl model, the Leuven model, the Valanis model, and the LuGre model; the later two are investigated in this chapter. The LuGre model is promising because it contains key features from other friction models

and it captures both sticking and sliding regimes of interfacial friction. The Valanis model is promising because it agrees well with experimental results of friction at a joint.

In this chapter, a description of the Valanis and LuGre friction models is given first. Secondly, a simple dynamic model is proposed to analyze the characteristics of the LuGre friction model. This model is then modified slightly to compare the LuGre friction model to the Valanis model. Next, the governing equations of the LuGre model are analyzed by using nondimensional terms and observing the dynamics of the linearized system. The dynamic system is then simulated using several explicit and implicit numerical integration techniques. Finally, conclusions are made concerning the most efficient technique to simulate the LuGre friction model.

## 2.1 Valanis Model

Often, the selection of a friction model is motivated by an observed response in a system. In one study, the force-displacement hysteresis response in a bolted lap joint was represented using the Valanis friction model [23]. Comparisons between experimental and simulated results showed good agreement between the Valanis model and the measured joint behavior. For the Valanis model, the rate of change in the generalized friction force,  $F_V$ , is given by

$$\dot{F}_V = \frac{e_o V \left[ 1 + \frac{\lambda}{e_o} \operatorname{sgn}(V)(e, X - F_V) \right]}{1 + \kappa \frac{\lambda}{e_o} \operatorname{sgn}(V)(e, X - F_V)} \quad (2.1)$$

where  $X$  is the relative displacement,  $V$  is the relative velocity, and an overdot denotes a derivative with respect to time. The function  $sgn(V)$  is the signum function and is defined as  $V/|V|$  when  $V \neq 0$ . The dimensionless parameter  $\lambda$  is defined as

$$\lambda = \frac{e_o}{\alpha_o \left( 1 - \kappa \frac{e_t}{e_o} \right)} \quad (2.2)$$

The stiffness parameters  $e_o$ ,  $e_b$ , and  $\alpha_o$  can be identified from the closed hysteresis loop in Figure 2.1. The dimensionless parameter  $\kappa$  indicates the smoothness of the stick-to-slip transition. A value of 0.99 is for a sharp transition, whereas a value less than 0.99 cause a smooth transition. For the system shown in Figure 2.1, the  $\kappa$  value is 0.01.

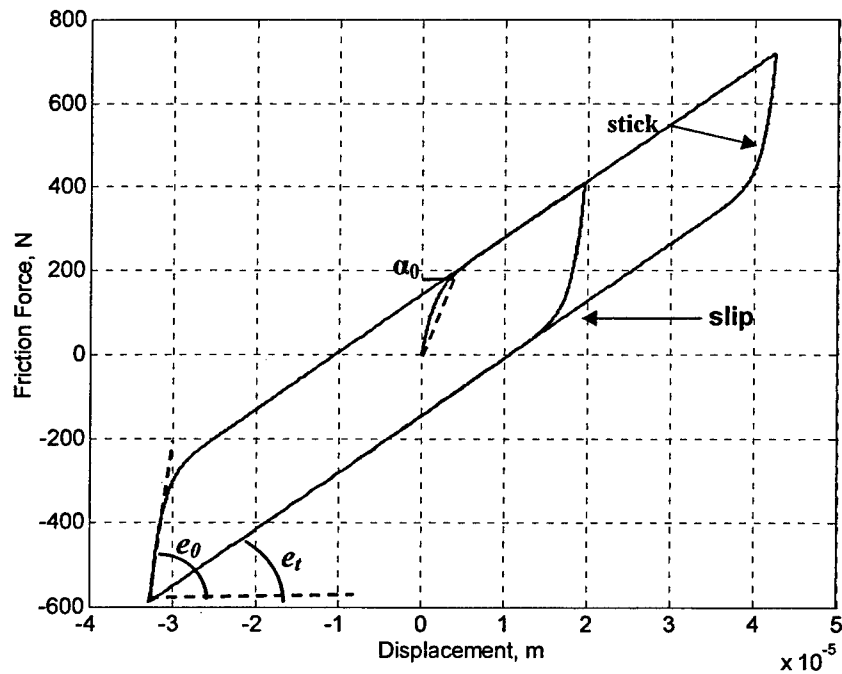


Figure 2.1. Closed hysteresis of the Valanis friction model.

## 2.2 LuGre Model

As discussed previously, the LuGre model has become popular because it incorporates many of the observed features of frictional behavior. For example, imbedded within the LuGre model is the Stribeck effect, displayed in Figure 1.1(c). For small levels of slip velocity, the friction force exhibits a negative derivative with respect to slip velocity. This negative slope is one of the key features of friction that contributes to limit-cycle behavior and stick-slip oscillations in frictional systems. Furthermore, the LuGre model behaves like a linear spring/damper pair when it is linearized for small motions.

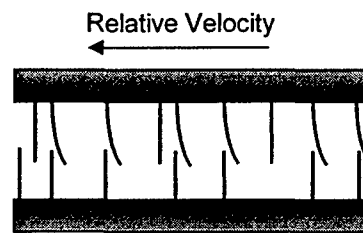


Figure 2.2. Description of the frictional interface in the LuGre model.

A qualitative description of the LuGre model is shown in Figure 2.2. At the microscopic level, two surfaces make contact at various asperities. These asperities are represented with bristles, and the bristles deflect like a spring when there is a relative velocity between the two surfaces. The deflection of the springs gives rise to the friction force. If the deflection is sufficiently large, then the bristles will slip in a highly random manner because of the irregular surfaces. Although the deflection of the bristles is

random, the LuGre model only considers the average deflection. The average deflection of the bristles,  $Z$ , is modeled by the first-order differential equation

$$\dot{Z} = V - \frac{|V|}{G(V)} Z \quad (2.3)$$

where  $V$  is the relative velocity between the two surfaces and  $G(V)$  is a function that describes the Stribeck effect. The function  $G(V)$  also allows the LuGre model to accommodate a higher static coefficient of friction than dynamic coefficient of friction:

$$G(V) = \frac{1}{\sigma_o} \left\{ F_C + (F_S - F_C) \exp\left(-\left(\frac{V}{V_S}\right)^2\right) \right\} \quad (2.4)$$

where  $F_C$  is the kinetic friction force,  $F_S$  is the static friction force,  $\sigma_o$  is the aggregate bristle stiffness, and  $V_S$  is the Stribeck velocity. Finally, the LuGre friction force is given by

$$F_L(V, Z) = \sigma_o Z + \sigma_1 \dot{Z} + \sigma_2 V \quad (2.5)$$

where  $\sigma_1$  is a damping coefficient and  $\sigma_2$  accounts for viscous friction. For this study, the values used for the LuGre parameters are listed in Table 2.1. Note that  $V_S$  is a very small slip velocity, below which the frictional interface can be thought of as being “stuck” or undergoing microslip.

Table 2.1. LuGre Friction Model Parameters [28]

Parameter	Value	Unit
$\sigma_0$	$10^5$	N/m
$\sigma_1$	$\sqrt{10^5}$	Ns/m
$\sigma_2$	0.4	Ns/m
$F_c$	1	N
$F_s$	1.5	N
$V_s$	.001	m/s

As discussed in Section 2.1, the Valanis model agreed well with an experimental result of a bolted lap joint. Therefore, a comparison was made between the Valanis model and the LuGre model. However, an additional stiffness term is needed in the LuGre model because the stiffness of the bolted lap joint is included in the Valanis model, but not in the LuGre model. If a stiffness term equivalent to  $e$ , in the Valanis model is added to the LuGre friction force in (2.5), then the LuGre model can exhibit the Valanis hysteresis loop shown in Figure 2.1. Figure 2.3 shows the hysteresis of the modified LuGre model and the Valanis model. Parameters of the LuGre model were varied to get the best fit.

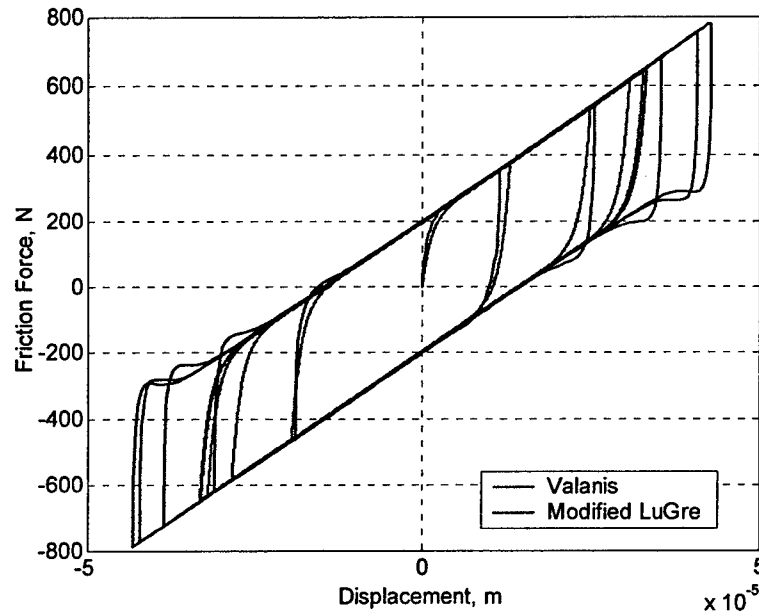


Figure 2.3. Hysteresis loops for the modified LuGre and the Valanis models.

From Figure 2.3, it is seen that the LuGre model can approximate the Valanis model well. Because the LuGre model can exhibit both classical frictional behavior (Stribeck effect) as well as experimental results, it is a good candidate for further investigation.

### 2.3 System Modeling and Analysis

To analyze the characteristics of the LuGre model, a system proposed by Canudas de Wit, *et al* is used to focus the present discussion [28]. The system, shown in Figure 2.4, represents a mass,  $M$ , connected to a spring  $K$  that is being pulled by a constant velocity,  $\dot{U} = R$ . As the mass slides along, the LuGre friction force,  $F_L(V, Z)$ , opposes the motion of the mass. The position of the mass is denoted by  $X$  and its velocity is  $V$ . Two first-order, differential equations govern the motion of the mass:

$$\dot{X} = V \quad (2.6)$$

$$\dot{V} = (KU - KX - F_L(V, Z)) / M \quad (2.7)$$

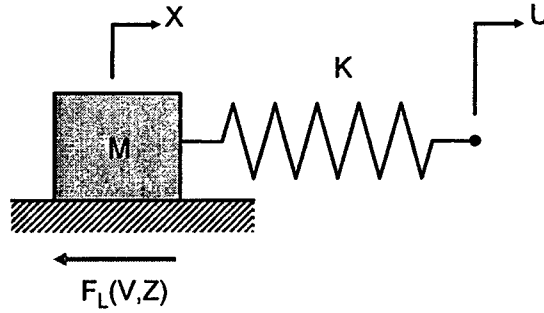


Figure 2.4. Stick-slip system ( $M = 1$  kg,  $K = 2$  N/m, and  $U = 0.1$  t m).

It is useful to nondimensionalize the equations governing the mass as well as that of the LuGre force by introducing the following terms:

$$y_1 = \frac{KX}{F_C}, \quad y_2 = \frac{V}{V_S}, \quad y_3 = \frac{\sigma_0 Z}{F_C}, \quad u = \frac{KU}{F_C}, \quad \omega_n = \sqrt{K/M}, \quad \tau = \omega_n t \quad (2.8a)$$

$$\alpha = \frac{KV_S}{\omega_n F_C}, \quad \gamma = \frac{F_S - F_C}{F_C}, \quad \varepsilon = K/\sigma_0, \quad s_1 = \frac{\sigma_1 V_S}{F_C}, \quad s_2 = \frac{\sigma_2 V_S}{F_C} \quad (2.8b)$$

There are several points to notice from the nondimensional terms. First, the time is expanded into nondimensional terms by the natural frequency of the stick-slip system. Secondly, velocity is normalized to the Stribeck velocity, which is considered to be the threshold of sticking. Microslip occurs when the  $|V|$  is below  $V_S$ ; and conversely, macroslip happens when  $|V|$  is above  $V_S$ . Lastly, the stiffness ratio between the system and the friction model,  $\varepsilon$  (not to be confused with  $\varepsilon$  in Figures 1.2 and 1.3), is typically small due to the relatively high bristle stiffness.

When (2.8) is introduced into Equations (2.6), (2.7), and (2.3), the following three equations are obtained:

$$y_1' = \alpha y_2 \quad (2.9)$$

$$y_2' = (u - y_1 - f_L(y_2, y_3)) / \alpha \quad (2.10)$$

$$\varepsilon y_3' = \alpha y_2 - \alpha \frac{|y_2|}{g(y_2)} y_3 \quad (2.11)$$

where ' denotes a derivative with respect to nondimensional time,  $\tau$ . The friction force,  $F_L$ , and the function  $G(V)$  are also converted nondimensional forms as follows:

$$f_L(y_2, y_3) = y_3 + s_1 \left( y_2 - \frac{|y_2|}{g(y_2)} y_3 \right) + s_2 y_2 \quad (2.12)$$

$$g(y_2) = 1 + \gamma \exp(-y_2^2). \quad (2.13)$$

Equations (2.9), (2.10), and (2.11) can be conveniently represented in state-space form:

$$y' = f(y, u) \quad (2.14)$$

where  $y$  is the state vector  $[y_1 \ y_2 \ y_3]^T$ . The nondimensionalization of the terms associated with the LuGre friction model is very important. Due to the size of the bristle stiffness, the displacement  $Z$  is orders of magnitude smaller than  $X$  and  $V$ . Consequently, direct integration of the dimensional system of equations is less accurate due to round-off errors.

The analysis the dynamics of the stick-slip system began with examining the function  $g(y_2)$ , as shown in Figure 2.5. This function changes rapidly around  $y_2 = 0$  and is approximately equal to 1 for  $|y_2| > 3$ . Also, the slope of  $g$  is zero at  $y_2 = 0$  and is approximately zero outside the range  $|y_2| > 3$ . The magnitude of the slope is maximum at

$|y_2| = 1/\sqrt{2}$  (or 0.707), implying that the dynamics can change rapidly when the velocity is in the “sticking range,” defined to be  $|y_2| < 1$ .

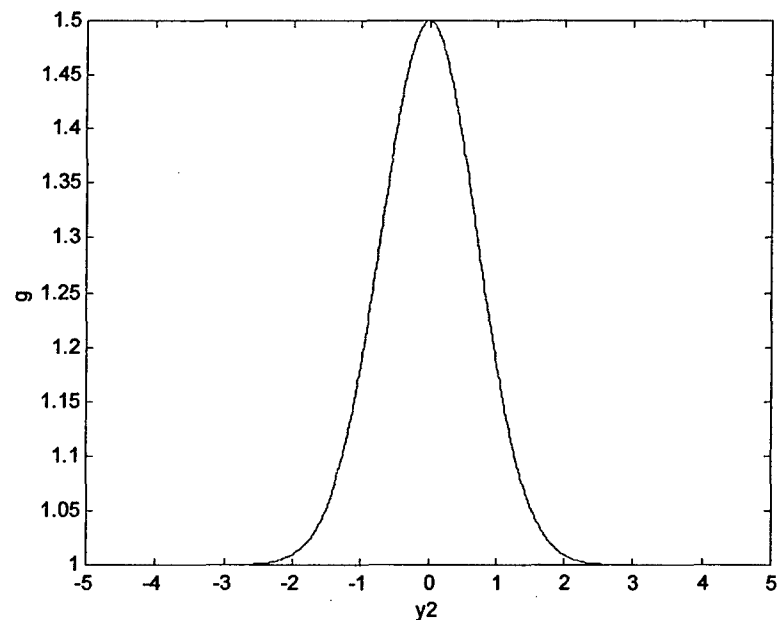


Figure 2.5. LuGre function  $g$  versus  $y_2$  using values in Table 1.

It may be noted that equations (2.9), (2.10) and (2.11) are in standard, singular perturbation form [32]. Using the numerical values of Table 2.1, the stiffness ratio between the system and the friction model,  $\varepsilon$ , is equal to  $2 \times 10^{-5}$ . The smallness of the parameter  $\varepsilon$  is partially to blame for the “numerical stiffness” of the system of equations. Numerical stiffness makes it difficult to simulate the response of the system because it requires very small time steps to ensure algorithm stability and accuracy. The problem is compounded when the system in question is more realistic, such as a multi-degree-of-freedom (MDOF) structure with multiple frictional interfaces. As the present system is

only single-degree-of-freedom (SDOF), it is possible to study the numerical stiffness problem analytically.

In order to examine the numerical stiffness of the LuGre dynamics, one can examine the Jacobian of the state dynamics:

$$J = \begin{bmatrix} \frac{\partial f_1}{\partial y_1} & \frac{\partial f_1}{\partial y_2} & \frac{\partial f_1}{\partial y_3} \\ \frac{\partial f_2}{\partial y_1} & \frac{\partial f_2}{\partial y_2} & \frac{\partial f_2}{\partial y_3} \\ \frac{\partial f_3}{\partial y_1} & \frac{\partial f_3}{\partial y_2} & \frac{\partial f_3}{\partial y_3} \end{bmatrix} = A + B(y_2, y_3) + C(y_2) \quad (2.15)$$

where

$$A = \begin{bmatrix} 0 & \alpha & 0 \\ -1/\alpha & -(s_1 + s_2)/\alpha & -1/\alpha \\ 0 & \alpha/\varepsilon & 0 \end{bmatrix}, \quad (2.16)$$

$$B(y_2, y_3) = \begin{bmatrix} 0 & 0 & 0 \\ 0 & s_1 y_3 / \alpha & 0 \\ 0 & -\alpha y_3 / \varepsilon & 0 \end{bmatrix} \left\{ \frac{g + 2\gamma y_2^2 \exp(-y_2^2)}{g^2} \right\} \text{Sgn}(y_2), \quad (2.17)$$

and

$$C(y_2) = \begin{bmatrix} 0 & 0 & 0 \\ 0 & 0 & s_1 / \alpha \\ 0 & 0 & -\alpha / \varepsilon \end{bmatrix} \left\{ \frac{|y_2|}{g} \right\}. \quad (2.18)$$

Because the Jacobian characterizes the local, linearized dynamics of a system, it is useful in analyzing the source of the numerical stiffness when (2.14) is time integrated. If the Jacobian was evaluated at each instant in time, insight can be gained into the local dynamics of (2.14), which would be of prime importance in numerical simulations. In particular, the eigenvalues of  $J$  are important because they represent the poles of the

dynamic system. These values determine how fast the system is behaving, and therefore the maximum allowable time step to integrate the system.

In the case of explicit numerical integration routines, the stability of the algorithm depends on the size of the nondimensional time step,  $h$ . The maximum allowable time step is inversely proportional to the largest magnitude eigenvalue of  $J$ . As seen in (2.16),  $A$  has no dependence on the state vector  $y$ . From (2.17), the negative term in the exponential function causes  $B$  to become independent of  $y_2$  for sufficiently large  $|y_2|$ . However,  $B$  is still dependent on the sign of  $y_2$ . The matrix  $C$ , however, grows linearly with  $|y_2|$ , dominating matrices  $A$  and  $B$  for high slip velocities ( $|y_2| \gg 10$ ). Thus, an expression for the largest magnitude eigenvalue of  $J$  that holds asymptotically as  $|y_2|$  gets larger and larger can be derived based on the nonzero eigenvalue of  $C$ :

$$\lambda_{\max}(J) = \frac{\alpha|y_2|}{\varepsilon g} \quad (2.19)$$

It is seen that  $\lambda_{\max}$  grows linearly with  $|y_2|$ . Therefore, as the velocity of the mass becomes large compared to the Stribeck velocity,  $V_S$ , the maximum allowable time step becomes smaller. It is also seen that  $\lambda_{\max}$  is inversely proportional to  $\varepsilon = K/\sigma_0$ . Thus as the aggregate bristle stiffness  $\sigma_0$  grows larger, the numerical stiffness problem worsens, especially during episodes of high slip velocity. In dimensional terms,  $\lambda_{\max}(J) = V\sigma_0/F_c$   $\text{sec}^{-1}$ .

An alternate interpretation of (2.19) is obtained by inspection of the LuGre dynamics (2.11). If, over a small interval, the nondimensionalized velocity ( $y_2$ ) is assumed to be constant, then the coefficients of (2.11) are constant over this interval as well. Subsequently, (2.11) becomes a linear first-order differential equation with a time constant,  $T_c$ :

$$y_3' = \frac{\alpha}{\varepsilon} y_2 - \frac{\alpha}{\varepsilon} \frac{|y_2|}{g(y_2)} y_3 = \frac{\alpha}{\varepsilon} y_2 - \frac{y_3}{T_c} \quad (2.20)$$

where

$$T_c = \frac{\varepsilon g}{\alpha |y_2|} . \quad (2.21)$$

From (2.21), it is evident that the time constant is equal to the inverse of the maximum eigenvalue given by (2.19). For very low values of  $y_2$ , the time constant is very large, indicating very slow friction dynamics. As the velocity emerges from the sticking range,  $|y_2| \approx 1$ ,  $g$  falls off rapidly, decreasing the time constant. For  $|y_2| > 3$ ,  $g(y_2)$  is approximately 1 and  $T_c$  decreases inversely to  $y_2$ . As the time constant tends to zero, the dynamics of the friction model are much faster than that of the mechanical system.

Qualitatively, this behavior can be attributed to the movement of the bristles. During microslip, the bristles move in a slow, linear manner. When the critical limit is reached, the bristles “snap” back to place and cause an increase in the speed of the friction dynamics. As the velocity increases, the frequency of contact between the bristles increases, therefore causing the bristles to move faster. The difference between the speed of the friction dynamics and that of the mass-spring-system is what leads to numerical stiffness. This difference results in the requirement of small time steps and the associated long computation times.

During sticking, which corresponds to small values of both  $y_2$  and  $y_3$ , the eigenvalues of  $J$  are given by  $A$  alone. By inspection, one eigenvalue of  $A$  is identically zero. Using the friction parameters of Table 2.1,  $K = 2$  N/m, and  $M = 1$  kg, the remaining two eigenvalues are  $-111.94 \pm 193.57i$ , which correspond to a magnitude of  $\lambda_{\max}(J) =$

223.61 and a damping ratio of 0.50. For small-to-moderate values of  $y_2$ , one must compute  $\lambda_{max}(J)$  numerically. Due to the presence of  $B$ ,  $\lambda_{max}$  is a function of both  $y_2$  and  $y_3$ . Also note that the matrix  $B$  describes sensitivity of the Jacobian to the high slope of the function  $g$  within the range  $|y_2| < 1$ . Figure 2.6 shows  $\lambda_{max}(J)$  versus  $y_2$  for  $y_3 = \pm 1$ . Also shown is the asymptotic expression for  $\lambda_{max}(J)$  given by (2.19). For small velocities, the bristle displacement  $y_3$  produces a difference in the maximum eigenvalue from the asymptotic result. However, as  $|y_2|$  increases, this difference becomes less and less significant when viewed as a percentage of  $\lambda_{max}(J)$ .

A number of conclusions can be drawn from Figure 2.6. It is seen that the system is relatively well conditioned for low velocities ( $|y_2| < 3$ ), including the microslip region. The system becomes more and more ill-conditioned as the slip velocity grows. This is in stark contrast to the regularization schemes portrayed in Figures 1.2 and 1.3. When the discontinuity is smoothed in the vicinity of the zero-slip point, the system of equations are ill-conditioned for small velocities (microslip) and become better conditioned as the slip velocity increases in magnitude.

This contrast may appear at first to be counterintuitive, because it is at odds with the behavior of standard approaches of friction modeling and simulation discussed in Chapter 1. Whether one smoothes the discontinuity or uses a switching between sticking and slipping dynamical systems, the numerical problems are all located in the vicinity of *small slip velocities*. In the LuGre model of friction, sticking and near-sticking conditions are where the system is *relatively well conditioned*; ill-conditioning develops as the slipping velocity gets larger.

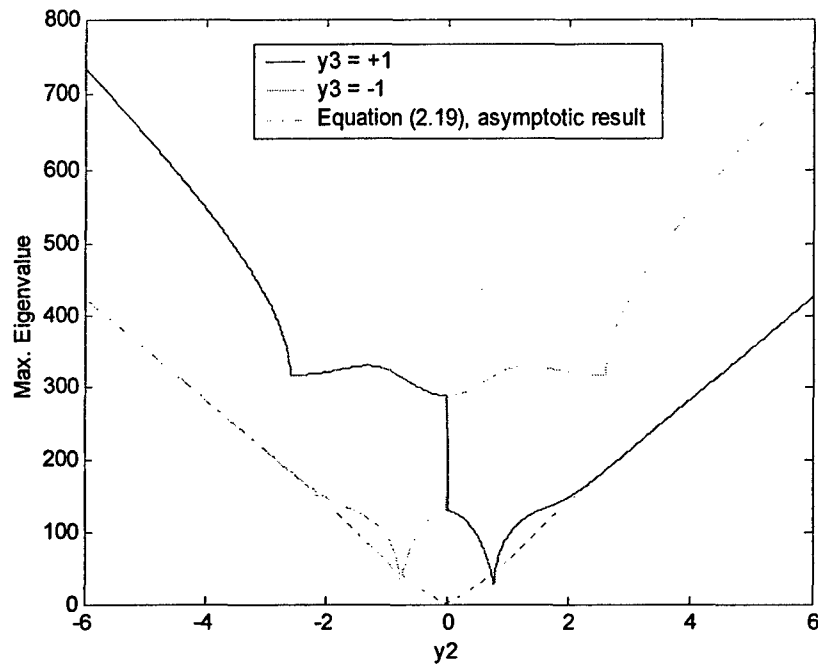


Figure 2.6. Maximum magnitude eigenvalue vs  $y_2$ .

#### 2.4 Numerical Simulation Results

To initially simulate the stick-slip system, the Matlab function *ode45* was used. The *ode45* function is based on an explicit Runge-Kutta formula, the Dormand-Prince pair [33, 34]. The routine uses a variable time step based on specified tolerances: a relative tolerance, *RelTol*, whose default value is  $10^{-3}$ , and an absolute tolerance, *AbsTol*, whose default value is  $10^{-6}$ . Figures 2.7 through 2.9 show the nondimensional state quantities while Figure 2.10 shows the nondimensional LuGre friction force,  $f_L(y_2, y_3)$ . In the case shown, the relative and absolute tolerances are  $10^{-4}$  and  $10^{-6}$ , respectively. Note that the friction force behaves irregularly during the stick-slip regions. This irregular behavior can be attributed to the sudden change from the static friction force to the kinetic friction force. Further examination shows that at the instant the system begins to

slip, the friction force initially decreases before increasing with increasing velocity. This phenomenon is consistent with the Stribeck effect. Lastly, like the elastic-plastic friction model, the friction force during the sticking phase acts like a linear spring.

From Figures 2.7 and 2.8, the nondimensional displacement ( $y_1$ ) and velocity ( $y_2$ ) are fairly smooth and accurate, with results closely matching scaled results from [28]. On the other hand, the LuGre force, shown in Figure 2.10, exhibits a noticeable “ringing” in time intervals of high slip velocity. The ringing largely disappears when the RelTol and AbsTol values are lowered to  $10^{-8}$ .

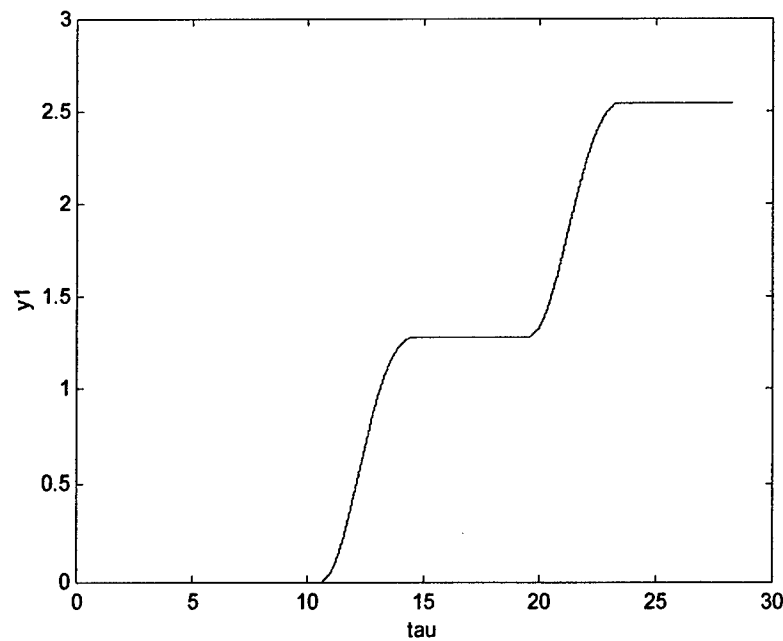


Figure 2.7. Nondimensional position vs.  $\tau$  using *ode45* with RelTol =  $10^{-4}$  and AbsTol =  $10^{-6}$ .

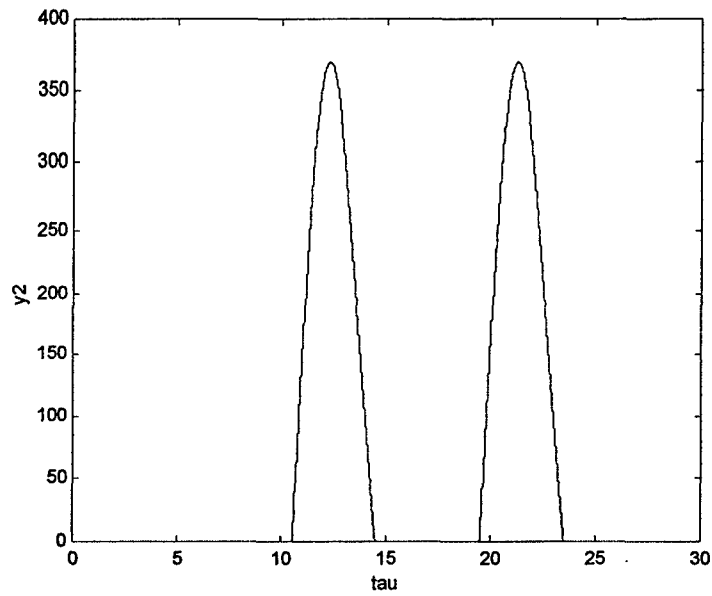


Figure 2.8. Nondimensional velocity vs.  $\tau$  using *ode45* with  $\text{RelTol} = 10^{-4}$  and  $\text{AbsTol} = 10^{-6}$ .

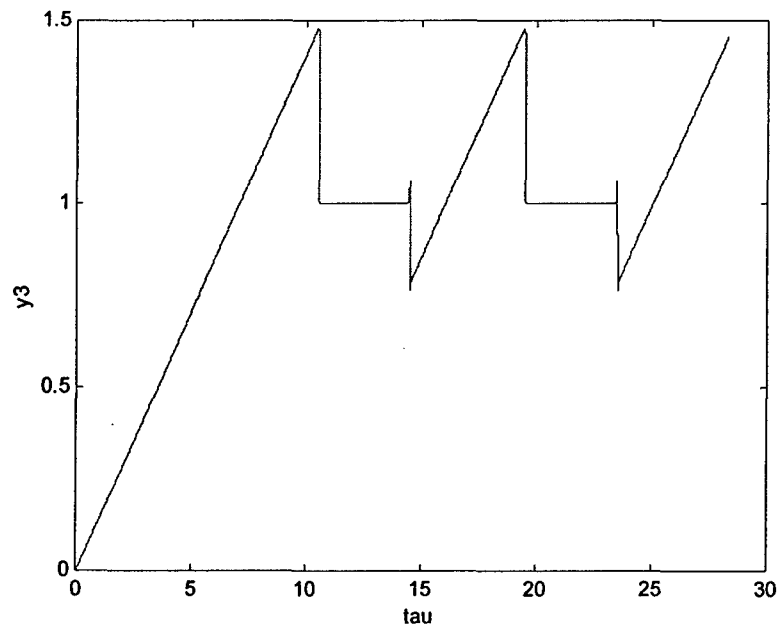


Figure 2.9. Nondimensional bristle displacement vs.  $\tau$  using *ode45* with  $\text{RelTol} = 10^{-4}$  and  $\text{AbsTol} = 10^{-6}$ .

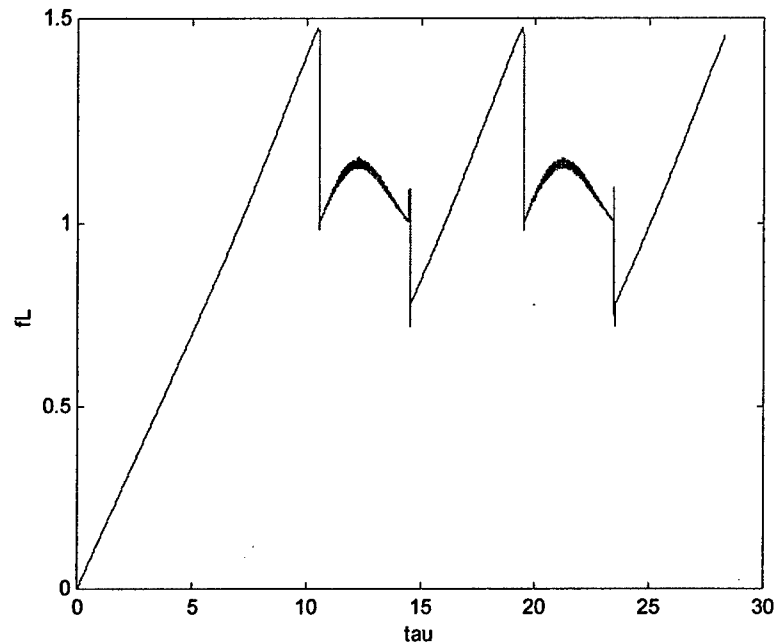


Figure 2.10. Nondimensional friction force vs.  $\tau$  using *ode45* with  $\text{RelTol} = 10^{-4}$  and  $\text{AbsTol} = 10^{-6}$ .

The reason for the ringing in the friction force is uncovered by examining the Jacobian at each point along the state trajectory. Figure 2.11 shows  $\lambda_{\max}(J)$  versus  $\tau$  from a more accurate simulation using *ode45* with  $\text{RelTol} = 10^{-7}$  and  $\text{AbsTol} = 10^{-7}$ . It is seen that the time intervals in which the largest eigenvalue magnitudes occur is closely related to occurrences of high slip velocities. Figures 2.12(a) shows a close up of  $\lambda_{\max}(J)$  just as the mass transitions from microslip to macroslip, and Figure 2.12(b) shows  $\lambda_{\max}(J)$  just after the first interval of macroslip comes to an end. For comparison, the figures also show the asymptotic result calculated by Equation (2.19).

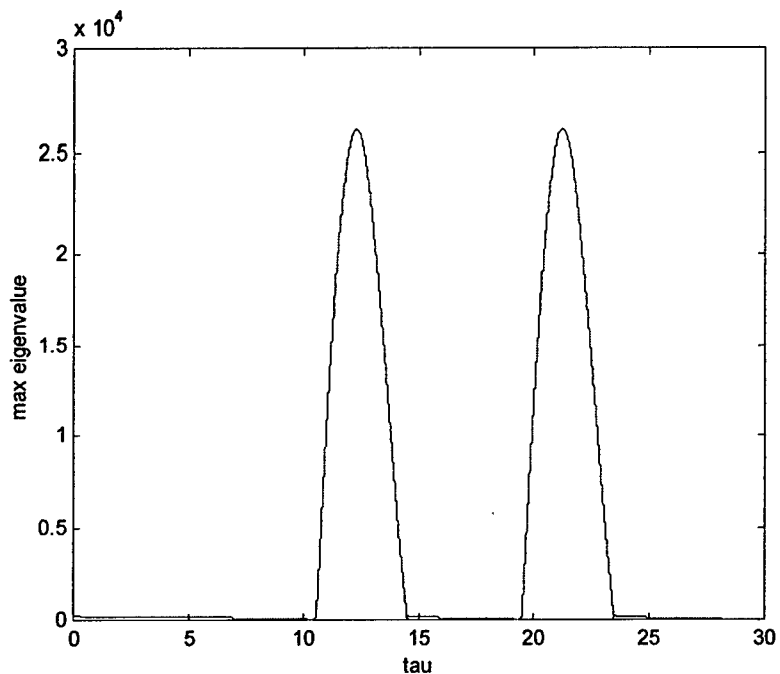
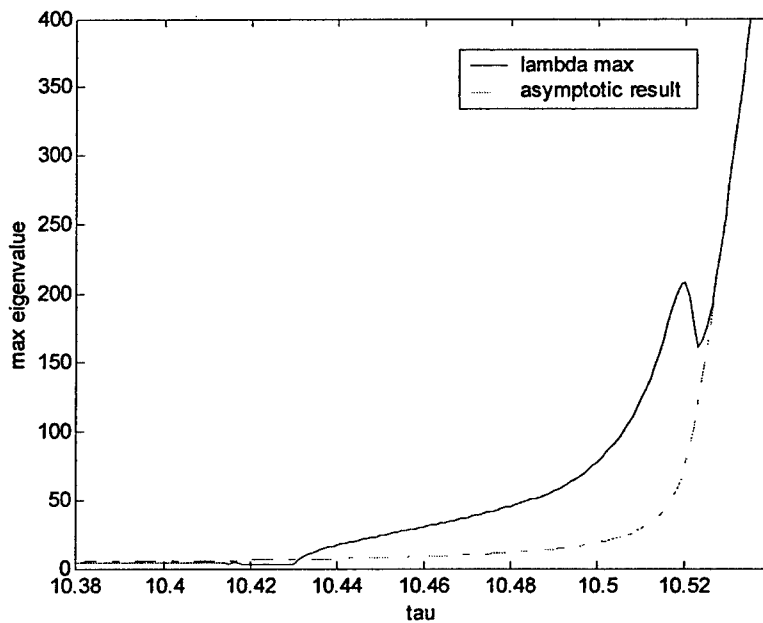
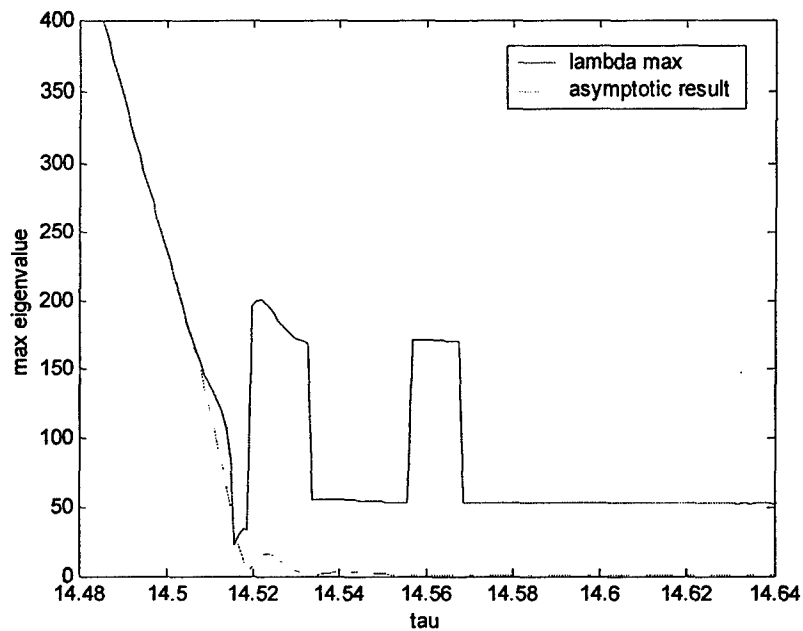


Figure 2.11.  $\lambda_{\max}(J)$  vs  $\tau$  from *ode45* with  $\text{RelTol} = 10^{-7}$  and  $\text{AbsTol} = 10^{-7}$ .



(a)



(b)

Figure 2.12. Maximum eigenvalue during the transition from (a) microslip to macroslip and (b) macroslip to microslip.

The large size of  $\lambda_{max}(J)$  during periods of high slip velocity is the major source of the ringing that is evident in the LuGre friction force. However, the ringing that is present in the state vector itself is far less pronounced. In fact, only the bristle displacement  $y_3$  displays any appreciable ringing during high slip rates. Figure 2.13 shows a close up of  $y_3$  during the period of maximum slip. It is seen that the ringing in  $y_3$  amounts to approximately 0.01% of the nominal value. The ringing is amplified in the LuGre force because of the way that  $f_L$  is calculated; in particular, the expression in parentheses in (2.12) involves the subtraction of two terms that are large, and almost exactly equal. Operations of this type are prone to round-off errors during computation.

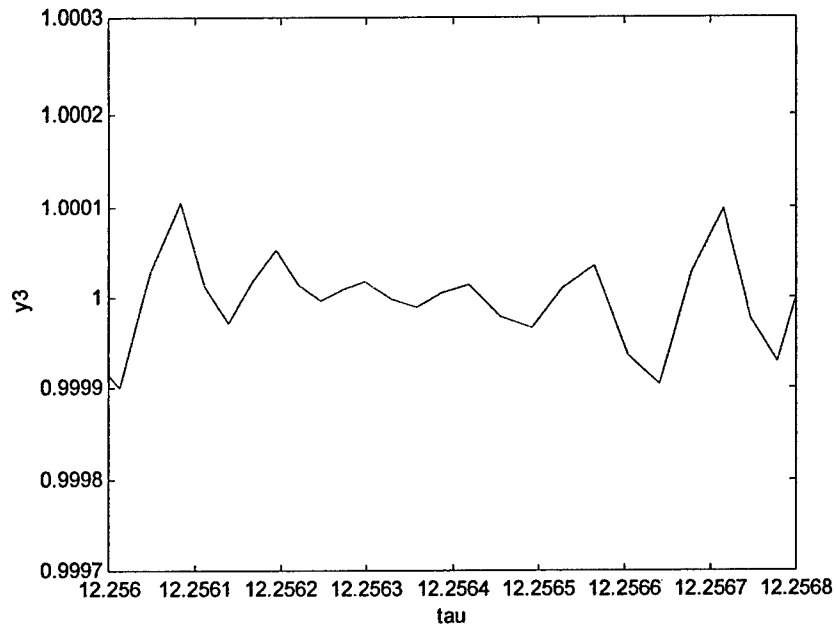


Figure 2.13. Close-up of  $y_3$  vs  $\tau$  using *ode45* with  $\text{RelTol} = 10^{-4}$  and  $\text{AbsTol} = 10^{-6}$ .

## 2.5 Comparison of Integration Methods

To find the best strategies to simulate the stick-slip system, several techniques were considered. Aside from using built-in Matlab functions, the techniques included user-defined explicit and implicit time integration methods. The main difference between explicit and implicit integration schemes is in the formulation. Explicit schemes use past states to define the current states, whereas implicit schemes define the current states using past and current results. Furthermore, implicit methods exhibit better stability characteristics than the explicit methods. As a note, all computer simulations were done using Matlab 6.1 on a Pentium 4, 2.4 GHz computer. Also, the simulation time was from 0 to 20 seconds.

### 2.5.1 Explicit Integration Methods

Although the use of a Matlab function was useful as a first attempt to solve the system, it was necessary to write a user-defined integration scheme to fully understand and control the simulation process. Because of its popularity and efficiency, the 4<sup>th</sup> order Runge-Kutta method was chosen as the explicit solver. Like the *ode45* function, this Runge-Kutta method is an explicit, time-marching scheme with a time step,  $h$ , a local error on the order of  $h^5$ , and a global error on the order of  $h^4$  [35]. Since the maximum allowable time step is proportional to the inverse of the largest magnitude eigenvalue of the Jacobian, a time step based on this value was used for the baseline simulation. From (2.19),  $\lambda_{max} = 2.62 \times 10^4$  for the maximum value of  $|y_2|$  in the simulation, which corresponds to a minimum time constant of  $3.82 \times 10^{-5}$ . To best capture the dynamics of the system, a time step of  $10^{-5}$  was used, which was more than three times less than the minimum time constant. Note that the time step used,  $h$ , is in nondimensional form defined by  $h = \omega_n H$ , where  $H$  is the dimensional time step.

Although the baseline simulation ( $h = 10^{-5}$ ) gave the best results, it was not necessary to use such a small time step at all times. From previous analyses, the dynamics of the system is fast during periods of slip, but slow during microslip. Hence, it would be advantageous to base the time step based on the local dynamics of the system. One way to vary the time step was to define  $h$  based on the inverse of the maximum eigenvalue, as shown in Figure 2.11. However, this would be cumbersome because finding the eigenvalues of the Jacobian at each time step requires too many calculations. The added overhead for such a technique would be prohibitive, especially for realistic systems having a higher number of degrees of freedom.

Another way to estimate the time step necessary to simulate the system was to use the time constant, as defined by (2.21). From Figures 2.12(a) and 2.12(b), the inverse of the time constant agrees well with the maximum eigenvalue during slip. The periods where these values do not agree are the transitional periods and during sticking. However, this disagreement was addressed by setting a maximum time constant such that the integration scheme remained stable. For the system under consideration here, this maximum time constant was set at  $10^{-3}$ . During periods of slip, estimated as  $T_c < 0.02$ , the time step was set to one-third of the time constant. Otherwise, the time step was set to  $10^{-3}$ .

To make the simulation more efficient, another method based on the velocity was used to estimate the time step. Because the dynamics of the system change rapidly at the stick/stick transition periods, a small time step ( $10^{-4}$ ) was used in this region. Otherwise, the time step was set to  $10^{-3}$ . This stick-slip transition region was defined as the range  $0.1 \leq |y_2| < 5$ . This range was relatively conservative because it assumed that the stick-slip transition period occurred between velocities much smaller and much greater than the Stribeck velocity ( $y_2 = 1$ ).

Table 2.2 compares the different explicit methods in order of decreasing simulation time. In addition to the baseline case (4th order Runge-Kutta with  $h = \text{constant} = 10^{-5}$ ), four other cases are shown: 4th order Runge-Kutta with  $h$  switched based on the time constant, *ode45* with  $\text{RelTol} = \text{AbsTol} = 10^{-8}$ , 4th order Runge-Kutta with  $h$  switched based on  $|y_2|$ , and 4th order Runge-Kutta with  $h = \text{constant} = 10^{-3}$ . Two different error metrics were employed. First, the error,  $E$ , was computed by taking the absolute value of the difference in the dimensionalized friction forces at each instant in time. The

first error metric listed in Table 2 is simply the maximum of  $E$  over the duration of the simulation. The second error metric is the root-mean-squared error,  $E_{RMS}$ , and is calculated by

$$E_{RMS} = \sqrt{\frac{1}{T} \int_0^T E^2 dt} \quad (2.22)$$

where  $T$  is the final time. Since the number of time steps was different for each method, the data was interpolated from the baseline data set for comparison. Lastly, the simulation time is reported as a percentage to the baseline simulation time, which is 1651s, or 27.5 minutes.

Table 2.2. Comparison of Explicit Methods

Simulation Method	Time Step	Error (N)		Simulation Time (%)	Number of Steps
		Max	RMS		
Runge-Kutta (Baseline)	$10^{-5}$	n/a	n/a	100	$2.828 \times 10^6$
Runge-Kutta (Time constant)	$(1/3)T_c$ or $10^{-3}$	0.207	$7.46 \times 10^{-4}$	14.8	$4.020 \times 10^5$
Ode45*	n/a	$1.68 \times 10^{-4}$	$4.22 \times 10^{-8}$	3.62	$1.476 \times 10^5$
Runge-Kutta (Velocity)	$10^{-4}$ or $10^{-3}$	0.320	$1.30 \times 10^{-3}$	1.17	$3.170 \times 10^4$
Runge-Kutta (Constant)	$10^{-3}$	$3.98 \times 10^{-4}$	$1.16 \times 10^{-6}$	1.14	$2.829 \times 10^4$

\* absolute tolerance = relative tolerance =  $10^{-8}$

Table 2.2 shows that there is a significant improvement in the simulation time by switching the time step based on the time constant of the system. However, the maximum error using this method is unacceptable (~14% error) and the number of steps required is still relatively large. The Runge-Kutta method with  $h$ -switching based on the velocity performed much better in terms of simulation time and number of steps, but its accuracy was the worst. The result using *ode45* had the best accuracy and a very short simulation time compared to the baseline. Finally, using the Runge-Kutta method with a constant time step of  $10^{-3}$  produced errors comparable to the *ode45* method, but with the smallest simulation time and least amount of steps. This last result is surprising since  $10^{-3}$  is roughly 26 times larger than the frictional time constant at the point of maximum slip velocity.

### 2.5.2 Implicit Integration Methods

Despite moderate successes with the explicit methods, implicit integration schemes were used to simulate the stick-slip system. The key advantage of the implicit integration methods is better stability characteristics versus the explicit methods. Therefore, it would be possible to use larger time steps (than the explicit methods) to simulate the LuGre model, even during slip. However, the disadvantage of implicit methods is the need to iterate at each time step. This iteration is necessary to solve for simultaneous equations at each time instant. Lastly, despite the improved stability characteristics, the accuracy of the implicit methods still depends upon the size of the time step.

The first implicit method to be applied to the stick-slip system was the Trapezoidal method, which is effective for solving stiff differential equations [35]. An extension of the Trapezoidal method is the Radau-IIA method [36]. Both the Trapezoidal integration scheme and the Radau-IIA scheme can be expressed in a common framework. At each time  $t_i$ , two sets of nonlinear equations must be solved for the unknown vectors,  $k_1$  and  $k_2$ :

$$k_1 = f(y(t_i) + c_1 k_1 + c_2 k_2, u(t_i + b_1)) \quad (2.23)$$

$$k_2 = f(y(t_i) + c_3 k_1 + c_4 k_2, u(t_i + h)) \quad (2.24)$$

where  $k_1$  and  $k_2$  are  $3 \times 1$  vectors that approximate in some sense the average dynamics over a time step. The value of the state vector at the next time step is expressed in terms of  $k_1$  and  $k_2$  as follows:

$$y(t_i + h) = y(t_i) + c_3 k_1 + c_4 k_2 \quad (2.25)$$

The difference in the Trapezoidal method and the Radau-IIA method is the values of the constants  $c_i$  and  $b_i$ . For Trapezoidal integration, the constant values are

$$c_1 = c_2 = 0, \quad c_3 = c_4 = h/2, \quad b_1 = 0, \quad (2.26)$$

and for the Radau-IIA method:

$$c_1 = 5h/12, \quad c_2 = -h/12, \quad c_3 = 3h/4, \quad c_4 = h/4, \quad b_1 = h/3 \quad (2.27)$$

For the explicit methods, various schemes were investigated for their accuracy and efficiency. Similarly, various schemes were also investigated for the implicit methods. The results of the implicit integration methods are summarized in Table 2.3. The Trapezoidal method was implemented with a constant time step of  $h = 0.005$ . The

Radau-IIA method was compared using three different schemes for selection of  $h$ :  $h = \text{constant} = 10^{-2}$ ,  $h$  switched based on velocity, and  $h$  switched based on the time constant.

When compared to the explicit methods in Table 2.2, the implicit methods on average require less time and much fewer integration steps. The primary reason for these improvements is that larger time steps (than the explicit methods) could be used to obtain an accurate solution. Although the equations of the LuGre model are numerically stiff, the implicit integration schemes are well suited to solve them.

Table 2.3. Comparison of Implicit Methods

Simulation Method	Time Step	Error (N)		Simulation Time (%)	Number of Steps
		Max	RMS		
Runge-Kutta (Baseline)	$10^{-5}$	n/a	n/a	100	$2.828 \times 10^6$
Trapezoidal	$5 \times 10^{-3}$	0.150	$7.54 \times 10^{-4}$	2.25	$5.658 \times 10^3$
Radau-IIA (Constant)	$10^{-2}$	$9.33 \times 10^{-2}$	$4.72 \times 10^{-4}$	1.08	$2.830 \times 10^3$
Radau-IIA (Velocity)	$10^{-2}$ or 0.02	0.497	$5.90 \times 10^{-3}$	0.56	$1.436 \times 10^3$
Radau-IIA (Time Constant)	$10^{-2}$ or 0.05	0.490	$7.20 \times 10^{-3}$	0.47	$1.216 \times 10^3$

Similar to the findings for the Runge-Kutta method, it is observed that the maximum error values for the variable time step methods were unacceptably large. A reason for the relatively large errors was that at the stick-slip transition regions, there was

a shift in the solution compared to the baseline. This shift occurred for both the explicit and implicit methods that used a variable time step. Since the transitions in the friction force occur very rapidly in time, even a small time shift in one simulation relative to the baseline result can give rise to relatively large maximum errors.

From Tables 2.2 and 2.3, it appears that the best choice to simulate the stick-slip system is to use the Radau-IIA method with a constant time step of  $10^{-2}$ . Surprisingly, the use of 4th order Runge-Kutta with a constant time step of  $10^{-3}$  also displayed a good balance between accuracy and efficiency. In terms of simulation time, both the 4th order Runge-Kutta and Radau-IIA methods are similar. The Runge-Kutta method has errors two orders of magnitude better than the Radau-IIA scheme, however, the Radau-IIA requires an order of magnitude fewer steps. Thus the best choice of integration scheme may depend on the users' preference for accuracy versus speed, as well as on the availability of computer memory. However, when simulating a large dynamical system, using a larger time step would greatly reduce the computation time. This advantage outweighs improved accuracy afforded by the Runge-Kutta method. Therefore, for large systems with LuGre friction, the Radau-IIA method appears to be the best method for numerical integration.

## CHAPTER 3

### ENERGY TRANSFER AND DISSIPATION: DISCRETE SYSTEM

Once the complexity and numerical difficulties associated with frictional systems are understood, an investigation into the effects of friction on the dynamics of a structural system is conducted. As discussed in Chapter 1, vibration in space structures poses a major problem because these structures have high precision and accuracy requirements. Since friction is responsible for the majority of mechanical energy loss in structures, this Chapter explores the energy dissipation caused by dry friction at a connecting joint. In particular, this study examines the ability of friction to serve as a catalyst for energy pumping. It is hypothesized that joint friction can be a means to pump low-frequency vibrational energy to high-frequency vibrational energy, through the action of stick-slip oscillations. Since energy can be dissipated faster at higher frequencies, this pumping of energy to excite higher resonances may serve as a tool for increased energy dissipation. In this manner, an inherent property of friction can be exploited to improve the overall damping capacity of the system.

A simplified model of a connecting joint with friction is presented first. The model consists of a 3 degrees-of-freedom (3DOF) spring-mass-damper system with a frictional interface. The algorithm used to calculate the friction forces and the simulation parameters are presented as well. Simulations were performed using Matlab and the equations of motion were solved using the 4<sup>th</sup> order Runge-Kutta method. Next, the steady-state and free vibration responses of the system are explored, followed by a parametric study of the energy dissipation in the system.

### 3.1 System Model

To model the friction contact at a connection joint, a 3 degrees-of-freedom spring-mass-damper system was used. This configuration is similar to a model used by Warren to study microdynamic frictional behavior in joints [4]. The 3DOF system, shown in Figure 3.1, represents two structures modeled as single-degree-of-freedom systems that are coupled by a mass sliding against a friction surface. The sliding mass ( $m_2$ ) is an order of magnitude smaller than masses  $m_1$  and  $m_3$ . The absolute position and velocity of each mass are denoted by  $x_i$  and  $v_i$ , respectively, while the parameters  $k_i$  and  $c_i$  denote spring and viscous damping constants, respectively. Note that these variables are different than the variables introduced in the previous chapters. The function,  $P(t)$ , represents an external force applied to mass 1.

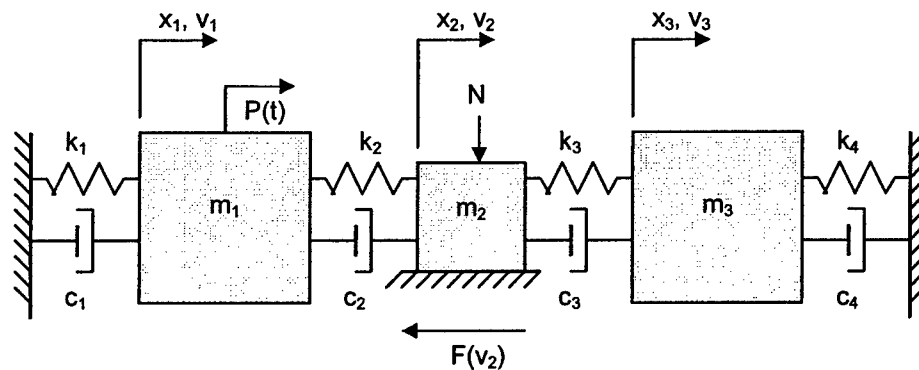


Figure 3.1. System model of frictional contact at a connection joint.

The friction force,  $F(v)$ , is defined as

$$F(v) = \mu N \operatorname{sgn}(v) \quad (3.1)$$

where  $v$  is the slip velocity,  $\mu$  is the friction coefficient,  $N$  is the normal force, and  $\operatorname{sgn}(v)$  is the signum function where  $\operatorname{sgn}(v) = v/|v|$ ,  $v \neq 0$ . Using the Stribeck friction model, the friction coefficient,  $\mu$ , is given by

$$\mu = \mu^* + \gamma(e^{-\beta|v|} - 1) + \alpha|v| \quad (3.2)$$

where  $\mu^*$  is the static friction coefficient and parameters  $\gamma$ ,  $\beta$ , and  $\alpha$  are constants [37].

There is one main reason why the Stribeck friction model is used in this case instead of the LuGre model or other friction models described in Chapter 2. Because the hypothesis is that stick-slip motion pumps energy to higher modes, it is necessary to isolate this stick-slip mechanism. Continuous friction models such as the LuGre model contain other internal dynamics that may obscure the phenomenon.

Figure 3.2 shows the relationship between the Stribeck friction force and the slip velocity. The key mechanism that causes stick-slip behavior is the decrease in friction force as  $|v|$  increases around zero [38]. In Equation (3.2), the parameter  $\gamma$  specifies the difference between the static and sliding friction coefficients while  $\beta$  determines the steepness of the transition. The coefficient  $\alpha$  was set to zero because it is typically associated with a viscous-damping characteristic of lubricated contact. Setting  $\alpha$  equal to zero allows one to distinguish between the energy dissipation by viscous damping from the energy dissipated due to dry friction.

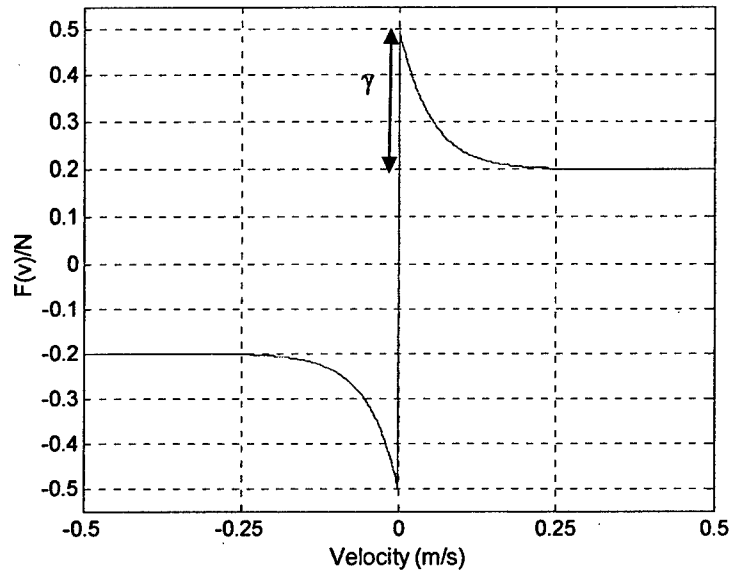


Figure 3.2. Stribeck friction coefficient as a function of velocity.

As seen in Figure 3.2, there is a discontinuity in the friction force when the slip velocity is zero. The numerical problems related to this condition are discussed in Chapter 2 as well as different methods to solve these problems. In this study, a sliding mode control (variable structure system theory) algorithm is used to handle the discontinuity and solve for the friction force [19]. This method is one of the “switching strategies” addressed in Chapter 2. Presented next is a derivation of the equations of motion and a discussion of the numerical solution technique.

The equations of motion for the 3DOF system can be written in the form

$$[M]\{\ddot{x}\} + [C]\{\dot{x}\} + [K]\{x\} = \{e_1\}P - \{e_2\}F \quad (3.3)$$

where  $\{x\} = [x_1 \ x_2 \ x_3]^T$ ,  $\{e_1\} = [1 \ 0 \ 0]^T$ ,  $\{e_2\} = [0 \ 1 \ 0]^T$ , and the overdot represents a derivative with respect to time. The matrices  $[M]$ ,  $[C]$ , and  $[K]$  are the mass, damping, and stiffness matrices, respectively, and are defined as

$$M = \begin{bmatrix} m_1 & 0 & 0 \\ 0 & m_2 & 0 \\ 0 & 0 & m_3 \end{bmatrix}, K = \begin{bmatrix} k_1 + k_2 & -k_2 & 0 \\ -k_2 & k_2 + k_3 & -k_3 \\ 0 & -k_3 & k_3 + k_4 \end{bmatrix}, C = \begin{bmatrix} c_1 + c_2 & -c_2 & 0 \\ -c_2 & c_2 + c_3 & -c_3 \\ 0 & -c_3 & c_3 + c_4 \end{bmatrix}$$

In order to simulate the response of the 3-DOF system, the equations given by (3.3) are rewritten in the first-order, state-space form

$$\{\dot{y}\} = [A]\{y\} + \{B\}F + \{\Gamma\}P \quad (3.4)$$

where  $\{y\} = [x1 \ x2 \ x3 \ v1 \ v2 \ v3]^T$ ,  $\{B\} = -[0 \ 0 \ 0 \ ([M]^{-1}\{e_2\})^T]^T$ , and  $\{\Gamma\} = [0 \ 0 \ 0 \ ([M]^{-1}\{e_1\})^T]^T$ . The 6x6 state matrix  $[A]$  is defined as

$$[A] = \begin{bmatrix} [0] & [I] \\ -[M]^{-1}[K] & -[M]^{-1}[C] \end{bmatrix}$$

where  $[0]$  is a 3x3 zero matrix and  $[I]$  is a 3x3 identity matrix. The friction force,  $F$ , was calculated using a sliding mode control algorithm, which is discussed next.

The techniques developed and used in the area of sliding mode control can be used to define the "equivalent dynamics" that exist when sticking takes place. Numerically, sticking is assumed to be possible when  $|v_2| \leq 0.001$  m/s. Note that  $v_2$  can be expressed as

$$v_2 = [T]\{y\} \quad (3.5)$$

where  $[T] = [0 \ 0 \ 0 \ 0 \ 1 \ 0]$ . During sticking, the slip velocity is identically zero; hence its time derivative must also be zero. Taking the time derivative of (3.5) yields

$$\dot{v}_2 = [T]\{\dot{y}\} = [T]\{[A]\{y\} + \{B\}F + \{\Gamma\}P\} = 0. \quad (3.6)$$

Since Equation (3.6) represents the condition when the slip velocity is zero, the friction force,  $F$ , must be the force necessary to impose the sticking condition. This force is known as the equivalent friction force,  $F_{eq}$ . Solving (3.6) for  $F$  yields

$$F_{eq} = -([T]\{B\})^{-1}[T]\{[A]\{y\} + \{\Gamma\}P\}. \quad (3.7)$$

Qualitatively, the equivalent friction force is the force necessary to oppose the inertial and external forces to impose the sticking condition. When this force is greater than the maximum allowable friction force, then the system breaks away and starts to slip.

Figure 3.3 shows a flow chart of the logic steps to calculate the friction force. If the slip velocity is equal to or smaller than the Stribeck velocity ( $v_s = 0.001$  m/s), then the equivalent friction force is calculated. However, if this equivalent force is greater than the maximum static friction force ( $\mu^*N$ ), then the mass is assumed to break free, and the friction force is set equal to the dynamic friction force given by (3.1) and (3.2).

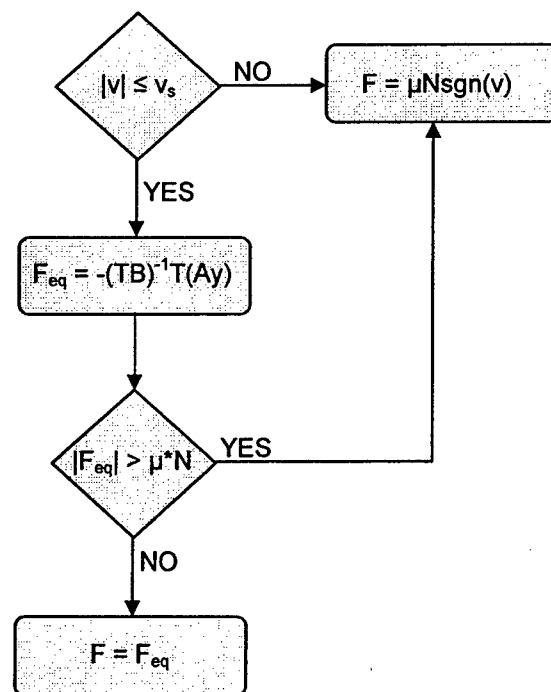


Figure 3.3. Flow chart to calculate friction force ( $P = 0$  case).

To observe the stick-slip behavior of the 2<sup>nd</sup> mass, the steady-state and free vibration responses of the system were simulated. The goal was to excite the 1<sup>st</sup> mass to

induce stick-slip motion in the 2<sup>nd</sup> mass. This stick-slip motion would pump energy from the vibration of the 1<sup>st</sup> subsystem to the 3<sup>rd</sup> subsystem.

### 3.2 System Simulation

Once the equations of motion and the sliding mode control algorithm were established, simulation of the 3DOF system was straight-forward. The method used to simulate the system was the 4<sup>th</sup> order Runge-Kutta scheme with a fixed time step of 1 ms. Table 3.1 summarizes the values used for the simulation.

Table 3.1. Simulation Parameters

System Parameters	Value	Friction Parameters	Value
$m_1, m_3$	100, 50 kg	$\mu^*$	0.50
$m_2$	0.25 kg	$\gamma$	0.30
$k_1, k_4$	1000 N/m	$\beta$	20.0
$k_2, k_3$	100 N/m	$v_s$	0.001 m/s
$\zeta_{1,2,4}, \zeta_3$	0.01, 0.05	N	100 N

The 3DOF system can be divided into three subsystems; each subsystem assumes only one of the masses is moving. The natural frequencies for each subsystem are therefore given by

$$\begin{aligned}
\omega_1 &= \sqrt{\frac{k_1 + k_2}{m_1}} \\
\omega_2 &= \sqrt{\frac{k_2 + k_3}{m_2}} \\
\omega_3 &= \sqrt{\frac{k_3 + k_4}{m_3}}
\end{aligned} \tag{3.8abc}$$

A small amount of viscous damping was added to the system in order to study the interaction of stick-slip energy dissipation and structural damping. The damping coefficients were chosen based on the following relations:

$$\begin{aligned}
c_1 &= 2\zeta_1\omega_1m_1 \\
c_2 &= 2\zeta_2\omega_2m_2 \\
c_3 &= 2\zeta_3\omega_3m_3 \\
c_4 &= 2\zeta_4\omega_4m_4
\end{aligned} \tag{3.9abcd}$$

where  $\zeta_j$  are closely related to the damping ratios of the individual subsystems. The damping ratios are all 1%, except for the 3<sup>rd</sup> damper, which is 5%. This higher damping ratio for  $\zeta_3$  was chosen to ensure adequate excitation of the third subsystem. The partition into three subsystems was useful in analyzing the behavior of the 3DOF system. During periods of sticking by the 2<sup>nd</sup> mass, the 1<sup>st</sup> and 3<sup>rd</sup> masses oscillate like linear single-degree-of-freedom (SDOF) systems with natural frequencies given by  $\omega_1$  and  $\omega_3$ , respectively.

### 3.3 Steady-State Vibration Response

In order to understand the behavior of the system, the 3DOF system was subjected to harmonic excitation of the form:

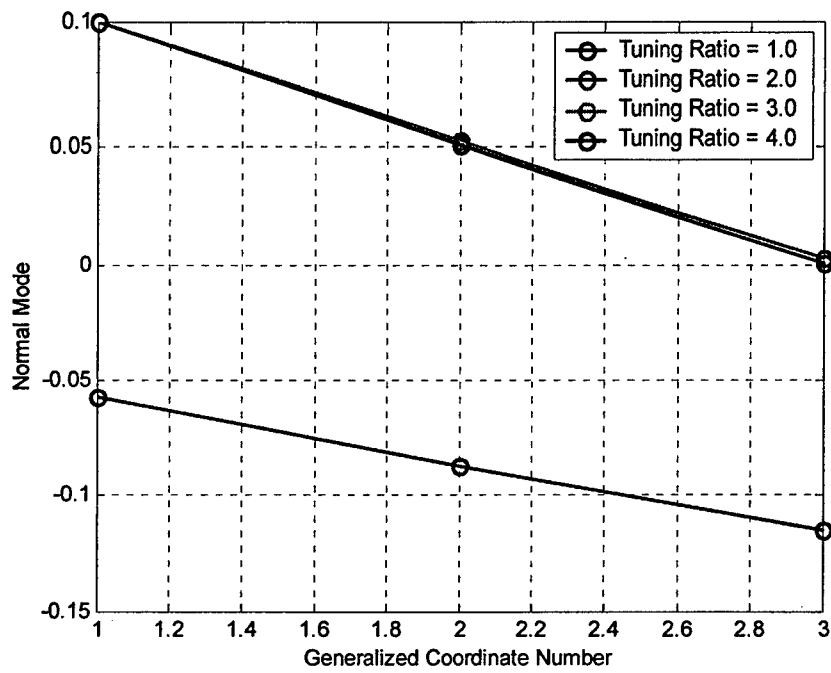
$$P(t) = W \sin(\omega_d t) \tag{3.10}$$

where  $W$  is the force amplitude (1500N),  $\omega_d$  is the driving frequency, and  $t$  is the time. Since the stick-slip motion of the 2<sup>nd</sup> mass exhibits odd numbered harmonics, tuning the 3<sup>rd</sup> subsystem to one of the harmonics would theoretically produce an internal resonance in the response [39]. The 3<sup>rd</sup> subsystem was tuned by keeping  $k_3$  and  $m_3$  constant and varying  $k_4$  so that

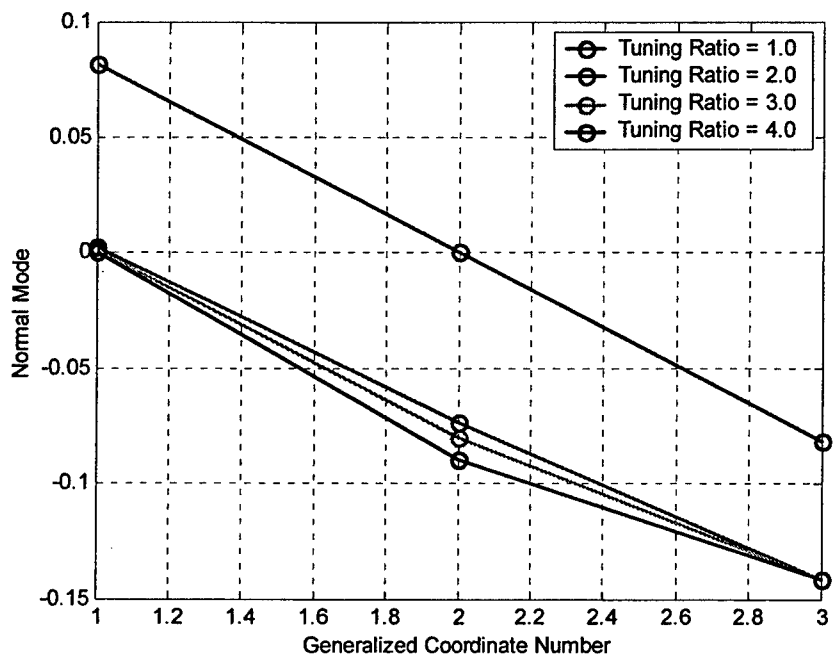
$$k_4 = \left( \frac{m_3}{m_1} \right) r^2 (k_1 + k_2) - k_3 \quad (3.11)$$

where  $r$  is the *tuning ratio* defined as  $\omega_3/\omega_1$ .

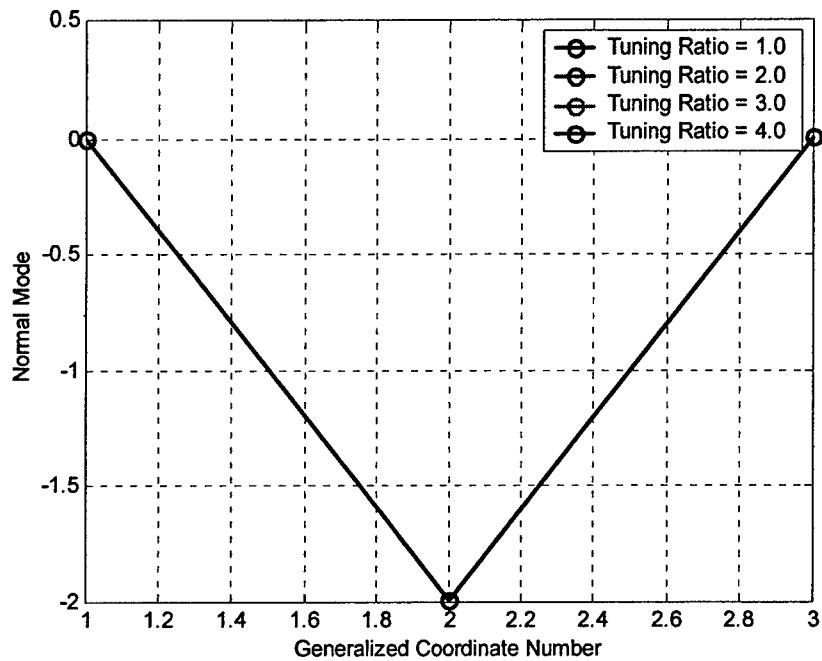
Before the steady-state response is presented, it is instructive to examine the linear modes of the 3DOF system in the absence of friction. In particular, the effect of the tuning ratio on the natural frequencies and mode shapes of the system are explored. As seen in Figures 3.4(a) through 3.4(c), mode 1 is mostly dominated by mass 1, mode 2 is dominated by mass 3, and mode 3 is dominated by mass 2. The modes are fairly localized, except when the tuning ratio is 1. At this tuning ratio, mode 1 is a combination of the motion of all three masses. Mode 2 is a symmetric mode where the motion of mass 1 mirrors that of mass 3 while mass 2 is largely immobile. However, mode 3 is seen to be invariant for tuning ratios from 1 to 4.



(a)



(b)



(c)

Figure 3.4. Modal amplitude versus generalized coordinate number for (a) Mode 1, (b) Mode 2, and (c) Mode 3.

The natural frequencies of the linear system follow the same pattern as the mode shapes. At a tuning ratio of 1, modes 1 and 2 have similar natural frequencies. As the tuning ratio is increased from 1, only the natural frequency of mode 2 is increased, whereas the natural frequencies of modes 1 and 3 remain relatively constant. Table 3.2 lists the natural frequencies of the modes for several tuning ratios.

Table 3.2. Natural Frequencies (rad/s)

Tuning Ratio	Mode 1	Mode 2	Mode 3
1.0	3.08	3.32	28.3
2.0	3.24	6.55	28.3
3.0	3.24	9.89	28.3
4.0	3.24	13.2	28.3

The steady-state response of the 3DOF system was obtained by simulating the system until the transient dynamics disappeared. Rather than using the peak displacement per cycle, the amplitude of the steady state response of each mass was described by its root-mean-squared (RMS) displacement:

$$X_{RMS} = \sqrt{\frac{1}{T} \int_{t_1}^{t_2} x^2 dt} \quad (3.12)$$

where  $T$  is some time duration in the steady-state and is given as  $T = t_2 - t_1$ . The time duration  $T$  is defined to be the last 5 periods of the forcing frequency at the end of each simulation. The RMS response was captured over a span of excitation frequency ratios,  $d$ , defined as  $d = \omega_d/\omega_1$ . To expedite the simulations, the end states of each steady-state response were used as the initial conditions for the next frequency ratio. Simulations were always terminated after an integer number of excitation periods had passed.

Figure 3.5 shows the RMS displacements of the 3<sup>rd</sup> mass as a function of excitation frequency ratio ( $d$ ) for four tuning ratios,  $r$ . This plot shows the presence of internal resonances when the excitation frequency is roughly one-third of the tuned natural frequency of the 3<sup>rd</sup> subsystem. For example, there is an internal resonance at an excitation ratio of 1.33 when the frequency ratio is 4.0. This phenomenon occurred at all

the tuning ratios except when  $r = 3.0$ . At this frequency ratio, the internal resonance would occur at  $d = 1.0$ , which is overshadowed by the resonance of the 1<sup>st</sup> subsystem. Also noticeable in Figure 3.5 are the internal resonances corresponding to one-fifth of the frequency ratio; e.g., the small peak at  $d = 0.6$  when  $r = 3$ . Lastly, the double peak near  $d = 1$  for the case  $r = 1$  is due to resonances of the 1<sup>st</sup> and 2<sup>nd</sup> modes being closely spaced together.

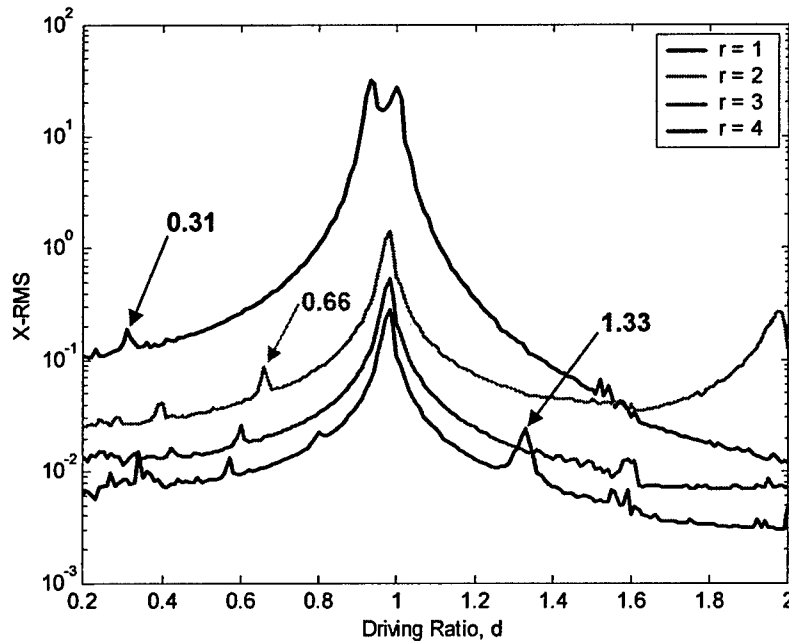


Figure 3.5. RMS displacement of the 3<sup>rd</sup> mass as a function of excitation frequency ratio.

An examination of the time histories of the steady-state responses revealed a significant amount of stick-slip of the 2<sup>nd</sup> mass. Thus, excitation at a single frequency is converted into multi-harmonic response by means of the friction nonlinearity. Under favorable tuning conditions, these higher harmonics excite internal resonances as

expected. In the following section, the extent to which subsystem tuning can lead to enhanced energy dissipation during free response is examined.

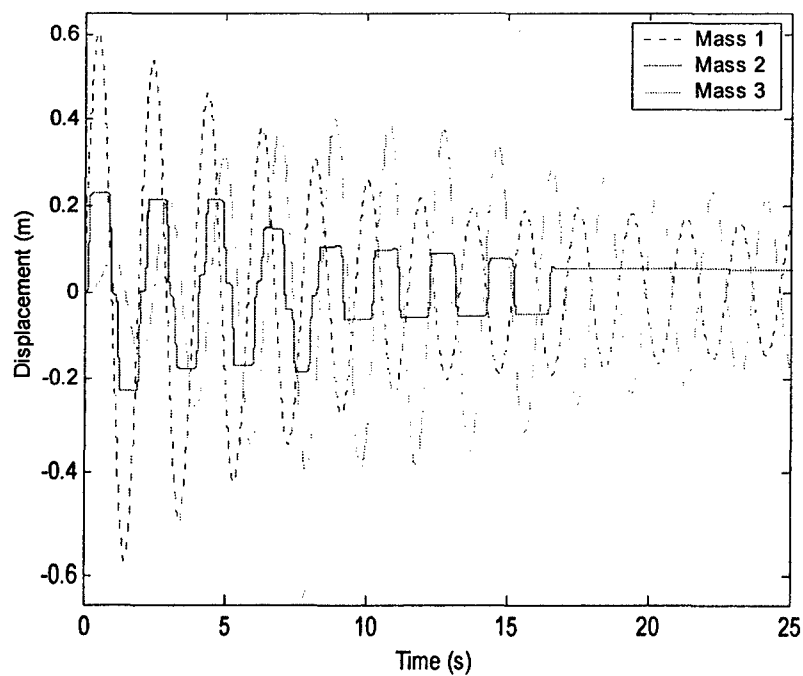
### 3.4 Free Vibration Response

The free vibration response of the 3DOF system was simulated to quantify the energy transfer from one subsystem to the other and from low frequencies to higher frequencies. Furthermore, it was important to understand under what states of excitation, friction level, and tuning of the 3<sup>rd</sup> subsystem did favorable conditions exist for maximum energy dissipation. To simulate the free response, the external force  $P(t)$  was set to zero and an initial velocity of 2.0 m/s was applied to mass 1.

Figure 3.6 shows a typical free response of the 3-DOF system for a normal force of 40 N and a tuning ratio of  $r = 1$ . While the displacement and velocity of the 1<sup>st</sup> mass decrease with approximately linear envelopes of decay, the 2<sup>nd</sup> mass shows periodic stick-slip behavior until it is completely stuck at a time of about 20 s. This stick-slip behavior is more evident in the velocity of the 2<sup>nd</sup> mass shown in Figure 3.6(b). The result demonstrates that there is a one-way transfer of vibratory energy from the 1<sup>st</sup> mass to the 3<sup>rd</sup> mass because once mass 2 is stuck, masses 1 and 3 oscillate like damped, isolated SDOF systems. Lastly, note that the free response of the 1<sup>st</sup> mass is similar to having a persistent, nearly harmonic excitation of masses 2 and 3 through the force in spring  $k_2$  and viscous damper  $c_2$ .

As shown in Figure 3.6, it is clear that there is a transfer of energy from the 1<sup>st</sup> mass to the 3<sup>rd</sup> mass. To quantify how much energy was transferred, it was necessary to look at the energies in the combined system as well as in the individual subsystems. Of

further interest was the energy transfer at frequencies higher than that of the fundamental frequency of the 1<sup>st</sup> mass. To accomplish this task, the 3<sup>rd</sup> subsystem was tuned for a range of tuning ratios,  $r$ . When the stick-slip motion excited a resonance of the 3<sup>rd</sup> subsystem, there would be a corresponding increase in displacement and velocity. This increased velocity would correlate to higher energy dissipation by the dampers connected to the 3<sup>rd</sup> mass. Therefore, by examining the energy dissipation in the 3-DOF system, one could quantify the amount of total energy transfer and the energy transfer at higher frequencies.



(a)

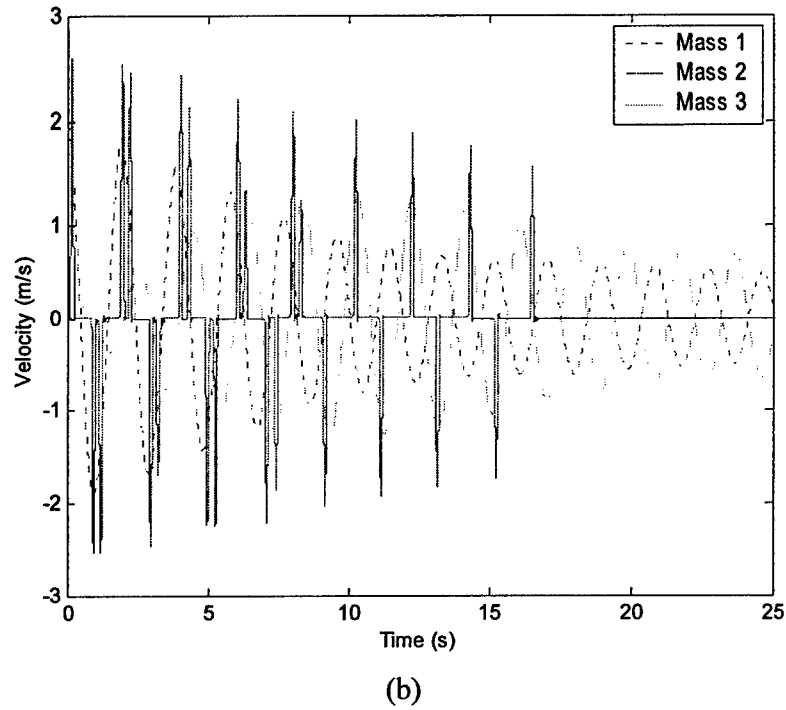


Figure 3.6. (a) Displacement and (b) velocity time histories of the 3-DOF system ( $N = 40N$ ,  $r = 1$ ).

### 3.5 Energy Dissipation

The total energy,  $E_{Total}$ , in the 3DOF system is defined as

$$E_{Total} = \frac{1}{2} \{y\}^T \begin{bmatrix} [K] & [0] \\ [0] & [M] \end{bmatrix} \{y\} \quad (3.13)$$

where  $[0]$  is a  $3 \times 3$  zero matrix. Therefore, the total energy dissipated,  $E_{dis}$ , is given by

$$E_{dis} = (E_{Total})_{t=0} - (E_{Total})_{t=t_f} \quad (3.14)$$

where  $t_f$  is the end time of the simulation. The total energy dissipated can be separated into the sum of the energy dissipated by viscous dampers and the energy dissipated by Coulomb friction. If the power dissipated by each viscous damper is denoted as  $P_i$ , the total dissipated energy can be expressed as

$$E_{dis} = \sum_{i=1}^4 \int_0^{t_f} P_i dt + (E_{dis})_{friction} \quad (3.15)$$

where

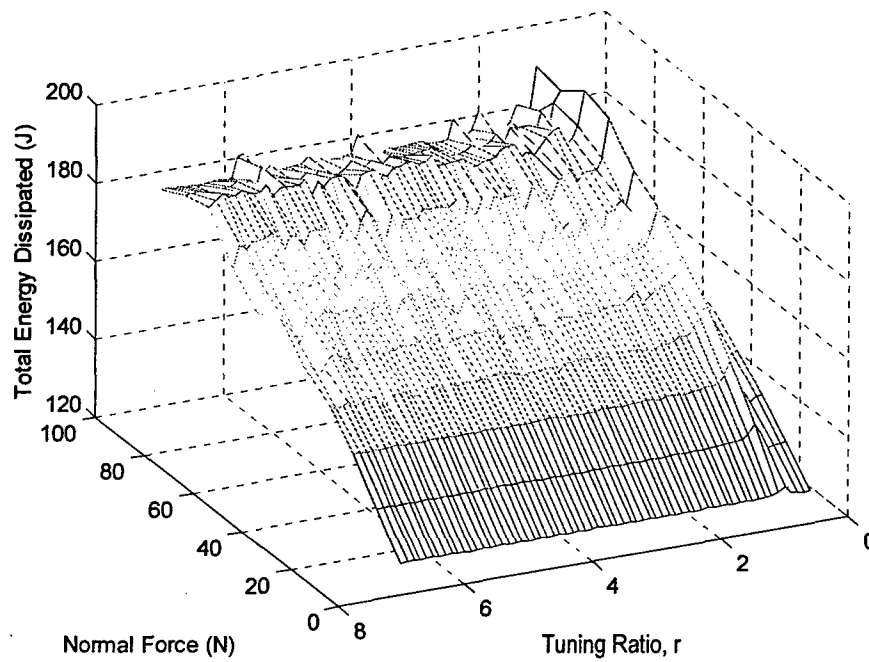
$$\begin{aligned} P_1 &= c_1 \cdot v_1^2 \\ P_2 &= c_2 (v_2 - v_1)^2 \\ P_3 &= c_3 (v_3 - v_2)^2 \\ P_4 &= c_4 \cdot v_3^2 \end{aligned} \quad (3.16abcd)$$

By (3.15), it is then possible to indirectly calculate the energy dissipated by friction.

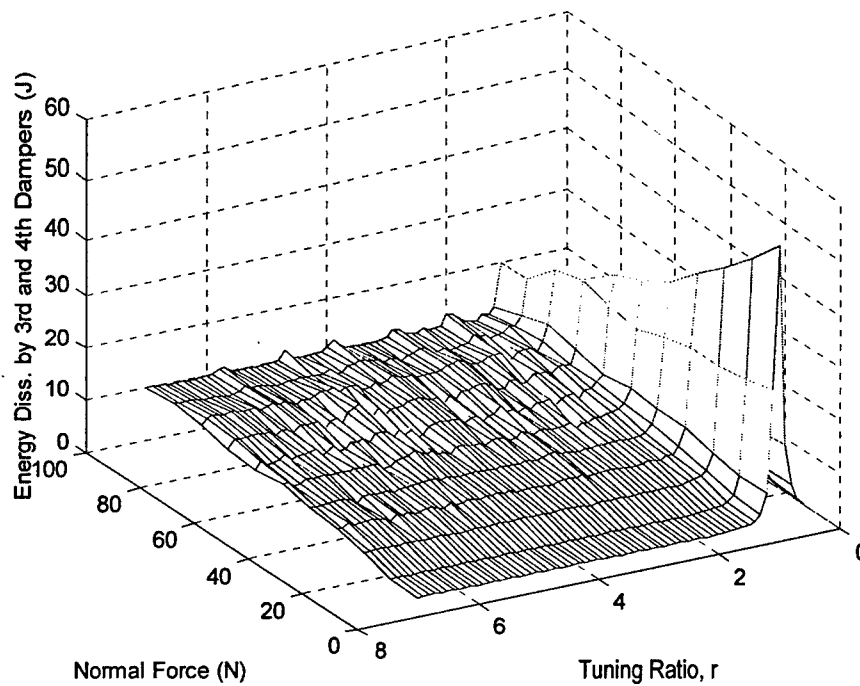
To find the optimal condition for friction to pump energy to higher frequencies, several factors were considered. The total energy of the system was evaluated as a function of the mass ratio ( $m_3/m_1$ ), the tuning ratio ( $r = \omega_3/\omega_1$ ), the normal force, and the simulation time. A mesh was used to visualize how the total dissipated energy varied as a function of two variables. For the meshes shown in Figures 3.7(a) and 3.7(b), the constant values are the mass ratio (0.5) and the simulation time (15.1 s). This simulation time corresponds to one-half of the time constant of the 1<sup>st</sup> subsystem, where the time constant =  $1/(\omega_1 \zeta_1)$ . The normal force is varied from 0 to 100 N, in increments of 10 N; and, the tuning ratio is varied from 0.6 to 8.0, in increments of 0.1. Figure 3.7(a) shows the total energy dissipated after 15.1 s of free response. There is a large peak near a tuning ratio of  $r = 1$ , but there are some smaller peaks as  $r$  is increased and  $N$  is greater than 80 N. To study this feature more closely, the energy dissipated by the 3<sup>rd</sup> and 4<sup>th</sup> dampers over the same time interval are examined, as shown in Figure 3.7(b).

From Figure 3.7(b), there is a large peak in dissipated energy near a tuning ratio of 1. This peak appears to be the result of a “vibration-absorber” effect. As the normal force increases, the absorber effect is less prominent and ripples in the energy dissipation

at higher tuning ratios can be seen. Finally, at  $N = 100$  N, there are definite peaks that are evident at certain tuning ratios. The peaks suggest that the force input to mass 3 excites a resonance, thereby causing greater energy dissipation.



(a)



(b)

Figure 3.7. Energy dissipated by the (a) entire system and (b) the 3<sup>rd</sup> and 4<sup>th</sup> dampers.

A slice of the mesh in Figure 3.7(b) at  $N = 100$  N is shown in Figure 3.8. This plot clearly shows five distinct peaks between the tuning ratios of 2 and 7. These peaks correspond to tuning ratios of  $r = 2.0, 2.9, 3.9, 4.7,$  and  $5.7$ . In other words, when tuned to these higher frequencies, the resonance of the 3<sup>rd</sup> subsystem was excited by the stick-slip motion of the 2<sup>nd</sup> mass. Therefore, friction on mass 2 pumps energy to higher frequencies. As mentioned previously, the natural frequencies of the 3<sup>rd</sup> subsystem and that of mode 2 in the linear (frictionless) system are closely related. In fact, the natural frequencies of the 3<sup>rd</sup> subsystem and that of mode 2 are nearly identical for tuning ratios above 1. Therefore, exciting a resonance of the 3<sup>rd</sup> subsystem is analogous to exciting the 2<sup>nd</sup> mode in the linear system.

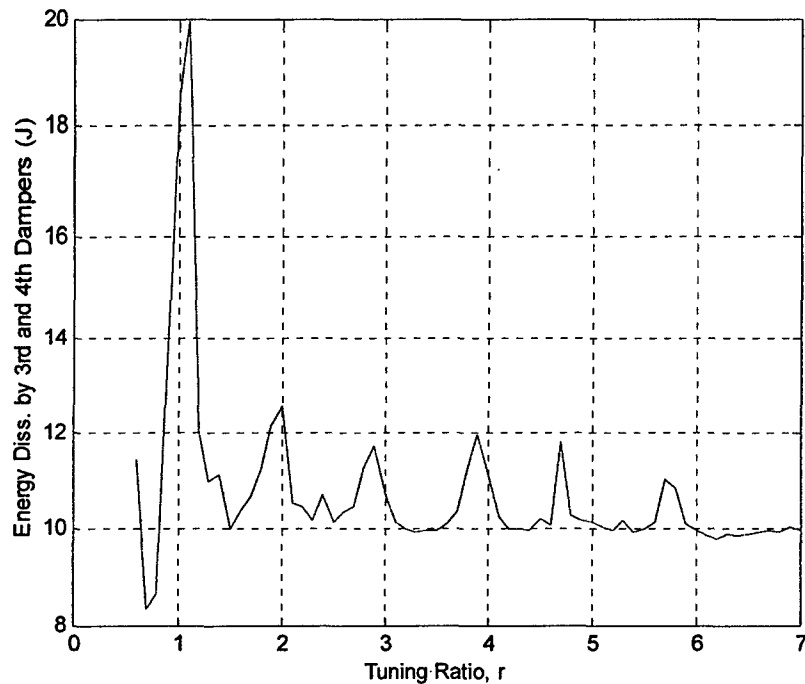


Figure 3.8. Energy dissipated by the 3<sup>rd</sup> and 4<sup>th</sup> dampers at  $N = 100$  N.

The result shown in Figure 3.8 is interesting because it does not agree with the result from the steady-state response. Although the peaks in Figure 3.8 appear in somewhat regular intervals, they do not occur at only odd harmonics of the frequency of free vibration of the 1<sup>st</sup> subsystem. This behavior could be attributed to the stick-slip motion during free response (see Figure 5(b)). Since the stick-slip lasts for a finite amount of time, the input into the 3<sup>rd</sup> subsystem looks like a series of impulses. The impulses have broad frequency content and can excite many frequencies.

To find the best condition for energy dissipation, the energy dissipated by the 3<sup>rd</sup> and 4<sup>th</sup> dampers was examined for different levels of normal force and mass ratios ( $m_3/m_1$ ). Figures 3.9 and 3.10 examine how the energy dissipated by the 3<sup>rd</sup> and 4<sup>th</sup> dampers varies with mass ratio and normal force, respectively. Simulation duration times

of longer than 15 s did not have a significant effect on the energy dissipation trends because permanent sticking occurred shortly after 15 s.

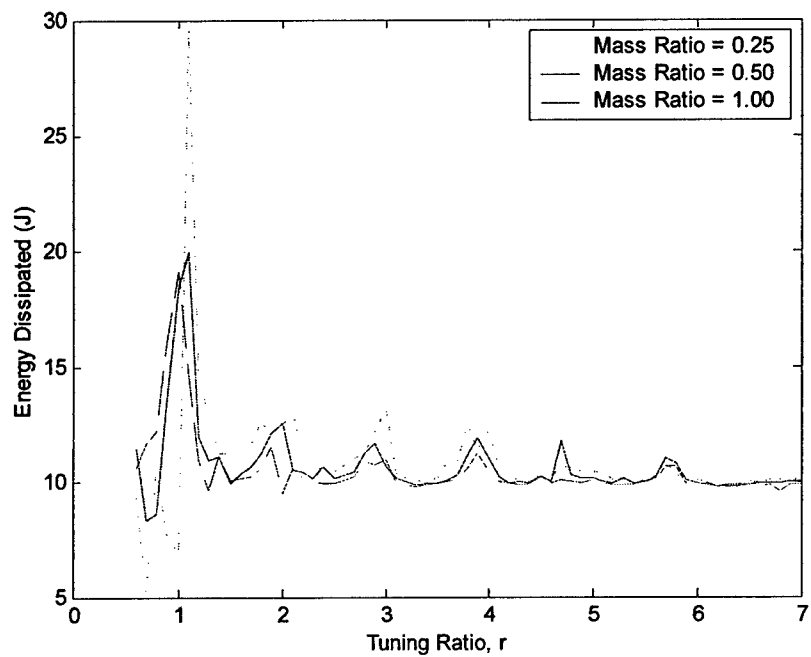


Figure 3.9. Energy dissipated by the 3<sup>rd</sup> and 4<sup>th</sup> dampers with varying mass ratios ( $N = 100$  N,  $t_f = 15.1$  s).

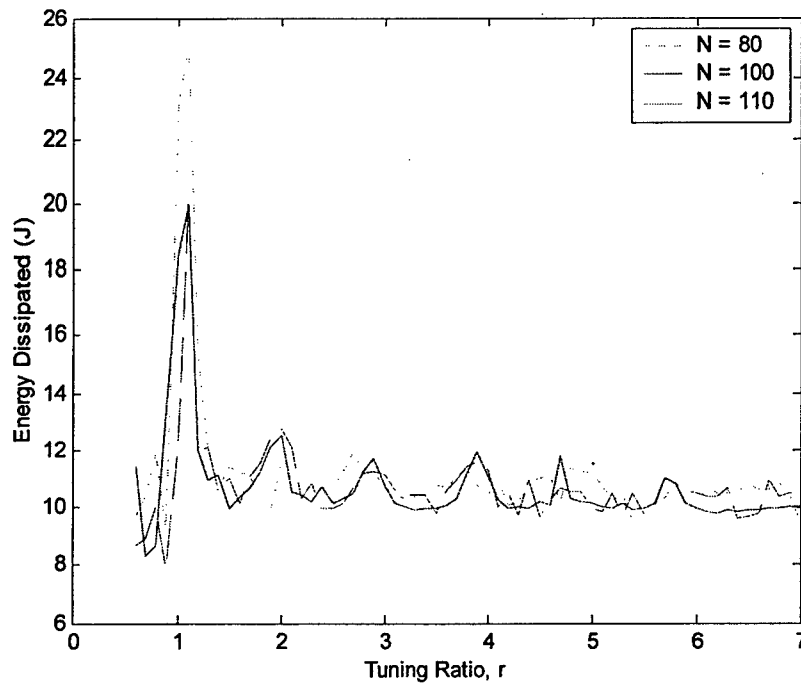


Figure 3.10. Energy dissipated by the 3<sup>rd</sup> and 4<sup>th</sup> dampers with varying  $N$  (mass ratio = 0.5,  $t_f = 15.1$  s).

Figures 3.9 and 3.10 show that the energy dissipation is sensitive to system parameters. In Figure 3.9, the peaks increase as the 3<sup>rd</sup> mass decreases. This trend is consistent with a vibration absorber, in which a smaller absorber mass leads to increased absorption over a smaller frequency range. At a mass ratio of 0.25, there is a sharp rise in the 1<sup>st</sup> peak. However, the 5<sup>th</sup> and 6<sup>th</sup> peaks are not as pronounced when compared to a mass ratio of 0.5. Similarly, a mass ratio of 1.0 does not produce noticeable peaks, except when  $r$  is near 1.

In Figure 3.10, the peaks at  $r = 1$  decrease as the normal force increases, as mentioned earlier. Similar to the mass ratio, the peaks at tuning ratios larger than 1 are best accentuated at a particular value. In this case, the value is a normal force of 100 N.

At normal forces above 110 N, mass 2 is completely stuck at all times for the initial condition considered here.

The previous results show that friction pumps energy to higher resonances, which serves to increase energy dissipation at the higher resonances. However, it is important to note that the majority of energy dissipation in the 3DOF system is due to friction on mass 2 and the dampers connected to the 1<sup>st</sup> mass, where the motion originated. For example, at a tuning ratio of 1.1, the energy dissipated by the 3<sup>rd</sup> and 4<sup>th</sup> dampers accounts for 11% of the total energy dissipated. At a tuning ratio of 2.0, the energy dissipated by the 3<sup>rd</sup> and 4<sup>th</sup> dampers accounts for 7% of the total energy dissipated.

Despite the modest amounts of energy dissipation attributed to the 3<sup>rd</sup> and 4<sup>th</sup> dampers, it is necessary to evaluate the advantage of the energy pumping phenomenon versus the case where friction is not present (normal force = 0). To make this comparison, the ratio of the energy dissipated by the 3<sup>rd</sup> and 4<sup>th</sup> dampers to the total energy dissipated was evaluated for the friction and non-friction cases. Table 3.3 summarizes the comparison when the normal force is 100 N versus 0 N at tuning ratios corresponding to the peaks in Figure 3.8. For the frictionless case, the energies dissipated are constant after an initial peak at a tuning ratio of 1.

Table 3.3. Percentage of Energy Dissipated by the 3<sup>rd</sup> and 4<sup>th</sup> Dampers to the Total Energy Dissipated

<b>Freq. Ratio</b>	<b>1.1</b>	<b>2.0</b>	<b>2.9</b>	<b>3.9</b>	<b>4.7</b>	<b>5.7</b>
<i>N</i> = 100 N	11	7.0	6.7	6.6	6.7	6.1
<i>N</i> = 0 N	42	2.7	2.7	2.7	2.7	2.7

Table 3.3 shows that there is greater dissipation for the friction case except when the tuning ratio is at 1.1. Although the advantage is small (about 4% of the total energy dissipated), this result demonstrates that the pumping of energy to higher resonances can serve as a tool for increased dissipation. As for the case where the tuning ratio is 1.1, there is greater dissipation by the 3<sup>rd</sup> and 4<sup>th</sup> dampers of the frictionless system; however, the total energy dissipation is greater in the system with friction. At this tuning ratio, the total energy dissipated by the frictionless system is 130.4 J, versus 189.7 J for the system with friction.

This investigation was admittedly simple in order to permit a more thorough understanding of the phenomenon. Specifically, the joint model was represented by simple SDOF subsystems. The next chapter applies the Stribeck friction model to a more complicated joint model. It is expected that the results seen in this study can be extended to higher order systems.

## CHAPTER 4

### ENERGY TRANSFER AND DISSIPATION: CONTINUOUS SYSTEM

Up to this point, the focus has been on the effects of friction in discrete systems. Because of the relative simplicity of the discrete systems, it is possible to thoroughly examine and understand the behavior and features of the frictional interface. Results from Chapter 3 suggest that a frictional interface can pump vibratory motion from one frequency to higher frequencies, thus exciting higher resonances. This chapter applies the concepts learned in Chapter 3 to a more complicated, and realistic, joint configuration. Similar to the analysis of the 3DOF system, the energy transfer and dissipation between subsystems connected by a frictional interface is explored in this chapter. In particular, the relationship between the tuning parameter and energy dissipation is examined.

Presented first is the model of the continuous beam system and the governing equations of motion. The beam dynamics are approximated using a finite modal (Ritz) series. Next, a state-space model is developed to simulate the response of the system. Following the development of the state-space model is an evaluation of the forced steady-state response of the beam alone, as well as the entire system. Afterwards, the energy transfer and dissipation between the subsystems during free response, as well as the controllability of the entire system are discussed. Finally, this chapter concludes with the sensitivity of the system to tuning parameters and friction laws.

#### 4.1 System Model

An improvement to the 3DOF joint model in Chapter 3 is shown in Figure 4.1. The jointed structure is represented by a cantilever beam connected to a SDOF spring-mass-damper system via a friction damper attachment. An advantage of this model over the 3DOF system is the “floating” joint configuration. This configuration means that the coupling between the two structures is through the frictional element itself. In contrast to the 3DOF system of Chapter 3, the two subsystems of the beam-mass system continue to interact, even when the interface is fully stuck. This configuration is more realistic for many types of structural connectors. Another advantage of this model is that, theoretically, the beam has an infinite amount of modes. Although a finite number of modes will be used in this study, the multi-mode property of the beam creates more complex interactions between the beam and the attached SDOF system.

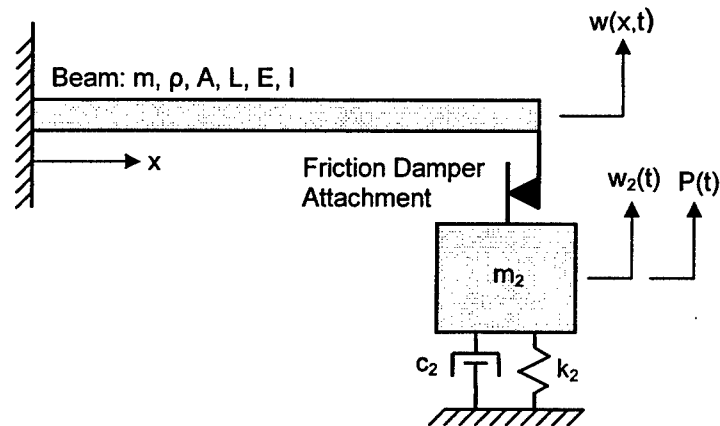


Figure 4.1. Beam-mass system model of a jointed structure.

The beam properties  $m$ ,  $\rho$ ,  $A$ ,  $L$ ,  $E$ , and  $I$  represent the mass, density, cross-sectional area, Young's Modulus, and moment of inertia, respectively. The parameter  $x$

denotes the displacement along the beam, with  $x = 0$  defined as the clamped end and  $x = L$  is at the friction attachment. Transverse displacement of the beam,  $w(x, t)$ , is a function of the spatial coordinate and time,  $t$ . For the attached SDOF system, the mass is  $m_2$ , the spring constant is  $k_2$ , the damper constant is  $c_2$ , and  $w_2(t)$  is the displacement. The function,  $P(t)$ , represents an external force applied directly to mass 2.

The friction attachment can be modeled as a pair of equal and opposite friction forces acting on the end of the beam and on mass 2. This friction force would be dependent on the relative velocity between mass 2 and the velocity at the end of the beam, defined as  $v_{rel} = \dot{w}_2(t) - \dot{w}(L, t)$ . Therefore, the friction force,  $F(v)$ , is given by

$$F(v) = \mu N \operatorname{sgn}(v_{rel}) \quad (4.1)$$

where  $N$  is the normal force and  $\mu$  is the Stribeck friction coefficient given by Equation (3.2). As in Chapter 3, the coefficient  $\alpha$  in Equation (3.2) is set to zero in this case as well. Furthermore, parameters for the friction model can be found in Table 3.1.

#### 4.1.1 Governing Equations

The governing equations of motion for the system shown in Figure 4.1 can be broken into two sets: a set of equations for the beam and a set for the attached SDOF system. For an unforced, uniform beam, the partial differential equation describing the flexural displacement is based on the Bernoulli-Euler model and is given by

$$EI \frac{\partial^4 w(x, t)}{\partial x^4} + \rho A \ddot{w}(x, t) = 0 \quad (4.2)$$

where  $\partial^n$  represents an  $n^{\text{th}}$  order partial derivative and the overdot represents a partial derivative with respect to time. The equation for the SDOF system is much simpler and is given by

$$m_2 \ddot{w}_2(t) + c_2 \dot{w}_2(t) + k_2 w_2(t) = P(t) - F(v). \quad (4.3)$$

The sign of the friction force in (4.3) is determined by examining a free body diagram of the system. Since  $v_{rel}$  is defined as the velocity of the mass minus the velocity at the end of the beam, the friction force must oppose the motion of the mass when  $v_{rel}$  is positive. At the end of the beam, this friction force acts in a positive (up) direction when  $v_{rel}$  is positive.

The solution to (4.2) can be approximated by a finite modal Ritz series

$$w(x,t) = \sum_{i=1}^{NM} z_i(t) \varphi_i(x) \quad (4.4)$$

where  $z_i(t)$  is the normal mode amplitude of the  $i^{\text{th}}$  mode,  $\varphi_i(x)$ , and  $NM$  is the number of modes. For a uniform cantilever beam, the normal mode is given by

$$\varphi_i(x) = \frac{1}{\sqrt{mL}} \left\{ \cosh \frac{\lambda_i x}{L} - \cos \frac{\lambda_i x}{L} - \left( \frac{\cosh \lambda_i + \cos \lambda_i}{\sinh \lambda_i + \sin \lambda_i} \right) \left( \sinh \frac{\lambda_i x}{L} - \sin \frac{\lambda_i x}{L} \right) \right\} \quad (4.5)$$

where  $\lambda_i$  is the  $i^{\text{th}}$  root of the characteristic equation

$$\cosh \lambda_i \cos \lambda_i + 1 = 0. \quad (4.6)$$

The first two nonzero roots of (4.6) can be found numerically and they are  $\lambda_1 = 1.8751$  and  $\lambda_2 = 4.6941$ . For  $i \geq 3$ , the root can be approximated by the asymptotic relationship

$$\lambda_i \approx \frac{2i-1}{2} \pi. \quad (4.7)$$

From the roots of the characteristic equation, the  $i^{\text{th}}$  natural frequency of the beam,  $\omega_i$ , is given by

$$\omega_i = \left( \frac{EI}{\rho AL^4} \right)^{1/2} \lambda_i^2. \quad (4.8)$$

The normal mode amplitudes,  $z_i$ , are governed by a set of 2<sup>nd</sup> order differential equations

$$\ddot{z}_i + 2\zeta_i \omega_i \dot{z}_i + \omega_i^2 z_i = F(v) \varphi_i(L) \quad (4.9)$$

where  $\zeta_i$  is the damping ratio for the  $i^{\text{th}}$  mode. Using orthogonality, it can be shown that the mode function,  $\varphi_i$ , is normalized such that the modal masses are unity. For a more thorough discussion of the equations of motion for a continuous beam, see References [20] and [40].

#### 4.1.2 System Properties

The properties for the beam system are given in Table 4.1. With the exception of the normal force, the values for the Stribeck friction model are the same as those used in the 3DOF system (see Table 3.1). The modal damping ratio,  $\zeta_i$ , is constant for all modes. As a note, the mass of the beam can be calculated by  $m = \rho AL = 0.636$  kg; and, the damper constant is calculated by  $c_2 = 2\xi_2 \sqrt{k_2 m_2}$ , where  $\xi_2$  is the prescribed damping ratio of the uncoupled mass-spring-damper system.

Table 4.1. Properties for the Beam-Mass System

Beam Properties	Value	Other	Value
$\rho A$	0.636 kg/m	$m_2$	1.0 kg
$L$	1.0 m	$k_2$	400 N/m
$E$	$7.3 \times 10^{10}$ N/m <sup>2</sup>	$\zeta_2$	0.01
$I$	$1.325 \times 10^{-10}$ m <sup>4</sup>	$N$	5 N
$\zeta_i$	0.01		

To better understand the beam system, it is useful to study the linear modes of each subsystem without the friction attachment. For the spring-mass subsystem, the undamped natural frequency,  $\omega_{n2}$ , is simply given by

$$\omega_{n2} = \sqrt{\frac{k_2}{m_2}}. \quad (4.10)$$

Later in this chapter, this frequency, also known as the tuning frequency, will be varied to study the energy dissipation in the entire system. For the beam, the undamped natural frequencies and mode shapes can be calculated using (4.8) and (4.5), respectively. Figure 4.2 shows the normalized mode shapes and natural frequencies for the first four modes of the beam.

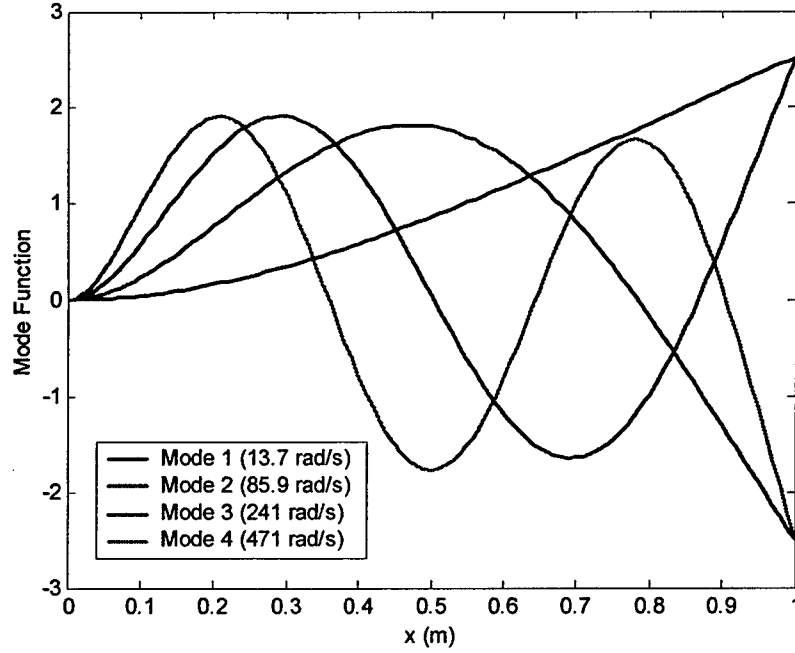


Figure 4.2. Mode function and natural frequencies for the cantilever beam.

#### 4.1.3 State-Space Formulation

Once the governing equations and properties for the beam system are established, a state-space formulation is used to simulate the system. The state-space contains both the modal coordinates,  $z_i$ , and the position coordinate of the attached mass,  $w_2(t)$ . Furthermore, the state vector contains the 1<sup>st</sup> time derivative of these coordinates as well. Therefore, the dimension of the state-space is  $2NM + 2$  and the state vector,  $\{q\}$ , is defined as

$$\{q\} = [z_1 \ z_2 \ \dots \ z_{NM} \ \dot{z}_1 \ \dot{z}_2 \ \dots \ \dot{z}_{NM} \ w_2 \ \dot{w}_2]^T. \quad (4.11)$$

With the state vector defined, the first-order, state-space equation can be expressed as

$$\{\dot{q}\} = [A]\{q\} + \{B\}F + \{\Gamma\}P \quad (4.12)$$

where  $[A]$  is the state matrix with dimension  $2NM + 2$ ,  $\{B\}$  is the state input vector associated with the friction force, and  $\{I\}$  is the state input vector associated with the external force. Notice that this equation is consistent with the form in (3.4) in Chapter 3; however, the variables are different in this case.

The state matrix,  $[A]$ , and state input vector,  $[B]$ , can be divided into sub-matrices and sub-vectors as follows

$$[A] = \begin{bmatrix} [A_B] & [0] \\ [0] & [A_M] \end{bmatrix}, \quad \{B\} = \begin{Bmatrix} \{B_B\} \\ \{B_M\} \end{Bmatrix} \quad (4.13)$$

where  $[A_B]$  and  $[A_M]$  are the state matrices for the beam and mass, respectively; and,  $\{B_B\}$  and  $\{B_M\}$  are the state input vectors for the beam and mass, respectively.

Correspondingly, the dimensions for  $[A_B]$  and  $\{B_B\}$  are  $2NM$ . For  $[A_M]$  and  $\{B_M\}$ , the dimension is 2. Lastly, the vector  $\{I\}$  is given by

$$\{I\} = [0 \dots 0 \ 1/m_2]^T. \quad (4.14)$$

The state matrix  $[A_B]$  can be further broken into diagonalized stiffness and damping matrices as follows

$$[A_B] = \begin{bmatrix} [0] & [I] \\ -[\tilde{K}] & -[\tilde{C}] \end{bmatrix}, \quad (4.15)$$

where

$$[\tilde{K}] = \begin{bmatrix} \omega_1^2 & 0 & \dots & 0 \\ 0 & \omega_2^2 & \dots & 0 \\ \vdots & \vdots & \ddots & \vdots \\ 0 & 0 & \dots & \omega_{NM}^2 \end{bmatrix}, \quad [\tilde{C}] = \begin{bmatrix} 2\zeta_1\omega_1 & 0 & \dots & 0 \\ 0 & 2\zeta_2\omega_2 & \dots & 0 \\ \vdots & \vdots & \ddots & \vdots \\ 0 & 0 & \dots & 2\zeta_{NM}\omega_{NM} \end{bmatrix}, \quad (4.16)$$

and  $[I]$  is the identity matrix. The dimension of the all the sub-matrices in (4.15) is  $NM$ .

The state input vector  $\{B_B\}$  is given by

$$\{B_B\} = [0 \dots 0 \ \varphi_1(L) \ \varphi_2(L) \dots \ \varphi_{NM}(L)]^T. \quad (4.17)$$

Finally, the state matrix,  $[A_M]$ , and state input vector,  $\{B_M\}$ , are defined as

$$[A_M] = \begin{bmatrix} 0 & 1 \\ -k_2/m_2 & -c_2/m_2 \end{bmatrix}, \quad \{B_M\} = -\begin{bmatrix} 0 \\ 1/m_2 \end{bmatrix}. \quad (4.18)$$

Since the state vector contains the modal coordinates, Equation (4.4) must be used to calculate the displacement of the beam. To calculate the velocity of the beam, (4.4) is differentiated with respect to time so that

$$\dot{w}(x, t) = \sum_{i=1}^{NM} \dot{z}_i(t) \varphi_i(x). \quad (4.19)$$

To calculate the friction force, the same switching algorithm used in Chapter 3 is used here (see Section 3.1). Following the steps outlined in Section 3.1, the relative velocity is given by

$$v_{rel} = \dot{w}_2(t) - \dot{w}(L, t) = \dot{w}_2(t) - \sum_{i=1}^{NM} \dot{z}_i(t) \varphi_i(L) = [T]\{q\} \quad (4.20)$$

where

$$[T] = [0 \dots 0 \ -\varphi_1(L) \ -\varphi_2(L) \dots \ -\varphi_{NM}(L) \ 0 \ 1]. \quad (4.21)$$

Similarly, the equivalent friction force,  $F_{eq}$ , in this case is

$$F_{eq} = -([T]\{B\})^{-1} [T]([A]\{y\} + \{\Gamma\}P). \quad (4.22)$$

## 4.2 System Simulation

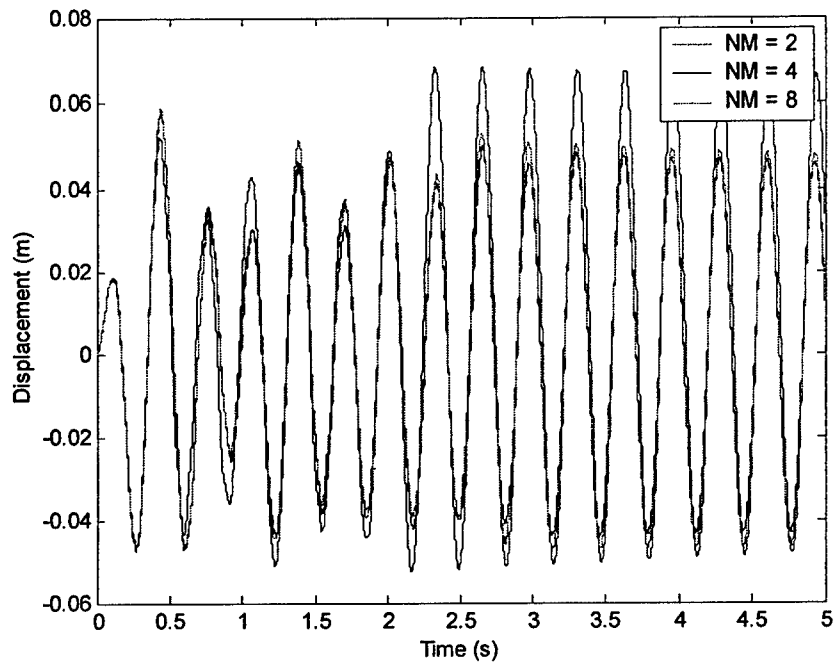
Initial simulation of the system of equations given by (4.12) was performed using the 4<sup>th</sup> order Runge-Kutta method with a fixed time step of  $5 \times 10^{-4}$  s. Not only does the accuracy of the solution hinge on the size of the time step, it also depends on the number

of modes,  $NM$ , used in the modal series. Theoretically, the approximate solution given by (4.4) approaches the true solution as  $NM$  approaches infinity.

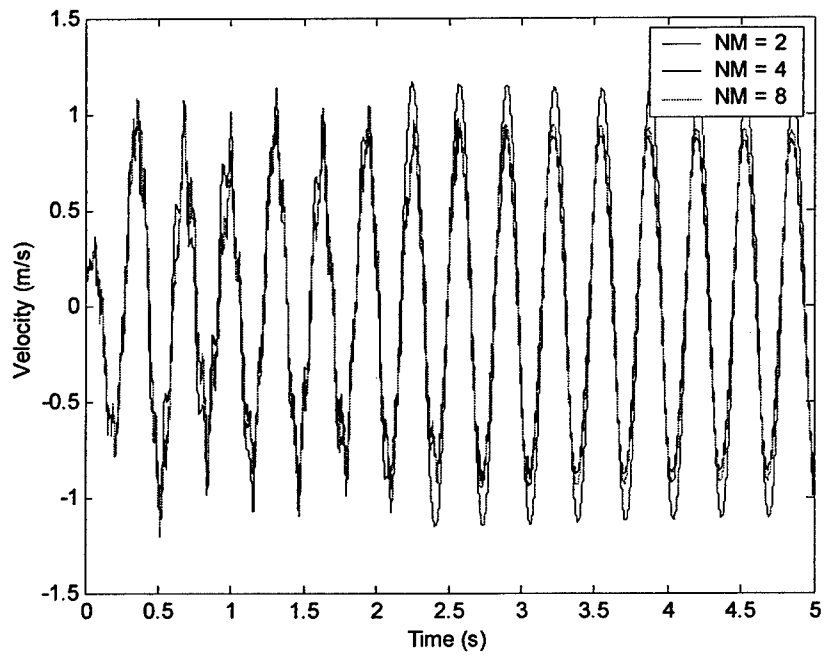
#### 4.2.1 Mode Number Convergence

A study was conducted to find out how many modes were necessary for the response of the beam to converge. Since the friction attachment is at the end of the beam, it was expected that the motion of the beam would be dominated by the first few modes. Figures 4.3(a) and 4.3(b) plots the response at  $x = L$  for several cases with different values of  $NM$ . The excitation was an initial velocity of 2.0 m/s applied onto the attached mass.

From the figures below, the responses using 2 modes is not accurate compared to the responses with 4 or 8 modes. However, the response using 4 modes accurately captures the response and there is little difference between using 4 modes and using 8 modes. Therefore, for the remainder of the studies in this Chapter, 4 modes are used to describe the beam dynamics.



(a)



(b)

Figure 4.3. (a) Displacement and (b) velocity response at  $x = L$  on the beam.

### 4.2.2 Steady-State Frequency Response

To gain insights into the beam system, the steady-state forced response was studied. First, the steady-state response of the beam without any attachments was examined. In this case, the forcing function,  $P(t)$ , is applied at the end of the beam and is given by

$$P(t) = W \sin(\omega_d t) \quad (4.23)$$

where  $W$  is the amplitude of the force and  $\omega_d$  is the driving frequency. Figure 4.4 shows the displacement magnitude of the frequency response function at the end of the beam ( $x = L$ ) for a driving frequency range of 5 to 100 rad/s. This range was selected because it captured the first two modes of the beam, which is the focus of further investigation in this chapter. From Figure 4.4, the 1<sup>st</sup> and 2<sup>nd</sup> modes of the beam at 13.7 and 85.9 rad/s, respectively, can be easily seen, as well as what appears to be a zero at 60.3 rad/s. In Figure 4.5, the phase angle of the response is shown. From this plot, the zero at 60.3 rad/s is confirmed because of the 180 degree phase shift near this frequency.

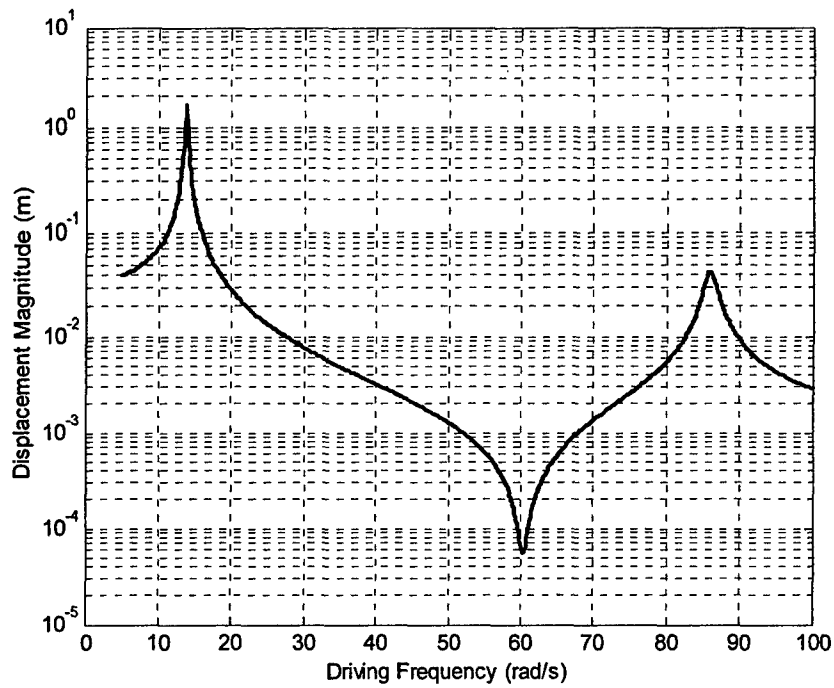


Figure 4.4. Magnitude of the frequency response of the beam at  $x = L$ .

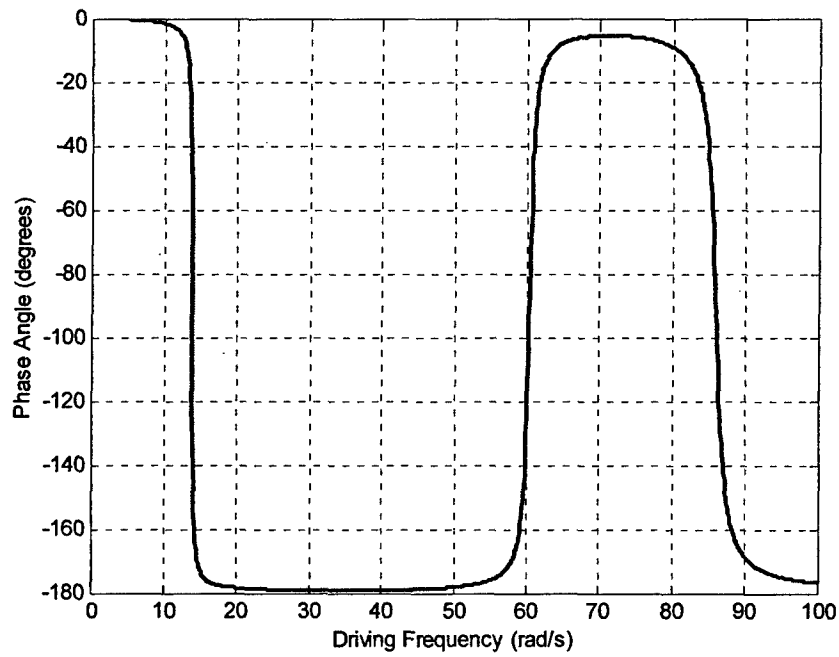


Figure 4.5. Phase angle of the response of the beam at  $x = L$ .

Once the steady-state response of the beam was characterized, the frequency response of entire beam system was evaluated. The forcing function given by (4.23) is now applied to the attached mass, as seen in Figure 4.1. Again, the response was evaluated at the end of the beam, where the friction damper is attached. For the case shown in Figures 4.6 and 4.7, the natural frequency of the attached SDOF system,  $\omega_{n2}$ , was tuned to 50 rad/s so that it was well separated from the modes of the beam. Like the 3DOF system, tuning was accomplished by keeping the mass of the SDOF system,  $m_2$ , constant while changing  $k_2$  such that

$$k_2 = m_2 \omega_{n2}^2. \quad (4.24)$$

This tuning parameter will be of greater importance in the next section.

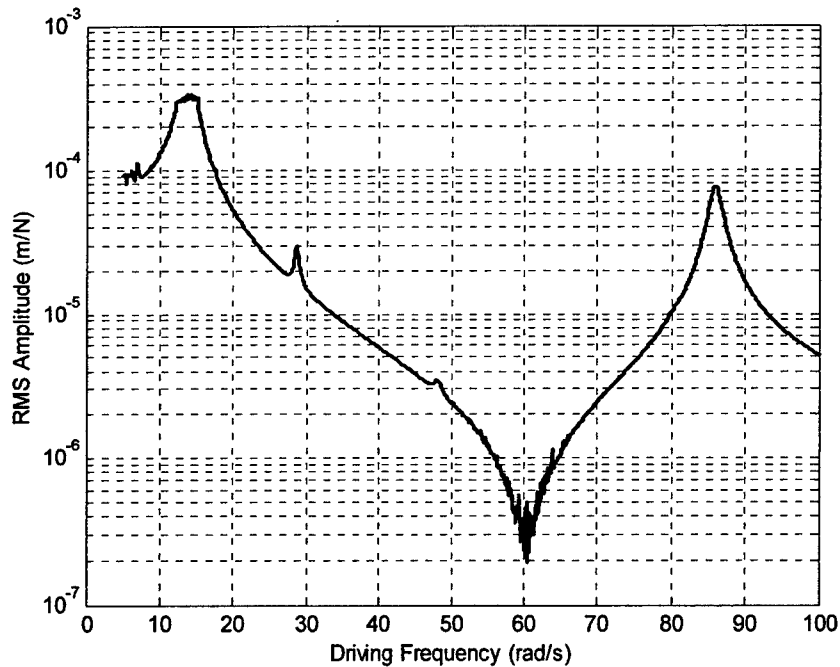


Figure 4.6. RMS Displacement frequency response of the beam system at  $x = L$ .

There are several interesting features about the frequency response of the beam in Figure 4.6. The first feature is the noisy areas of the plot, especially around the null in the vicinity of 60.3 rad/s. This problem can be attributed to a relative lack of precision in the switching algorithm caused by a coarse time step. The noisy areas diminish as the time step is reduced. Secondly, there is a flat top in the response in the region of the 1<sup>st</sup> mode of the beam (13.7 rad/s). This is caused by a variation in the resonant frequency as different levels of slip occur. If the interface is almost stuck, the beam-mass system will exhibit a resonance at a frequency somewhat lower than the first beam natural frequency. However, if excited at that resonance, the interface will break free, thereby adding damping while disrupting the resonance. This phenomenon creates a saturation-like appearance in this region. Lastly, the most important effect is the presence of internal resonances in the frequency response. In Figure 4.6, there is an internal resonance at 28.6 rad/s, corresponding to 1/3 of the frequency of the 2<sup>nd</sup> mode of the beam (85.9 rad/s). Also noticeable is a small internal resonance peak at 48.1 rad/s, or 1/5 of the frequency of the 3<sup>rd</sup> mode of the beam (241 rad/s). The presence of the internal resonances is much more evident in the modal response of the beam. Figure 4.7 shows the frequency response of the decoupled modal coordinates,  $z_i$ , of the beam. Aside from the noisy region around the 1<sup>st</sup> mode of the beam, the presence of internal resonances for each mode is clear. Each peak corresponds to an odd harmonic of the natural frequency of the particular mode, for example 1/3, 1/5, 1/7, etc.

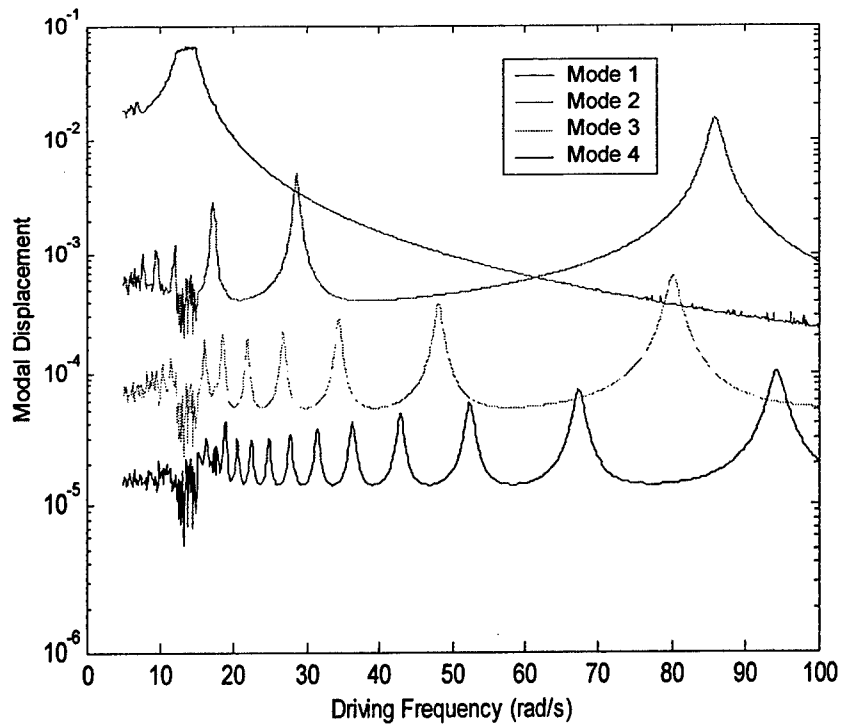


Figure 4.7. Modal displacement response of the beam system.

The appearance of internal resonances suggest that the friction damper in the beam-mass system pumps energy to higher modes, i.e., the friction nonlinearity converts excitation at one frequency into a multi-harmonic excitation. The next section examines how tuning the SDOF system to the internal resonances can affect the energy dissipation in the free response of the system.

### 4.3 Energy Dissipation

The energy dissipation of the beam-mass system was evaluated by observing the free response of the system. Excitation to the system was an initial velocity of 2.0 m/s applied onto the attached mass while the external force,  $P(t)$ , was set to zero. To isolate the energy dissipation to the beam and the friction damper, the viscous damper attached

to the mass,  $c_2$ , was set to zero as well. Lastly, the energy dissipated was evaluated after a time,  $tf$ , equal to 10 natural periods of the 1<sup>st</sup> mode of the beam. This time is approximately 4.6 s.

#### 4.3.1 System Energies

The energy dissipated in the system can be calculated by taking the initial system energy minus the system energy after  $tf$  seconds. Since the excitation is an initial velocity, the initial system energy,  $(E_{Total})_{t=0}$ , is therefore

$$(E_{Total})_{t=0} = \frac{1}{2} m_2 \dot{w}_2^2(t=0) \quad (4.25)$$

where  $\dot{w}_2(t=0)$  is the initial velocity. At any other time, the total energy in the system is the sum of the beam energy,  $E_{beam}$ , and the energy of the attached mass system,  $E_{mass}$ .

The beam and mass energies are composed of the kinetic and potential energies as follows:

$$E_{beam} = \frac{1}{2} \sum_{i=1}^{NM} \dot{z}_i^2 + \frac{1}{2} \sum_{i=1}^{NM} \omega_i^2 z_i^2 \quad (4.26)$$

$$E_{mass} = \frac{1}{2} m_2 \dot{w}_2^2 + \frac{1}{2} k_2 w_2^2. \quad (4.27)$$

Therefore, the total dissipated energy after  $tf$  seconds is given by

$$E_{dis} = (E_{Total})_{t=0} - (E_{beam} + E_{mass})_{t=tf}. \quad (4.28)$$

The energy dissipated in the system was evaluated as a function of the tuning frequency, or  $\omega_{n2}$ . Similar to the analysis of the 3DOF system in Chapter 3, the purpose of varying the tuning frequency was to determine favorable tuning conditions to maximize energy dissipation in the system. In particular, at what values of tuning

frequency and normal force would there exist a “sweet spot” where the energy dissipation is maximum? Intuitively, this sweet spot should occur when the tuning frequency is at an internal resonance of the system. If the tuning frequency is near a resonance of the beam, then the relative motion between the beam and mass would be small, thus causing the friction damper to be stuck. In this case, the majority of energy dissipation will be through the modal damping of the beam. Conversely, if the tuning frequency is far from a beam resonance, significant sliding should occur between the beam and the mass and energy dissipation would be primarily due to friction. However, if the tuning frequency is equal to that of an internal resonance, then both the modal damping in the beam and the friction would contribute to the energy dissipation. In this scenario, energy would be pumped to a higher mode in the beam, thus causing the energy to be dissipated faster. Also, since the beam is vibrating at an odd harmonic above the frequency of the mass, the motion between the two systems should be out of phase. This motion should induce slip in the friction damper, thus dissipating energy.

To explore the effects of tuning, the energy in the system was evaluated as a function of the tuning frequency and the normal force at the friction damper. Figure 4.8 shows a mesh of the total energy *remaining* after 4.6 s of free response. This parameter was chosen because it was easier to visualize than a mesh of the total energy dissipated. For the mesh shown in Figure 4.8, the high values indicate poor energy dissipation while low values signal good energy dissipation. The range for the tuning frequency and normal force are 5 to 100 rad/s and 1 to 10 N, respectively.

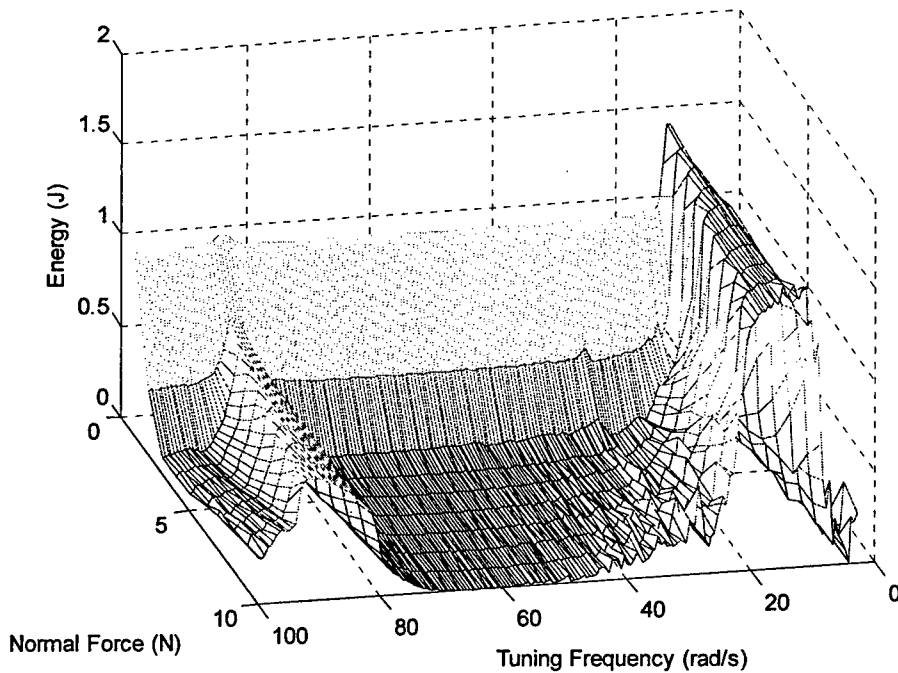


Figure 4.8. Total system energy after 4.6s of free response.

From Figure 4.8, it is clear that the poorest energy dissipation occurs when the tuning frequency is near natural frequencies of the beam modes. However, a surprising result is that the energy dissipation when the tuning frequency is at an internal resonance (28.6 rad/s) is worse than the energy dissipation when the system is completely mistuned. There are peaks in the energy at the internal resonance, especially as the normal force increases. On the other hand, the area around 60 rad/s stays relatively flat above  $N = 2$  and is the lowest point in the mesh.

The results suggest that friction plays the dominant role in dissipating energy in the system. From Figure 4.4, there is a zero in the beam-end frequency response function at 60.3 rad/s. At this frequency, there is very little motion at the end of the beam, thus facilitating sliding of the frictional interface and maximizing the work done by the

friction force. At 28.6 rad/s, some of the energy is transferred to the 2<sup>nd</sup> mode of beam via stick-slip motion. Although there is a slight increase in the energy dissipated by the modal damping of the beam, the energy dissipation provided by the friction damping is still dominant, especially given the small modal damping ratios used in this study. Another way to interpret these results is by examining the controllability of the beam-mass system.

#### 4.3.2 Controllability of the Beam-Mass System

Controllability is defined as the ability of an input to transfer the state vector of a system from any initial value to any final value in finite time [41]. In other words, controllability is a measure of whether or not the state-space equation can be controlled from the input. In the case of the beam-mass system, there is no “control input” *per se*, but we are interested to know the degree to which the friction force acting between the beam’s end and the mass  $m_2$  can effectively remove energy from the system. Treating the friction force as a control input, and setting the external disturbance  $P(t)$  to zero, equation (4.12) reduces to

$$\{\dot{q}\} = [A]\{q\} + \{B\}F \quad (4.29)$$

To investigate the controllability of (4.29), it is assumed that  $F$  can attain any functional form. In reality, however, it is limited in magnitude and can only oppose the relative motion during slip. Since (4.29) is linear and time-invariant, a simple test exists to determine controllability [41]. According to linear system theory, the system is controllable if and only if the controllability matrix,  $\Lambda$ , has full rank:

$$\Lambda = [B \ AB \ A^2B \ \dots \ A^{n-1}B] \quad (4.30)$$

where  $n$  is the dimension of the state and input matrices,  $n = 2(NM+1)$ . Thus, (4.29) is controllable if and only if  $\Lambda$  has  $n$  linearly independent columns. Note that the first column of  $\Lambda$  is the input vector  $\{B\}$ , and each subsequent column amounts to  $[A]$  times the previous column.

Initial attempts to compute  $\Lambda$  were unsuccessful because of numerical overflow/underflow problems, which were tied to the relative disparity in the size of the elements of the  $A$  matrix. To alleviate this problem, each column of the  $\Lambda$  matrix was normalized prior to multiplication by  $[A]$ . This operation alleviates the roundoff errors, while preserving the column space of the  $\Lambda$  matrix.

While the rank of  $\Lambda$  determines whether or not the system is controllable, the *degree to which the system is controllable* can be quantified by the condition number of  $\Lambda$ . The condition number of  $\Lambda$  can be defined by:

$$\text{cond}(\Lambda) = \|\Lambda\| \cdot \|\Lambda^{-1}\| = \sigma_{\max} / \sigma_{\min} \quad (4.31)$$

where  $\sigma_{\max}$  and  $\sigma_{\min}$  are the maximum and minimum singular values of  $\Lambda$ , respectively. If the columns of  $\Lambda$  are orthogonal,  $\text{cond}(\Lambda) = 1$ . As the linear independence of the columns of  $\Lambda$  degrades, the condition number of  $\Lambda$  will get larger and larger. If the columns of  $\Lambda$  become linearly-dependent,  $\text{cond}(\Lambda) = \infty$ , indicating a loss of rank. In practical terms, if  $\text{cond}(\Lambda)$  is high, it indicates that high magnitudes of control force will be necessary to reach various points in the state space. This has increased significance in the beam-mass system under consideration because the control input in this case is the friction force, which has bounded magnitude.

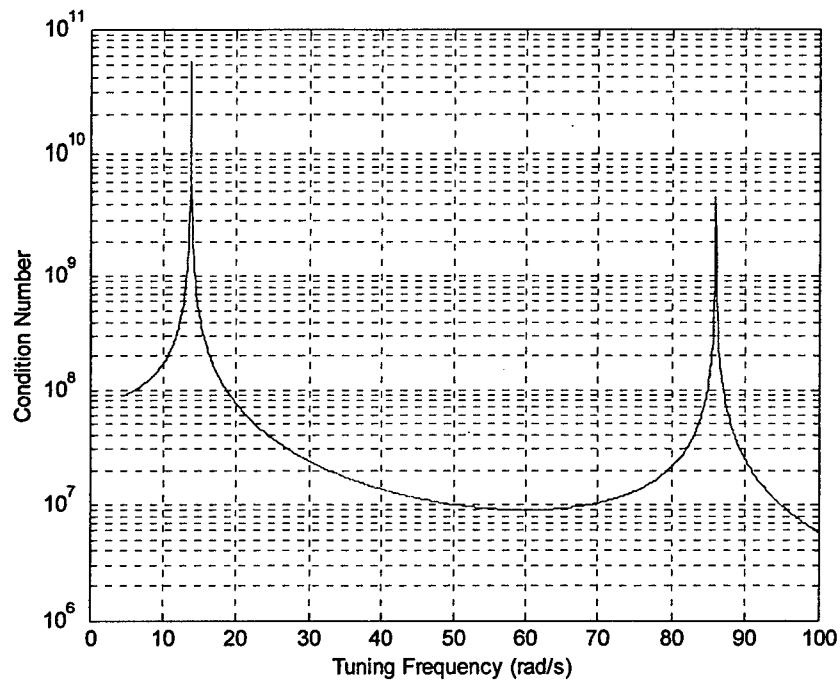


Figure 4.9. Condition number of the controllability matrix versus tuning frequency.

Figure 4.9 shows the condition number of  $\Lambda$  for tuning frequencies between 5 and 100 rad/s. Qualitatively, the figure shows relatively poor controllability when the tuning frequency coincides with a natural frequency of the beam. This indicates that it is more difficult for the friction force to affect the dynamics of the system at these tuning frequencies. Therefore, the friction force does less work and has poor energy dissipation capabilities. On the other hand, the condition number is lowest at a tuning frequency of 59.9 rad/s. At this frequency, the control input has the most control over the dynamics of the system; therefore, the friction force has the greatest potential to damp out the system response. The reason why 59.9 rad/s is associated with high energy dissipation can be found by looking at the phase angle in Figure 4.5. This frequency is just to the left of the zero phase angle associated with the zero at 60.3 rad/s. At 59.9 rad/s, the phase

difference between the response of beam and the input, coupled with the small response of the beam, contribute to high slip in the friction interface and maximizes the work done by the friction force. Similarly, frequencies just to the right of 60.3 rad/s can also contribute to high energy dissipation because of the phase difference.

For the most part, the controllability result is consistent with the results shown in Figure 4.8. However, controllability only applies to linear systems and this method cannot predict the nature of the system at the internal resonances. Furthermore, the friction force is not fully variable, but must follow the Stribeck relation given in (4.1). Only a full simulation of the nonlinear system can reveal the entire story. The next section describes the sensitivity of the nonlinearities to the tuning frequency and friction law.

#### **4.4 Sensitivity of the Beam-Mass System**

The previous section shows that energy dissipation is poor when the tuning frequency is near the beam frequencies and the best energy dissipation occurs when the beam and mass systems are mistuned. This behavior stands in contrast with that of the 3DOF system in Chapter 3. In Chapter 3, the best energy dissipation occurred when one of the subsystems was tuned to the natural frequency of another subsystem (or a harmonic thereof). This difference of results illustrates an important point – that the behavior of frictional systems is highly sensitive, and that results vary considerably depending on the system model. Therefore, this section explores the sensitivity of the energy dissipation results to the tuning parameter and the nature of the friction law.

#### 4.4.1 Sensitivity to Tuning Parameter

To analyze the sensitivity of the energy results, a slice of the mesh in Figure 4.8 was examined. This slice, shown in Figure 4.10, is the total system energy remaining after 4.6 s of free response for a constant normal force of 10 N. The point of least energy remaining (or most energy dissipated) appears to be to the right of the zero at 60.3 rad/s. Displayed on a semi-log scale, Figure 4.10 appears very noisy, especially at low energy levels. To determine whether this feature was an artifact of the simulation method or an actual characteristic of the system, the time histories at different tuning ratios were examined.

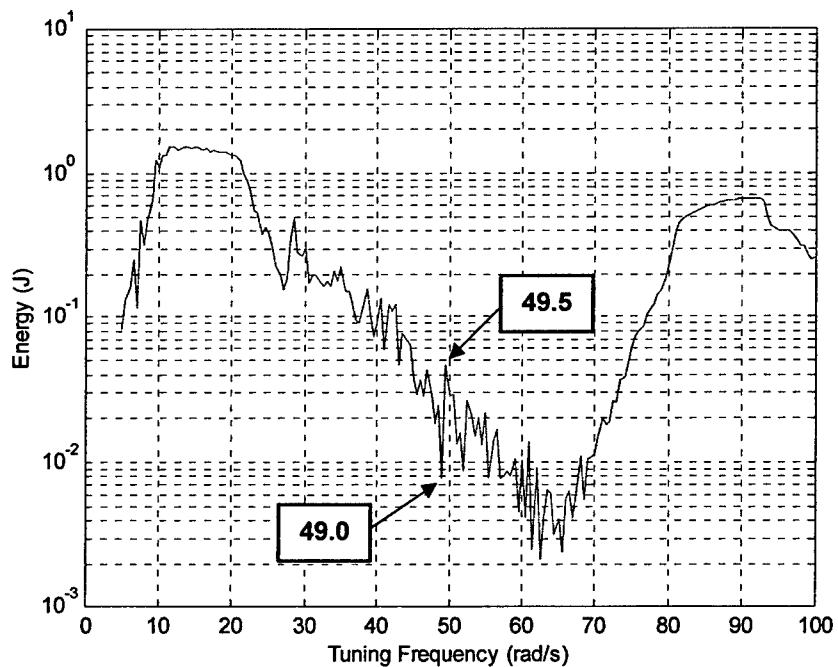


Figure 4.10. Total system energy as a function of tuning frequency for  $N = 10$  N.

The time histories of two adjacent points at tuning frequencies of 49.0 and 49.5 rad/s were studied. These points were selected because there is a relatively large difference in energy between them (see Figure 4.10). Figure 4.11 shows the time histories of the relative displacements between the end of the beam ( $x = L$ ) and the attached mass for the two tuning frequencies. From this plot, it is evident that a noticeable difference in the time response of the system exists despite the fact that only one system parameter was varied slightly. The difference between a system with a tuning frequency of 49.0 rad/s versus 49.5 rad/s is a 2% increase in the spring stiffness,  $k_2$ . Figure 4.11 also shows why there is more energy remaining at 49.5 rad/s than at 49.0 rad/s. For a tuning frequency of 49.5 rad/s, the relative displacement is constant beyond  $t = 1.5$  s, indicating that the friction interface becomes stuck. However, when the tuning parameter is set to 49.0 rad/s, the friction interface goes through another half-cycle of stick-slip before becoming completely stuck, thereby dissipating more energy.

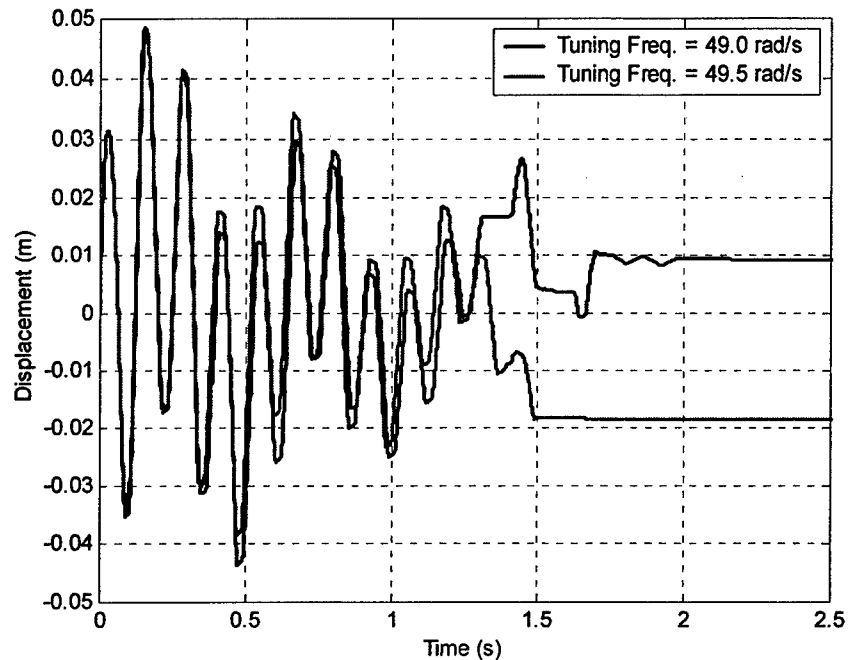


Figure 4.11. Relative displacement versus time for two tuning frequencies.

#### 4.4.2 Sensitivity to Friction Laws

Although the Stribeck friction model is used in this case, it is instructive to see how the system behavior changes with differences in the friction law characteristics. The cases that were evaluated were an equivalent viscous damper and a frictional interface with a simple Coulomb friction law. The friction force for the Coulomb law is exactly as is given by (4.1), except that the coefficient of friction is constant with slip velocity. For this analysis, the friction coefficient of the Coulomb model is equal to the dynamic friction coefficient of the Stribeck law. These cases were chosen because they represent more simple models of a frictional interface.

The value of the equivalent viscous damper can be derived from expressions of energy dissipated over one cycle of motion [21]. The purpose is to identify a viscous

damping constant that approximates the energy loss per cycle by a friction damper.

Assuming harmonic motion, the energy dissipated by the viscous damper is equated to the energy dissipated by a friction damper over one period. The energy dissipated by a viscous damper,  $(E_{dis})_{vis}$ , over one cycle of oscillation is given by

$$(E_{dis})_{vis} = \int_0^{(2\pi/\omega)} c_{eq} \dot{y}^2 dt \quad (4.32)$$

where  $c_{eq}$  is the damper constant,  $\omega$  is the frequency of oscillation, and  $y$  is the assumed harmonic displacement with amplitude  $Y$  and frequency  $\omega$ . Therefore, the time derivative of  $y$  is

$$\dot{y} = Y\omega \cos(\omega t). \quad (4.33)$$

Substituting (4.33) into (4.32) and integrating results in

$$(E_{dis})_{vis} = c_{eq} Y^2 \omega^2 \int_0^{(2\pi/\omega)} \cos^2(\omega t) dt = c_{eq} Y^2 \omega \pi. \quad (4.34)$$

The energy dissipated over one cycle by a friction damper can be shown to be

$$(E_{dis})_{fric} = 4Y\mu N, \quad (4.35)$$

therefore, equating (4.35) and (4.36) and solving for  $c_{eq}$  results in

$$c_{eq} = \frac{4\mu N}{\pi\omega Y}. \quad (4.36)$$

From (4.36), the damping constant is a function of the frequency and amplitude of motion. In this case, the viscous damper was chosen to approximate the damping done by the friction damper when the tuning frequency is at 13.7 rad/s. The friction coefficient used was the dynamic coefficient.

The system energies remaining after 4.6 s of free response are compared in Figure 4.12 for the viscous damping, Coulomb, and Stribeck cases. From this plot, two

differences between the viscous and the friction dampers are apparent. First, the peaks corresponding to excitation of the beam modes are much more narrow for the viscous damper case than the friction cases. The broad peaks in the friction cases are due to the saturation-like feature discussed in Section 4.2.2. Secondly, unlike the friction dampers, the system with the viscous damper shows no pronounced minimum near a tuning parameter of 60.0 rad/s.

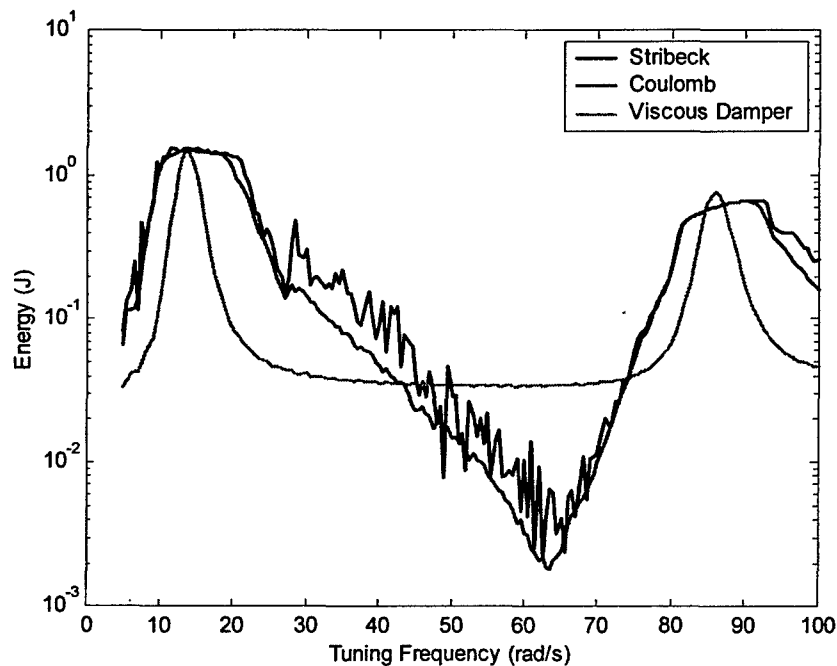


Figure 4.12. Total energy remaining after 4.6s versus tuning frequency for different friction laws.

The differences between the dry friction laws are more subtle. In the vicinity of the peaks, the two friction laws agree well. However, as the energy decreases, the Stribeck case fluctuates much more than the Coulomb case. This lack of fluctuations in the Coulomb case is due to the constant friction coefficient, which allows for sticking to

take place more consistently as the tuning parameter is varied. In the Stribeck case, the friction coefficient changes rapidly when the velocity is small, therefore, the point when the friction interface sticks is more sensitive to changes in the system. Furthermore, since the friction coefficient for the Coulomb case is the dynamic coefficient (which is smaller than the static coefficient), more sliding is allowed, thus more energy is dissipated.

Lastly, the Stribeck case picks up the effects of the internal resonance at 28.6 rad/s, as seen by a spike at this frequency in Figure 4.12. However, any indication that an internal resonance is present in the Coulomb case is negligible.

As the results show, the behavior of the beam-mass system varies greatly with system parameters. In particular, the complexity of the frictional interface significantly affects the dissipated energy. For some applications, using a viscous damper to approximate a frictional interface may be appropriate. However, accurate simulations of precision space structures (as discussed in Chapter 1) require greater modeling detail. The Stribeck model revealed dynamics and mechanisms of energy transfer that the other methods did not exhibit. Certainly, the Stribeck model is not the best friction model by any means. The purpose of this study was not to show that the Stribeck case is better than the others, but to show the importance of selecting an appropriate friction law to model a given system.

## CHAPTER 5

### SUMMARY AND CONCLUSIONS

The purpose of this thesis is to explore two aspects of modeling the behavior of joint friction in structures. The first aspect deals with the accurate and efficient simulation of a simple system that incorporates an advanced friction law. Energy transfer and dissipation in a structural joint model is the second topic of this thesis. Motivation for this study stems from the need to have accurate models of high-precision space structures. Because friction at connecting joints plays a major role in the dynamics of the structure, a good understanding of this mechanism is necessary to predict the vibratory response of the structure.

#### 5.1 Summary

The nature of the friction law can have a significant impact on the behavior of a jointed structure. Good friction models are desirable to predict the dynamic response of a structure, and a wide variety of friction laws have been proposed to date. However, it is well known that frictional systems are numerically difficult to simulate. Chapter 2 addresses these issues by simulating a simple system with a frictional interface modeled using the LuGre friction law. The LuGre friction law is chosen because it incorporates many characteristics of other friction models. The main purpose of Chapter 2 is to analyze the dynamics of the frictional system and to determine the best and most efficient numerical method to simulate the system.

To analyze the behavior of the frictional system, a SDOF spring-mass system sliding against a fixed surface was considered. The equations of motion for this system were converted to a nondimensional form for convenience as well as to prevent round-off errors in the calculations. The spring-mass system was analyzed by observing the linearized dynamics of the entire system as well as the time constant of the LuGre model alone. The analysis showed that the friction dynamics can be very fast and therefore numerically stiff during periods of high slip velocity. Furthermore, the dynamics changed rapidly at stick-slip transitions. It was found that the system dynamics were relatively well-conditioned during periods of sticking, which stood in contrast to the standard behavior of other friction models.

To determine the best and most efficient simulation method for the SDOF system, explicit and implicit time integration methods were considered. In general, the explicit methods required smaller time steps than the implicit methods. Consequently, this requirement led to longer simulation times as well as a larger number of integration steps. However, the explicit methods performed better in terms of accuracy. Attempts to reduce the simulation time by varying the time steps performed poorly for both explicit and implicit methods. This poor performance was attributed to a slight time shift in the solution, which caused relatively large errors. The best simulation methods were found to be the explicit Runge-Kutta and implicit Radau-IIA methods with constant time steps of  $10^{-3}$  and  $10^{-2}$ , respectively. Determining which is the best method depended on one's need for better accuracy (Runge-Kutta) or reduced memory usage (Radau-IIA). However, when simulating a large dynamical system, using a larger time step would greatly reduce the computation time. This advantage outweighs improved accuracy

afforded by the Runge-Kutta method. Therefore, for large systems with LuGre friction, the Radau-IIA method is determined to be the best method for numerical integration.

Chapters 3 and 4 are concerned with the second topic of this thesis. This topic deals with the concepts of energy pumping and energy dissipation in a jointed structure. The hypothesis is that joint friction can be a means to pump low-frequency vibrational energy to high-frequency vibrational energy, through the action of stick-slip oscillations. Since energy can be dissipated faster at higher frequencies, this pumping of energy to excite higher resonances may serve as a tool for increased energy dissipation.

In Chapter 3, a discrete 3DOF system was used to model a jointed structure. To isolate the mechanism that caused stick-slip motion, the frictional interface was modeled using the Stribeck friction model. From numerical simulations of the steady-state forced and free responses, several aspects of the system were observed. In the case of harmonic excitation, the frictional interface produced a stick-slip response that excited internal resonances at odd harmonics of the driving frequency. Second, there was a one-way transfer of energy from one subsystem to the other. Finally, by studying the energies in the 3DOF system, it was shown that, depending on the tuning ratio, friction could pump energy from one frequency to higher frequencies. When the 3<sup>rd</sup> subsystem was tuned to be receptive to these higher frequencies, there was an increase in energy dissipation versus the case where friction was not present. This increase in energy dissipation could lead to an improved damping capacity of the overall system.

The investigation in Chapter 3 was admittedly simple in order to permit a more thorough understanding of the phenomenon. The subsystems were SDOF spring-mass-damper systems and the friction model was of the Stribeck type. In Chapter 4, the

concepts learned in Chapter 3 are applied to a more complicated, and realistic, jointed system. This model incorporates a continuous beam and a floating joint configuration. Furthermore, the multi-mode nature of the beam gives rise to more interesting dynamics.

The analyses done to the beam-mass system of Chapter 4 paralleled that of Chapter 3. The frequency response of the beam-mass system showed the presence of internal resonances. These resonances corresponded to the odd harmonics of the drive frequency coinciding with various modes of the beam. Similar to the energy study in Chapter 3, the energy dissipation of the beam-mass system was evaluated during the free response of the system. However, the result from this simulation was opposite of the results from Chapter 3. In this case, there was poor energy dissipation when the mass subsystem was tuned to the resonances of the beam. Even at the internal resonances, where energy was pumped to the higher modes of the beam, there was worse energy dissipation than when the system was completely mistuned. These surprising results were attributed to the fact that friction was much more efficient in dissipating energy than the modal damping in the beam. The results were also partially confirmed by looking at the controllability of the linear state-space system.

The difference in results between Chapters 3 and 4 demonstrates that the behavior of frictional systems is very sensitive to system parameters and to structural configuration. The last part of Chapter 4 shows that the energy dissipation of the system is sensitive to slight changes in the tuning parameter. Furthermore, the response of the system using the Stribeck model reveals many features that other, simpler friction models do not.

## 5.2 Conclusions and Future Work

Although this thesis is a preliminary study of the behavior of joint friction, it can provide a framework to accurately model and design jointed structures. For example, Chapter 2 presents an analysis of the numerical issues associated with the simulation of a frictional system. Results from this chapter could be useful in simulating a large structural system, especially if the system employs the LuGre friction model.

In Chapters 3 and 4, the models of the jointed structure are general and not specific to any joint geometry. In essence, they represent two structures connected by a frictional interface. This generalization could apply to different joint geometries such as sleeve or revolute joints. Results from Chapters 3 and 4 could lead to design guidelines to enhance energy dissipation in the system. For example, it is shown that friction indeed pumps energy to higher modes. Structural designers should take advantage of this phenomenon whenever possible in order to maximize the passive damping capacity of a system. However, difference in results between Chapters 3 and 4 demonstrates that frictional systems are sensitive to parameter changes, and that design rules will often be application-specific. Lastly, the sensitivity of observed results to friction laws and system tuning reinforces the need to model a system with the appropriate level of detail.

In reality, however, the behavior of a jointed structural system is a large puzzle with many pieces. Many variables and nonlinearities contribute to the actual behavior of such a system. The results of this thesis provide a clue to one of those puzzle pieces.

A natural extension of this thesis is to apply the LuGre friction model to the joint models in Chapters 3 and 4, as well as more complicated structural systems. Furthermore, future studies could employ more complicated friction models as well as

attempt to quantify the contribution of joint friction to the damping of a structural system. Finally, it is important to experimentally study and validate the simulated behavior found in this study. Ultimately, observations of space-deployed structures are needed to confirm the predictions of numerical simulations.

## REFERENCES

- [1] Dubowsky, Steven, "Dealing With Vibrations in the Deployment Structures of Space Robotic Systems," *5<sup>th</sup> International Conference on Adaptive Structures*, Sendai, Japan, December 5-7, 1994.
- [2] NASA Fact Sheet, FS-1996-08-09-LaRC, August, 1996.
- [3] Lake, Mark S., Lee D. Peterson, M. Roman Hachkowski, Jason D. Hinkle, and Lisa R. Hardaway, "Research on the Problem of High-Precision Deployment for Large-Aperture Space-Based Science Instruments," *Space Technology and Applications International Forum*, Albuquerque, New Mexico, January 25-29, 1998.
- [4] Warren, Peter A., "Sub-Micron Non-Linear Shape Mechanics of Precision Deployable Structures," Ph.D. Dissertation, University of Colorado, Boulder, 1996.
- [5] Silver, Mark J., Lee D. Peterson, and Lisa M.R. Hardaway, "Picometer Scale Spontaneous Vibrations in a Deployable Boom Under Thermal Loading," *42<sup>nd</sup> Structures, Structural Dynamics and Materials Conference*, Seattle, Washington, April 16-19, 2001.
- [6] Hardaway, Lisa M.R. and Lee D. Peterson, "Nanometer Scale Spontaneous Vibrations in a Deployable Truss Under Mechanical Loading," *42<sup>nd</sup> Structures, Structural Dynamics and Materials Conference*, Seattle, Washington, April 16-19, 2001.
- [7] Ungar, E.E., "The Status of Engineering Knowledge Concerning the Damping of Built-up Structures," *Journal of Sound and Vibration*, vol. 26, pgs. 141-154, 1973.
- [8] Beards, C.F., "Damping in Structural Joints," *The Shock and Vibration Digest*, vol. 24, pgs. 3-7, 1992.
- [9] Ferri, A.A. and B.S. Heck, "Analytical Investigation of Damping Enhancement Using Active and Passive Structural Joints," *AIAA Journal of Guidance, Control, and Dynamics*, vol. 15, no. 5, pgs. 1258-1264, 1992.
- [10] Gaul, L. and R. Nitsche, "Friction Control for Vibration Suppression," *Mechanical Systems and Signal Processing*, vol. 14, no. 2, pgs. 139-150, 2000.
- [11] Gaul, L. and R. Nitsche, "The Role of Friction in Mechanical Joints," *Applied Mechanics Reviews*, vol. 54, pgs. 93-105, 2001.

- [12] Folkman, S.L. and F.J. Redd, "Gravity Effects on Damping of a Space Structure with Pinned Joints," *AIAA Journal of Guidance, Control, and Dynamics*, vol. 13, pgs. 228-233, 1990.
- [13] Folkman, S.L., E.A. Rowsell, and G.D. Ferney, "Influence of Pinned Joints on the Damping and Dynamic behavior of a Truss," *AIAA Journal of Guidance, Control, and Dynamics*, vol. 18, pgs. 1398-1403, 1995.
- [14] Hertz, T.J. and E.F. Crawley, "Displacement Dependent Friction in Space Structural Joints," *AIAA Journal*, vol. 23, pgs. 1998-2000, 1985.
- [15] Ferri, Aldo A., "Modeling and Analysis of Nonlinear Sleeve Joints at Large Space Structures," *AIAA Journal of Spacecraft and Rockets*, vol. 25, pgs. 354-360, 1988.
- [16] Armstrong-Hélouvry, B., P. Dupont, and C. Canudas de Wit, "A Survey of Models, Analysis Tools and Compensation Methods for the Control of Machines with Friction," *Automatica*, vol. 30, no. 7, pgs. 1083-1138, 1994.
- [17] Mitiguy, P.C. and A.K. Banerjee, "Efficient Simulations of Motion Involving Coulomb Friction," *AIAA Journal of Guidance, Control, and Dynamics*, vol. 22, no. 1, January-February, pgs. 78-86, 1999.
- [18] Pfeiffer, F. and C. Glocker, *Multibody Dynamics with Unilateral Contact*, John Wiley and Sons, 1996.
- [19] Ferri, A.A., and B.S. Heck, "Analysis of Stick-Slip Motion in Coulomb Damped Systems Using Variable Structure System Theory," *Proceedings of the 1997 ASME Design and Technical Conferences*, Sacramento, CA, September 14-17, 1997
- [20] Whiteman, W.E. and A.A. Ferri, "Multi-Mode Analysis of Beam-Like Structures Subjected to Displacement-Dependent Dry Friction Damping," *Journal of Sound and Vibration*, vol. 201, no. 3, pgs. 403-418, 1997.
- [21] Ferri, A.A., "Friction Damping and Isolation Systems," *ASME Journal of Vibration and Acoustics*, vol. 117B, June, pgs. 196-206, 1995.
- [22] Dahl, P.R., "Solid friction damping of mechanical vibrations", *AIAA Journal*, vol. 14, pgs. 1675-1682, 1976.
- [23] Gaul, L., J. Lenz, and D. Sachau, "Active Damping of Space Structures by Contact Pressure Control in Joints," *Mechanical Structures and Machines*, vol. 26, no. 1, pgs. 81-100.
- [24] Valanis, K.C., 1971, "A Theory of Viscoplasticity Without a Yield Surface," *Archives of Mechanics*, vol. 23, no. 4, pgs. 171-191.

- [25] Swevers, J., F. Al-Bender, C.G. Ganesman, and T. Prajogo, "An Integrated Friction Model Structure with Improved Presliding Behavior for Accurate Friction Compensation," *IEEE Transactions on Automatic Control*, vol. 45, no. 4, April, pgs. 675-686, 2000.
- [26] Lampaert, V., J. Swevers, and F. Al-Bender, "Modification of the Leuven Integrated Friction Model Structure," *IEEE Transactions on Automatic Control*, vol. 47, no. 4, April, pp. 683-687, 2002.
- [27] Haessig, D.A., Jr. and B. Friedland, "On the modeling and simulation of friction", *ASME Journal of Dynamic Systems, Measurement, and Control*, vol. 113, pgs. 354-362, 1991.
- [28] Canudas de Wit, C., H. Olsson, K.J. Astrom, and P. Lischinsky, "A New Model for Control of Systems with Friction," *IEEE Transactions on Automatic Control*, vol. 40, no. 3, pgs. 419-425, 1995.
- [29] Gendelman, O., L.I. Manevitch, A.F. Vakakis, and R. M'Closkey, "Energy Pumping in Nonlinear Mechanical Oscillators: Part I – Dynamics of the Underlying Hamiltonian Systems," *ASME Journal of Applied Mechanics*, vol. 68, pgs. 34-41, 2001.
- [30] Onoda, Junjiro, Tetsuji Sano, and Kenji Minesugi, "Passive Vibration Suppression of Truss by Using Backlash," *The 34<sup>th</sup> AIAA/ASME/ASCE/AHS/ASC Structures, Structural Dynamics, and Materials Conference*, La Jolla, CA, April 19-22, 1993.
- [31] Ferri, A.A. and E. H. Dowell, "Frequency Domain Solutions to Multi-Degree-of-Freedom, Dry Friction Damped Systems," *Journal of Sound and Vibration*, vol. 124, no. 2, pgs. 207-224, 1988.
- [32] Kokotovic, P., H. Khalil, and J. O'Reilly, *Singular Perturbation Methods in Control: Analysis and Design*, Academic Press, London, 1986.
- [33] Forsythe, G., M. Malcolm, and C. Moler, *Computer Methods for Mathematical Computations*, Prentice-Hall, New Jersey, 1977.
- [34] Kahaner, D., C. Moler, and S. Nash, *Numerical Methods and Software*, Prentice-Hall, New Jersey, 1989.
- [35] Faires, J.D. and R. Burden, *Numerical Methods, 2nd Edition*, Brooks/Cole Publishing Co., Pacific Grove, CA, 1998.
- [36] Hairer, E. and G. Wanner, *Solving Ordinary Differential Equations II: Stiff and Differential-Algebraic Problems*, Springer-Verlag, Berlin, 1991.

- [37] Bindemann, A.C., and A.A. Ferri, "The Influence of Friction Models on the Passive Damping and Dynamic Response of a Flexible Beam Structure," *Proceedings of the 36th AIAA/ASME/ASCE/AHS/ASC Structures, Structural Dynamics, and Materials Conference*, New Orleans, LA April 10-12, pgs. 180-189, 1995.
- [38] Ibrahim, R.A., "Friction Induced Vibration, Chatter, Squeal, and Chaos: Part I – Mechanics of Friction," *Applied Mechanics Reviews*, vol. 47, no. 7, pgs. 209-253, 1994.
- [39] Nayfeh, Ali Hasan, and Dean T. Mook, *Nonlinear Oscillations*, John Wiley and Sons, New York, 1979.
- [40] Ginsberg, Jerry H., *Mechanical and Structural Vibrations*, 1<sup>st</sup> ed., John Wiley and Sons, New York, 2001.
- [41] Chen, Chi-Tsong, *Linear System Theory and Design*, 3<sup>rd</sup> ed., Oxford University Press, New York, 1999.